

Modeling and Control of Joint-Actuated Buoys

by Roger Cortesi

B.S. in Mechanical Engineering, June 1999, Massachusetts Institute of Technology
M.S. in Mechanical Engineering, September 2000, Massachusetts Institute of Technology

A Dissertation submitted to

The Faculty of
The School of Engineering and Applied Science
of The George Washington University
in partial satisfaction of the requirements
for the degree of Doctor of Philosophy

May 20, 2012

Dissertation directed by

Dr. David Chichka

Assistant Research Professor of Engineering

The School of Engineering and Applied Science of George Washington University certifies that Roger Cortesi has passed the Final Examination of the degree of Doctor of Philosophy as of 15 February 2012. This is the final and approved form of the dissertation.

MODELING AND CONTROL OF JOINT-ACTUATED BUOYS

Roger Cortesi

Dissertation Research Committee:

David Chichka, Assistant Research Professor of Engineering,

Dissertation Director

Pinhas Ben-Tzvi, Assistant Professor of Engineering and Applied Science,

Committee Member

Azim Eskandarian, Professor of Engineering and Applied Science,

Committee Member

Eric Justh, Electronics Engineer, Naval Research Laboratory, Washington DC,

Committee Member

James Lee, Professor of Engineering and Applied Science,

Committee Member

Adam Wickenheiser, Assistant Professor of Engineering and Applied Science,

Committee Member

Dedication

To my family. Thank you for your patience and support.

Acknowledgments

This research would not have been possible without the support of numerous people and groups. I would like to thank Dr. David Chichka and Dr. Eric Justh for all their assistance, ideas, suggestions, and guidance. The staff of the Naval Academy's Hydrodynamics laboratory were particularly helpful and generous with their resources. I would like to thank Kenan Cole for her help in conducting the testing at the Hydrodynamics Laboratory. The Naval Research Laboratory's Edison Program for supporting the work. I would like to thank Dr. Jeffrey Heyer for suggesting the question which started this investigation. And most of all, I would like to thank my wife Jen, for all her support throughout this process.

Abstract

Our motivation is the practical problem of aiming a payload on a small floating buoy at an arbitrary point in the sky. The buoy payload might be a camera, a directional antenna, or some other sensor with a narrow field of view. Such a sensor could, for example, perform some meteorological measurements of the air column above the ocean surface, or provide directional communications with a satellite in a remote sensing application.

Specifically, we develop a control law which solves the pointing and stabilization problem for a particular two-body buoy configuration. The buoy's mechanical design is central to the development as well. The buoy configuration considered here is a long cylindrical buoy with a driven two axis universal joint near the middle. The buoy is ballasted to float upright and the joint is used to stabilize the buoy such that the payload can be pointed at any point within 35 degrees of the vertical.

A numerical model and simulation framework are developed to experiment with control strategies for this system. The dynamics and kinematics of the two-body buoy problem are derived as a self-contained system. The external forces and moments modeled by the simulation are buoyancy, gravity, and drag. Additionally, the effects of regular and irregular surface waves are also modeled. Several experiments are conducted to inform and validate the numerical model of the buoy dynamics.

Both a sliding mode control law with feed forward (SMC+FF) and a proportional integral and derivative control law with feed forward (PID+FF) seem to be able to control the payload well. The feed forward term allows the SMC or PID elements of the control law to handle only the disturbance rejection needs.

The buoy system's simulated performance in regular and irregular seas is mixed. If there is significant wave energy at the buoy's resonant frequency, the buoy becomes uncontrollable. This is not a function of the control law, but rather of the passive characteristics of the buoy's structure.

Additionally the effects of system latency, control rate, initial condition, actuator acceleration limits, and payload position with respect to the vertical are all compared and characterized.

An alternate joint design of an "elevation over azimuth" joint was considered and discarded. An alternate method of solving for the system dynamics in the simulation using constraint equations was implemented and evaluated, as well.

Table of Contents

Dedication	v
Acknowledgments	vii
Abstract	ix
Table of Contents	xi
List of Figures	xv
List of Tables	xix
List of Acronyms	xxi
1 Chapter 1 - Introduction	1
1.1 Motivating Example	2
1.2 Dissertation Outline	3
1.3 Relevant Literature	4
1.4 The Design Process	6
2 Chapter 2 - Model Derivation	9
2.1 Simulation Geometry	9
2.2 Model Dynamics (6DOF)	11
2.3 Buoyant Forces and Moments	17
2.4 Gravity Forces and Moments	23
2.5 Drag Forces and Moments	24
2.6 Modeling Wave Effects	25
2.7 Joint Kinematics	27
2.8 Joint Axis Controller Model	32
2.9 Estimating the Structure's Resonant Peak	33
2.10 Model Summary	34
3 Chapter 3 - Model Verification	39
3.1 Small Test Cylinder Experiment	39
3.2 Large Test Cylinder Experiment	45
3.3 Resonant Peak Comparison	55
3.4 Model Validation Summary	57

4	Chapter 4 - Buoy Control Laws	59
4.1	Sliding Mode Theory	61
4.2	SMC+FF Control Law	67
4.3	PID+FF Control	71
4.4	The Integral Gain K_i	71
4.5	Feed Forward Gain K_{ff}	72
4.6	Composite Pointing Error	73
4.7	Guaranteeing SMC Stability	75
5	Chapter 5 - Simulation Results	81
5.1	Prototype Buoy Configuration	82
5.2	SMC Gain Search	86
5.3	Control Rate Effects	90
5.4	System Latency Effects	91
5.5	Fin Effects	92
5.6	Yaw Damper Effects	93
5.7	Acceleration Limit Effects	95
5.8	Initial Condition Effects	96
5.9	Vertical Angle Effects	100
5.10	PID+FF Control Results	101
5.11	Vertical Oscillation Results	103
5.12	Regular Ocean Wave Effects	104
5.13	Irregular Ocean Wave Effects	112
5.14	Results Summary	120
6	Chapter 6 - Other Design and Modeling Issues	121
6.1	Perfect vs. Imperfect State Information	121
6.2	System CM Location	121
6.3	El. Over Az. Joint vs. a Universal Joint Configuration	122
6.4	Joint Motion in SMC vs. PID Control	124
6.5	Hydrodynamic (Added) Mass Effects	125
7	Chapter 7 - Conclusions & Future Work	131
7.1	Conclusion	131
7.2	Future Work	133
	References	135
	Appendices	139
A	Appendix A - Modeling Ocean Waves	139
A.1	Regular Waves	139
A.2	Irregular Waves	143
A.3	Pierson-Moskowitz Spectral Distribution	144
B	Appendix B - Additional Buoy Sizes	147

C	Appendix C - Detailed Joint Controller Discussion	151
C.1	The Primitive Motion Model	151
C.2	Acceleration Control	151
C.3	Velocity Control	152
C.4	Position-Velocity Control	153
D	Appendix D - Solutions By Constraint Equations	163
D.1	Planar Solution Using Constraint Equations	163
D.2	Spatial Solution Using Constraint Equations	171
E	Appendix E - Use of a Tuned Mass Damper	179
F	Appendix F - Large Cylinder Trial Data	187

List of Figures

1.1	The Motivating Example for the Problem	2
1.2	Alternative Possible Design Choices	7
2.1	Buoy Model Coordinate Systems and Significant Vectors	10
2.2	The 5 Buoyant Cases for a Cylinder	19
2.3	Parameters for Calculating the Submerged Volume of a Cylinder	21
2.4	The Two Universal Joint Angle Pairs: $\{\phi_x, \phi_y\}$ and $\{\phi_v, \phi_z\}$	29
2.5	Maximum Joint Vertical Angle vs. Joint Azimuth Angle	31
3.1	The Small Test Cylinder	40
3.2	A Typical Small Cylinder Trial Video and Animation	41
3.3	Simulation of Small Cylinder with Linear and Quadratic Drag Terms	43
3.4	Small Cylinder Simulation with Offset CM	44
3.5	The assembly drawing of the large instrumented cylinder.	47
3.6	Filtered and Unfiltered Roll and Pitch Measurements for Trial B	48
3.7	Large Cylinder Inclined Release Trial B Video Frames	49
3.8	Large Cylinder Inclined Release Trials B, F, J, and N	50
3.9	Large Cylinder Inclined Release Trials, The First 15 Seconds	51
3.10	Large Cylinder Yaw Rate Trials E, H, and I	52
3.11	Large Cylinder Vertical Translation Trials D, L, and M	53
3.12	Large Cylinder Vertical Translation Trials D, L, and M, the first 20 seconds	54
3.13	Large Cylinder Small Wave Tank Trials O, P, and Q: Pitch and Roll Angles	54
3.14	Large Cylinder Small Wave Tank Trials O, P, and Q: Vertical Acceleration	55
3.15	Large Cylinder Large Wave Tank Trial T Video Frames	56
4.1	A phase portrait of an SMC system.	62
4.2	Chattering in an SMC system	63
4.3	Commanded, Payload, and Joint Azimuth Angles	69
4.4	Payload Reference Angles and Joint Axis Angles for Different K_{ff} Values	74
4.5	The System Used to Guarantee SMC Stability	76
4.6	The SMC controller model $h(\mathbf{x})$ w/ and w/o f_{sub} effects.	78
4.7	The SMC controller model $h(\mathbf{x})$ and $g(\mathbf{x})$ vs. Payload Angle.	79
4.8	The minimum magnitude of $k(\mathbf{x})$ to guarantee stability.	80
5.1	Images from the animated results of the numerical simulation.	82
5.2	The Housing and Payload Sections of the Prototype Buoy	83
5.3	The Complete Prototype Buoy	84
5.4	One Dimensional Search for SMC Gain C	87
5.5	One Dimensional Search for SMC Gain α	88

5.6	One Dimensional Search for SMC Gain δ	89
5.7	Control Loop Rate Effects Comparison Plot	90
5.8	System Latency Effects Comparison Plot	91
5.9	Passive Yaw Fin Effects Comparison Plot	92
5.10	Active Yaw Damper Effects Comparison Plot	93
5.11	An active yaw damper comparison for the J10 buoy configuration.	94
5.12	Joint Acceleration Limit Effects Comparison Plot	95
5.13	Initial Conditions 1-5	96
5.14	Initial Condition Effects Comparison Plot	97
5.15	Initial Condition and Intermediate Move Effects Comparison Plot	98
5.16	Initial Conditions Effects When Commanded to Vertical First	99
5.17	Vertical Angle Effects Comparison Plot	100
5.18	PID+FF vs. SMC+FF Comparison Plot (prototype buoy)	101
5.19	PID+FF vs. SMC+FF Comparison Plot (J15 buoy)	102
5.20	Buoy Heights for the Vertical Oscillation Test	103
5.21	Composite Payload Error for Regular Seas Trial 1	105
5.22	Wave Elevation for Regular Seas Trial 1	106
5.23	Buoy Heights for Regular Seas Trial 1	106
5.24	Composite Payload Error for Regular Seas Trial 2	108
5.25	Wave Elevation for Regular Seas Trial 2	109
5.26	Buoy Heights for Regular Seas Trial 2	109
5.27	The Buoy's Resonant Peak for Regular Seas	111
5.28	Composite Payload Error for Irregular Seas Trial 1	114
5.29	Wave Elevation for Irregular Seas Trial 1	115
5.30	Buoy Heights for Irregular Seas Trial 1	115
5.31	Composite Payload Error for Irregular Seas Trial 2	116
5.32	Wave Elevation for Irregular Seas Trial 2	117
5.33	Buoy Heights for Irregular Seas Trial 2	117
5.34	Composite Payload Error for Irregular Seas Trial 3	118
5.35	Wave Elevation for Irregular Seas Trial 3	119
5.36	Buoy Heights for Irregular Seas Trial 3	119
6.1	El. Over Az. and Universal Joints Side by Side	122
6.2	Joint Vertical Angle for SMC+FF vs. PID+FF	124
6.3	Using Strip Theory to Calculate the Added Mass of a 3-D Object	127
A.1	Direction of Seas Variables	140
A.2	Wave Height, Velocity, and Acceleration Phase Relationships	141
A.3	A fluid particle's trajectory in the presences of waves.	142
A.4	The Pierson-Moskowitz Spectral Distribution: $H_{1/3} = 1$ to 7 m	145
A.5	The Pierson-Moskowitz Spectral Distribution: $H_{1/3} = 0.25$ to 1.5 m	146
B.1	Nominal Mass Distributions and Joint Locations	148
C.1	PVA Profiles for Equal Discrete Intervals	153
C.2	PVA Profiles for Specified & Unequal Intervals	155
C.3	Acceleration as a Function of Λ	156
C.4	PVA Cost Functions vs. Λ , I	157
C.5	PVA Cost Functions vs. Λ , II	158

C.6	PVA Profiles for Velocity Saturating Response	159
C.7	PVA Profiles for Non-Velocity Saturating Response	160
D.1	The Planar System Geometry	164
D.2	Body and hinge angles vs. time for a planar solution.	170
D.3	Joint Geometry in the Spatially Constrained Equations Model	172
E.1	The Tuned Mass Damper Model for Resonant Response Control	180
E.2	Impulse and Bode Plots with and without a TMD.	183
E.3	Impulse and Bode Plots with and without a TMD.	184
E.4	The Relative Motion of Two TMD Implementations	185
F.1	Large Cylinder Inclined Release Trial B, 55 Seconds	187
F.2	Large Cylinder Inclined Release Trial F, 55 Seconds	188
F.3	Large Cylinder Inclined Release Trial J, 55 Seconds	189
F.4	Large Cylinder Inclined Release Trial N, 55 Seconds	190

List of Tables

2.1	Variables used in the dynamics derivation.	12
3.1	A summary of the large instrumented test cylinder trials.	46
3.2	A comparison of estimated and observed vertical oscillation frequencies. . .	56
4.1	The angular parameters used in the SMC+FF and PID+FF control laws. . .	67
4.2	The feed forward gain values for each buoy configuration.	73
5.1	The prototype buoy mass and geometry parameters.	85
5.2	The roll and pitch angles for each initial condition configuration.	97
5.3	The energy fraction above 3 rad/s for the PM wave spectrum.	112
6.1	Added mass terms for various 2-D shapes.	128
B.1	The mass parameters used by the J series buoy configurations.	148
B.2	The housing and payload lengths for the J series buoy configurations. . . .	149
B.3	The system CM location for the J series buoy configurations.	149
D.1	The variables used in the planar two body system.	166
D.2	The Jacobian and RHS components for solutions by constraint equation. . .	174
E.1	Model parameters for a cylindrical buoy w/ and w/o a tuned mass damper. .	181

List of Acronyms

6DOF	6 Degree of Freedom
CAD	Computer Aided Design
CB	Center of Buoyancy
CM	Center of Mass
DCM	Direction Cosine Matrix
ELAZ	Elevation Over Azimuth
ENU	East North Up
EOM	Equations of Motion
FEA/CDF	Finite Element Analysts / Computational Fluid Dynamics
FF	Feed Forward
HTM	Homogeneous Transformation Matrix
IC	Initial Condition
LHS	Left Hand Side
LQR	Linear Quadratic Regulator
LQI	Linear Quadratic Integrator
NED	North East Down
PID	Position, Integral, Derivative Control
PV	Position-Velocity
PVA	Position, Velocity, and Acceleration
RHS	Right Hand Side
RMS	Root Mean Square
SE(3)	Special Euclidean Group of Rigid Motions in \mathbb{R}^3
SMC	Sliding Mode Control
SO(3)	Special Orthogonal Group of 3×3 matrices

Chapter 1

Introduction

Our motivation is the practical problem of aiming a payload on a small floating buoy at an arbitrary point in the sky. The buoy payload might be a camera, a directional antenna, or some other sensor with a narrow field of view. Such a sensor could, for example, perform some meteorological measurements of the air column above the ocean surface, or provide directional communications with a satellite in a remote sensing application.

Specifically, we develop a control law which solves the pointing and stabilization problem for a particular two-body buoy configuration. The buoy's mechanical design is central to the development as well, and to narrow the trade space, we impose the following restrictions:

1. The buoy is essentially a long cylinder. This is to facilitate deploying it from existing launch mechanisms above and below the water's surface.
2. The payload mass makes up a "significant" portion of the total buoy mass (not necessarily a majority).
3. The payload is required to be mechanically aimed in the desired direction.
4. It is desirable to minimize the number of actuation axes to minimize cost and maximize payload volume.

To study this problem a model is derived for a jointed two body buoy floating in the water. The joint can be actuated in two axes, and our model includes the effects of buoyancy, gravity, and drag for the two-body system. The objective here is not to precisely describe all of these effects (e.g., precise drag or added mass modeling would be very complicated), but instead to supply a sufficiently qualitatively reasonable model for purposes of control law development. As long as the modeling errors are not too extreme, we will rely on feedback control to suppress them.

This dissertation will show that it should be possible to mechanically point and stabilize a payload on a small buoy at an arbitrary point in the sky within approximately 35 degrees of the zenith to an accuracy of 5 to 10 degrees. This made difficult by the non-linear effects of buoyancy, drag, inertia, and surface waves.

The major contributions of this dissertation are:

1. An understanding of and a model for the dynamics of a jointed two body system floating on the ocean's surface in the presence of waves.
2. A pair of control strategies which can be used to stabilize and point such a system.

1.1 Motivating Example

As a motivating example, consider the problem of using a directional antenna on a small buoy to communicate with a satellite for a remote sensing application. In this application, a narrow beamwidth for the antenna might be considered 10 degrees wide. Given this scenario, a reasonable minimum performance threshold might be to point to within one beamwidth (10 degrees) of the satellite. A preferred performance objective would be to point to within half a beamwidth (5 degrees) of the satellite. Additionally, it should be clear from this example that it is desirable to go beyond simply stabilizing the payload about the vertical as the satellite will not always be directly overhead. The electro-magnetic considerations (antenna pattern, transmitter specifications, etc.) of this problem are not part of this work.

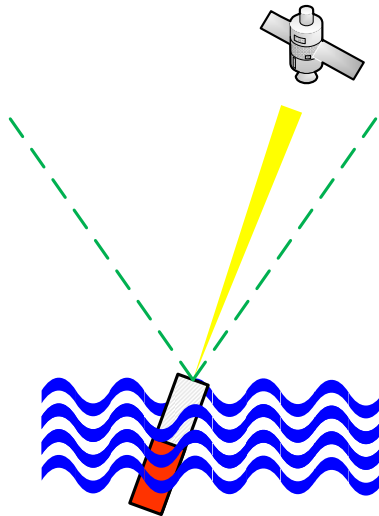


Figure 1.1: As an application example, a small buoy performing directional communication with a satellite in the presence of waves.

Given such a problem, we would like a framework to understand and answer the following questions:

1. How much of the sky can be covered by such a system?
2. How accurately can the payload be pointed?
3. What are the implications on the selection of the structure, actuators, and sensors for the device?
4. Which control laws are appropriate and effective at controlling such a system?
5. What are the critical parameters which drive the design of the system?

In addition to the above requirements, the requirement to point the payload at a non-vertical angle favors a solution which uses buoyant moments to drive the payload to the desired attitude. Buoyant moments are the only moments available to the system which can maintain the payload at a non-vertical angle in *static* equilibrium. Using thrusters or flapping fins as actuators will *not* accomplish the shifting of buoyancy required for static equilibrium at off vertical angles. This need to shift the location of the center of buoyancy

and center of mass of the system is the primary motivation for selecting a jointed buoy to aim the payload.

The ability for the system to put itself in a configuration to passively point in the desired direction, once all the transients have decayed away, results in an active controller which is only responsible for transient suppression, disturbance rejection, and small corrections to the steady state condition. This allows the active controller to be significantly simpler and more effective.

1.2 Dissertation Outline

This dissertation is organized as follows. In Chapter 2 the buoy model is derived. The kinematics of the universal joint connecting the buoy payload and housing are also presented.

In Chapter 3, the results of qualitative experiments undertaken to validate and supply parameters for the analytical buoy model derived in Chapter 2 are presented. Because drag is a major source of model uncertainty for the buoy, a pair of experiments was conducted to inform the choice of, and validate, the implemented drag model. The first experiment used a small non-instrumented cylinder. The second experiment was performed with a larger instrumented cylinder in wave tanks at the US Naval Academy’s Hydrodynamics Laboratory. These experimental results were compared with numerical simulation results, and the model was refined accordingly.

Chapter 4, provide a short introduction to sliding mode control, and in particular, provides a mathematical justification of its robustness to parametric uncertainty and external disturbances. Indeed, formulating the sliding mode controller properly is a key step, as illustrated by a cautionary example of how not to implement a sliding mode controller. Also in this chapter, the nominal prototype buoy configuration we focus on is described and the feedback controllers for the actuated joint connecting the payload and housing are presented. Our primary focus is on a sliding mode controller with feed-forward term (SMC+FF), but a proportional-integral-derivative controller with feed-forward term (PID+FF) is also described for purposes of comparison. A metric for evaluating closed-loop system performance, the composite payload pointing error, is also introduced.

In Chapter 5, numerous simulation results are presented to illustrate the performance of these controllers. In particular, the following effects are considered: (1) control update rate, (2) feedback latency, (3) active and passive yaw damping, (4) joint acceleration limits, (5) initial conditions, (6) commanded pointing angle, (7) SMC+FF vs. PID+FF control, and (8) the effects of regular and irregular ocean waves.

In Chapter 6, various topics arising in the development and implementation of the buoy model are discussed, including (1) the use of perfect state information, (2) the suggested CM location, (3) a comparison between the universal joint and elevation-over-azimuth joint configurations, and (4) a discussion of how “added mass” would affect the buoy.

In Chapter 7 we summarize the conclusions drawn from the research and provide suggestions for future work.

A collection of appendices is also provided. Appendix A presents the derivation of the equations used to describe the sea in the presence of ocean waves using a first order linear model. We are interested in the wave elevation and fluid velocity as functions of time and position. Equations for both regular sinusoidal and irregular waves are included, as is the process for generating models of irregular waves with a spectral content similar to that of the open ocean.

Although we ultimately settled on a particular prototype buoy configuration for the bulk of the numerical studies, prior to that we had developed a family of buoy configurations based on the NATO size A sonobuoy dimensions. This buoy family consists of four buoys of the same size and similar mass distribution, except with the joint at different locations. The details and rationale for these crude “J Series” buoy models are presented in Appendix B.

Appendix C presents the details of the low level actuator controller which models the physical actuators and their associated control circuitry. Like actual motor controllers, this low level controller has a number of different modes. Higher level controllers, like the SMC+FF and PID+FF control laws, interact with actuators through these low level controllers which enforce position, velocity and acceleration limits on the actuator.

Appendix D presents an alternative method of deriving and solving the dynamics and kinematic equations for the two body system using constraint equations. As shown in Chapter 2, the two-body buoy problem is simple enough that its dynamical equations can be derived directly in an intuitively appealing way. However, for more than two bodies, a direct derivation is more involved, and the method of constraint equations may provide a more suitable tool to use.

Appendix E presents an analysis of using a tuned mass damper to improve a cylindrical buoy’s passive response to vertical oscillation. This show that including a tuned mass damper in the buoy’s structure has the potential to significantly improve is performance in various sea states.

Appendix F Contains the detailed plots showing the large instrumented cylinder’s performance in roll and pitch for the four included release tests.

1.3 Relevant Literature

There is a significant body of work on the practice of pointing antennas at satellites from moving vehicles. A maritime example is described by Timothy et al. in their U.S. Patent [27]. They describe an elevation over azimuth mechanism for pointing the antenna via a pair of servo motors. They include provisions for sensing the antenna’s attitude directly to improve servo stiffness. Finally, they use the pointing errors in the antenna to find the direction of maximum signal strength. This example is typical in that it assumes the antenna mass is small compared with the mass of the vessel. Therefore, the movement of the antenna does not impart any motion on the vessel. Tseng and Teo present a fuzzy logic controller for ship based antenna pointing in [28]. Here again an elevation over azimuth mechanism is used and the antenna pointing dynamics do not affect the platform’s dynamics.

For the concept of pointing a directional antenna at a satellite from a floating buoy, the closest match in the literature is by Frye et al. in their technical report on “Design and Evaluation of Directional Antennas on Ocean Buoys” [6]. However, this work concentrates on the RF design of the antenna and laboratory testing of a mechanical, azimuth only, servo mechanism. This system was designed with an antenna beamwidth of ± 15 degrees in azimuth and elevation. It assumed the antenna would be mechanically steered with an elevation over azimuth mechanism. It also assumed that the buoy would be large enough that the motion of the antenna would not influence the motion of the buoy. The shape of the buoy was assumed to be a large discus approximately 3 m in diameter.

Using a multibody buoy structure to position an antenna is proposed by Briguglio in [5]. In this system the antenna is an omni-directional antenna and it is mounted on a

four bar linkage with the flotation body in the middle and a counterweight on the other end. This pantograph linkage unfolds by spring action and gravity from the buoy’s housing. Its purpose is to raise the antenna to a sufficient height for a sensor to have a view over the ocean waves, while at the same time, providing the sensor with isolation from the angular displacement due to wind and waves. This is an implementation of a multibody buoy for antenna stabilization, however, it is in no way suitable for solving the problem in our notional scenario.

Developing a control strategy for the two body buoy requires a framework for solving the dynamics of a multibody system. The approach we take (in Chapter 2) involves directly solving for the dynamics of the buoy payload in terms of the housing body. This solution is presented using a Lie group formulation similar to Galloway, Cortesi, and Justh in [22] and Leonard in [16]. The advantage of this formulation lies in providing physical insight into system.

Alternatively, multibody dynamics problems can be solved using a constraint equation approach (which is discussed in Appendix D). This requires three steps: (1) derive the equations of motion (EOM) for each body as if it is a single isolated body; (2) derive the set of kinematic constraint equations which specify the relationships between the connected bodies; and (3) simultaneously solve the combined system of EOMs and constraint equations at each time step to determine the system’s trajectory. Nikravesh in [20] is the authoritative reference on this approach.

Our two body buoy problem is fundamentally an attitude control problem. There is a significant body of work on multibody attitude control of spacecraft and underwater vehicles.

Leonard [16] presents the dynamics and control of a single body underactuated spacecraft and a single body underactuated underwater vehicle, and also uses a Lie group formulation of the system to inform the choice of control laws. In particular, the use of roll and pitch effects to drive a change in yaw motion is demonstrated. Another example involving an underactuated underwater vehicle is discussed by Leonard in [17].

In [23], M. Romano and B.N. Agrawal discuss the dynamics and control of a dual body spacecraft in which the two bodies are connected by a single degree of freedom rotational joint. Their concept is to use the satellite as an optical relay to redirect a ground based laser from one ground station to another. Some notable differences between this system and our buoy system are: (1) In the spacecraft, *both* bodies need to be aimed at their respective targets. (2) In the spacecraft the center of mass of both bodies is at the joint. Therefore rotating the joint does not change the location of the system’s center of mass. (3) The joint is a single degree of freedom joint in the spacecraft. (4) The spacecraft uses Variable Speed Control Moment Gyros to manipulate the craft’s total angular momentum to control its attitude.

L. S. Wang and P. S. Krishnaprasad, in [31], present the dynamics of a dual body spacecraft connected by a three degree of freedom spherical joint. The spacecraft is controlled by rotors on each body, including driven and damping rotors. Additional damping is placed on the joint. The dynamics and control of this system is presented using a Lie group formulation.

Our buoy problem can be differentiated from the cases presented above in that our buoy must contend with the free surface effects of water. This includes the buoyant and drag moments which are non-linear functions of buoy position and attitude. For modeling ocean waves and their effects on structures, Faltinsen [8] is an excellent reference. Additionally, Fossen [9] is another useful reference.

For discussion and guidance on implementing numerical six DOF simulations there are many references used by aeronautical engineers. Stevens and Lewis [26] is an excellent example of one such reference. It covers the modeling, dynamics, and kinematics of a 6 DOF system in a variety of coordinate systems (NED, WGS84, and ECEF). It also includes an excellent summary of the relationships between Euler angles, direction cosine matrices, and quaternions.

We considered three principal control schemes for our buoy problem: Proportional-Integral-Derivative (PID), the Linear Quadratic Regulator (LQR) and its variants, and Sliding Mode Control (SMC).

PID control is one of the most widely implemented control schemes due to its simple implementation and robust performance with respect to disturbances for single variable systems. Much has been written about PID control in both its continuous and discrete forms. Dorf [4, Chapter 12] and Ogata [21, Section 3.5] introduce the PID controller in its continuous and discrete form respectively. An application note [1] for a Maxon brand positioning controller describes a PID implementation which is representative of current best practice in industry, including the controller’s anti-windup features and the benefits of using a feed forward gain to improve the system’s response.

Prior to settling on the sliding mode controller, we considered various forms of the Linear Quadratic Regulator (LQR). Again Stevens and Lewis [26, Chapter 5.3] is useful as it presents many practical considerations for using LQR controllers. Additionally, [26, Chapter 5.4] introduces a linear quadratic tracker for tracking non-zero reference signals. A linear quadratic integrator (LQI) presented by Young and Willems in [33] is another method to track non-zero reference signals. This LQI approach is implemented by MATLAB’s LQI function. Friedland [11] is another excellent reference on LQR control.

We have found sliding mode control to be a highly effective approach for our buoy problem. SMC is introduced in Khalil [14, Section 14.1]. Utkin [29] is a very complete treatment of sliding mode control. In particular [29, Chapter 5] covers SMC in linear systems and [29, Chapter 8] discusses solutions to the chattering problem. Finally, Young, Utkin and Ozguner in [13] provide a concise summary of some advanced sliding mode topics.

Due to the small buoy size proposed in this research, the system is sensitive to the high frequency energy of the ocean waves at frequencies higher than is typically reported in the literature. Some of the highest reported spectral content is presented by Robinson et. all in [30]. Their spectral estimates are limited to data collected up to 2.2 rad/sec (a 2.9 second period). While this is significantly higher than the 1 rad/sec presented by most texts, it is still significantly short of the resonant frequency for the size buoys envisioned here.

Steel and Earl present work on estimating wave spectra from magnetic field measurements made by a buoy in [25]. Here the buoy was 3 meters in diameter and spectral content was only characterized up to 0.68 rad/sec (a period of 10 seconds).

1.4 The Design Process

The design process comprised the following steps:

1. Pick desired primary system requirements for system geometry and performance.
2. Derive, from first principles, the system dynamics to build a “truth model” in simulation. This truth model is used to develop and test the proposed solutions. As part of this model development process, it is important to:

- (a) Identify areas of the model with the most uncertainty or in which significant approximations are made.
 - (b) Devise experiments to reduce the model’s uncertainty (or at least bound it) and validate any significant approximations.
 - (c) Quantitatively and qualitatively compare the tuned model with reality as much as possible.
3. Use the “features” of the system dynamics to inform the selection of the structure, actuators, and control schemes of the device. In this problem, the “features” of the dynamics include the effects of symmetry, the existence of a preferred direction due to gravity and buoyancy, and the significant rotational coupling between the axes.
 4. Use the truth model to explore the limits of the proposed solution by numerical simulation.
 5. Repeat some or all of these steps as time, money and performance permit or require to refine the model and solution.

The possibilities for the physical implementation to solve the problem posed by the motivational example encompass a wide variety of configurations. Figure 1.2 shows some of the design choices which could have been made in attempting to solve this problem. The choices which are presented in detail in this work are in yellow. Some alternate choices which also presented here (though in less detail) are shown in blue.

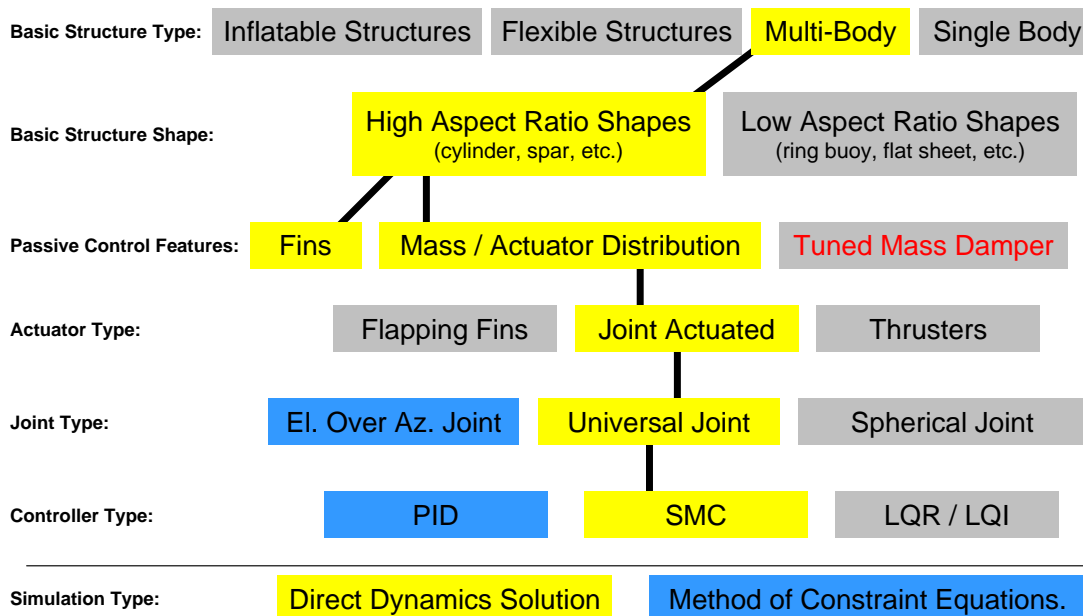


Figure 1.2: Some of the high level design choices selected in this work. Choices in yellow are presented in detail, choices in blue were considered and tested as alternatives, but ultimately not used in the detailed solution. Choices in gray were not considered in detail. Some analysis was performed for the tuned-mass-damper, but only applying damping to the vertical oscillation of a cylinder and not for the two body buoy system.

Chapter 2

Model Derivation

This chapter presents the numerical simulation model for the buoy system. Section 2.1 introduces the notation used to describe the geometry of the problem. Section 2.2 derives a self-contained system for the dynamics of the coupled two body buoy system, including the inertial effects between the bodies, and external forces and moments.

The external forces and moments that are applied to the system are buoyancy, gravity, and drag. The buoyancy calculations are covered in Section 2.3, gravity in Section 2.4 and drag in Section 2.5.

Up to this point in the model derivation, the details of the joint configuration have not been required. In Section 2.7, the kinematics of a universal joint is derived. The numerical simulation also models a low level controller for each joint axis actuator. The highlights of this low level controller are presented in Section 2.8. The details of the low level controller implementation are in Appendix C. Section 2.9 derives some simple expressions for estimating the resonant frequency at which the buoy will bob up and down in the water. Finally, Section 2.10 summarizes the equations and procedure for implementing a numerical model of the buoy system.

Hydrodynamic “added mass” effects are *not* explicitly included in this derivation and added mass effects were not included in the numerical simulations. A further discussion of how added mass would effect the buoy and the rationale for neglecting it in this work is presented in Section 6.5.

2.1 Simulation Geometry

2.1.1 Buoy Geometry

The buoy system is modeled as a pair of rigid cylinders connected by a joint. Body 1 is the buoy housing (the lower cylinder). Body 2 is the payload (the upper cylinder). Each body has a body coordinate system located on its bottom face. The body coordinate system’s Z axis points along the long axis of the body. Each body also has a pivot point associated with it. The pivot point on the housing is described by the vector \mathbf{R}_{J1} in the housing coordinate system. The pivot point on the payload is specified by the vector \mathbf{R}_{J2} in the payload coordinate system.

The bodies’ roll and pitch angles are measured about the cylinder’s X and Y axes respectively with respect to the horizontal.

The navigation (or global) coordinate system used in this model is a tangent plane coordinate system of the East-North-Up type. The navigation system’s x axis points east,

its y axis points north, and its z axis points up. The x-y plane of the navigation coordinate system is located at the mean water height of the ocean surface. Additionally, in this research, yaw angles are referenced counter-clockwise from the x axis (East) to keep all calculations in right handed coordinate systems.

Figure 2.1 shows the major variables used in defining the buoy geometry. Table 2.1 lists the geometry variables in the model. Upper case vectors are in the housing or payload body frames. Lower case vectors are in the navigation frame. The attitudes of each cylinder are tracked and specified using direction cosine matrices.

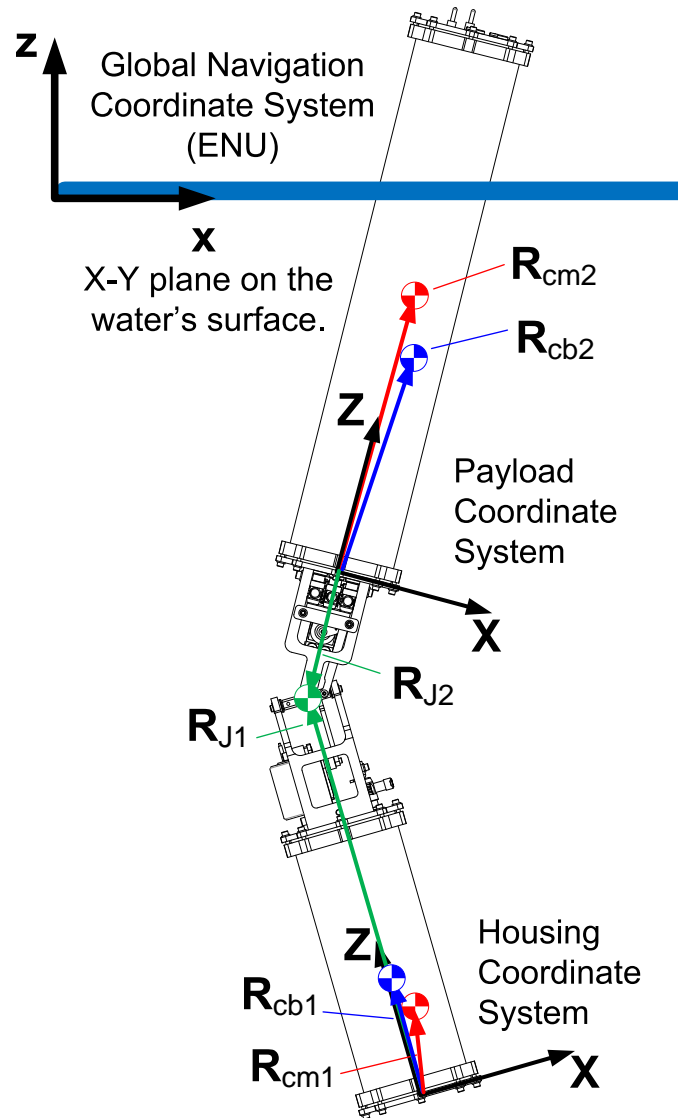


Figure 2.1: The significant coordinate systems for the buoy model. Vectors in the housing and payload reference frames are upper case. Vectors in the navigation reference frame are lower case.

The values associated with each body include: mass, radius, length, center of mass (CM) location, an inertia tensor, and the location of the pivot point.

2.1.2 Vertical Angle vs. Elevation Angle

When discussing traditional pan/tilt units typically used for camera or antenna pointing applications, it is common to specify the angle in the vertical plane as the *elevation* angle. The elevation angle specifies the angle above the horizon. At an elevation angle of zero, the system is pointing at the horizon. An elevation angle of 90 degrees means the system is pointing straight up at the zenith. Throughout this research, angles in the vertical plane are referred to as *vertical* angles. **The vertical angle is NOT the same as the elevation angle.** The vertical angle is measured from the *zenith*. Thus it measures deflection away from vertical. If the vertical angle is zero then the system is pointing straight up. A vertical angle of 90 degrees is pointing at the horizon. A similar distinction can be made about the joint angles. A *joint vertical angle* can be used to describe the amount of misalignment between the housing and payload sides of the joint. If the joint vertical angle is zero, then the housing and payload long axes are co-linear. Likewise for a joint vertical angle of 90 degrees, the housing and payload long axes are perpendicular to each other.

2.2 Model Dynamics (6DOF)

This section derives a self-contained system for the rotational and translational accelerations of the buoy system. The buoy is modeled as a pair of rigid bodies connected by a joint. This self-contained system can then be numerically integrated forward in time to generate the buoy velocity and position trajectories.

A two body system has 12 degrees of freedom (DOFs). Each body has 3 translational and 3 rotational DOFs. A joint connecting the two bodies, which only allows rotation, constrains relative translation between the bodies. This removes 3 DOFs from the system. If the joint is a 3 axis joint, then no further reduction in the system's DOFs occur. If the joint is a two axis joint, then one more DOF is removed from the system, resulting in a two body system with 8 degrees of freedom.

Consider a state vector for the full system given by $\mathbf{x}_{full} = [\mathbf{d}_0 \ \phi_2 \ \phi_J]^T$ ($\mathbf{x}_{full} \in \mathbb{R}^8$), and an unspecified (for now) control input vector, \mathbf{u} ($\mathbf{u} \in \mathbb{R}^2$). In this state vector the translational degrees of freedom are specified by the coordinates of the joint in the navigation frame, \mathbf{d}_0 . The rotational degrees of freedom are specified by the vector of the payloads attitude angles in the navigation frame, ϕ_2 , and the vector of joint axis angles, ϕ_J .

The dynamics for such a system will evolve according to a nonlinear system with the general form

$$\ddot{\mathbf{x}}_{full}(t) = f(\mathbf{x}_{full}(t), \dot{\mathbf{x}}_{full}(t), \mathbf{u}(t), \dot{\mathbf{u}}(t), \ddot{\mathbf{u}}(t), t), \quad (2.1)$$

where we have assumed that the effects of derivatives higher than those in (2.113) are negligible and we assume that $\ddot{\mathbf{u}}(t)$ is piecewise continuous.

This is the system that the numerical simulation must model accurately to serve as a truth model for system development. The controller design will require a simplified form of this model.

For the purposes of model derivation and numerical simulation, the rotational states are calculated using direction cosine matrices (DCMs) instead of the individual angles. While this increases the number of variables it does not change the fundamental number of degrees of freedom represented by the truth model.

2.2.1 Variables and Matrix Properties

Table 2.1 defines the variables used in this dynamics and kinematic analysis.

Table 2.1: The variables used for the model's dynamics analysis.

Parameter	Joint	Housing	Payload
Body CM Location (body frame)		\mathbf{R}_{cm1}	\mathbf{R}_{cm2}
Body CB Location (body frame)		\mathbf{R}_{cb1}	\mathbf{R}_{cb2}
Body Joint Location (body frame)		\mathbf{R}_{J1}	\mathbf{R}_{J2}
Attitude Direction Cosine Matrix	\mathbf{B}	\mathbf{B}_1	\mathbf{B}_2
Rotational Velocity Vector (body frame)	$\mathbf{\Omega}$	$\mathbf{\Omega}_1$	$\mathbf{\Omega}_2$
Rotational Acceleration Vector (body frame)	$\mathbf{\dot{\Omega}}$	$\mathbf{\dot{\Omega}}_1$	$\mathbf{\dot{\Omega}}_2$
Body Inertia Tensor <i>About the Body CM</i>		\mathbf{J}_h	\mathbf{J}_p
Body Inertia Tensor <i>About the System CM</i>		\mathbf{J}_1	\mathbf{J}_2
Joint Torques (body frame)		\mathbf{T}_1	\mathbf{T}_2
External Torques (body frame)		\mathbf{T}_{ext1}	\mathbf{T}_{ext2}
Body CM (navigation frame)		\mathbf{r}_1	\mathbf{r}_2
Joint Forces (navigation frame)		\mathbf{f}_1	\mathbf{f}_2
External Forces (navigation frame)		\mathbf{f}_{ext1}	\mathbf{f}_{ext2}
Body Mass		m_1	m_2
Joint Position (navigation frame)	\mathbf{d}_0		
Joint to Body CM Vector (body frame)		\mathbf{D}_1	\mathbf{D}_2

The kinematic relationship between orientation and angular velocity is

$$\mathbf{\dot{B}} = \mathbf{B}\hat{\mathbf{\Omega}}, \quad (2.2)$$

where \mathbf{B} is a member of the Special Orthogonal Group $SO(3)$, where

$$SO(3) = \{ \mathbf{B} \in \mathbb{R}^{3 \times 3} \mid \mathbf{B}^T \mathbf{B} = \mathbf{I} \text{ and } \det \mathbf{B} = 1 \}. \quad (2.3)$$

Note that a direction cosine matrix is automatically an element of $SO(3)$.

The hat operator transforms a vector in \mathbb{R}^3 into a skew symmetric matrix, ie.,

$$\hat{\mathbf{a}} = \begin{bmatrix} 0 & -a_3 & a_2 \\ a_3 & 0 & -a_1 \\ -a_2 & a_1 & 0 \end{bmatrix}. \quad (2.4)$$

In addition,

$$\hat{\mathbf{a}}\mathbf{b} = \mathbf{a} \times \mathbf{b}, \quad (2.5)$$

where \times denotes the vector cross product, and we have

$$\hat{\mathbf{a}}\mathbf{a} = \mathbf{0}. \quad (2.6)$$

Since $\hat{\mathbf{a}}$ is skew symmetric, we have

$$\hat{\mathbf{a}}^T = -\hat{\mathbf{a}}, \quad (2.7)$$

and we also have the identity

$$\mathbf{B}\hat{\mathbf{a}}\mathbf{B}^T = \widehat{\mathbf{B}\mathbf{a}}. \quad (2.8)$$

where $\mathbf{B} \in SO(3)$.

The joint DCM is related to the housing and payload attitudes by:

$$\mathbf{B} = \mathbf{B}_1^T \mathbf{B}_2. \quad (2.9)$$

A vector \mathbf{Q} in one coordinate system can be converted to a vector \mathbf{q} in an alternate coordinate system using a homogeneous transformation matrix (HTM). The HTM is a member of the Special Euclidean Group $SE(3)$. Members of $SE(3)$ can be used to apply translations and rotations to rigid bodies. In the HTM the direction cosine matrix, \mathbf{B} , applies the rotation, and the vector, \mathbf{r}_0 , applies the translation.

$$\begin{bmatrix} \mathbf{q} \\ 1 \end{bmatrix} = \begin{bmatrix} \mathbf{B} & \mathbf{r}_0 \\ 0 & 1 \end{bmatrix} \begin{bmatrix} \mathbf{Q} \\ 1 \end{bmatrix}, \quad (2.10)$$

or equivalently, $\mathbf{q} = \mathbf{B}\mathbf{Q} + \mathbf{r}_0$. If the vector is a “free” vector, i.e. not tied to a particular point in the coordinate system, then the only the rotational part of the transformation needs to be applied. As an example, consider a force vector in the housing coordinate system, \mathbf{F}_h . \mathbf{F}_h can be converted to the payload coordinate system through the joint direction cosine matrix by $\mathbf{F}_p = \mathbf{B}^T \mathbf{F}_h$ and back by $\mathbf{F}_h = \mathbf{B} \mathbf{F}_p$. The force could be specified in the navigation frame by $\mathbf{f}_h = \mathbf{B}_1 \mathbf{F}_h$ and $\mathbf{f}_p = \mathbf{B}_2 \mathbf{F}_p$.

2.2.2 Rotation

To calculate and propagate the rotational states of the buoy system we need an expression for the payload’s rotational acceleration, $\dot{\hat{\Omega}}_2$, as a function of the payload rotational velocity, and the joint axes’ position, velocity and acceleration. With this expression we will be able to integrate the payload’s attitude forward in time. To derive this expression, first we will use the kinematic relationships to find expressions for the housing rotational velocity and acceleration, which will allow us to substitute them into the dynamics equations to eliminate the housing variables from the expression for the payload rotational acceleration.

2.2.2.1 Rotational Kinematics

We desire an expression for the housing rotational velocity $\hat{\Omega}_1$, in terms of the joint and payload rotational velocities, $\hat{\Omega}$ and $\hat{\Omega}_2$. Starting by differentiating (2.9) using (2.2) yields

$$\begin{aligned} \mathbf{B} &= \mathbf{B}_1^T \mathbf{B}_2 \\ \dot{\mathbf{B}} &= \dot{\mathbf{B}}_1^T \mathbf{B}_2 + \mathbf{B}_1^T \dot{\mathbf{B}}_2 \\ \mathbf{B} \hat{\Omega} &= (\mathbf{B}_1 \hat{\Omega}_1)^T \mathbf{B}_2 + \mathbf{B}_1^T \mathbf{B}_2 \hat{\Omega}_2 \\ \mathbf{B} \hat{\Omega} &= \hat{\Omega}_1^T \mathbf{B}_1^T \mathbf{B}_2 + \mathbf{B}_1^T \mathbf{B}_2 \hat{\Omega}_2 \\ \mathbf{B} \hat{\Omega} &= \hat{\Omega}_1^T \mathbf{B} + \mathbf{B} \hat{\Omega}_2 \\ \hat{\Omega}_1^T \mathbf{B} &= \mathbf{B} \hat{\Omega} - \mathbf{B} \hat{\Omega}_2 \\ \hat{\Omega}_1^T &= \mathbf{B} (\hat{\Omega} - \hat{\Omega}_2) \mathbf{B}^T \\ \hat{\Omega}_1 &= \mathbf{B} (\hat{\Omega}_2 - \hat{\Omega}) \mathbf{B}^T \\ \hat{\Omega}_1 &= \widehat{\mathbf{B} (\hat{\Omega}_2 - \hat{\Omega})} \\ \hat{\Omega}_1 &= \mathbf{B} (\hat{\Omega}_2 - \hat{\Omega}). \end{aligned} \quad (2.11)$$

We used the identity in (2.8) to get from the 8th to the 9th line.

We can differentiate (2.11) to find the housing acceleration vector, $\dot{\hat{\Omega}}_1$, as:

$$\begin{aligned}
\dot{\hat{\Omega}}_1 &= \dot{\mathbf{B}} (\Omega_2 - \Omega) + \mathbf{B} (\dot{\hat{\Omega}}_2 - \dot{\hat{\Omega}}) \\
&= \mathbf{B} \hat{\Omega} (\Omega_2 - \Omega) + \mathbf{B} (\dot{\hat{\Omega}}_2 - \dot{\hat{\Omega}}) \\
&= \mathbf{B} \hat{\Omega} \Omega_2 + \mathbf{B} \dot{\hat{\Omega}}_2 - \mathbf{B} \dot{\hat{\Omega}} \\
&= \mathbf{B} (\hat{\Omega} \Omega_2 + \dot{\hat{\Omega}}_2 - \dot{\hat{\Omega}}). \tag{2.12}
\end{aligned}$$

2.2.2.2 Rotational Dynamics

Next we can find expressions for the rotational dynamics of the system. Starting by differentiating the angular momentum expression, $\mathbf{h}_2 = \mathbf{B}_2 \mathbf{H}_2$ with $\mathbf{H}_2 = \mathbf{J}_2 \Omega_2$, gives

$$\frac{d\mathbf{h}_2}{dt} = \mathbf{B}_2 (\dot{\mathbf{J}}_2 \Omega_2 + \mathbf{J}_2 \dot{\Omega}_2 + \hat{\Omega}_2 \mathbf{J}_2 \Omega_2), \tag{2.13}$$

so including the $\dot{\mathbf{J}}$ terms in Euler's equations of rigid motion gives:

$$\mathbf{J}_1 \dot{\hat{\Omega}}_1 + \dot{\mathbf{J}}_1 \Omega_1 + \Omega_1 \times \mathbf{J}_1 \Omega_1 = \mathbf{T}_1 + \mathbf{T}_{ext1}, \tag{2.14}$$

$$\mathbf{J}_2 \dot{\hat{\Omega}}_2 + \dot{\mathbf{J}}_2 \Omega_2 + \Omega_2 \times \mathbf{J}_2 \Omega_2 = \mathbf{T}_2 + \mathbf{T}_{ext2}, \tag{2.15}$$

where the torques \mathbf{T}_1 and \mathbf{T}_2 are the joint torques on each body. The torques \mathbf{T}_{ext1} and \mathbf{T}_{ext2} are the external torques on each body (buoyancy, drag, etc.). All these torques are expressed in their respective body coordinates. The joint torques, when expressed in global coordinates, are equal and opposite,

$$\tau_1 = \mathbf{B}_1 \mathbf{T}_1, \tag{2.16}$$

$$\tau_2 = \mathbf{B}_2 \mathbf{T}_2, \tag{2.17}$$

$$\tau_1 = -\tau_2. \tag{2.18}$$

Combining (2.14) and (2.15) via (2.18) results in a fundamental equation of rotational motion for the buoy system of:

$$\mathbf{B}_2 (\mathbf{J}_2 \dot{\hat{\Omega}}_2 + \dot{\mathbf{J}}_2 \Omega_2 + \hat{\Omega}_2 \mathbf{J}_2 \Omega_2 - \mathbf{T}_{ext2}) = -\mathbf{B}_1 (\mathbf{J}_1 \dot{\hat{\Omega}}_1 + \dot{\mathbf{J}}_1 \Omega_1 + \hat{\Omega}_1 \mathbf{J}_1 \Omega_1 - \mathbf{T}_{ext1}). \tag{2.19}$$

Next we need to find an expression for the rotational acceleration of the payload, $\dot{\hat{\Omega}}_2$, in terms of all the joint states, and the payload attitude and velocity.

$$\begin{aligned}
\dot{\mathbf{J}}_2 \Omega_2 + \mathbf{J}_2 \dot{\hat{\Omega}}_2 + \hat{\Omega}_2 \mathbf{J}_2 \Omega_2 - \mathbf{T}_{ext2} &= -\mathbf{B}_2^T \mathbf{B}_1 (\mathbf{J}_1 \dot{\hat{\Omega}}_1 + \dot{\mathbf{J}}_1 \Omega_1 + \hat{\Omega}_1 \mathbf{J}_1 \Omega_1 - \mathbf{T}_{ext1}) \\
\mathbf{J}_2 \dot{\hat{\Omega}}_2 &= -\hat{\Omega}_2 \mathbf{J}_2 \Omega_2 - \dot{\mathbf{J}}_2 \Omega_2 - \mathbf{B}^T \dot{\mathbf{J}}_1 \Omega_1 - \mathbf{B}^T \mathbf{J}_1 \dot{\hat{\Omega}}_1 - \mathbf{B}^T \hat{\Omega}_1 \mathbf{J}_1 \Omega_1 + \mathbf{B}^T \mathbf{T}_{ext1} + \mathbf{T}_{ext2}. \tag{2.20}
\end{aligned}$$

Substituting (2.12) in for $\dot{\hat{\Omega}}_1$ gives

$$\begin{aligned}
\mathbf{J}_2 \dot{\hat{\Omega}}_2 &= -\hat{\Omega}_2 \mathbf{J}_2 \Omega_2 - \mathbf{B}^T \mathbf{J}_1 \mathbf{B} (\hat{\Omega} \Omega_2 + \dot{\hat{\Omega}}_2 - \dot{\hat{\Omega}}) \\
&\quad - \mathbf{B}^T \hat{\Omega}_1 \mathbf{J}_1 \Omega_1 - \dot{\mathbf{J}}_2 \Omega_2 - \mathbf{B}^T \dot{\mathbf{J}}_1 \Omega_1 + \mathbf{B}^T \mathbf{T}_{ext1} + \mathbf{T}_{ext2}, \tag{2.21}
\end{aligned}$$

so that

$$\begin{aligned}
(\mathbf{J}_2 + \mathbf{B}^T \mathbf{J}_1 \mathbf{B}) \dot{\hat{\Omega}}_2 &= -\hat{\Omega}_2 \mathbf{J}_2 \Omega_2 - \mathbf{B}^T \mathbf{J}_1 \mathbf{B} (\hat{\Omega} \Omega_2 - \dot{\hat{\Omega}}) - \mathbf{B}^T \hat{\Omega}_1 \mathbf{J}_1 \Omega_1 \\
&\quad - \dot{\mathbf{J}}_2 \Omega_2 - \mathbf{B}^T \dot{\mathbf{J}}_1 \Omega_1 + \mathbf{B}^T \mathbf{T}_{ext1} + \mathbf{T}_{ext2}. \tag{2.22}
\end{aligned}$$

Substituting (2.11) to eliminate Ω_1 ,

$$\begin{aligned}
(\mathbf{J}_2 + \mathbf{B}^T \mathbf{J}_1 \mathbf{B}) \dot{\Omega}_2 &= -\hat{\Omega}_2 \mathbf{J}_2 \Omega_2 - \mathbf{B}^T \mathbf{J}_1 \mathbf{B} (\hat{\Omega} \Omega_2 - \dot{\Omega}) - \dot{\mathbf{J}}_2 \Omega_2 - \mathbf{B}^T \dot{\mathbf{J}}_1 \mathbf{B} (\Omega_2 - \Omega) \\
&\quad - \mathbf{B}^T \widehat{\mathbf{B}(\Omega_2 - \Omega)} \mathbf{J}_1 \mathbf{B} (\Omega_2 - \Omega) + \mathbf{B}^T \mathbf{T}_{ext1} + \mathbf{T}_{ext2} \\
&= -\hat{\Omega}_2 \mathbf{J}_2 \Omega_2 - \mathbf{B}^T \mathbf{J}_1 \mathbf{B} (\hat{\Omega} \Omega_2 - \dot{\Omega}) - \dot{\mathbf{J}}_2 \Omega_2 - \mathbf{B}^T \dot{\mathbf{J}}_1 \mathbf{B} (\Omega_2 - \Omega) \\
&\quad - \mathbf{B}^T \widehat{\mathbf{B}(\Omega_2 - \Omega)} \mathbf{B}^T \mathbf{J}_1 \mathbf{B} (\Omega_2 - \Omega) + \mathbf{B}^T \mathbf{T}_{ext1} + \mathbf{T}_{ext2}, \tag{2.23}
\end{aligned}$$

resulting in

$$\boxed{
\begin{aligned}
(\mathbf{J}_2 + \mathbf{B}^T \mathbf{J}_1 \mathbf{B}) \dot{\Omega}_2 &= -\hat{\Omega}_2 \mathbf{J}_2 \Omega_2 - \mathbf{B}^T \mathbf{J}_1 \mathbf{B} (\hat{\Omega} \Omega_2 - \dot{\Omega}) \\
&\quad - (\hat{\Omega}_2 - \hat{\Omega}) \mathbf{B}^T \mathbf{J}_1 \mathbf{B} (\Omega_2 - \Omega) \\
&\quad - \dot{\mathbf{J}}_2 \Omega_2 - \mathbf{B}^T \dot{\mathbf{J}}_1 \mathbf{B} (\Omega_2 - \Omega) + \mathbf{B}^T \mathbf{T}_{ext1} + \mathbf{T}_{ext2}.
\end{aligned}
} \tag{2.24}$$

Equation (2.24) is significant because given the Joint Parameters (\mathbf{B} , Ω , and $\hat{\Omega}$) as functions of time, and the initial conditions for Ω_2 , we can determine Ω_2 for all future time. We can then compute Ω_1 from (2.11), and integrate the payload attitude forward in time using

$$\dot{\mathbf{B}}_2 = \mathbf{B}_2 \hat{\Omega}_2, \tag{2.25}$$

from the initial conditions on \mathbf{B}_2 . This in turn gives us the housing attitude as

$$\mathbf{B}_1 = \mathbf{B}_2 \mathbf{B}^T. \tag{2.26}$$

Note that in (2.24) the moment of inertia terms, \mathbf{J}_1 and \mathbf{J}_2 , are about the *system CM*. These inertia terms will change as a function of the joint position.

2.2.3 Calculating the \mathbf{J} and $\dot{\mathbf{J}}$ Terms

In (2.24) the terms $\dot{\mathbf{J}}_1$ and $\dot{\mathbf{J}}_2$, need to be calculated. These are time rates of change for the housing and payload moments of inertia about the *buoy system's* center of mass. The location of this center of mass changes as a the joint position changes.

The first step is to calculate the system CM location in terms of joint position and the housing and payload CMs. The system CM location in *housing body coordinates* is given by

$$\mathbf{R}_{cmsys1} = \frac{m_1 \mathbf{R}_{cm1} + m_2 [\mathbf{R}_{J1} + \mathbf{B} (\mathbf{R}_{cm2} - \mathbf{R}_{J2})]}{m_1 + m_2}, \tag{2.27}$$

where \mathbf{R}_{cm1} and \mathbf{R}_{J1} are the housing CM and joint locations in the housing body coordinate system. Also, \mathbf{R}_{cm2} and \mathbf{R}_{J2} are the payload CM and joint locations in the payload body coordinate system. Similarly, the system CM location in *payload body coordinates* is given by

$$\mathbf{R}_{cmsys2} = \frac{m_2 \mathbf{R}_{cm2} + m_1 [\mathbf{R}_{J2} + \mathbf{B}^T (\mathbf{R}_{cm1} - \mathbf{R}_{J1})]}{m_1 + m_2}. \tag{2.28}$$

Next we calculate the moments of inertia for the housing and payload about the system CM. Recall that the parallel axis theorem for inertia tensors is

$$\mathbf{J}_{disp} = \mathbf{J}_{cm} + m (\mathbf{R}^T \mathbf{R} \mathbf{I} - \mathbf{R} \mathbf{R}^T), \tag{2.29}$$

where \mathbf{J}_{disp} is the inertia tensor about the displaced point, \mathbf{J}_{cm} is the inertia tensor about the body CM, \mathbf{R} is the vector between the body CM and the displaced point, and \mathbf{I} is the 3x3 identity matrix.

So given the housing CM and system CM in housing body coordinates we can calculate the housing's inertia about the system CM as

$$\begin{aligned}\mathbf{R}_1 &= \mathbf{R}_{cm1} - \mathbf{R}_{cmsys1} \\ &= \mathbf{R}_{cm1} \left(1 - \frac{m_1}{m_1 + m_2} \right) - \frac{m_2}{m_1 + m_2} [\mathbf{R}_{J1} + \mathbf{B} (\mathbf{R}_{cm2} - \mathbf{R}_{J2})],\end{aligned}\quad (2.30)$$

$$\mathbf{J}_1 = \mathbf{J}_h + m_1 (\mathbf{R}_1^T \mathbf{R}_1 \mathbf{I} - \mathbf{R}_1 \mathbf{R}_1^T), \quad (2.31)$$

where \mathbf{J}_h is the inertia tensor of the housing about the housing CM. Similarly, the payload inertia about the system CM is given by

$$\begin{aligned}\mathbf{R}_2 &= \mathbf{R}_{cm2} - \mathbf{R}_{cmsys2} \\ &= \mathbf{R}_{cm2} \left(1 - \frac{m_2}{m_1 + m_2} \right) - \frac{m_1}{m_1 + m_2} [\mathbf{R}_{J2} + \mathbf{B}^T (\mathbf{R}_{cm1} - \mathbf{R}_{J1})],\end{aligned}\quad (2.32)$$

$$\mathbf{J}_2 = \mathbf{J}_p + m_2 (\mathbf{R}_2^T \mathbf{R}_2 \mathbf{I} - \mathbf{R}_2 \mathbf{R}_2^T), \quad (2.33)$$

where \mathbf{J}_p is the inertia tensor of the payload about the payload CM.

There are two methods of finding time rates of change of the inertia tensors \mathbf{J}_1 and \mathbf{J}_2 . The first method takes the derivative numerically. Since \mathbf{J}_1 and \mathbf{J}_2 are calculated at each time step, $\dot{\mathbf{J}}_1$ and $\dot{\mathbf{J}}_2$ can be approximated by finding the difference between the inertia values at the current and previous simulation time steps and dividing by the simulation step size.

Alternatively, $\dot{\mathbf{J}}_1$ and $\dot{\mathbf{J}}_2$ can be calculated analytically. Differentiating (2.29) with respect to time gives

$$\dot{\mathbf{J}}_{disp} = \dot{\mathbf{J}}_{CM} + \frac{d}{dt} [m (\mathbf{R}^T \mathbf{R} \mathbf{I} - \mathbf{R} \mathbf{R}^T)]. \quad (2.34)$$

If we assume that the mass and mass distribution internal to the body is not changing then (2.34) reduces to

$$\dot{\mathbf{J}}_{disp} = m (2\mathbf{R}^T \dot{\mathbf{R}} \mathbf{I} - \dot{\mathbf{R}} \mathbf{R}^T - \mathbf{R} \dot{\mathbf{R}}^T). \quad (2.35)$$

So to find $\dot{\mathbf{J}}_1$ and $\dot{\mathbf{J}}_2$ we need to calculate $\dot{\mathbf{R}}_1$ and $\dot{\mathbf{R}}_2$ and use (2.35) appropriately. Differentiating (2.30) and (2.32) with respect to time gives

$$\dot{\mathbf{R}}_1 = -\frac{m_2 \dot{\mathbf{B}} (\mathbf{R}_{cm2} - \mathbf{R}_{J2})}{m_1 + m_2}, \quad (2.36)$$

$$\dot{\mathbf{R}}_2 = -\frac{m_1 \dot{\mathbf{B}}^T (\mathbf{R}_{cm1} - \mathbf{R}_{J1})}{m_1 + m_2}. \quad (2.37)$$

Equations (2.36) and (2.37), along with (2.30) and (2.32), can be substituted into (2.35) to find the change in inertia terms at the current time step. Because of how the problem was formulated, the only time varying term is the joint velocity.

2.2.4 Translational Dynamics

The CM positions \mathbf{r}_1 and \mathbf{r}_2 of the bodies are given (in the navigation coordinate system) by

$$\mathbf{r}_1 = \mathbf{d}_0 + \mathbf{B}_1 \mathbf{D}_1, \mathbf{r}_2 = \mathbf{d}_0 + \mathbf{B}_2 \mathbf{D}_2, \quad (2.38)$$

where \mathbf{d}_0 is the joint position. The joint position \mathbf{d}_0 is a quantity we still need to solve for. We also have

$$m \mathbf{r}_0 = m_1 \mathbf{r}_1 + m_2 \mathbf{r}_2, \quad (2.39)$$

where $m = m_1 + m_2$ is the total mass and \mathbf{r}_0 is the CM of the coupled system. As with the torques in the rotational analysis, we will distinguish between the joint forces and the external forces on each body. These are designated \mathbf{f}_1 , \mathbf{f}_2 , \mathbf{f}_{ext1} , and \mathbf{f}_{ext2} . These forces are expressed in the navigation coordinate system, so the joint forces on each body are equal and opposite. Writing Newton's second law for each body in the translational system gives

$$m_1 \ddot{\mathbf{r}}_1 = \mathbf{f}_1 + \mathbf{f}_{ext1}, \quad (2.40)$$

$$m_2 \ddot{\mathbf{r}}_2 = \mathbf{f}_2 + \mathbf{f}_{ext2}. \quad (2.41)$$

Using the joint forces to combine these equations results in

$$m_1 \ddot{\mathbf{r}}_1 - \mathbf{f}_{ext1} = -m_2 \ddot{\mathbf{r}}_2 + \mathbf{f}_{ext2}. \quad (2.42)$$

We can differentiate (2.38) twice to find the acceleration of the individual bodies as functions of the joint translational acceleration and body attitudes:

$$m_1 (\ddot{\mathbf{d}}_0 + \ddot{\mathbf{B}}_1 \mathbf{D}_1) - \mathbf{f}_{ext1} = -m_2 (\ddot{\mathbf{d}}_0 + \ddot{\mathbf{B}}_2 \mathbf{D}_2) + \mathbf{f}_{ext2}, \quad (2.43)$$

so

$$m \ddot{\mathbf{d}}_0 = - (m_1 \ddot{\mathbf{B}}_1 \mathbf{D}_1 + m_2 \ddot{\mathbf{B}}_2 \mathbf{D}_2) + \mathbf{f}_{ext1} + \mathbf{f}_{ext2},$$

or

$$\boxed{\begin{aligned} m \ddot{\mathbf{d}}_0 = & -m_1 \left(\dot{\mathbf{B}}_1 \hat{\Omega}_1 + \mathbf{B}_1 \dot{\hat{\Omega}}_1 \right) \mathbf{D}_1 \\ & -m_2 \left(\dot{\mathbf{B}}_2 \hat{\Omega}_2 + \mathbf{B}_2 \dot{\hat{\Omega}}_2 \right) \mathbf{D}_2 \\ & + \mathbf{f}_{ext1} + \mathbf{f}_{ext2}. \end{aligned}} \quad (2.44)$$

All the terms in (2.44) have been found in solving for the rotational dynamics. At each simulation step we calculate the rotational dynamics first and then the translational dynamics. We only need the initial conditions of the joint position and velocity, \mathbf{d}_0 and $\dot{\mathbf{d}}_0$, to be able to integrate \mathbf{d}_0 forward in time. Once \mathbf{d}_0 and the rotational terms are known, the position and attitude of all parts of the buoy system are known.

2.3 Buoyant Forces and Moments

2.3.1 The Buoyant Cases

To calculate the buoyant forces and moments on the housing and payload cylinders, one must calculate the housing and payload cylinder's buoyant force and the location of the center of buoyancy. The buoyant force is weight of the water displaced by the cylinder and

the center of buoyancy is located at the volumetric center of the displaced water. In the buoyancy calculation we assume that the water’s surface is locally smooth and horizontal in the immediate vicinity of the buoy.

The buoyant forces and moments can result from one of several different positions and orientations with respect to the waterline. For a single cylinder, there are 5 cases:

1. The cylinder is completely out of the water. The buoyant calculations in this case are trivial.
2. The cylinder is completely submerged. The buoyant calculations in this case are trivial.
3. The cylinder is floating at the surface such that the waterline intersects only the cylindrical face of the cylinder.
4. The cylinder is floating at the surface such that the waterline intersects one end face in addition to the cylindrical face.
5. The cylinder is floating at the surface such that the waterline intersects both end faces in addition to the cylindrical face.

Additionally, in all the non-trivial cases (3 through 5) it is possible for the cylinder to be upside down. All these cases are illustrated in the inclined coordinate system in Figure 2.2.

It is desirable to have a method for calculating the submerged volume and center of buoyancy for all of the above cases.

2.3.2 The Inclined Coordinate System

Since the cylinders are symmetric about their long axes, the three dimensional buoyancy calculation can be reduced to a two dimensional problem in an intermediate coordinate system which we will call the “inclined coordinate system.” The inclined coordinate system is found by rotating the cylinder’s body coordinate system about its Z axis, until the body’s Y axis is parallel to the water surface (the navigation coordinate system’s x-y plane). This does not change the physical location of the center of buoyancy in the navigation frame, because of the cylinder’s symmetry about its Z axis. This rotation provides a much more convenient coordinate system for calculating the center of buoyancy and the submerged volume of the cylinder. All of the illustrations in Figure 2.2 show the cylinder in the inclined coordinate system.

Section 2.3.3 derives the cylinder’s center of buoyancy in the inclined coordinate system. It is then necessary to transform the center of buoyancy into the body coordinate system for use in the cylinder model. For this analysis we define some direction cosine matrices with the following notations.

The direction cosine matrix $\mathbf{B}_{b/i}$ converts a vector in the inclined coordinate system to the cylinder’s body coordinate system. The inclined and body coordinate systems have the same origin.

The cylinder’s attitude in the navigation frame is specified by the DCM $\mathbf{B}_{n/b}$. To find $\mathbf{B}_{b/i}$, we first check to see if the body coordinate system is already the inclined coordinate system. This will occur when there is no roll about the cylinder’s X axis, i.e. $\mathbf{B}_{n/b}(3, 2) = 0$. In this case $\mathbf{B}_{b/i}$ equals the identity matrix.

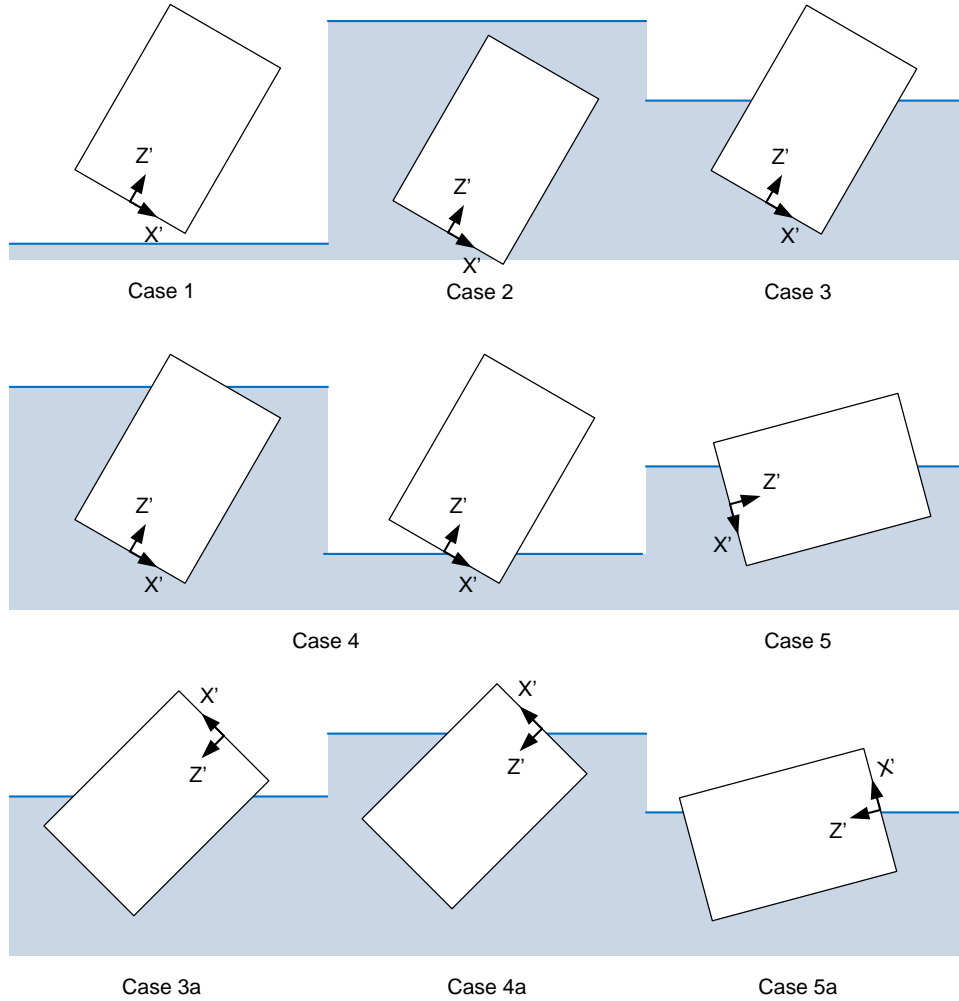


Figure 2.2: The possible cases for calculating the buoyant force and center of buoyancy. Cases 1 and 2 are have trivial solutions. Cases 3 through 5 are more complicated and have alternate cases (3a, 4a, and 5a) where the cylinder is upside down. The x' and z' axes are in the inclined coordinate system.

If the body coordinate system can not be used as the inclined coordinate system, then the inclined coordinate system will use the same Z axis vector as the body coordinate system. We first calculate the DCM $\mathbf{B}_{n/i}$ which describes the attitude of the inclined coordinate system in the navigation frame from

$$\mathbf{B}_{n/i} = [\mathbf{x}_i \quad \mathbf{y}_i \quad \mathbf{z}_i], \quad (2.45)$$

where

$$\mathbf{z}_i = \begin{bmatrix} \mathbf{B}_{n/b}(1, 3) \\ \mathbf{B}_{n/b}(2, 3) \\ \mathbf{B}_{n/b}(3, 3) \end{bmatrix}, \quad (2.46)$$

$$\mathbf{y}_i = \begin{bmatrix} \left(1 + \left(\frac{\mathbf{B}_{n/b}(1,3)}{\mathbf{B}_{n/b}(2,3)}\right)^2\right)^{-1/2} \\ -\frac{\mathbf{B}_{n/b}(1,3)}{\mathbf{B}_{n/b}(2,3)} \left(1 + \left(\frac{\mathbf{B}_{n/b}(1,3)}{\mathbf{B}_{n/b}(2,3)}\right)^2\right)^{-1/2} \\ 0 \end{bmatrix}, \quad (2.47)$$

$$\mathbf{x}_i = \mathbf{y}_i \times \mathbf{z}_i. \quad (2.48)$$

Once $\mathbf{B}_{n/i}$ has been found, $\mathbf{B}_{b/i}$ can be found from

$$\mathbf{B}_{b/i} = \mathbf{B}_{n/b}^T \mathbf{B}_{n/i}. \quad (2.49)$$

2.3.3 Submerged Volume and Center of Buoyancy Calculations

To calculate the submerged volume and its center, the locations of cylinder ‘‘vertices’’ in the incline plane are calculated. The matrix \mathbf{V} is built using the coordinates of the vertices in a form that is compatible with applying coordinate transforms using an SE(3) homogeneous transformation matrix (HTM),

$$\mathbf{V} = \begin{bmatrix} R & -R & -R & R \\ 0 & 0 & 0 & 0 \\ 0 & 0 & L & L \\ 1 & 1 & 1 & 1 \end{bmatrix}, \quad (2.50)$$

where R and L are shown in Figure 2.3.

The buoyant case is determined by calculating the vertices’ location in the navigation frame to determine which vertices are submerged by

$$\mathbf{v} = \mathbf{C}_{HTM} \mathbf{V}, \quad (2.51)$$

where

$$\mathbf{C}_{HTM} = \begin{bmatrix} \mathbf{B}_{n/i} & \mathbf{r}_{body} \\ \mathbf{0} & 1 \end{bmatrix}, \quad (2.52)$$

$$\mathbf{r}_{body} = \mathbf{r}_{cm} - \mathbf{B}_{n/b} \mathbf{R}_{cm}. \quad (2.53)$$

Next the coordinates of where the waterline intersects the cylinder are calculated in the body frame. The trivial cases of completely submerged or completely clear of the water are checked first. If all the vertices, specified in \mathbf{v} , have negative z components then the cylinder is completely submerged and

$$V_{sub} = \pi R^2 L, \quad (2.54)$$

$$\mathbf{R}_{cb} = \begin{bmatrix} 0 \\ 0 \\ L/2 \end{bmatrix}. \quad (2.55)$$

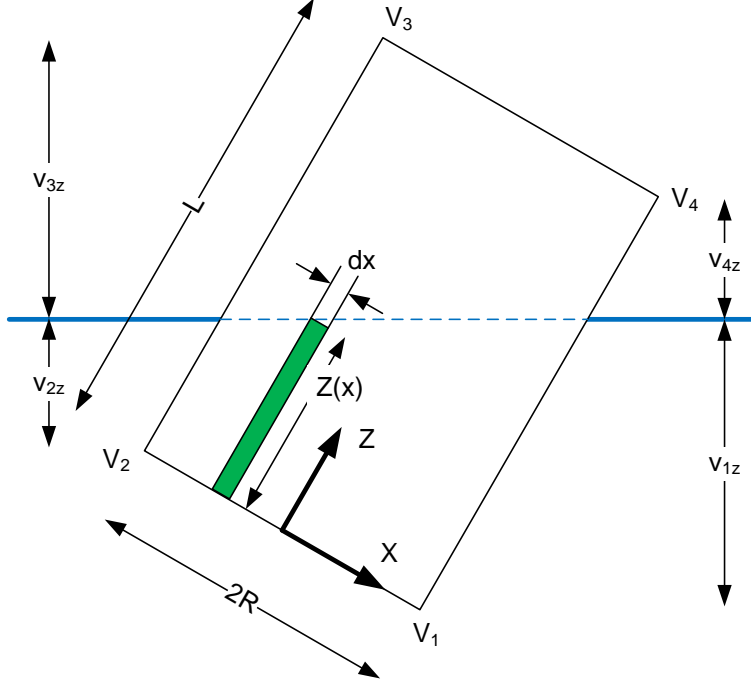


Figure 2.3: The key parameters for the integration of the submerged volume and center of buoyancy. The vertices used for this calculation are labelled V_1 through V_2 .

If all the z components of the vertices are positive then the cylinder is completely out of the water, $V_{sub} = 0$, and \mathbf{R}_{cb} is undefined but set to zero for simulation purposes.

Otherwise the cylinder is partially submerged and we need to find where the water line intersects the cylinder. This is accomplished by checking the z coordinate of vertices in the navigation frame, and finding the edge segments where one vertex is above the water and the other is below the water. We define v_{1z} , v_{2z} , v_{3z} , and v_{4z} as in Figure 2.3.

If $\text{sign}(v_{1z}) \neq \text{sign}(v_{2z})$, then the waterline intersects the bottom face of the cylinder between vertices 1 and 2. Therefore one of the waterline intersection points in the inclined coordinate system is given by

$$\mathbf{WL}_{1-2} = \begin{bmatrix} R \left(1 - 2 \frac{|v_{1z}|}{|v_{1z}| + |v_{2z}|} \right) \\ 0 \\ 0 \end{bmatrix}. \quad (2.56)$$

If $\text{sign}(v_{2z}) \neq \text{sign}(v_{3z})$, then the waterline intersects the left face of the cylinder between vertices 2 and 3. Therefore one of the waterline intersection points in the inclined coordinate system is given by

$$\mathbf{WL}_{2-3} = \begin{bmatrix} -R \\ 0 \\ L \frac{|v_{2z}|}{|v_{2z}| + |v_{3z}|} \end{bmatrix}. \quad (2.57)$$

If $\text{sign}(v_{3z}) \neq \text{sign}(v_{4z})$, then the waterline intersects the top face of the cylinder between vertices 3 and 4. Therefore one of the waterline intersection points in the inclined

coordinate system is given by

$$\mathbf{WL}_{3-4} = \begin{bmatrix} R \left(-1 + 2 \frac{|v_{3z}|}{|v_{3z}| + |v_{4z}|} \right) \\ 0 \\ L \end{bmatrix}. \quad (2.58)$$

If $\text{sign}(v_{4z}) \neq \text{sign}(v_{1z})$, then the waterline intersects the right face of the cylinder between vertices 4 and 1. Therefore one of the waterline intersection points in the inclined coordinate system is given by

$$\mathbf{WL}_{4-1} = \begin{bmatrix} R \\ 0 \\ L \frac{|v_{1z}|}{|v_{1z}| + |v_{4z}|} \end{bmatrix}. \quad (2.59)$$

Two of the four equations (2.56) - (2.59) will be used, depending on which two sides the waterline intersects. \mathbf{WL}_a will refer to the first intersected segment in the above list and \mathbf{WL}_b the second.

Next we can calculate the slope of the waterline in the inclined coordinate systems as

$$s_{wl} = \frac{\mathbf{WL}_{bz} - \mathbf{WL}_{az}}{\mathbf{WL}_{bx} - \mathbf{WL}_{ax}}. \quad (2.60)$$

If $\mathbf{WL}_{bx} = \mathbf{WL}_{ax}$ then s_{wl} is either positive or negative infinity and the model sets s_{wl} to $\pm 1e17$.

Next, the submerged volume is integrated numerically, by creating an array X of x coordinates from $-R$ to R . From this X array we calculate the Y (width) array and Z (height) arrays. All operations listed below are element by element operations. The values in the Z array are limited to the range 0 to L . n_x is the number of x points used in the approximation of the cylinder volume.

$$dx = 2R/n_x, \quad (2.61)$$

$$X = -R : dx : R, \quad (2.62)$$

$$Y = 2\sqrt{R^2 - X^2}, \quad (2.63)$$

$$Z'' = s_{wl}X + (\mathbf{WL}_{az} - s_{wl}\mathbf{WL}_{ax}),$$

$$Z = \begin{cases} L & \text{if } Z'' > L, \\ Z'' & \text{if } 0 \geq Z'' \leq L, \\ 0 & \text{if } Z'' < 0. \end{cases} \quad (2.64)$$

The clamping of the Z values is to correctly handle cases 4 and 5 (and 4a/5a), where the water line intersects an end face of the cylinder. Once the X , Y , and Z arrays have been populated, the numerical integration to find the submerged volume and center of buoyancy in the inclined plane can proceed using

$$V_{sub} = \sum_{k=1}^{n_x} dx Y_k Z_k, \quad (2.65)$$

$$\mathbf{R}_{cb_i} = \begin{bmatrix} \sum_{k=1}^{n_x} dx X_k Y_k Z_k / V_{sub} \\ 0 \\ \sum_{k=1}^{n_x} dx Z_k Y_k Z_k / 2V_{sub} \end{bmatrix}, \quad (2.66)$$

where \mathbf{R}_{cb_i} is the center of buoyancy in the inclined coordinate system.

However, if the cylinder is upside down (cases 3a, 4a, or 5a), then an alternate procedure is needed to calculate the Z components and submerged volume. The cylinder is upside down if $\mathbf{B}_{n/b}(3, 3) < 0$. In this case

$$Z^{alt} = L - Z, \quad (2.67)$$

$$V_{sub} = \sum_{k=1}^{n_x} dx Y_k Z_k^{alt}, \quad (2.68)$$

$$\mathbf{R}_{cb_i} = \begin{bmatrix} \sum_{k=1}^{n_x} dx X_k Y_k Z_k^{alt} / V_{sub} \\ 0 \\ L - \sum_{k=1}^{n_x} dx Z_k^{alt} Y_k Z_k^{alt} / 2V_{sub} \end{bmatrix}. \quad (2.69)$$

It is necessary to check that the submerged volume, V_{sub} is non-zero after these calculations. In some cases when one vertex is barely underwater, the above integration will still return $V_{sub} = 0$ or close enough to zero that \mathbf{R}_{cb_i} explodes to infinity.

Finally, we convert the center of buoyancy from the inclined coordinate system back to the cylinder's body coordinate system by

$$\mathbf{R}_{cb} = \mathbf{B}_{i/b}^T \mathbf{R}_{cb_i}. \quad (2.71)$$

2.3.4 Calculating the Buoyant Force and Moment

The buoyant forces and moments are calculated in the body frame by

$$\mathbf{F}_{buoyant} = \mathbf{B}_{b/n} \begin{bmatrix} 0 \\ 0 \\ \rho g V_{sub} \end{bmatrix} \quad (2.72)$$

and

$$\mathbf{M}_{buoyant} = (\mathbf{R}_{cb} - \mathbf{R}_{cm}) \times \mathbf{F}_{buoyant}. \quad (2.73)$$

2.4 Gravity Forces and Moments

The gravity forces and moments are calculated separately for the payload and housing cylinders. For the housing cylinder they are calculated by:

$$\mathbf{f}_{grav_1} = \begin{bmatrix} 0 \\ 0 \\ -m_1 g \end{bmatrix}, \quad (2.74)$$

$$\mathbf{M}_{grav_1} = (\mathbf{R}_{cmsys1} - \mathbf{R}_{cm1}) \times (-\mathbf{F}_{grav_1}), \quad (2.75)$$

where \mathbf{f}_{grav_1} is the gravitational force vector in the *navigation* frame and \mathbf{M}_{grav_1} is the gravitational moment vector in the *body* frame. g is the acceleration due to gravity. The gravity force is converted to the body frame by $\mathbf{F}_{grav_1} = \mathbf{B}_1^T \mathbf{f}_{grav_1}$. As in the buoyancy section, Section 2.3, \mathbf{R}_{cmsys1} is the overall system's CM and \mathbf{R}_{cm1} is the housing CM in the housing's coordinate system. To calculate gravity forces and moments on the payload, we use the corresponding payload values (all subscript 1's are replaced by 2's).

2.5 Drag Forces and Moments

2.5.1 The Basic Drag Model

The estimation and modeling of the drag forces and moments are the most uncertain components of the model. As Sections 2.2 through 2.4 show, the inertial, buoyant, and gravity components can all be solved directly and reliably from the geometry of the situation. The modeling of the drag effects is fundamentally different. The drag model is an approximation of a much more complicated phenomenon. There is a wide range of possible models which could be used to approximate the drag effects. At one extreme a simple linear viscous relationship could be used. At the other extreme a full FEA/CFD type model could be implemented and rerun at each time step. The drag model presented in this section is on the simpler end of the range of models. The choice and tuning of this drag model was informed by the experiments described in Chapter 3.

Additionally, some more complicated and detailed drag models were considered initially. These are presented in Appendix ???. They were found to not provide a significant improvement over the model implemented here.

It is important that the numerical simulation have a well behaved drag model. The drag effects are the only source of damping for the numerical system. If the drag is not present, or too small, the simulation will become numerically unstable.

The drag forces and moments are calculated for the payload and the housing. The translational drag forces, in the navigation frame, are assumed to be linear in nature and are calculated by:

$$\mathbf{F}_{drag} = \begin{bmatrix} -f_{sub}C_{D_{fXY}}LR & 0 & 0 \\ 0 & -f_{sub}C_{D_{fXY}}LR & 0 \\ 0 & 0 & -C_{D_{fZ}}R^2 \end{bmatrix} \dot{\mathbf{R}}_{cm}, \quad (2.76)$$

where L is the cylinder length, R is the cylinder radius, f_{sub} is the submerged fraction of the buoy, $C_{D_{fXY}}$ and $C_{D_{fZ}}$ are drag force scaling terms which includes the effects of density and the coefficient of drag. $\dot{\mathbf{R}}_{cm_i}$ is the translational velocity vector for the cylinder's CM.

The components of the drag moment vector, in the cylinder's body frame, are calculated using a quadratic function of the form

$$M_{drag_i} = -\text{sign}(\Omega_i)f_{sub}LR C_{D_{mi}}\Omega_i^2, \text{ where } i = X, Y, \text{ or } Z. \quad (2.77)$$

Here Ω_i is the cylinder's rotational velocity about its i th axis, and $C_{D_{mi}}$ are drag moment scaling terms which include the effects of density and the coefficient of drag. $C_{D_{mX}} = C_{D_{mY}}$ because the body is a cylinder.

2.5.2 Passive Yaw Damping

The cylinder model can optionally specify a number of radial fins, to increase the drag moment about the long axis of the cylinder. This implements a form of passive yaw control for the buoy system. The fins are modeled as being at the buoy's center of mass so they have minimal effect on the buoy's roll and pitch motions. Therefore for modeling purposes, the simulation only applies a drag moment proportional to the cylinder's yaw rate squared, and in the opposite direction, applied about the cylinder's long (Z) axis,

$$M_{yawpass} = -\text{sign}(\Omega_z)n_{fins}\frac{1}{8}C_D\rho w_{fin}\Omega_z^2[(r_{cyl} + l_{fins})^4 - r_{cyl}^4], \quad (2.78)$$

where Ω_z is the cylinder rotation rate about its long axis, C_D is the coefficient of drag for a flat plate perpendicular to the fluid velocity, ρ is the density of the fluid, and r_{cyl} is the radius of the cylinder.

The value calculated for $M_{yawpass}$ is added to the M_{drag_z} value to estimate the total drag moment about the long axis of the cylinder.

2.5.3 Translational Drag Coupling into Rotation

In the dynamics model derived in Section 2.2, we assumed that there was no coupling from the translational dynamics into the rotational dynamics. This assumption allows the rotational dynamics to be solved independently at each time step and then the rotational results are used to calculate translational dynamics. This assumption is not strictly true as will be shown next.

Assume that the buoy has a translational velocity with respect to the fluid. The translational drag force does *not* act at the center of mass of the buoy, but rather at the center of pressure. Given the symmetry of the buoy payload and housing cylinders, the translational drag force can be approximated to act on the volumetric center of the submerged portion of each body. This is the location of the body’s center of buoyancy, \mathbf{R}_{cb} . Normally these locations will not be located at the system’s center of mass, and therefore the translational drag forces will apply a moment to the system. The moment due to translational drag can be calculated for each body by

$$\mathbf{M}_{drag_T} = (\mathbf{R}_{cb} - \mathbf{R}_{cmsys}) \times \mathbf{F}_{drag}, \quad (2.79)$$

where the terms on the right hand side are from the body the moment is being calculated for. Recall that \mathbf{R}_{cmsys} is the location of the system’s CM in the body’s coordinate system.

If the buoy is not experiencing significant translation with respect to the fluid, then these effects can likely be ignored. In the numerical simulation, the \mathbf{M}_{drag_T} value from the previous time step is used when solving for the rotational dynamics.

2.6 Modeling Wave Effects

2.6.1 The 2-D Wave Models

The wave model implemented in the simulation describes a wave train of regular or irregular waves propagating in a *single* direction in the navigation frame’s x-y plane. Appendix A presents the basis for the wave elevation and fluid velocity equations, (2.80) and (2.82). Appendix A also describes the procedure for generating irregular waves with a spectral content approximating that of the open ocean. The wave modeling in this research draws heavily on Fossen [9] and Faltinsen [8]. However, because of the extremely small size of the buoy envisioned in this work compared with open ocean wavelengths, the methods typically suggested in the literature for modeling surface wave effects on ocean structures are less applicable.

Wave elevation, ζ , is the height of the water’s surface above its mean height, located at $z = 0$ in the navigation frame. As a function of position and time, the wave elevation is given by

$$\zeta(x, y, t) = \sum_{j=1}^N A_j \sin[\omega_j t - k_j (x \cos \beta + y \sin \beta) + \phi_j], \quad (2.80)$$

where A_j , ω_j , k_j , and ϕ_j are the amplitude, circular frequency, wave number, and phase angle respectively of the component waves. x and y are the horizontal coordinates in the navigation frame. β specifies the direction of seas referenced to the navigation frame's x axis.

The *dispersion relationship* relates the wave number, k_j , and circular frequency, ω_j . For “infinite” water depth this relationship is given in [9] and [8, (2.18)] as

$$k_j = \omega_j^2/g, \quad (2.81)$$

where g is the acceleration due to gravity.

Since k_j can be calculated from (2.81), the wave can be approximated by specifying one or more values for A_j , ω_j , and ϕ_j ; and a value for the direction of seas, β .

The velocity of a fluid particle in the navigation frame due to wave action can be approximated by

$$\mathbf{v}_{fluid}(x, y, z, t) = \sum_{j=1}^N \omega_j A_j e^{k_j z} \begin{bmatrix} \sin[\omega_j t - k_j(x \cos \beta + y \sin \beta) + \phi_j] \cos \beta \\ \sin[\omega_j t - k_j(x \cos \beta + y \sin \beta) + \phi_j] \sin \beta \\ \cos[\omega_j t - k_j(x \cos \beta + y \sin \beta) + \phi_j] \end{bmatrix}, \quad (2.82)$$

where \mathbf{v}_{fluid} is the fluid velocity in the navigation frame. x , y , and z are the particle's coordinates in the navigation frame. When $z = \zeta(x, y, t)$, (2.82) gives the velocity of the fluid at the surface. Because of the exponential term in (2.82), particles that are significantly below the mean height of the surface, $z \ll 0$, will have negligible velocity. This is expected, as far away from the surface the wave action has no effect on the fluid.

2.6.2 Wave Driven Buoyant Effects

The most obvious effect of the waves on the buoy is to lift it up and down as the waves pass. This effect is implemented in the model by adjusting the height of the buoy in the opposite direction from the wave elevation. This adjusted height is *only* used in the buoyant calculations. This adjustment is made by changing (2.53) to

$$\mathbf{r}_{body} = \mathbf{r}_{cm} - \mathbf{B}_{n/b} \mathbf{R}_{cm} - \begin{bmatrix} 0 \\ 0 \\ \zeta(x, y, t) \end{bmatrix}, \quad (2.83)$$

where x and y are the horizontal coordinates of the cylinder's CM¹ in the navigation frame. With this change, the buoyancy calculations for the housing and payload cylinders then proceed as described in Section 2.3.

2.6.3 Wave Driven Drag Effects

The motion of the fluid near the water's surface, as approximated by (2.82), will move the buoy with it. If the buoy is very light and has a lot of drag, then its motion will be

¹Strictly, the horizontal coordinates should be that of the center of buoyancy. However, since the center of buoyancy is found as part of the buoyant calculation, this would result in an iterative solution. Because the size of the cylinder is small compared to the waves, it is assumed that the wave elevation is constant in the immediate vicinity of the cylinder. Furthermore, the error in horizontal position will be proportional to the sine of deviation from the vertical. There will be no error when the buoy is vertical and the CM will then have the same horizontal coordinates as the CB.

dominated by the motion of the fluid. On the other hand, if the buoy has significant mass and low drag, then it will be less affected by the motion of the fluid around it.

To implement the effects of fluid velocity on the buoy, the translational drag force is calculated using the difference in velocity between the buoy and fluid. This difference is calculated at the housing and payload cylinders' center of buoyancy. Since the center of buoyancy is the volumetric center of the submerged portion of cylinders, it is a reasonable approximation of the center of pressure. In Section 2.5 the translational drag force equation, (2.76), is adjusted to

$$\mathbf{F}_{drag} = -f_{sub} \begin{bmatrix} C_{DfXY}LR & 0 & 0 \\ 0 & C_{DfXY}LR & 0 \\ 0 & 0 & C_{Dfz}R^2 \end{bmatrix} (\dot{\mathbf{R}}_{cb} - \mathbf{B}_i^T \mathbf{v}_{fluid}(\mathbf{r}_{cb}, t)), \quad (2.84)$$

where \mathbf{B}_i is the attitude direction cosine matrix for the housing, $i = 1$, or the payload, $i = 2$. The drag calculation then proceeds as described in Section 2.5. Because this calculation is performed for both cylinders in the model, and the fluid velocity used is the fluid velocity at the cylinders' center of buoyancy, when the buoy is near the vertical, this captures the twisting effects on the buoy due to the change in fluid velocity with depth.

2.7 Joint Kinematics

Up to this point, the dynamics and kinematic calculations have only required that the joint prevent any translational motion between the two bodies. By specifying the kinematics of the joint, we will define what sorts of rotations are permitted between the bodies, and therefore how the joint quantities \mathbf{B} , $\boldsymbol{\Omega}$, and $\dot{\boldsymbol{\Omega}}$, are permitted to change. As an extreme example, if the joint did not allow any rotation, then the joint DCM, \mathbf{B} , would specify the fixed attitude between the two bodies, and $\boldsymbol{\Omega}$ and $\dot{\boldsymbol{\Omega}}$ would both be $\mathbf{0}$.

Alternatively, the bodies could be connected by a single degree of freedom pivot (a hinge), whose axis of rotation is aligned with one of the bodies' coordinate system axes. This is the configuration of the two body spacecraft presented in [23]. For this configuration, the $\boldsymbol{\Omega}$ and $\dot{\boldsymbol{\Omega}}$ vectors will have, at most, one non-zero element, and the joint DCM, \mathbf{B} , will be one of the elementary rotation matrices (depending on which axis the hinge is aligned with).

At the other extreme, the joint could permit the bodies to rotate with respect to each other about all three axes. A spherical joint is one possible implementation for such a joint. In this case, all the elements of $\boldsymbol{\Omega}$ and $\dot{\boldsymbol{\Omega}}$ might be non-zero. The joint DCM, \mathbf{B} , would be the product of all three elementary rotation matrices. The physical implementation of the joint would determine the order of multiplication for the elementary rotation matrices to properly calculate the joint DCM from the individual joint axis angles.

In the very early phases of this research, an "elevation over azimuth" joint configuration was considered as the joint implementation between the two bodies. However, it was rejected in favor of a universal (a.k.a. Hooke) joint. The benefits of the universal joint over an elevation over azimuth joint are presented in Section 6.3. Both of these joint implementations permit rotation between the bodies in *two* degrees of freedom.

2.7.1 The Universal Joint Angles: ϕ_x , ϕ_y , ϕ_z , and ϕ_v

The joint between the housing and payload section of the buoy is a universal or Hooke joint. The joint's x axis is attached to the housing and is aligned with the housing's x axis. The

joint's y axis and is attached to the payload and is aligned with the payload's y axis. We define the following joint angles (see Figure 2.4):

ϕ_v : The joint vertical angle is the angle between the housing's and payload's, z (long) axes. When $\phi_v = 0$ the housing and payload are co-linear.

ϕ_z : The joint azimuth angle is the angle between the payload's z (long) axis projected into the housing's x-y plane, and the housing's x axis. When $\phi_z = 0$, the payload is in the housing's x-z plane. When $\phi_z = \pi/2$ then the payload is in the housing's y-z plane.

ϕ_x : The angle of the of joint's x axis. When $\phi_x = 0$, the payload's z-axis is constrained to the housing's x-z plane.

ϕ_y : The angle of the of joint's y axis. When $\phi_y = 0$, the payload's z-axis is constrained to the housing's y-z plane.

Either pair of angles, $\{\phi_x, \phi_y\}$ or $\{\phi_v, \phi_z\}$, completely describes the position of the joint and therefore the orientation of the payload with respect to the housing. Conversions from one pair of angles to the other may be performed using

$$\phi_x = \arcsin \left(\frac{\sin \phi_z \sin \phi_v}{\sqrt{1 - \cos^2 \phi_z \sin^2 \phi_v}} \right), \quad (2.85)$$

$$\phi_y = -\arcsin(\cos \phi_z \sin \phi_v), \quad (2.86)$$

and

$$\phi_v = \arccos(\cos \phi_x \cos \phi_y), \quad (2.87)$$

$$\phi_z = \text{atan2}(\sin \phi_x \cos \phi_y, -\sin \phi_y), \quad (2.88)$$

where $\text{atan2}(y, x)$ is the four quadrant arctan function with the order of arguments as specified.

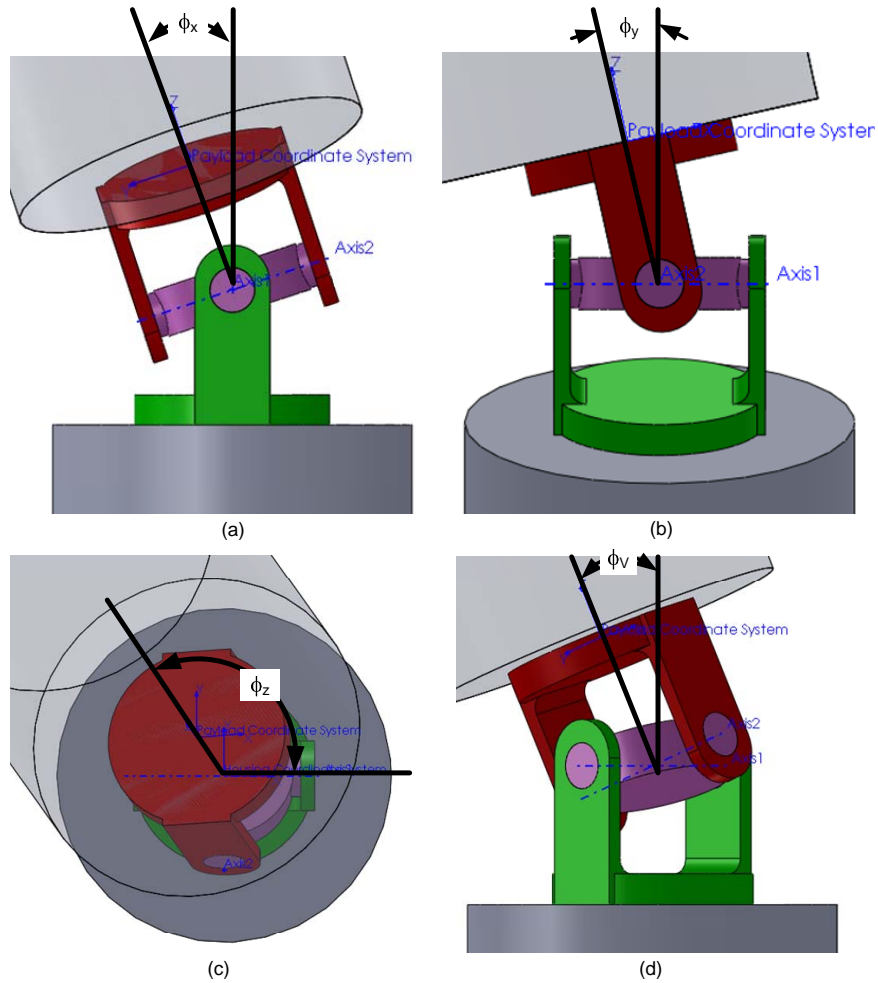


Figure 2.4: An illustration of the four universal joint angles associated with the joint. (a) and (b) illustrate the joint axis angles ϕ_x and ϕ_y . (c) and (d) illustrate the joint's azimuth and vertical angles, ϕ_z and ϕ_v respectively. Axis 1, through the green yoke, is aligned with the housing's x axis. Axis 2, through the red yoke, is aligned with the payload's y axis.

2.7.2 The Joint Direction Cosine Matrix

Equation (2.24) requires the joint position to be specified as the direction cosine matrix, \mathbf{B} . This joint direction cosine matrix can be calculated from the joint angles ϕ_x and ϕ_y , using the elementary rotation matrices

$$\mathbf{B}_x = \begin{bmatrix} 1 & 0 & 0 \\ 0 & \cos \phi_x & \sin \phi_x \\ 0 & -\sin \phi_x & \cos \phi_x \end{bmatrix}, \quad (2.89)$$

$$\mathbf{B}_y = \begin{bmatrix} \cos \phi_y & 0 & -\sin \phi_y \\ 0 & 1 & 0 \\ \sin \phi_y & 0 & \cos \phi_y \end{bmatrix}. \quad (2.90)$$

The overall joint DCM is calculated from the DCM for each joint axis by

$$\mathbf{B} = \mathbf{B}_x \mathbf{B}_y. \quad (2.91)$$

Since Euler angle rotations are not commutative, the order of the rotations is significant in (2.91). It is important to understand that both axis angles are applied to the joint simultaneously. Here “order” does not refer to temporal order, but rather the order in which the rotations are encountered when progressing from the payload to the housing coordinate systems. Recall that the joint DCM, \mathbf{B} , transfers a vector in the payload coordinate system, \mathbf{Q}_2 , to a vector in the housing coordinate system, \mathbf{Q}_1 , by

$$\mathbf{Q}_1 = \mathbf{B} \mathbf{Q}_2 = \mathbf{B}_x \mathbf{B}_y \mathbf{Q}_2. \quad (2.92)$$

We can see in (2.92) that starting with the payload vector, \mathbf{Q}_2 , it is left multiplied by the DCM for rotation about the payload’s Y axis, \mathbf{B}_y . This transforms the vector into the intermediate coordinate system of the joint. This intermediate coordinate system is located on the cross of the universal joint with its X and Y axes aligned with the arms of the cross. Next the vector is left multiplied by the DCM for rotation about the X axis, \mathbf{B}_x . This transforms the vector into the housing’s coordinate system. This order comes about because in our buoy the universal joint is configured such that the axis attached to the payload is parallel to the payload’s Y axis, and the axis attached to the housing is parallel to the housing’s X axis.

If the joint was attached to the payload and housing such that the axes were switched (i.e. the payload joint axis was aligned with the payload’s X axis, and the housing joint axis was aligned with the housing’s Y axis), then the overall joint DCM would be computed from $\mathbf{B} = \mathbf{B}_y \mathbf{B}_x$. Using this alternate joint configuration and “order of rotations”, would require rederiving equations (2.85) through (2.88) to get the correct relationship between ϕ_x , ϕ_y and ϕ_v , ϕ_z .

2.7.3 Maximum Joint Vertical Angle

Each joint axis, ϕ_x and ϕ_y , is limited to a maximum angular displacement before physical hardstops or software limits the axis’ range of motion. For the prototype buoy configuration this limit is ± 45 degrees. This results in a maximum vertical angle, ϕ_{vmax} , which varies as a function of joint azimuth angle. The maximum joint vertical angle varies between 45 degrees (when one joint axis is at 45 degrees and the other axis is at zero degrees) to 60 degrees (when both joint axes are at 45 degrees). Figure 2.5 plots the maximum vertical

angle as a function of azimuth angle for a system where each axis is limited to ± 45 degrees and the joint is align such that the $\mathbf{B} = \mathbf{B}_x \mathbf{B}_y$.

The maximum value for the joint vertical angle can be calculated by

$$\phi_{v_{max}} = \arccos(\cos^2 \phi_{axis_{max}}), \quad (2.93)$$

where $\phi_{axis_{max}}$ is the maximum angular displacement for each joint axis.

An interesting point about these results, is that four joint azimuth angles where the maximum vertical angle occurs are *not* equally spaced around the azimuth angles. In this case the maximum vertical angle occurs at joint azimuth angles of approximately 35.5, 144.5, 215.5 (-144.5), and 324.5 (-35.5) degrees. This is shown in Figure 2.5. The results are symmetric about the x axis (the 0 and 180 degrees joint azimuth plane) and the y axis (the 90 and 270 degree joint azimuth plane). The maximum points are closer to the x axis. This is another manifestation of the fact that Euler angle rotations are *not* commutative.

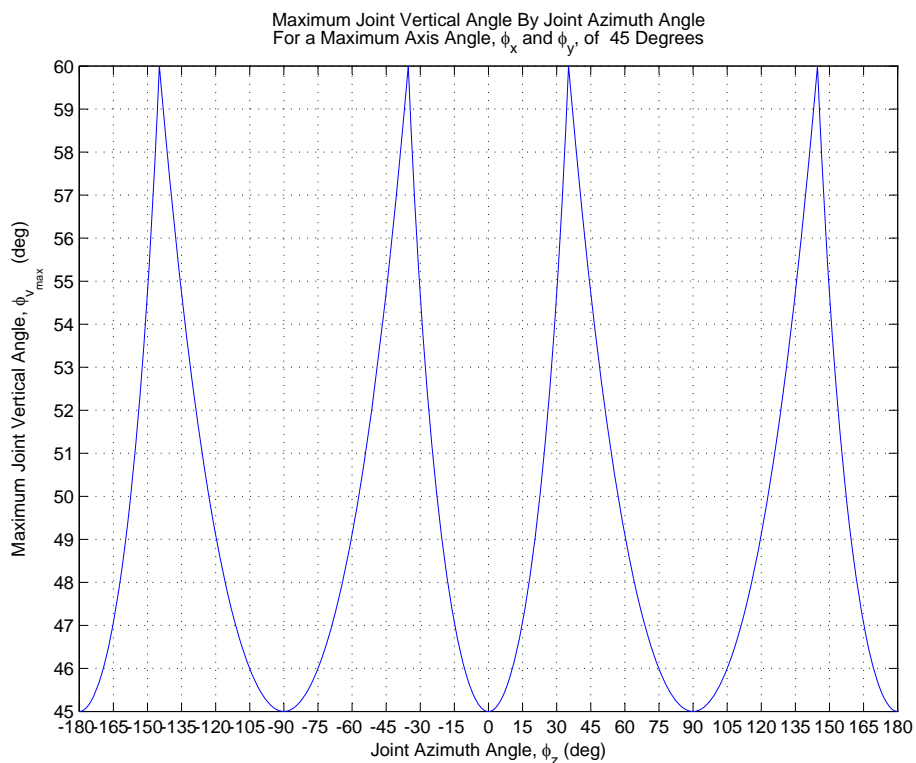


Figure 2.5: The maximum joint vertical angle, $\phi_{v_{max}}$, as a function of joint azimuth angle, ϕ_z , for a universal joint whose axes are limited to ± 45 degrees of motion.

2.7.4 The Joint Angle Partial Derivatives

It is also useful to differentiate (2.85) and (2.86), with respect to ϕ_z and ϕ_v . Doing this gives:

$$\frac{\partial \phi_x}{\partial \phi_z} = \frac{\frac{\cos \phi_z \sin \phi_v}{(1 - \cos^2 \phi_z \sin^2 \phi_v)^{1/2}} - \frac{\cos \phi_z \sin^3 \phi_v \sin^2 \phi_z}{(1 - \cos^2 \phi_z \sin^2 \phi_v)^{3/2}}}{\left(\frac{\sin^2 \phi_z \sin^2 \phi_v}{\cos^2 \phi_z \sin^2 \phi_v - 1} + 1 \right)^{1/2}}, \quad (2.94)$$

$$\frac{\partial \phi_y}{\partial \phi_z} = \frac{-\sin \phi_z \sin \phi_v}{\sqrt{1 - \cos^2 \phi_z \sin^2 \phi_v}} \quad (2.95)$$

and

$$\frac{\partial \phi_x}{\partial \phi_v} = \frac{\frac{\cos \phi_v \sin \phi_z}{(1 - \cos^2 \phi_z \sin^2 \phi_v)^{1/2}} + \frac{\cos \phi_v \cos^2 \phi_z \sin^2 \phi_v \sin \phi_z}{(1 - \cos^2 \phi_z \sin^2 \phi_v)^{3/2}}}{\left(\frac{\sin^2 \phi_z \sin^2 \phi_v}{\cos^2 \phi_z \sin^2 \phi_v - 1} + 1 \right)^{1/2}}, \quad (2.96)$$

$$\frac{\partial \phi_y}{\partial \phi_v} = \frac{\cos \phi_z \cos \phi_v}{\sqrt{1 - \cos^2 \phi_z \sin^2 \phi_v}}. \quad (2.97)$$

The partial derivatives calculated from (2.94) through (2.97) allow one to calculate how much the joint axis angles, ϕ_x and ϕ_y , should be changed by to effect a specified change in joint azimuth and vertical angles, ϕ_z and/or ϕ_v using

$$\Delta \phi_x = \frac{\partial \phi_x}{\partial \phi_z} \Delta \phi_z + \frac{\partial \phi_x}{\partial \phi_v} \Delta \phi_v, \quad (2.98)$$

$$\Delta \phi_y = \frac{\partial \phi_y}{\partial \phi_z} \Delta \phi_z + \frac{\partial \phi_y}{\partial \phi_v} \Delta \phi_v. \quad (2.99)$$

Note that (2.98) and (2.99) linearize the angular changes about the current operating point, so they are approximations and will therefore become inaccurate for large changes.

2.8 Joint Axis Controller Model

Each joint axis is modeled as having an independent low level axis controller. The axis controller allows the axis to be commanded in four possible modes: position-velocity, velocity, acceleration, and jerk (the derivative of acceleration). In position-velocity mode the axis controller drives the axis to a commanded position such that when it reaches the commanded position it will be traveling at the commanded velocity. In all these modes, the joint controller enforces position, velocity, and acceleration (PVA) limits on the motion of the axis.

The axis controller models are integrated at the base simulation rate. In all the implemented and presented here, the joint axis controllers are commanded in position-velocity mode, with the commanded velocity set to zero. This effectively makes the axis controller a position only controller.

A detailed discussion of implementation of each of the axis controller modes is presented in Appendix C.

2.9 Estimating the Structure's Resonant Peak

Numerical simulations of the buoy system excited by regular surface waves, presented in Section 5.12, indicate that the buoy will become uncontrollable if there is significant wave energy at the period with which it will naturally bob up and down in the water.

This resonant peak can be estimated by using a second order mass-spring-damper model of the system

$$m\ddot{z} + d\dot{z} + kz = 0, \quad (2.100)$$

where z is the vertical displacement of the floating object, m is the mass of the object, d is the viscous drag, and k is the restoring force provided by buoyancy. $z = 0$ is height of the object at static equilibrium, and is measured positive upwards.

The restoring (buoyant) force applied to an axially symmetric object floating in the water (with the axis vertical) is proportional to the water line area and the vertical displacement away from its equilibrium height. Therefore

$$F_{res} = A\rho gz, \quad (2.101)$$

where A is the waterline area, ρ is the density of the fluid, and g is the acceleration due to gravity. Modeling our buoy as a vertical cylinder results in

$$F_{res} = \pi R^2 \rho gz, \quad (2.102)$$

where R is the radius of the cylinder.

Recall that when a second order system is in regular form, its natural frequency and damping ratio are readily apparent from the characteristic equation

$$s^2 + 2(\xi\omega_n)s + \omega_n^2 = 0, \quad (2.103)$$

where ξ is the damping ratio and ω_n is the natural frequency.

Given our second order mass-spring-damper model, we can combine (2.100), (2.102), and (2.103) to calculate the natural frequency for the cylinder's vertical motion in the water of

$$\omega_n = \sqrt{\pi\rho g \frac{R^2}{m}} = 175.46 \frac{R}{\sqrt{m}} = 87.73 \frac{D}{\sqrt{m}}, \quad (2.104)$$

or, equivalently, a natural period of

$$T_n = 0.0358 \frac{\sqrt{m}}{R} = 0.0716 \frac{\sqrt{m}}{D}. \quad (2.105)$$

The natural frequency of the system is the frequency it would oscillate at if there were no damping in the system. In the presence of damping the system oscillates at the *damped frequency of oscillation*, ω_d . The damped frequency of oscillation is related to the natural frequency and damping ratio by

$$\omega_d = \sqrt{\omega_n^2 - (\xi\omega_n)^2} = \omega_n \sqrt{1 - \xi^2}. \quad (2.106)$$

This is equivalent to the imaginary part of the solution to the second order characteristic equation for the system. ω_d can also be estimated by measuring the period of oscillation of $z(t)$ in the presence of damping.

The damping ratio can be estimated from the settling time, T_s of the system using the relationships:

$$T_s = \frac{4}{\xi\omega_n}, \quad \xi\omega_n = \frac{4}{T_s}, \quad \xi = \frac{4}{T_s\omega_n}. \quad (2.107)$$

Here the settling time is defined as *four* system time constants, or the time at which the system stays within 98% of its final value.

This allows the damped frequency of oscillation to be predicted based on the cylinder's radius, mass, and settling time from

$$\omega_d = \sqrt{\left(175.46 \frac{R}{\sqrt{m}}\right)^2 - \frac{16}{T_s^2}}. \quad (2.108)$$

If there is not much damping in the system, then the settling time will be “long” and the difference between the natural frequency and the damped frequency of oscillation will be small. It can be shown that if

$$T_s > \frac{9.2}{\omega_n}, \quad (2.109)$$

then the damped frequency of oscillation will be within 10% of the value for the natural frequency. For all the buoy systems here, measured and simulated, this is the case. The buoy's resonant peak (in rad/s) can be accurately predicted by

$$\omega_d \approx \omega_n = 175.46 \frac{R}{\sqrt{m}} = 87.73 \frac{D}{\sqrt{m}}. \quad (2.110)$$

The magnitude of the viscous drag term, d , in (2.100) can be estimated from the settling time of the system as

$$d = \frac{8}{T_s}. \quad (2.111)$$

The magnitude of the damping ratio, ξ , can be estimated by

$$\xi = \frac{4}{T_s R} \sqrt{\frac{m}{\pi \rho g}}. \quad (2.112)$$

2.10 Model Summary

Recall that the dynamics of our system will evolve according to a nonlinear system with 8 DOF and the general form

$$\ddot{\mathbf{x}}_{full}(t) = f(\mathbf{x}_{full}(t), \dot{\mathbf{x}}_{full}(t), \mathbf{u}(t), \dot{\mathbf{u}}(t), \ddot{\mathbf{u}}(t), t), \quad (2.113)$$

where we have assumed that the effects of derivatives higher than those in (2.113) are negligible, we assume that $\ddot{\mathbf{u}}(t)$ is piecewise continuous, $\mathbf{x}_{full} = [\mathbf{d}_0 \ \phi_2 \ \phi_J]^T$ ($\mathbf{x}_{full} \in \mathbb{R}^8$), and $\mathbf{u} \in \mathbb{R}^2$.

What follows is a summary of the equations used to execute the numerical model in the simulation. In this summary the subscript i designates which body is being referred to, where $i = 1$ is the housing and $i = 2$ is the payload. At each simulation step the following sequence occurs:

1. If it is time to update the control signal, then the commanded joint angles are calculated based on the control algorithm selected and the current state information. These commanded joint angles are then sent to the low level controllers for each joint axis. This calculation may not occur at every simulation step because control loop may run at a slower rate than the base simulation rate. This updated each joint axis' position, velocity, and acceleration values. The joint PVA values determine the joint terms, \mathbf{B} , $\dot{\mathbf{B}}$, $\boldsymbol{\Omega}$, and $\dot{\boldsymbol{\Omega}}$.
2. Calculate the forces and moments on the payload and housing bodies by:
 - (a) Calculate and update the buoyant forces and moments on each body by:

- i. Calculate the inclined coordinate system DCM using the procedure in Section 2.3.2.
- ii. Calculate the submerged volume, V_{sub} , and the location of the center of buoyancy, \mathbf{R}_{cb} using the procedure in Section 2.3.3. To include sea state effects calculate \mathbf{r}_{body} using

$$\mathbf{r}_{body_i} = \mathbf{r}_{cm_i} - \mathbf{B}_i \mathbf{R}_{cm_i} - \begin{bmatrix} 0 \\ 0 \\ \zeta(\mathbf{r}_{cm_i}, t) \end{bmatrix}, \quad (2.114)$$

where the subscript i is 1 for the housing and 2 for the payload, and the wave elevation ζ is given by

$$\zeta(x, y, t) = \sum_{j=1}^N A_j \sin[\omega_j t - k_j (x \cos \beta + y \sin \beta) + \phi_j]. \quad (2.115)$$

Here $k_j = \omega_j^2/g$ and N, A_j, ω_j, ϕ_j are generated using a statistical description of the sea state (see Appendix A). β is the direction of seas. If no waves are present, set $\zeta = 0$. Here the index j refers individual component waves used to make up the wave model.

- iii. Calculate the actual buoyant forces and moments on each body in their body frame by:

$$\mathbf{F}_{buoyant_i} = \mathbf{B}_i \begin{bmatrix} 0 \\ 0 \\ \rho g V_{sub_i} \end{bmatrix}, \quad (2.116)$$

$$\mathbf{M}_{buoyant_i} = (\mathbf{R}_{cb_i} - \mathbf{R}_{cm_i}) \times \mathbf{F}_{buoyant_i}. \quad (2.117)$$

- (b) Calculate the gravity forces and moments on each body in their body frame by:

$$\mathbf{F}_{grav_i} = \mathbf{B}_i^T \begin{bmatrix} 0 \\ 0 \\ -m_i g \end{bmatrix}, \quad (2.118)$$

$$\mathbf{M}_{grav_i} = (\mathbf{R}_{cmsys_i} - \mathbf{R}_{cm_i}) \times (-\mathbf{F}_{grav_i}). \quad (2.119)$$

- (c) Calculate the drag forces and moments on each body in their body frame by defining the matrix

$$\mathbf{K}_{drag_i} = \begin{bmatrix} -f_{sub_i} C_{D_{fXY_i}} L_i R_i & 0 & 0 \\ 0 & -f_{sub_i} C_{D_{fXY_i}} L_i R_i & 0 \\ 0 & 0 & -C_{D_{fzi}} R_i^2 \end{bmatrix}, \quad (2.120)$$

and then calculating

$$\mathbf{F}_{drag_i} = \mathbf{K}_{drag_i} [\dot{\mathbf{R}}_{cm_i} - \mathbf{B}_i^T \mathbf{v}_{fluid_i}(\mathbf{r}_{cm_i}, t)], \quad (2.121)$$

$$\mathbf{M}_{drag_i} = -f_{sub_i} L_i R_i \begin{bmatrix} \text{sign}(\Omega_{xi}) C_{D_{mXY}} \Omega_{xi}^2 \\ \text{sign}(\Omega_{yi}) C_{D_{mXY}} \Omega_{yi}^2 \\ \text{sign}(\Omega_{zi}) C_{D_{mZ}} \Omega_{zi}^2 \end{bmatrix}, \quad (2.122)$$

$$\mathbf{M}_{yawpass_i} = \begin{bmatrix} 0 \\ 0 \\ -\text{sign}(\Omega_{zi}) n_{fins_i} \frac{1}{8} C_D \rho w_{fin_i} \Omega_{zi}^2 [(R_i + l_{fins_i})^4 - R_i^4] \end{bmatrix}, \quad (2.123)$$

$$\mathbf{M}_{dragTi} = (\mathbf{R}_{cb_i} - \mathbf{R}_{cmsys_i}) \times \mathbf{F}_{drag_i}, \quad (2.124)$$

where, if waves are present, the fluid velocity is given by

$$\mathbf{v}_{fluid}(x, y, z, t) = \sum_{j=1}^N \omega_j A_j e^{k_j z} \begin{bmatrix} \sin[\omega_j t - k_j(x \cos \beta + y \sin \beta) + \phi_j] \cos \beta \\ \sin[\omega_j t - k_j(x \cos \beta + y \sin \beta) + \phi_j] \sin \beta \\ \cos[\omega_j t - k_j(x \cos \beta + y \sin \beta) + \phi_j] \end{bmatrix}, \quad (2.125)$$

otherwise $\mathbf{v}_{fluid} = \mathbf{0}$.

- (d) Sum the forces and moments on each body and convert the forces to the navigation coordinate frame using

$$\mathbf{f}_{ext_i} = \mathbf{B}_i (\mathbf{F}_{buoyant_i} + \mathbf{F}_{grav_i} + \mathbf{F}_{drag_i}), \quad (2.126)$$

$$\mathbf{T}_{ext_i} = \mathbf{M}_{buoyant_i} + \mathbf{M}_{grav_i} + \mathbf{M}_{drag_i} + \mathbf{M}_{yawpass_i} + \mathbf{M}_{dragTi}. \quad (2.127)$$

3. Calculate the payload's rotational acceleration, $\dot{\mathbf{\Omega}}_2$, by:

- (a) Calculate each body's inertia about the *system's CM* by:

$$\mathbf{R}_1 = \mathbf{R}_{cm1} \left(1 - \frac{m_1}{m_1 + m_2} \right) - \frac{m_2}{m_1 + m_2} [\mathbf{R}_{J1} + \mathbf{B} (\mathbf{R}_{cm2} - \mathbf{R}_{J2})], \quad (2.128)$$

$$\mathbf{R}_2 = \mathbf{R}_{cm2} \left(1 - \frac{m_2}{m_1 + m_2} \right) - \frac{m_1}{m_1 + m_2} [\mathbf{R}_{J2} + \mathbf{B}^T (\mathbf{R}_{cm1} - \mathbf{R}_{J1})], \quad (2.129)$$

$$\mathbf{J}_1 = \mathbf{J}_h + m_1 (\mathbf{R}_1^T \mathbf{R}_1 \mathbf{I} - \mathbf{R}_1 \mathbf{R}_1^T), \quad (2.130)$$

$$\mathbf{J}_2 = \mathbf{J}_p + m_2 (\mathbf{R}_2^T \mathbf{R}_2 \mathbf{I} - \mathbf{R}_2 \mathbf{R}_2^T). \quad (2.131)$$

- (b) Find the time rate of change of the inertia terms by either: (a) finding the difference between the current value and the value at the previous time step, or

(b) by solving the system analytically for $\dot{\mathbf{J}}_i$ using:

$$\dot{\mathbf{R}}_1 = -\frac{m_2 \dot{\mathbf{B}} (\mathbf{R}_{cm2} - \mathbf{R}_{J2})}{m_1 + m_2}, \quad (2.132)$$

$$\dot{\mathbf{R}}_2 = -\frac{m_1 \dot{\mathbf{B}}^T (\mathbf{R}_{cm1} - \mathbf{R}_{J1})}{m_1 + m_2}, \quad (2.133)$$

$$\dot{\mathbf{J}}_1 = m_1 \left(2\mathbf{R}_1^T \dot{\mathbf{R}}_1 \mathbf{I} - \dot{\mathbf{R}}_1 \mathbf{R}_1^T - \mathbf{R}_1 \dot{\mathbf{R}}_1^T \right), \quad (2.134)$$

$$\dot{\mathbf{J}}_2 = m_2 \left(2\mathbf{R}_2^T \dot{\mathbf{R}}_2 \mathbf{I} - \dot{\mathbf{R}}_2 \mathbf{R}_2^T - \mathbf{R}_2 \dot{\mathbf{R}}_2^T \right). \quad (2.135)$$

(c) Solve for the payload's rotational acceleration, $\dot{\hat{\boldsymbol{\Omega}}}_2$, using

$$\begin{aligned} (\mathbf{J}_2 + \mathbf{B}^T \mathbf{J}_1 \mathbf{B}) \dot{\hat{\boldsymbol{\Omega}}}_2 &= -\hat{\boldsymbol{\Omega}}_2 \mathbf{J}_2 \boldsymbol{\Omega}_2 - \mathbf{B}^T \mathbf{J}_1 \mathbf{B} (\hat{\boldsymbol{\Omega}} \boldsymbol{\Omega}_2 - \hat{\boldsymbol{\Omega}}) \\ &\quad - (\hat{\boldsymbol{\Omega}}_2 - \hat{\boldsymbol{\Omega}}) \mathbf{B}^T \mathbf{J}_1 \mathbf{B} (\boldsymbol{\Omega}_2 - \boldsymbol{\Omega}) \\ &\quad - \dot{\mathbf{J}}_2 \boldsymbol{\Omega}_2 - \mathbf{B}^T \dot{\mathbf{J}}_1 \mathbf{B} (\boldsymbol{\Omega}_2 - \boldsymbol{\Omega}) + \mathbf{B}^T \mathbf{T}_{ext1} + \mathbf{T}_{ext2}, \end{aligned} \quad (2.136)$$

where \mathbf{T}_{ext1} and \mathbf{T}_{ext2} are the total moments applied to the housing and payload bodies respectively. \mathbf{T}_{ext1} and \mathbf{T}_{ext2} are in the bodies' coordinate systems.

4. Calculate the translational acceleration of the joint by

$$\ddot{\mathbf{d}}_0 = \frac{-m_1 \left(\dot{\mathbf{B}}_1 \hat{\boldsymbol{\Omega}}_1 + \mathbf{B}_1 \dot{\hat{\boldsymbol{\Omega}}}_1 \right) \mathbf{D}_1 - m_2 \left(\dot{\mathbf{B}}_2 \hat{\boldsymbol{\Omega}}_2 + \mathbf{B}_2 \dot{\hat{\boldsymbol{\Omega}}}_2 \right) \mathbf{D}_2 + \mathbf{f}_{ext1} + \mathbf{f}_{ext2}}{m_1 + m_2}, \quad (2.137)$$

where \mathbf{f}_{ext1} and \mathbf{f}_{ext2} are the total force applied to each body in the *navigation* coordinate system. The values used for \mathbf{B}_1 , $\dot{\mathbf{B}}_1$, and $\boldsymbol{\Omega}_1$ are from the previous time step.

5. Integrate the system forward in time using:

(a) Integrate the low level joint controller models forward in time to get the new position, velocity, and acceleration values for joint axis.

(b) Find the new joint location and velocity in the navigation frame by:

$$\mathbf{d}_{0_{k+1}} = \mathbf{d}_{0_k} + \dot{\mathbf{d}}_{0_k} dt + \frac{1}{2} \ddot{\mathbf{d}}_{0_k} dt^2, \quad (2.138)$$

$$\dot{\mathbf{d}}_{0_{k+1}} = \dot{\mathbf{d}}_{0_k} + \ddot{\mathbf{d}}_{0_k} dt, \quad (2.139)$$

where k is current time step and $k + 1$ is the next time step.

(c) Find the payload attitude and rotational velocity using

$$\mathbf{B}_{2_{k+1}} = \mathbf{B}_{2_k} + \dot{\mathbf{B}}_{2_k} dt, \quad (2.140)$$

$$\boldsymbol{\Omega}_{2_{k+1}} = \boldsymbol{\Omega}_2 + \dot{\hat{\boldsymbol{\Omega}}}_{2_k} dt. \quad (2.141)$$

(d) Normalize the payload attitude DCM using the Gram-Schmidt algorithm. Without periodic renormalization, the payload DCM would accumulate round off errors and become an invalid DCM. This renormalization does not need to occur at every simulation step.

- (e) Update the housing's rotational and translational position, velocity, and acceleration values using:

$$\mathbf{B}_1 = \mathbf{B}_2 \mathbf{B}^T, \quad (2.142)$$

$$\boldsymbol{\Omega}_1 = \mathbf{B} (\boldsymbol{\Omega}_2 - \boldsymbol{\Omega}), \quad (2.143)$$

$$\dot{\boldsymbol{\Omega}}_1 = \mathbf{B} (\hat{\boldsymbol{\Omega}} \boldsymbol{\Omega}_2 + \dot{\boldsymbol{\Omega}}_2 - \dot{\boldsymbol{\Omega}}), \quad (2.144)$$

$$\mathbf{r}_{cm1} = \mathbf{d}_0 - \mathbf{B}_1 \mathbf{D}_{J1}, \quad (2.145)$$

$$\dot{\mathbf{r}}_{cm1} = \dot{\mathbf{d}}_0 - \mathbf{B}_1 \hat{\boldsymbol{\Omega}}_1 \mathbf{D}_{J1}, \quad (2.146)$$

$$\ddot{\mathbf{r}}_{cm1} = \ddot{\mathbf{d}}_0 - \mathbf{B}_1 \dot{\hat{\boldsymbol{\Omega}}}_1 \mathbf{D}_{J1}. \quad (2.147)$$

- (f) Update the payload's translational position, velocity, and acceleration by:

$$\mathbf{r}_{cm2} = \mathbf{d}_0 - \mathbf{B}_2 \mathbf{D}_{J2}, \quad (2.148)$$

$$\dot{\mathbf{r}}_{cm2} = \dot{\mathbf{d}}_0 - \mathbf{B}_2 \hat{\boldsymbol{\Omega}}_2 \mathbf{D}_{J2}, \quad (2.149)$$

$$\ddot{\mathbf{r}}_{cm2} = \ddot{\mathbf{d}}_0 - \mathbf{B}_2 \dot{\hat{\boldsymbol{\Omega}}}_2 \mathbf{D}_{J2}. \quad (2.150)$$

This completes one iteration of the simulation loop. For clarity, the integration method presented above is an implementation of Euler's method. In the actual numerical simulation, the integration is performed using an Improved Euler's method. The Improved Euler's method is implemented by:

- I At the completion of step 4, the system state values are copied to temporary variables.
- II The integration described in step 5 is performed on the temporary variables.
- III Steps 2 through 4 are run on the temporary variables to calculate the derivatives $\dot{\boldsymbol{\Omega}}_2$ and $\dot{\mathbf{d}}_0$ at the end of the time step.
- IV The improved values for $\dot{\boldsymbol{\Omega}}_2$ and $\dot{\mathbf{d}}_0$ are calculating by averaging their values in the temporary and non-temporary variables.
- V The integration step, step 5, is then run on the non-temporary variables using the averaged derivative values computed in step IV.

Chapter 3

Model Verification

The model developed in Chapter 2 allows an investigation of the dynamics and control of the coupled two body buoy in the presence of gravity, buoyancy, and drag. The inertial effects of the two bodies on each other are solved analytically in the dynamics model. The gravity, buoyancy, and drag effects are specified by external forces and moments applied to the model.

The gravity and buoyancy effects can be calculated directly from the geometry of the system. The drag calculations are more complicated, and a reasonable drag model is required for the numerical simulation of the coupled system. But what is a “reasonable” drag model?

The two experiments presented in this chapter were designed to inform the choice of drag model and subsequently validate the drag model. Two cylinders were built, a small non-instrumented cylinder and large instrumented cylinder. These cylinders were placed in water and released from various initial conditions and their responses recorded. Then their geometry and mass distributions were modeled in the simulation, and the simulation parameters were adjusted until the simulated results approximated the experimental results.

These results were applied to the numerical simulation in two manners:

1. The simulation framework was used to model a single cylinder which closely matched the experimental cases. The global simulation parameters were adjusted to bring the numerical simulation into agreement with the experimental results.
2. When simulating the jointed two body buoy, the buoy was configured to run with the joint locked in the vertical position. Thus, the two body buoy system was mimicking a single cylindrical buoy.

3.1 Small Test Cylinder Experiment

Because the small test cylinder has no instrumentation mounted on it, for this experiment the quantitative measurements were made by analyzing video recordings of the trials. The principal quantitative comparisons are:

1. Settling time
2. Period of oscillations

3. Approximate magnitude of first several rotational and translational oscillations after release.

Because of the crudeness of these measurements, much of the comparisons in this experiment are qualitative in nature. The following qualitative parameters were of interest:

1. The coupling between roll and pitch motions.
2. The coupling between the roll/pitch and yaw motions.
3. The coupling between the vertical translation and angular rotations.

3.1.1 Experimental Setup

A small cylinder was constructed out of a 24 inch long piece of 3 inch schedule 40 PVC pipe, with an actual outer diameter of 3.5 inches. An end cap was placed on the bottom and a threaded cap was placed on the top. The body of the pipe was painted in alternating red and white stripes 1 inch wide to help with position and attitude determination. The cylinder was then ballasted with two sealed plastic bags of lead shot, a 1.8 lbs bag and a 1.0 lbs bag. Figure 3.1 shows the approximate ballast position in the cylinder and a photograph.

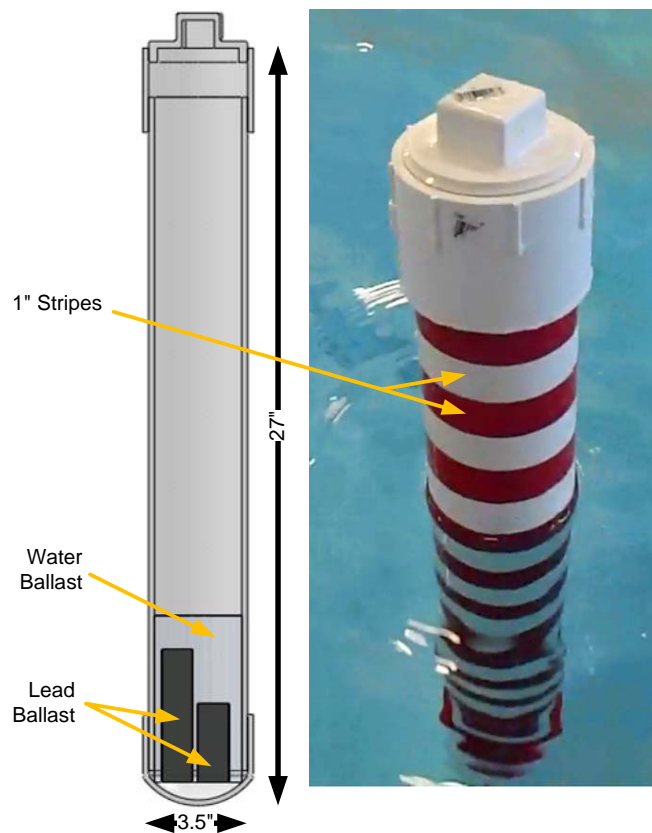


Figure 3.1: The diagram of the approximate ballast position in the cylinder and photo of the cylinder during testing. The 1 inch markings aid in determining the position response of the cylinder from the recorded video.

The buoy was released from various initial positions and attitudes and the response recorded by video for later review and measurement.

3.1.2 Measurement and Simulation Comparison

A video clip showing video footage from three experimental trials and the corresponding animation of the numerical simulation results is available at “<http://www.youtube.com/watch?v=1s0JFz7MHD0>”. The three trials presented in the video show a vertical drop test, a moderate (45 degree) inclined release test, and an extreme (85 degree) inclined release test. For each of these trials a numerical simulation was run of the cylinder with the same initial conditions. The animation and the video footage were then synced together and merged into a single video where they play side by side using the SIMDIS visualization software.

Viewing the three trials side by side with their corresponding simulation animations it is clear that the simulation does behave in a similar manner to the actual cylinder. Figure 3.2 shows four frames from this video.

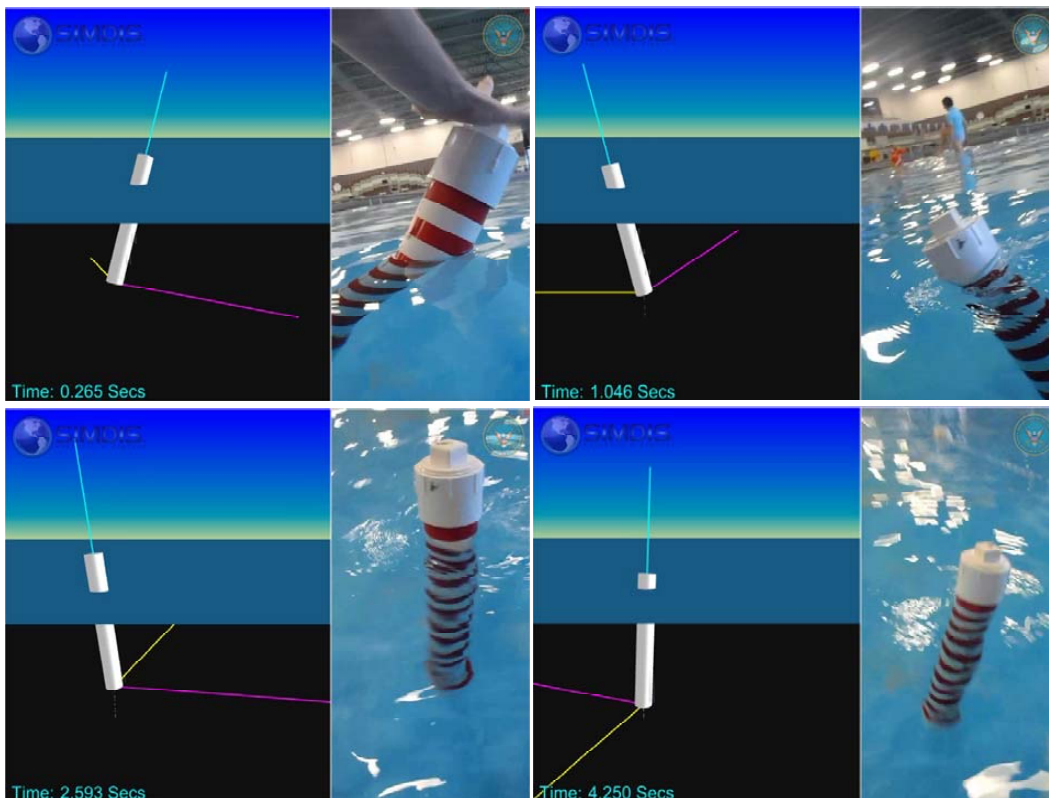


Figure 3.2: This shows four frames from the video of the combined video footage and the animated results from the numerical simulation. The cylinder was released from approximately a 45 degree angle. The animated simulation results seem qualitatively reasonable when compared to the actual response in that the settling times, period of oscillation, amount of coupling between axes, and magnitude of oscillations are all similar.

3.1.2.1 Quadratic vs. Linear Drag Comparison

In most of the trials, significant angular displacements had dissipated by 20 to 30 seconds after cylinder release. This provides a good quantitative metric of the cylinder's settling time.

A quadratic drag relationship for the moment resisting rolling and pitching motions is

$$M_{d\perp z} = -\text{sign}(\Omega)\frac{1}{8}\rho C_{D_{XY}}\Omega^2 D(z_1^4 + z_2^4). \quad (3.1)$$

Here Ω is the rotational rate about the CM along the X or Y directions. $C_{D_{XY}}$ is the coefficient of drag for flow perpendicular to the cylinder. ρ is the density of the fluid. D is the diameter of the cylinder. And z_1 and z_2 are the distances between the center of mass and the waterline and center of mass and the bottom of the buoy, respectively.

An alternative drag model is based on a linear relationship with the rotational velocity. Making a slight modification to (3.1) gives

$$M_{d\perp z} = -\frac{1}{8}\rho C_{D_{XY}}\Omega D(z_1^4 + z_2^4). \quad (3.2)$$

In (3.2), $C_{D_{XY}}$ is no longer dimensionless to maintain dimensional consistency.

With this linear relationship the angular oscillations decay completely to zero as expected.

Figure 3.3 shows a comparison of the simulated buoy response when released from an initial inclined angle of 45 degrees using linear drag model (red) against the quadratic drag model (blue).

In reviewing the video of the 20 trials performed, it is clear that 1) the oscillations decay to a fraction of the initial displacement within 3 or 4 periods and 2) that oscillations do seem to come close to zero magnitude. However, measuring the magnitude of the small angular displacements is difficult and the oscillations predicted by the quadratic drag model are ± 2 degrees. Oscillations of this magnitude are likely to be too small to see in the video. Thus, qualitatively, the quadratic model seems to approximate the the initial transient response better.

3.1.2.2 Asymmetric Center of Mass Comparison

The illustration of the ballast locations in Figure 3.1 are notional. The volume displayed in the illustration is correct, but the bags of ballast were not positioned as shown. When the test buoy was first put in the water, with just the lead ballast, at equilibrium it would list to one side indicating that the center of mass was not located on the central longitudinal axis (Z) of the buoy. This listing was reduced as much as possible by resettling the ballast and adding a couple pounds of water to the buoy as additional ballast.

In all cases when the buoy was released with any inclined angle, some amount of azimuthal rotation would become evident. This occurred even when great care was taken to not impart any azimuthal rotation on release. The CAD model of the test buoy (used in Figure 3.1) was used to determine a nominal center of mass location and inertia tensor for the test buoy. The CAD software gives a center of mass, in meters, of

$$\mathbf{R}_{CM_{CAD}} = \begin{bmatrix} -0.0023 \\ 0 \\ 0.2042 \end{bmatrix}. \quad (3.3)$$

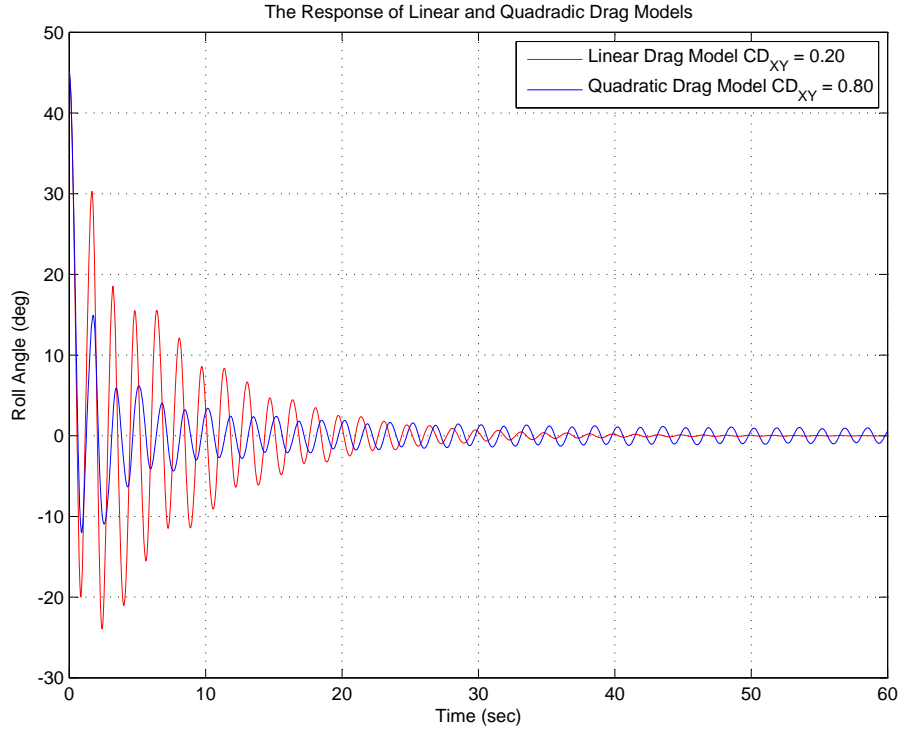


Figure 3.3: This plot compares the cylinder’s simulated response between the quadratic drag model (blue) against the linear drag model (red). The linear model does bring the angular oscillations to zero. The $C_{D_{XY}}$ values used were to give both responses similar settling times of about 30 seconds. The quadratic model does not go all the way to zero within a minute because at very low rotational velocities the velocity squared term is even smaller and the drag becomes negligible. In this plot, the oscillation of the quadratic model at 60 seconds is approximately ± 1 degree. This would appear as stationary to the naked eye.

So the center of mass is nominally less than 3 mm off the long axis of the buoy. The corresponding inertia tensor, in $kg\ m^2$, is

$$\mathbf{J}_{CAD} = \begin{bmatrix} 0.14444 & 0 & 0.00083 \\ 0 & 0.14477 & 0 \\ 0.00083 & 0 & 0.00366 \end{bmatrix}. \quad (3.4)$$

When these parameters are entered into the simulation, and the initial incline angle is NOT in the plane of the center of mass and the Z axis, rotational coupling between the axes is observed. The results of one of these simulations are shown in Figure 3.4. Additionally, the steady state list in pitch is noticeable, due the off axis center of mass. The initial azimuthal rotation rate in the model is significantly higher than was observed in the trials. In the trials, azimuthal rotational periods were more typically between 6 and 12 seconds.

It is noteworthy that these results show that shifting the cylinder’s CM by only 2.5% (of the cylinder’s diameter) off the long axis is enough to cause significant coupling between the axes.

If the initial angular displacement of the cylinder is in the plane of the CM off-axis direction, then no rotational coupling is observed. So the difference between modeled azimuthal rotation rate and observed rotation rate could be due to:

1. The actual initial angular displacement is closer to the plane of the CM off-axis direction than in the simulation.
2. The actual CM is less off axis than the modeled CM.
3. The quadratic drag model needing additional tuning.

There was insufficient data in this experiment to determine which of the above causes was the dominant cause of the azimuthal rotation mismatch.

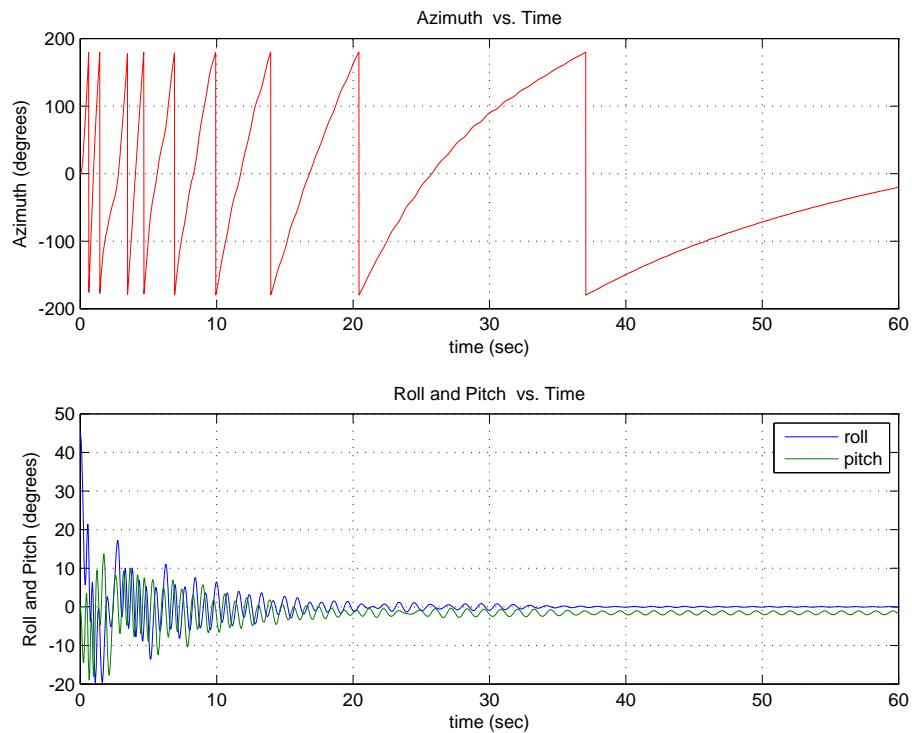


Figure 3.4: The simulation’s response to being released from an initial angular displacement out of plane with the asymmetric center of mass. The center of mass was off axis by less than 3 mm. When the cylinder was released, the asymmetry caused the roll motion (blue) to be coupled into the pitch (green) and azimuthal (red) motion.

3.1.3 Small Cylinder Experiment Conclusions

The small test cylinder experiment suggested the following results:

1. The quadratic drag model was more appropriate than the linear drag model.
2. The peak of the second oscillation was significantly smaller than the initial release angle.

3. A slightly off-axis CM will produce noticeable coupling from roll and pitch motion into yaw motion and between the roll and pitch axes.
4. Significant cylinder motion decays away within 30 to 60 seconds of release.

However, any quantitative results derived from the small cylinder test were calculated by reviewing the video footage frame by frame and making crude measurements of the angles and heights visible in the frame. This procedure was extremely time consuming and tedious. The quantitative results are useful as approximate bounds on the cylinder's response. However, given all the quantitative uncertainties in this experiment, this led to a desire for an instrumented cylinder that could generate better and higher resolution quantitative results with some form of automated on-board instrumentation.

3.2 Large Test Cylinder Experiment

3.2.1 Instrumented Cylinder Description

The goal of this series of tests was to validate the numerical model of a cylinder floating in the water. An instrumented cylinder 6.375 inches in diameter and 36 inches long was tested at the United States Naval Academy's hydrodynamics laboratory.

An instrumented cylindrical buoy was constructed to hold a CrossBow NAV440 Inertial Measurement System (INS), and a Microhard Nano 920 spread spectrum radio. Figure 3.5 shows assembly drawing for the buoy. A pair of 7.2 volt 1800 mAh batteries in series supply electrical power for the INS and radio. The data from the INS is transmitted by the radio to a matching radio where it is displayed and logged by a laptop.

The CrossBow NAV440 INS is a GPS and magnetometer aided inertial measurement system. Since the testing was completed indoors, GPS aiding was disabled. Since there were significant ferrous materials near the tanks, the magnetometer measurements may not be accurate in an absolute sense. This resulted in significant low frequency errors in the measured roll and pitch data. These errors were later removed by a digital high pass filter. Also, yaw angle measurements were not used, rather the yaw rate data was used to evaluate yaw effects and performance. Additionally, without GPS, the principal measurements by the IMU for this analysis are: roll and pitch angles, yaw rate, and vertical (z axis) translational acceleration.

3.2.2 Trial Descriptions

We performed 26 individual tests, designated A through Z. Five kinds of tests were performed:

Inclined Release (IR): In this test the cylinder is placed approximately horizontal on the water's surface and then released. This type of test allows for characterization of the buoyant and drag moments about the cylinder's X and Y axes, and the coupling between all three axis. It also provided a good measure of the cylinder's settling time.

Yaw Rotation (YR): In this test the cylinder starts floating vertically at equilibrium. A spin about the long axis (Z) is imparted to the cylinder. This test allows for characterization of the rotational drag about the cylinder's long axis, and coupling between the rotation about the Z axis into the roll and pitch axes.

Table 3.1: A summary of the large instrumented test cylinder trials.

Trial	Test Type	Comments
A	IR	
B	IR	About the Y axis, raw IMU measurements have low frequency errors.
C	IR	About the X axis.
D	VT	Roll and pitch measurements have bias errors.
E	YR	
F	IR	Possibly imparted spin about the Z axis on release.
G	IR	About the X axis.
H	YR	
I	YR	
J	IR	About the Y axis.
K	IR	About the Y axis.
L	VT	No Video Recorded. Roll and pitch measurements both have errors.
M	VT	Buoy hit wall at 1 min.
N	IR	Roll and pitch values reasonable at end.
O	SW	2 inch wave at 2 sec. period. Evidence of resonance.
P	SW	4 inch wave at 3 sec. period.
Q	SW	2 inch wave at 5 sec. period.
R	LW	12 inch wave at 5 sec. period.
S	LW	33 inch wave at 2.5 sec. period. Wave tank pump shutdown fault.
T	LW	33 inch wave at 2 sec. period. Evidence of resonance.
U	LW	24 inch wave at 2 sec. period. Evidence of resonance.
V	LW	6 inch wave at 8.25 sec. period. Almost no motion.
W	LW	6 inch wave at 6 sec period.
X	LW	6 inch wave at 4 sec period.
Y	LW	6 inch wave at 2 sec period. Evidence of resonance.
Z	LW	6 inch wave at 1 sec period.

Vertical Translation (VT): In this test the cylinder starts vertically in the water submerged such that its top surface is at the water's surface and then released. This test allows the characterization of the vertical translational drag and the cylinder's characteristic frequency.

Small Wave Tank (SW): In this test the cylinder starts at equilibrium and is excited by waves generated in the small wave tank.

Large Wave Tank (LW): In this test the cylinder starts at equilibrium and is excited by waves generated in the large wave tank.

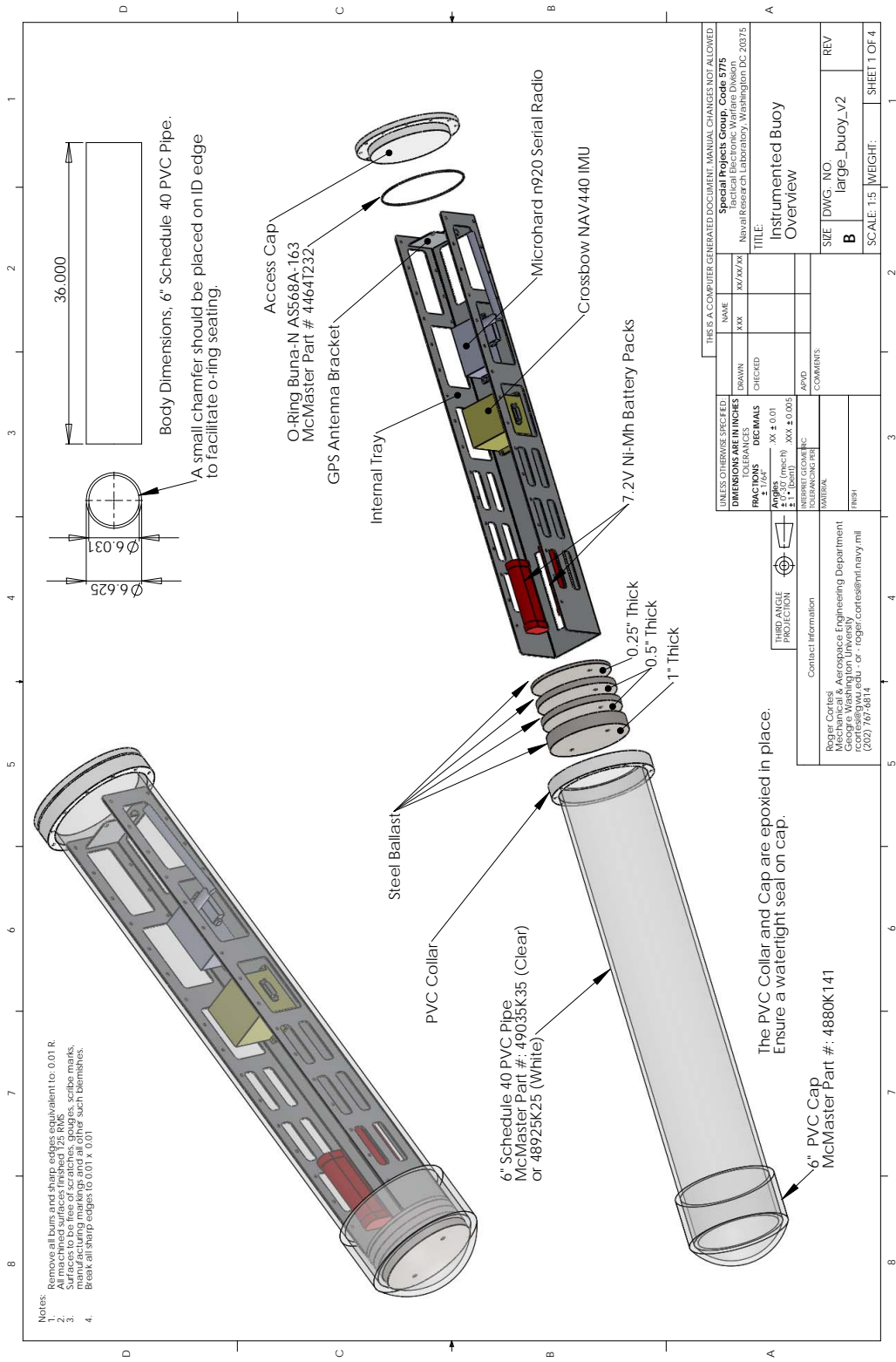


Figure 3.5: The assembly drawing of the large instrumented cylinder.

3.2.3 Angular Data Filtering

Due to the lack of GPS input and the significant amount of ferrous metal in and around the tank where the testing occurred, there were significant low frequency errors in the measured roll and pitch angles. These error were removed by applying a 200 point high pass digital filter to the measured roll and pitch angles [24].

The number of elements in the filter z is $n = 200$. The value of each filter element is given by

$$z[i] = \begin{cases} -1/n & \text{if } i \neq n/2, \\ 1 & \text{if } i = n/2. \end{cases} \quad (3.5)$$

The filtered output, y , is found by the convolution of the input signal, x , with the filter, z , using the MATLAB convolution command,

$$y = x * z. \quad (3.6)$$

Figure 3.6 shows the raw measured roll and pitch angles (blue) for Trial B. The slow large amplitude oscillation indicated by the measured data did not occur. This is clear from the video footage of the trial. The filtered data (green) has been centred about zero by the digital high pass filter.

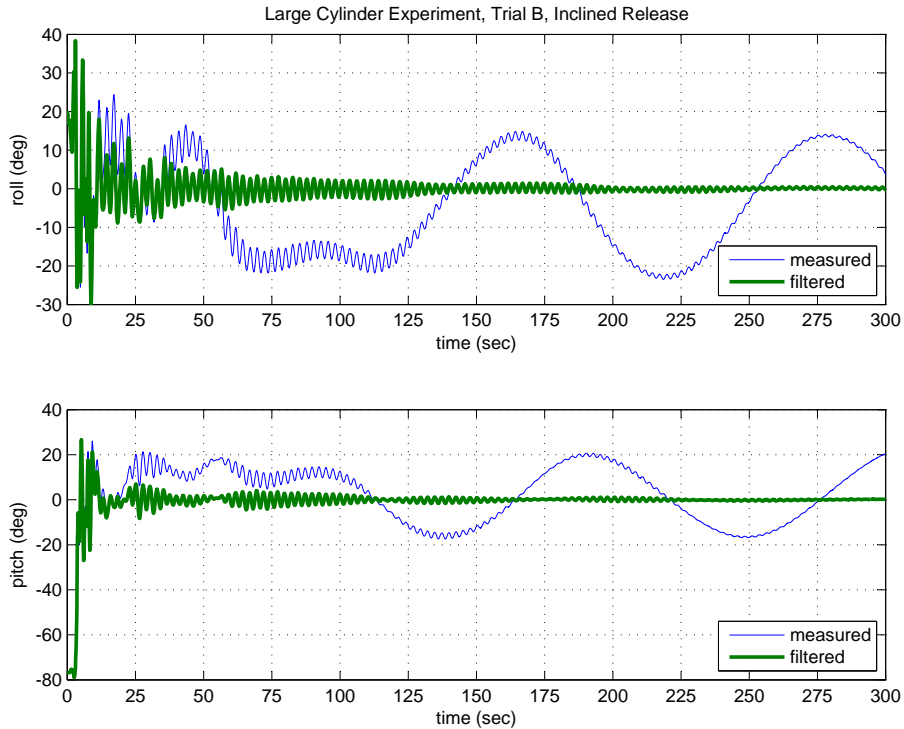


Figure 3.6: Roll and Pitch Values from the Large Test Cylinder Experiment, Trial B. Trial B was an inclined release trial where the cylinder was released from 78 degrees away from the vertical (15 degrees in roll and -80 degrees in pitch). The filtered data was generated by running the data through a 200 point high pass digital filter to remove the low frequency error in the data.

3.2.4 Incline Release Results

The inclined release trials were trials B, F, J, and N. Video footage for the first 60 seconds of each of these trials is viewable at “<http://www.youtube.com/watch?v=0PQfiAA-rsU>”. Figure 3.7 shows four frames 1 second apart from the trial B video.

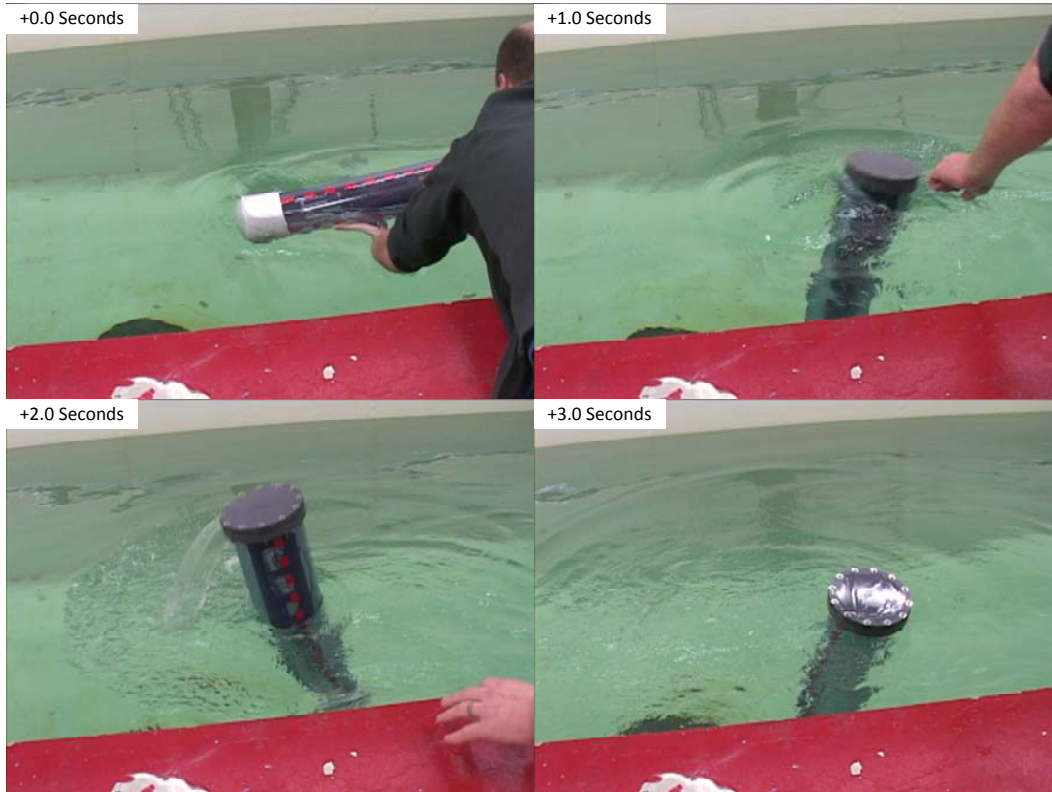


Figure 3.7: Four frames, one second apart, for Trial B, an inclined release trial.

Plots of the roll and pitch from the inclined release trials are plotted next in Figures F.1 through F.4, showing approximately 55 second after release of the filtered and unfiltered data. Next Figures 3.8 and 3.9 show the filtered data for Trials B, F, J, and N. plotted together.

Looking at these plots a couple things stand out.

1. The magnitude of the peak of the oscillation after the buoy has been release is consistently less than one half the initial angle.
2. It takes 1.5 to 2 seconds for the cylinder to complete its first oscillation after release.
3. With the exception of Trial J, the oscillations settle to proximately ± 10 degrees within 10 to 15 seconds after buoy release.

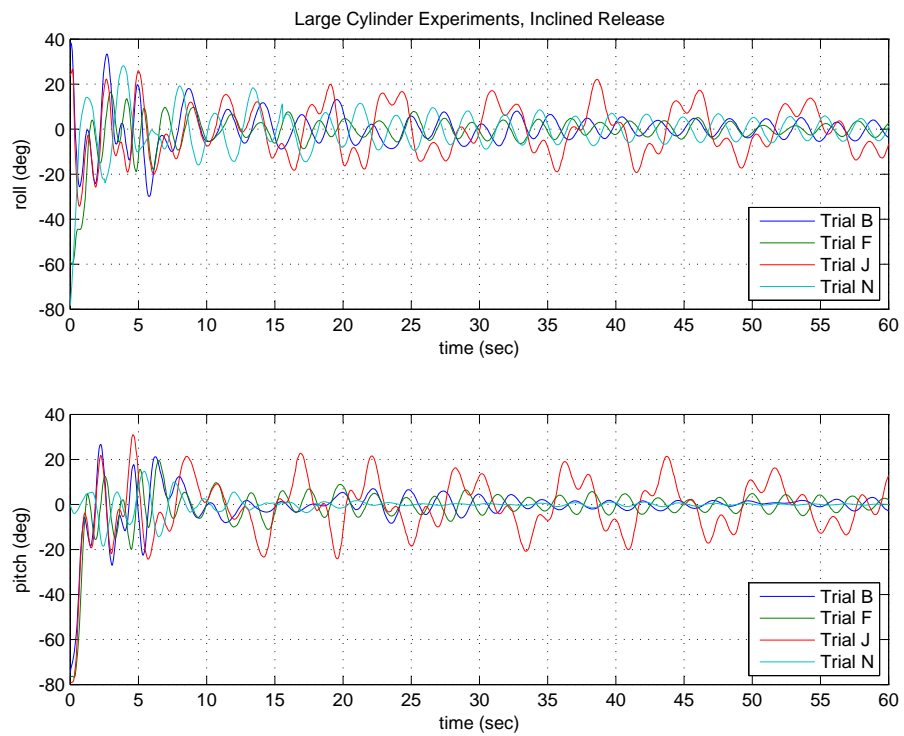


Figure 3.8: The filtered roll and pitch values from the large test cylinder experiment, trials B, F, J, and N. The oscillations in Trial J are noticeably worse than the other trials.

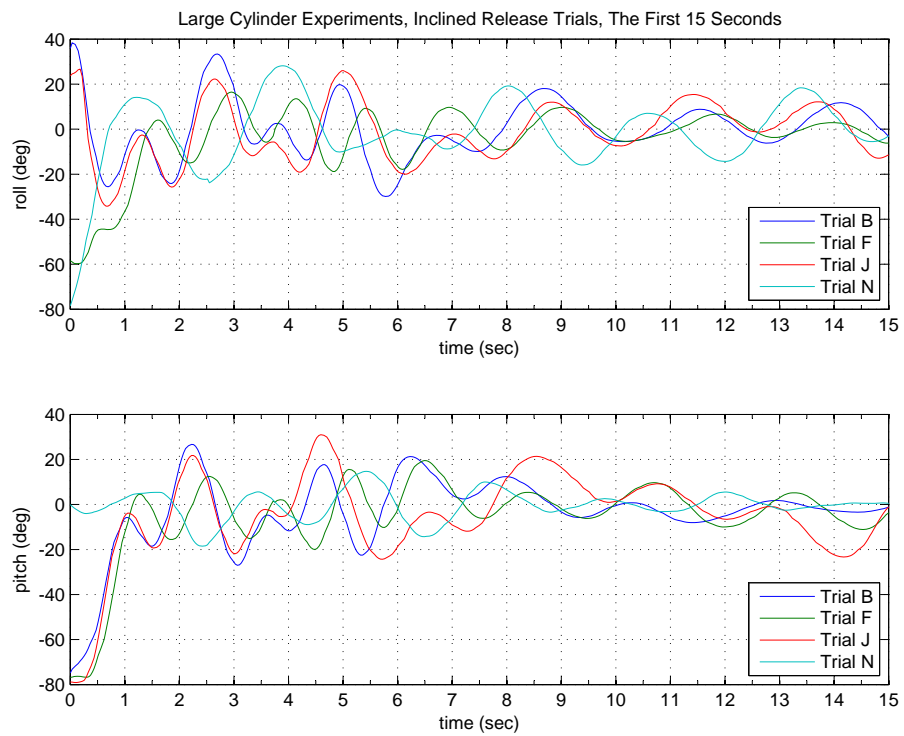


Figure 3.9: The first 15 seconds of filtered roll and pitch values from the large test cylinder experiment, trials B, F, J, and N.

3.2.5 Yaw Rotation

The Figure 3.10 shows the yaw rate vs. time for the three yaw rotation trials (Trials E, H, and I). For these trials the cylinder started at vertical equilibrium and then a spin was imparted about its long axis. The data from the three trials appears to be consistent. The following items are noteworthy about these results:

1. Over half of the rotational velocity seems to be dissipated in the first 5 seconds, then the rate of deceleration slows significantly, indicating a quadratic drag relationship might be appropriate.
2. The shape of the bounding envelope from approximately 5 seconds onward indicates that a linear or quadratic drag relationship may be an appropriate model.
3. The “wobble” in the yaw rate is due to the cylinder’s center of mass being slightly off the long axis.
4. The IMU’s rate gyros saturate at just under 250 degrees per second.

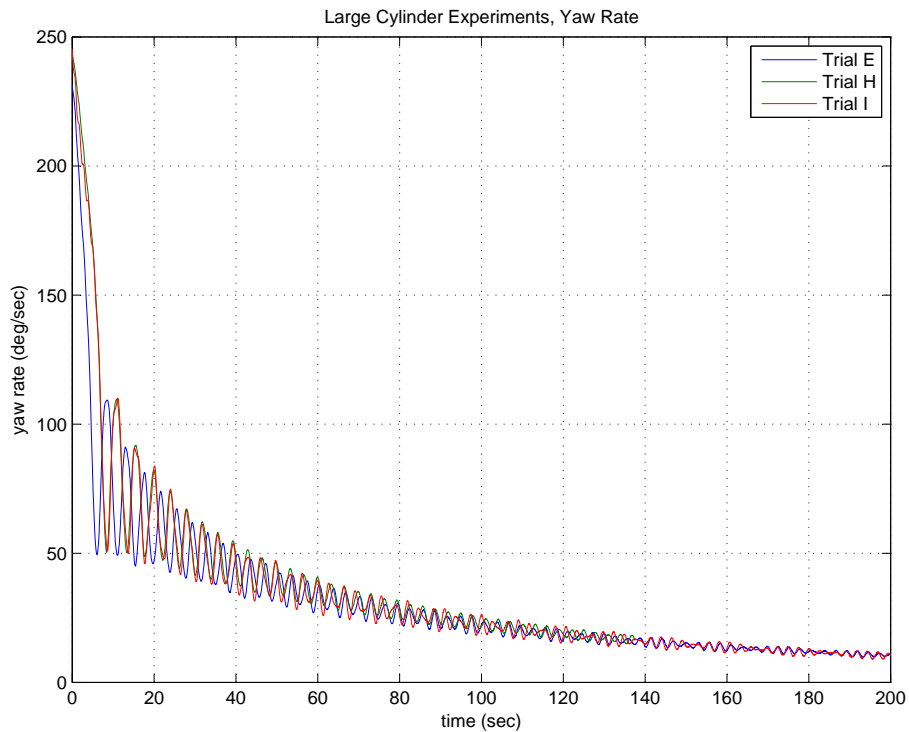


Figure 3.10: The yaw rate data for the yaw rotation trials E, H, and I. The shape of the bounding envelope from approximately 5 seconds onward indicates that a linear or quadratic drag relationship may be appropriate. The “wobble” in the yaw rate is due to the cylinder’s center of mass being slightly off the long axis.

3.2.6 Vertical Translation Results

The vertical translation trials were to characterize the translational drag effects on the cylinder. Since the IMU was running without GPS, measuring vertical position directly would be problematic due to acceleration and velocity errors integrating into ever increasing position errors. Figure 3.11 plots the cylinder’s vertical acceleration for the three vertical translation trials. The envelope of the oscillations approximates a linear drag relationship. Figure 3.12 shows just the first 20 seconds of data for these trials. For all these trials it is clear that cylinder is oscillating with approximately a 2 second period. This natural frequency of 0.5 Hz will result in significant resonances during the wave tank trials when the buoy is excited by waves with a 2 second period.

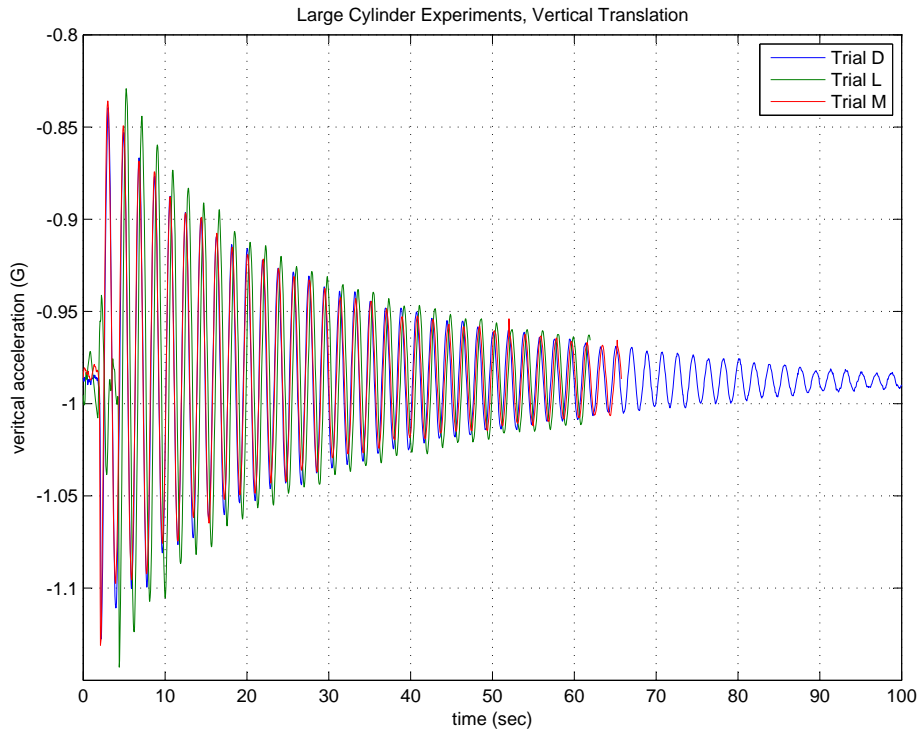


Figure 3.11: The vertical acceleration data for trials D, L, and M. The bounding envelope of the oscillations approximate a linear drag relationship.

3.2.7 Small Wave Tank Results

A video of the small wave tank trials is available at “<http://www.youtube.com/watch?v=gPIW0TBvswU>”. Of the 3 trials performed in the small wave tank, Trial O had a wave period of 2 seconds, which is very close to the natural frequency of cylinder, resulting in a significantly larger response amplitude compared with other trials. Even though Trial P had a wave height twice that of Trial O, it produced less vertical acceleration. Figure 3.13 shows the filtered roll and pitch angles for small wave tank trials O, P, and Q. Figure 3.14 shows the acceleration along the cylinder’s long axis (Z) for the small wave tank trials O, P, and Q.

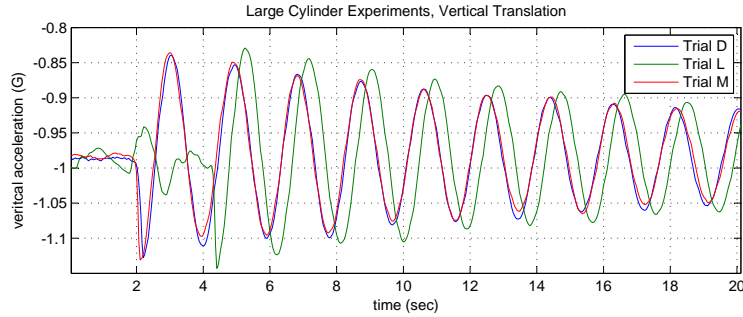


Figure 3.12: The first 20 seconds of vertical acceleration data for trials D, L, and M. The natural frequency of 0.5 Hz is evident.

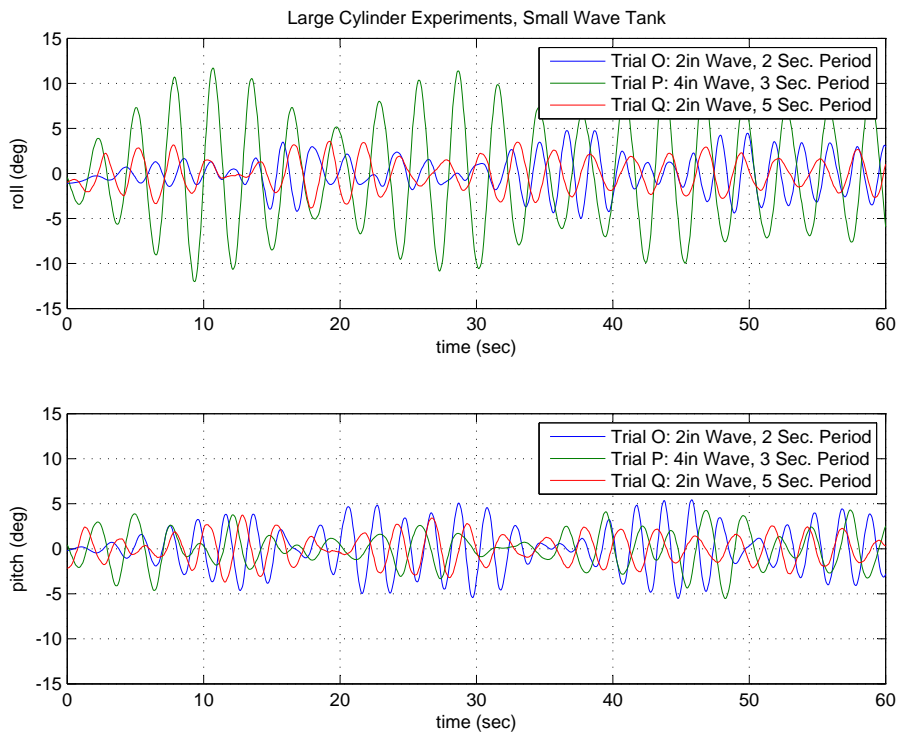


Figure 3.13: The filtered roll and pitch data for the small wave tank trials O, P, and Q.

3.2.8 Large Wave Tank Results

While testing the large instrumented cylinder at the Naval Academy’s Hydrodynamics Laboratory, the opportunity presented itself to test the cylinder in the laboratory’s “large” wave tank. The large wave tank is 380 feet long and can generate waves almost 3 feet high. Some of these trials were conducted in the spirit of applying the most extreme conditions which could be generated to just to see what happens.

A video of the large wave tank trials is available at “<http://www.youtube.com/watch?v=YJhcfNE6vaU>”. A couple of video frames of these trials shown in Figure 3.15. In reviewing the video of these trails two major characteristics become apparent. 1) Wave periods of 2

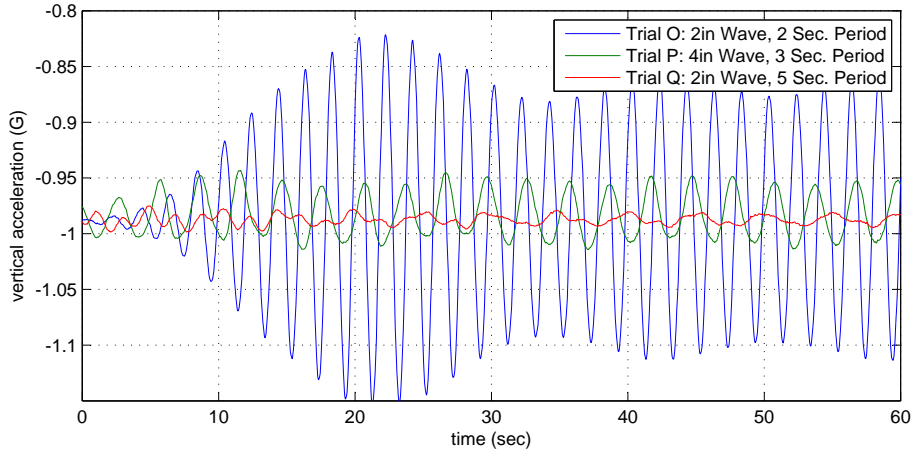


Figure 3.14: The long axis (z) acceleration data for the small wave tank trials O, P, and Q. The resonance effects due to the 2 second period of Trial O are clearly evident.

seconds are very effective at exciting the large instrumented cylinder. 2) If the waves and buoy are of a similar magnitude in size, the buoy will be subject to extreme angular and horizontal displacements. The oscillatory horizontal displacements of the buoy are clear in the video as well.

These results lead to the following design and operating requirements:

1. The buoy must be significantly smaller than the wave heights in the operating area.
2. The buoy's resonant frequency should be above that of significant wave energy in the operating area.
3. The buoy will not be effective in breaking surf.

All of these requirements mean that such a buoy system will be more effective in open deep water where the wave heights are larger, the wave periods longer, and breaking surf less likely.

The modeling and simulation of wave inputs are discussed in Appendix A.

3.3 Resonant Peak Comparison

The large and small cylinder experiments were also used to validate the modeling of the buoy's resonant peak for vertical oscillation. A comparison of the estimated and actual damped frequency of oscillation is listed in Table 3.2. The resonant frequency of oscillation was estimated using (2.110). For both the large and small cylinders the settling time was significantly greater than $9.2/\omega_n$. Therefore, drag effects can be neglected for the purpose of estimating the resonant frequency of oscillation. This is shown in Table 3.2 where there is no significant difference between the estimate natural frequency, $\omega_{n_{est}}$, and the estimated damped frequency of oscillation, $\omega_{d_{est}}$, calculated using (2.108). The predicted period of oscillation closely matches the measured period for the large test cylinder. The match is not as close for the small cylinder trial. This could be due to the difficulty in accurately measuring the period from the video footage of the small cylinder.



Figure 3.15: Two frames for Trial T, testing the large instrumented cylinder in the large wave tank.

Table 3.2: A comparison of the estimated and observed vertical oscillations frequencies for the small and large test cylinders. The predicted period of oscillation closely matches the measured period for the large test cylinder. The match is not as closed for the small cylinder trial. This could be due to the difficulty in accurately measuring the period from the video footage of the small cylinder.

Parameter	Units	Small Cylinder	Large Cylinder
R	(m)	0.044	0.081
m	(kg)	3.3	18.0
$T_{s_{meas}}$	(s)	41	90
$\omega_{n_{est}}$	(rad/s)	4.2	3.3
$\omega_{d_{est}}$	(rad/s)	4.2	3.3
$T_{d_{est}}$	(s)	1.5	1.88
$T_{d_{meas}}$	(s)	1.7	1.86

The long settling times mean that there is virtually no difference between the natural frequency, ω_n , and the damped frequency of oscillation, ω_d for the buoy systems. This means that the buoy's resonant frequency of vertical oscillation can be predicted from its radius and mass alone.

3.4 Model Validation Summary

These experiments shaped the numerical model in the following ways:

1. The translational drag force are modeled as being linearly dependent on translational velocity based on the findings in Section 3.2.6.
2. The rotational drag moments are modeled as being quadratically dependent on the rotational velocity based on the roll and pitch testing with both cylinders, Sections 3.1.2.1 and 3.2.4.
3. Placing the CM of the a cylinder only slightly off of the longitudinal axis is sufficient to generate coupling between the roll/pitch motions into yaw motions.
4. Settling times for the buoy system that are approximately 1 minute or less are reasonable.
5. The results of the small wave tank trials prompted the study of the resonant peak response modeled in Section 2.9 and validated in Section 3.3.
6. The results of the large wave tank trials (the trails with non-breaking waves), prompted the examination of the effects of wave induced fluid velocity on the buoy system. The wave model we use is presented in Sections A.1.2 and A.2.3 and simulation results are presented in Sections 5.12 and 5.13.
7. The buoy's resonant peak for the frequency of vertical oscillation can be well predicted by its natural frequency, which can be calculated from the buoy's radius and mass.

Chapter 4

Buoy Control Laws

For this problem there are two phenomena which drive the design of a suitable controller for the system.

The first phenomenon is the complexity of the air-water interface at the ocean surface. The effects of surface waves produce significant disturbances across a very broad spectrum of frequencies in all buoy states (translational and rotational). These disturbances are stochastic in nature and extremely difficult to anticipate in the short time scales of the buoy's motion.

The second phenomenon is the rotational coupling between all three rotational axes of the buoy. This is driven by the asymmetric structure of the buoy when the joint is at a non-zero vertical angle, and the buoy's changing relationship with the water's surface. This structural asymmetry results in torques about all three axes due to gravity, buoyancy, and inertial coupling.

The first phenomenon requires a controller with extremely good disturbance rejection. The second phenomenon requires that the controller either have an accurate model of the coupling effects between all the rotational axes to perform coordinated control of both axes, or that it treat the coupling from the other axis as a disturbance to be rejected, and controls each axis without accounting for the actions of the other axis.

To accurately predict the rotational coupling in the system, the controller would need to sense or estimate the full attitude of the payload, the position, velocity, and acceleration of both joint axes, and the submerged fraction of the housing and payload. With these sensed (or estimated) quantities, the model developed in Chapter 2 could (conceivably) be used to predict the coupling and a therefore allow a coupled control law to be developed. This approach places a significant sensing and computational burden on the controller (or imposes a significant challenge in designing an estimator).

An alternate approach, and the one advocated here, is that since the surface wave effects already require a controller with good disturbance rejection properties, the coupling from the other axis's motion should be treated as a disturbance to be rejected. Given this approach, it will be shown that the only states the controller needs to measure are the payload attitude in the navigation frame and its rotational rates about its body axes. This approach results in very simple control laws. Effectively, we are designing a *maximum ignorance* controller. Additionally, when a state is needed for the purpose of control, we assume it is available to the controller.

For the purpose of designing the controller, the 8 DOF plant (see Section 2.2) is reduced to a 4 DOF plant. In this reduced order plant, the 4 DOFs are the payload roll and pitch

angles in the navigation frame and the two joint axis angles. These 4 DOFs are controlled by the active controller. The remaining 4 DOFs for the full plant (three translational DOFs and the payload yaw angle) are governed by the passive characteristics of the plant.

Furthermore, if we can design a controller which is robust with respect to disturbances, we can treat the coupling between the payload roll and pitch motion as disturbances. This allows us to further decompose the plant model from a coupled 4 DOF system to a pair of identical and uncoupled 2 DOF systems. In the 2 DOF plant model, the degrees of freedom are the payload angle and the joint axis angle.

Using uncoupled 2 DOF controllers, the only parameters which each controller needs to sense are the payload angle (in roll or pitch in the navigation frame) and the payload angular rate (about the roll and pitch body axes).

Most of the simulated trials were conducted using a sliding mode control law with a feed forward term (SMC+FF). This SMC+FF law was bench-marked against a traditional proportional, integral and derivative control law with a feed forward term (PID+FF). Both control law implementations are fundamentally single axis controllers. They drive each joint axis independently, and treat coupling from the other axis as a disturbance to be rejected. Both laws use the same overall structure of:

1. A common “mixing” algorithm converts the commanded payload azimuth and vertical angles to reference payload roll and pitch angles. All these angles are in the navigation frame.
2. The SMC+FF or PID+FF law drives the individual joint axes to achieve the reference payload roll and pitch angles.
3. An optional active yaw damping feature can be engaged to help stabilize the buoy in yaw.

Both control laws were effective at stabilizing the buoy payload in simulation.

Section 4.1 provides a short introduction to sliding mode control theory and includes the derivation of the stabilizing control, a some techniques for minimizing chattering, and examples of analyzing SMC systems for robustness with respect to parameter uncertainty and external disturbances. Section 4.2 of this chapter describes SMC+FF law used for most of this research. It includes the implementations for the mixing algorithm and active yaw damper. Section 4.3 describes the PID+FF control law. Both the SMC+FF and PID+FF laws have an integral gain term. In practice, for these simulations, this term was set to zero. Section 4.4 presents the rationale by which this term was included in the first place and some of the issues surrounding its use. Section 4.5 discusses the feed forward (FF) gain term which is also common to both the SMC+FF and PID+FF laws and is *critical* for good system performance. Finally, the mathematics of the “composite payload pointing error” is presented in Section 4.6. This allows for the calculation of the angular difference between the commanded aim point and actual payload aim point. This is the primary metric of how well the payload is pointing at the target.

A summary of the angular parameters used in these control laws is presented in Table 4.1.

4.1 Sliding Mode Theory

4.1.1 Finding the Stabilizing Control

Sliding Mode Control (SMC) is a useful form of non-linear control. Its principal advantages are:

1. It does not require a linearized model assumption of a fundamentally non-linear plant.
2. It is particularly well suited to plants and actuators that are discrete in nature.
3. It can be extremely robust to parameter variations in the plant.
4. It can be extremely robust with respect to external disturbances.

Its main disadvantage is the potential for actuator “chatter” in many applications.

The following introduction to SMC is a condensed form of the introduction presented in [14, Section 14.1]. Additionally, Young and Utkin in [13] and Utkin in [29] provide an in depth coverage of sliding mode control and its more advanced implementations.

Consider the second order system

$$\begin{aligned}\dot{x}_1 &= x_2, \\ \dot{x}_2 &= h(x) + g(x)u,\end{aligned}\tag{4.1}$$

where $h(x)$ and $g(x)$ are unknown, non-linear, scalar-valued functions of the state variable $x = (x_1, x_2) \in \mathbb{R}^2$. If the input weighting function $g(x)$ is always positive, i.e. $g(x) \geq g_0 > 0$, we can design a state feedback law to stabilize the system about the origin using sliding mode control.

The control law will stabilize the system on the surface (or manifold)

$$s(x) = Cx_1 + x_2 = 0,\tag{4.2}$$

where $C \in \mathbb{R}$ is prescribed. When the system is “on” this surface, its trajectory is governed by the dynamics of $\dot{x}_1 = -Cx_1$. These dynamics will drive the system to zero, with a rate that is dependent on the magnitude of C as long as $C > 0$. **Once the system is on the sliding surface $s = 0$, its motion is independent of the non-linear functions $h(x)$ and $g(x)$.** The system trajectory consists of two phases, a *reaching* phase where the system travels from a point in state space not on the sliding surface, to the sliding surface; and the *sliding* phase where the system is maintained on the sliding surface. A phase portrait of this behavior is shown in Figure 4.1.

If, in some region of interest, $h(x)$ and $g(x)$ satisfy the inequality

$$\left| \frac{Cx_2 + h(x)}{g(x)} \right| \leq k_1,\tag{4.3}$$

where k_1 is a known, non-negative constant, then the *sliding mode control* can be written as

$$u = -k(\mathbf{x}) \text{sign}(s), \text{ for } k(\mathbf{x}) > k_1,\tag{4.4}$$

where $\text{sign}(s)$ is

$$\text{sign}(s) = \begin{cases} 1, & s > 0, \\ 0, & s = 0, \\ -1, & s < 0. \end{cases}\tag{4.5}$$

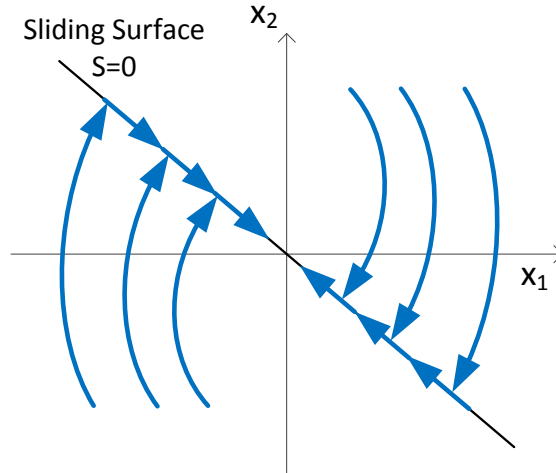


Figure 4.1: A phase portrait of a system under sliding mode control, reaching the sliding surface and being maintained on it. The slope of the sliding surface is determined by the magnitude of C in our example.

We can informally explain this behavior by showing that, given the above assumptions, the product $s(x)\dot{s}(x) < 0$ for all non-zero values of s , and therefore the system will converge to the manifold $s = 0$. To show this, we substitute (4.1) and (4.4) into the expression for \dot{s} and rearrange the terms to get the LHS of (4.3). Performing these steps give

$$\begin{aligned}
 \dot{s}(x) &= C\dot{x}_1 + \dot{x}_2, \\
 &= Cx_2 + h(x) + g(x)u, \\
 &= Cx_2 + h(x) + g(x) [-k\text{sign}(s)], \\
 &= g(x) \left[\frac{Cx_2 + h(x)}{g(x)} - k\text{sign}(s) \right].
 \end{aligned} \tag{4.6}$$

Our assumptions of $g(x) > 0$ and $|(Cx_2 + h(x))/g(x)| \leq k_1 < k$, where C , k_1 , and k are all non-negative constants, are enough to show that (4.6) will always have a sign opposite s for non-zero values of s .

The power of sliding mode control technique is from what is implied by (4.3). Only the maximum *magnitude* of the non-linear effects (parameter variations and external disturbances) need to be known to implement a robust SMC control law. More formal proofs of the stability and convergence for sliding mode control are given by Khalil in [14] and Utkin in [29].

4.1.2 Minimizing Chattering

SMC systems can be susceptible to *chattering* as the sign function in the control law switches back and forth to keep the system on the sliding surface. Chattering can occur due to numerous reasons, including: system latencies (sensors and actuators), discrete control loops driving a continuous plant, and unmodelled dynamics in the system. Figure 4.2 shows a notional system state trajectory oscillating back and forth about the switching surface.

Numerous techniques are discussed in the SMC literature to minimize or eliminate chattering. [29, Chapter 8] and [13] are particularly noteworthy. A common method suggested

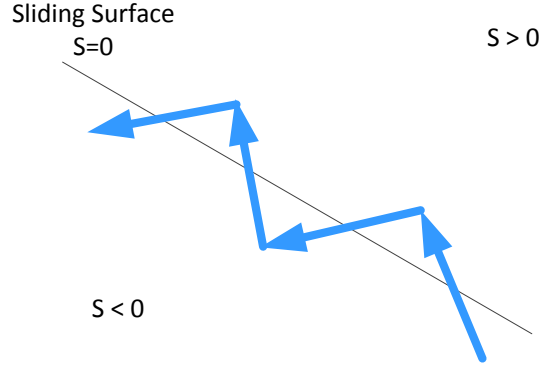


Figure 4.2: Chattering due to control delay in an SMC system.

in the literature, is the *boundary layer* solution. This involves replacing the sign function with a saturation function of the form,

$$\text{sat}(s, \epsilon) = \begin{cases} 1, & s > \epsilon, \\ s/\epsilon, & -\epsilon \leq s \leq \epsilon, \\ -1, & s < -\epsilon, \end{cases} \quad (4.7)$$

where ϵ defines the region beyond which the value is set to ± 1 . This replaces the discrete switching surface of the ideal SMC controller with a linearized region within a boundary layer of thickness ϵ of the sliding surface. This technique, while simple to implement, may not always produce the desired results. So considerable research has been done on other techniques to reduce chattering.

4.1.3 Invariant Systems via Regular Form

4.1.3.1 The General Case

As mentioned above a principal strength of sliding mode control is that it can be made extremely robust to plant parameter variations and external disturbances, thus making the system *invariant* to these effects. The conditions that must be met for a system to be invariant are derived by Utkin in [29, Section 3.3]. In summary the variations (external disturbances and parameter variations) should be in states that are directly affected by the control vector, \mathbf{u} . If this is true, the system can be written in *regular form* where the state space is partitioned in a subspace that is directly affected by the control vector and a subspace that is not.

As an example consider the affine system

$$\dot{\mathbf{x}} = \mathbf{f}(\mathbf{x}, t) + \mathbf{B}(\mathbf{x}, t)\mathbf{u} + \mathbf{h}(\mathbf{x}, t), \quad x \in \mathbb{R}^n, \quad u \in \mathbb{R}^m, \quad (4.8)$$

where $\mathbf{h}(\mathbf{x}, t)$ characterizes the external disturbances and parameter variations we wish to suppress. From Utkin in [29] These can be suppressed if

$$\mathbf{h}(\mathbf{x}, t) \in \text{range}(\mathbf{B}(\mathbf{x}, t)), \quad \text{for all } x \text{ and } t, \quad (4.9)$$

where ‘range’ is the subspace of \mathbb{R}^n spanned by the columns of the matrix $\mathbf{B}(\mathbf{x}, t)$.

The system (4.8) is written in regular form as

$$\dot{\mathbf{x}}_1 = \mathbf{f}_1(\mathbf{x}_1, \mathbf{x}_2, t), \quad (4.10)$$

$$\dot{\mathbf{x}}_2 = \mathbf{f}_2(\mathbf{x}_1, \mathbf{x}_2, t) + \mathbf{B}_2(\mathbf{x}_1, \mathbf{x}_2, t)\mathbf{u} + \mathbf{h}(\mathbf{x}_1, \mathbf{x}_2, t). \quad (4.11)$$

The state space has been partitioned such that the state vector \mathbf{x}_1 is in the null space of the input matrix $\mathbf{B}(\mathbf{x}, t)$. Additionally, the disturbance/variation function, $\mathbf{h}(\mathbf{x}_1, \mathbf{x}_2, t)$, only affects the states driven directly by the control input.

4.1.3.2 Invariance In Linear Systems

Sections 3.4 and 5.2 of [29] discuss the invariance of affine and linear systems respectively. The linear example shows this more clearly. Consider the system [29, (5.2.1)]

$$\dot{\mathbf{x}} = (\mathbf{A} + \Delta\mathbf{A}(t))\mathbf{x} + \mathbf{B}\mathbf{u} + \mathbf{Q}d(t). \quad (4.12)$$

As in the general non-linear case, the parameter variations, $\Delta\mathbf{A}(t)$, and the external disturbances, $\mathbf{Q}d(t)$, must be only be linear combinations of the input vector \mathbf{B} [7, (8)-(13)]. Mathematically this requirement can be expressed as

$$\text{rank} \begin{bmatrix} \mathbf{B} & \Delta\mathbf{A} \end{bmatrix} = \text{rank} \begin{bmatrix} \mathbf{B} \end{bmatrix} \quad \text{and} \quad \text{rank} \begin{bmatrix} \mathbf{B} & \mathbf{Q} \end{bmatrix} = \text{rank} \begin{bmatrix} \mathbf{B} \end{bmatrix}. \quad (4.13)$$

Or there exists matrices Λ_A and Λ_Q such that

$$\Delta\mathbf{A} = \mathbf{B}\Lambda_A \quad \text{and} \quad \mathbf{Q} = \mathbf{B}\Lambda_Q. \quad (4.14)$$

The significance of (4.14) is that it gives us a tool for determining if a linear system can be placed in regular form, and therefore be made invariant to parameter variation and external disturbances.

4.1.4 A Poor Planar SMC Implementation

This section illustrates how a poorly formulated system model leads to an SMC formulation that is less robust against model parameter variations and external disturbances.

In this implementation the system's roll and pitch response are modeled as independent planar systems. Coupling from the other axis can be viewed as an external disturbance in each planar system. So if this formulation can be put into regular form, then it should be robust against external disturbances (and therefore coupling from the other axis). Additionally, in regular form each system should be robust against parameter variations in its matrix \mathbf{A} as well. This is desirable because the spatial buoy model is non-linear and the linearized parameters can vary significantly over the buoy's operating envelope.

This model is assumes that that roll and pitch motion and can be modeled and controlled as independent planar systems. The system description that follows is for one of these planar systems. The effects of the coupling from the other axis are modeled as external disturbances.

In this model the joint is driven by an jerk (derivative of acceleration) command. This is desirable because it result in a smoothly varying acceleration for the joint. The joint acceleration affects the the payload angular acceleration due to inertial coupling between the housing and payload. This coupling is captured by the term a_5 in the matrix \mathbf{A} . The joint velocity affects the payload's angular acceleration due to drag effects, which are

linearized and captured by the term a_4 in the matrix \mathbf{A} . The joint position affects the payload's angular acceleration due to buoyancy effects, which are linearized and captured by the term a_3 in the matrix \mathbf{A} . The term a_2 models the payload's acceleration due to payload rate, which could be caused by payload drag effects. Finally, the a_1 term models the payload's acceleration due to payload angle, which could be caused by payload buoyancy effects.

This seems a reasonable linearization of the two body buoy model. The buoyant and drag effects of the payload have been captured by the a_1 and a_2 parameters. The inertia, drag, and buoyant effects of shifting the housing with respect to the payload can all be described by the a_3 , a_4 , and a_5 terms. Presenting this system in state space form gives:

$$\dot{\mathbf{x}} = \mathbf{A}\mathbf{x} + \mathbf{B}\mathbf{u} + \mathbf{Q}d(t), \quad (4.15)$$

$$\mathbf{x} = \begin{bmatrix} x_1 \\ x_2 \\ x_3 \\ x_4 \\ x_5 \end{bmatrix}, \begin{matrix} \text{payload angle} \\ \text{payload angular rate} \\ \text{joint angle} \\ \text{joint velocity} \\ \text{joint acceleration} \end{matrix} \quad (4.16)$$

$$\mathbf{u} = [u], \text{ joint jerk} \quad (4.17)$$

$$\mathbf{A} = \begin{bmatrix} 0 & 1 & 0 & 0 & 0 \\ a_1 & a_2 & a_3 & a_4 & a_5 \\ 0 & 0 & 0 & 1 & 0 \\ 0 & 0 & 0 & 0 & 1 \\ 0 & 0 & 0 & 0 & 0 \end{bmatrix}, \quad (4.18)$$

$$\mathbf{B} = [0 \ 0 \ 0 \ 0 \ 1]^T, \quad (4.19)$$

$$\mathbf{Q} = [0 \ 1 \ 0 \ 0 \ 0]^T. \quad (4.20)$$

The rationale for the selection of \mathbf{Q} is that the disturbances, $d(t)$, from the non-linear effects of the model (including coupling from the other axis) are going to be moments on the payload. Moments cause changes in the payload angular acceleration value, \dot{x}_2 .

Looking at the matrix \mathbf{A} , we can see that the only place where parameter uncertainty could occur is in the second row. So the matrix $\Delta\mathbf{A}$ has the form

$$\Delta\mathbf{A} = \begin{bmatrix} 0 & 0 & 0 & 0 & 0 \\ \Delta a_1 & \Delta a_2 & \Delta a_3 & \Delta a_4 & \Delta a_5 \\ 0 & 0 & 0 & 0 & 0 \\ 0 & 0 & 0 & 0 & 0 \\ 0 & 0 & 0 & 0 & 0 \end{bmatrix}. \quad (4.21)$$

Next we can use (4.14) to check this system formulation for invariance with respect to the parameter variations,

$$\mathbf{B}\boldsymbol{\Lambda}_A = \begin{bmatrix} 0 \\ 0 \\ 0 \\ 0 \\ 1 \end{bmatrix} \boldsymbol{\Lambda}_A = \begin{bmatrix} 0 \\ 0 \\ 0 \\ 0 \\ 1 \end{bmatrix} [\Lambda_{A1} \ \Lambda_{A2} \ \Lambda_{A3} \ \Lambda_{A4} \ \Lambda_{A5}] = \begin{bmatrix} 0 & 0 & 0 & 0 & 0 \\ 0 & 0 & 0 & 0 & 0 \\ 0 & 0 & 0 & 0 & 0 \\ 0 & 0 & 0 & 0 & 0 \\ \Lambda_{A1} & \Lambda_{A2} & \Lambda_{A3} & \Lambda_{A4} & \Lambda_{A5} \end{bmatrix}. \quad (4.22)$$

It is clear from (4.21) and (4.22) that $\Delta\mathbf{A} \neq \mathbf{B}\Lambda_A$, and we conclude that the system cannot be put into regular form. Therefore the parameter variations, $\Delta\mathbf{A}$, are not in the range of the control input, \mathbf{B} . So sliding mode control applied to this formulation will *not* be robust with respect to the parameter variations.

Using (4.14) to check this system formulation for invariance with respect to the external disturbances,

$$\mathbf{B}\Lambda_Q = \begin{bmatrix} 0 \\ 0 \\ 0 \\ 0 \\ 1 \end{bmatrix} \Lambda_Q = \begin{bmatrix} 0 \\ 0 \\ 0 \\ 0 \\ 1 \end{bmatrix} [\Lambda_Q] = \begin{bmatrix} 0 \\ 0 \\ 0 \\ 0 \\ \Lambda_Q \end{bmatrix}. \quad (4.23)$$

It is clear that (4.23) does not equal the external disturbances, $\mathbf{Q}d(t)$, with \mathbf{Q} specified by (4.20). Therefore the external disturbances are also not in the range of the control input \mathbf{B} . So sliding mode control applied to this formulation will *not* be robust with respect to external disturbances.

4.1.5 Analyzing the Implemented SMC Controller

We ultimately reached the conclusion, perhaps counter-intuitively at first, that the key to reformulating our system in regular form is to reduce the number of system states in the model used to generate the control law.

In this system model there are only two states for each axis, payload angle and payload rate. The joint axis angle is commanded in position mode. The linearized system is

$$\dot{\mathbf{x}} = \mathbf{A}\mathbf{x} + \mathbf{B}\mathbf{u} + \mathbf{Q}d(t), \quad (4.24)$$

$$\mathbf{x} = \begin{bmatrix} x_1 \\ x_2 \end{bmatrix}, \quad \begin{array}{l} \text{payload angle} \\ \text{payload angular rate} \end{array} \quad (4.25)$$

$$\mathbf{u} = [u], \quad \text{joint angle} \quad (4.26)$$

$$\mathbf{A} = \begin{bmatrix} 0 & 1 \\ a_1 & a_2 \end{bmatrix}, \quad (4.27)$$

$$\mathbf{B} = [0 \quad b_1]^T, \quad (4.28)$$

$$\mathbf{Q} = [0 \quad 1]^T. \quad (4.29)$$

Using (4.14) to check this system formulation for invariance with respect to the parameter variations, we find

$$\Delta\mathbf{A} = \begin{bmatrix} 0 & 0 \\ \Delta a_1 & \Delta a_2 \end{bmatrix}, \quad (4.30)$$

and

$$\mathbf{B}\Lambda_A = \begin{bmatrix} 0 \\ b \end{bmatrix} \Lambda_A = \begin{bmatrix} 0 \\ b \end{bmatrix} [\Lambda_{A1} \quad \Lambda_{A2}] = \begin{bmatrix} 0 & 0 \\ b\Lambda_{A1} & b\Lambda_{A2} \end{bmatrix}. \quad (4.31)$$

Since (4.30) and (4.31) can be made equal by an appropriate selection of Λ_{A1} and Λ_{A2} , the parameter variations, $\Delta\mathbf{A}$, are in the range of the control input \mathbf{B} . So sliding mode control applied to this formulation *will* be robust with respect to parameter variations.

Using (4.14) to check this system formulation for invariance with respect to the external disturbances,

$$\mathbf{Q} = \begin{bmatrix} 0 \\ 1 \end{bmatrix}, \quad (4.32)$$

and

$$\mathbf{B}\Lambda_Q = \begin{bmatrix} 0 \\ b \end{bmatrix} \Lambda_Q = \begin{bmatrix} 0 \\ b \end{bmatrix} [\Lambda_Q] = \begin{bmatrix} 0 \\ b\Lambda_Q \end{bmatrix}. \quad (4.33)$$

Since (4.32) and (4.32) can be made equal by an appropriate selection of Λ_Q , the external disturbances, $\mathbf{Q}d(t)$, are in the range of the control input \mathbf{B} . So sliding mode control applied to this formulation *will* be robust with respect to external disturbances.

Table 4.1: The angular parameters used in the SMC+FF and PID+FF control laws. The possible reference frames for each parameter are N = navigation, H = housing, P = payload, or J = joint axis.

Var	Name	Frame	Description
r_z	Commanded Payload Azimuth Angle	N	The azimuth angle to point the payload at.
r_v	Commanded Payload Vertical Angle	N	The vertical angle to point the payload at.
ϕ_z	Joint Azimuth Angle	H	The angle in the housing's X-Y plane that the payload makes with the respect to the housing's X axis.
ψ	Payload Heading	N	The angle of the payload's X axis with respect to the nav. frame's x axis.
r_x, r_y	Payload Reference Angles	N	The roll and pitch angles the payload should achieve in the navigation frame.
u_x, u_y	Desired Joint Axis Angles	J	The joint angles each joint controller is trying to achieve.
u_{max}	Maximum Joint Axis Angles	J	The maximum joint angle permitted for each axis.
ϕ_x, ϕ_y	Joint Axis Angles	J	The actual joint axis angles.
ϵ_x, ϵ_y	Axis Error Signal	N	The payload's roll and pitch error.
Ω_x, Ω_y	Payload Body Rate	P	The payload's roll and pitch rates.
ω_z	Payload Yaw Rate	N	The payload's yaw rate.
$\Delta\phi_z$	Nominal Joint Azimuth Angle Rate	H	The rate to shift the joint azimuth angle at for yaw damping.

4.2 SMC+FF Control Law

Sliding Mode Control (SMC) is a well known form of non-linear control. SMC can be very robust with respect to parameter uncertainty and external disturbances. Some notable features of SMC include: 1) it does not require the linearization of a fundamentally non-linear plant, 2) its implementation typically has low computational overhead, and 3) it is particularly well suited for plants which are discontinuous in nature (i.e. on-off type actuators, sensors, and/or dynamics).

Fundamentally, if a system can be shown to meet certain assumptions, then a simple control law can be formulated which will drive the system to a reduced order manifold (a.k.a. the sliding surface). Once on the manifold, the control law will maintain the system on the manifold, and the dynamics restricted to the manifold then stabilize the system at the desired point.

For the purpose of designing the sliding mode controller, the 8 DOF plant (see Section ??) is reduced to a 4 DOF plant. In this reduced order plant, the 4 DOFs are the payload roll and pitch angles in the navigation frame and the two joint axis angles. These 4 DOFs are controlled by the active controller. The remaining 4 DOFs for the full plant (three translational DOFs and the payload yaw angle) are governed by the passive characteristics of the plant.

Furthermore, if we can design a controller which is robust with respect to disturbances, we can treat the coupling between the payload roll and pitch motion as disturbances. This allows us to further decompose the plant model from a coupled 4 DOF system to a pair of identical and uncoupled 2 DOF systems. In the 2 DOF plant model, the degrees of freedom are the payload angle and the joint axis angle.

Using uncoupled 2 DOF controllers, the only parameters which each controller needs to sense are the payload angle (in roll or pitch in the navigation frame) and the payload angular rate (about the roll and pitch body axes).

The SMC+FF implementation here combines a discontinuous sliding mode control law with a continuous integral term and continuous feed forward term. This control law coordinates the motion of both joint axes to achieve the desired payload pointing angle in the navigation frame. It also implements an optional active yaw rate damping feature.

The control law is executed as follows:

1. The commanded payload azimuth angle, r_z , and commanded payload vertical angle, r_v , are specified. The vertical angle is the angle away from the zenith. The azimuth angle is referenced to navigation frame's x axis, North (in NED) or East (in ENU). These are the angles that the payload's long axis (Z axis) should achieve in the navigation frame.
2. The required *joint* azimuth angle, ϕ_z , is calculated based on the payload heading, ψ , in the navigation frame:

$$\phi_z = r_z - \psi. \quad (4.34)$$

Figure 4.3 illustrates the relationship between these angles.

3. The joint azimuth angle, ϕ_z , and commanded vertical angle, r_v , are used to calculate the reference payload roll and pitch angles, r_x and r_y , using the universal joint kinematic relationships from section 2.7:

$$\begin{bmatrix} r_x \\ r_y \end{bmatrix} = f_{J_x J_y}(r_v, \phi_z) = \begin{bmatrix} \arcsin\left(\frac{\sin \phi_z \sin r_v}{\sqrt{1 - \cos^2 \phi_z \sin^2 r_v}}\right) \\ -\arcsin(\cos \phi_z \sin r_v) \end{bmatrix}. \quad (4.35)$$

4. The reference payload roll and pitch angles, r_x and r_y , are then passed to each axes' respective sliding mode controller. These are the reference payload roll and pitch angles, in the *navigation* frame, that the two *independent* planar controllers are trying to achieve. Taking the x axis as an example, the calculation for the desired joint x axis angle, u_x , proceeds as:

- (a) Calculate the axis error as the difference between the actual payload roll angle and the reference roll angle, in the navigation frame, using

$$\epsilon_x = \theta_x - r_x. \quad (4.36)$$

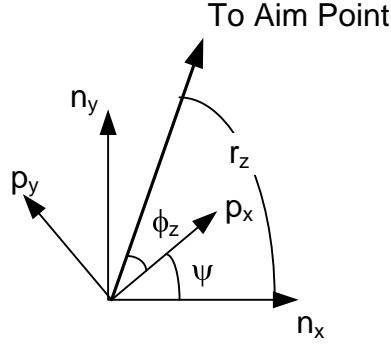


Figure 4.3: This top-down view (in the navigation frame) shows the relationship between the commanded payload azimuth angle, r_z , the joint azimuth angle, ϕ_z , and payload yaw angle, ψ . The navigation frame's x and y axes are labelled n_x and n_y . The projection of the payload frame's x and y axes into the navigation frame's x-y plane are labelled p_x and p_y .

- (b) Calculate the sliding parameter for the x axis from

$$s_x = \Omega_x + C\epsilon_x, \quad (4.37)$$

where Ω_x is the rotational velocity of the payload about its X axis, and C is the SMC gain which determines the slope of the sliding surface.

- (c) Calculate the desired joint x axis angle from the SMC+FF law as

$$u_x = - \left(\alpha \left| \begin{bmatrix} \Omega_x \\ \epsilon_x \end{bmatrix} \right| + \delta \right) \text{sat}(s_x, h) + K_{ff}r_x - K_i \int \epsilon_x d\tau, \quad (4.38)$$

where $\text{sat}(s, h)$ is a linearized saturation function of the form

$$\text{sat}(s, h) = \begin{cases} 1 & \text{if } s > h, \\ s/h & \text{if } -h \leq s \leq h, \\ -1 & \text{if } s < -h. \end{cases} \quad (4.39)$$

α and δ are the discontinuous sliding mode gains. K_i is the continuous integral gain term. K_{ff} is the continuous feed forward gain term. The discontinuous sliding mode term is of the form suggested by Utkin in [29, (5.1.7)]. The gain α increases the magnitude of the sliding mode term when the system is further away from the manifold $s = 0$. The gain δ is the minimum amount by which sliding mode term will change when s changes from $-h$ to h or vice versa. h is the size of the boundary layer around the sliding surface to help minimize chattering by the controller. See Appendix ?? for a more complete explanation.

The desired y axis joint angle is calculated in a similar manner.

- Next the optional active yaw damper is implemented. The yaw damper works by adjusting the joint's x and y axis angles to cause the housing and payload to rotate about their long axes, without changing the joint vertical angle, ϕ_v . The rate of housing and payload rotation is proportional to the payload yaw rate in the navigation frame. The active yaw damping calculations are:

- (a) Calculate the payload yaw rate in the navigation frame as

$$\omega_z = \begin{bmatrix} 0 & 0 & 1 \end{bmatrix} \mathbf{B}_2 \boldsymbol{\Omega}_2. \quad (4.40)$$

Where \mathbf{B}_2 is the direction cosine matrix giving the payload's attitude in the navigation frame, and $\boldsymbol{\Omega}_2$ is the payload's rotational velocity vector in the payload body coordinates.

- (b) Calculate the nominal change in joint azimuth angle as

$$\Delta\phi_z = -K_{yaw}\omega_z, \quad (4.41)$$

where $K_{yaw} > 0$ is a constant gain. Note that $\Delta\phi_z$ is an angular rate with units of *rad/sec*.

- (c) Calculate the partial derivatives $\frac{\partial\phi_x}{\partial\phi_z}$ and $\frac{\partial\phi_y}{\partial\phi_z}$ using (2.94) and (2.95) with the current values of ϕ_z and ϕ_v .
- (d) Adjust the desired joint axis angles by

$$u_x = u_x + \frac{\partial\phi_x}{\partial\phi_z} \Delta\phi_z \Delta t, \quad (4.42)$$

$$u_y = u_y + \frac{\partial\phi_y}{\partial\phi_z} \Delta\phi_z \Delta t, \quad (4.43)$$

where Δt is control loop step size. Under (4.42) and (4.43) the magnitude of the yaw damper contribution is independent of control loop execution rate.

6. Soft limits are applied to each of the desired axis angles to ensure that each joint axis is not driven beyond its stops, i.e. $|u_x| \leq u_{max}$ and $|u_y| \leq u_{max}$. For the prototype buoy configuration, these soft limits are set to ± 47 degrees to prevent hitting the mechanical hard stops included in the joint model.
7. The updated desired joint axis angles, u_x and u_y , are sent to each of the low level axis controllers, and the control loop repeats.

This calculation sequence is performed and sent to the low level (hardware) joint axis controllers at a nominal control rate of 12.5 Hz for most of the trials. The low level joint controllers drive their axes toward their desired control angles, while enforcing both velocity and acceleration limits on the axis motion. The details of the modeling the low level axis controllers is presented in Appendix C.

Because of the joint velocity and acceleration limits, if the desired joint axis angle changes significantly from control interval to control interval, then the joint may never reach a particular desired axis angle. A good example of this behavior is when the system is maintaining itself close to the sliding surface. The sliding surface parameter will vary from positive to negative at each control interval, and this will cause the actual joint angle to be an "average" of the the oscillating desired axis value. The low level axis controller also acts as a low pass filter which helps reduce chatter.

4.3 PID+FF Control

As an alternative to the SMC+FF control law presented above, the buoy can also be controlled using a proportional-integral-derivative controller with a feed forward term (PID+FF). PID control is one of the most common control strategies for single variable systems. There is a vast body of literature on PID control. Additionally, many industrial control products are readily available to apply PID control to an almost limitless range of sensors and actuators. The digital motor controller discussed in [1] is an excellent example of one such product. It is for this reason that PID control was selected to bench-mark the SMC controller against.

The same mixing logic, feed forward term, and optional active yaw damper are used with the continuous PID law replacing the discontinuous SMC law. This results in the SMC+FF control law specified by (4.38) being replaced by the following:

$$u_x = -K_p \epsilon_x - K_d \Omega_x - K_i \int \epsilon_x d\tau + K_{ff} r_x. \quad (4.44)$$

Here the proportional gain, K_p , weights the effects of the payload axis error signal. The derivative gain, K_d , weights the effects of payload rate and most strongly affects the transient response of the system. And the integral gain, K_i , weights the effects of accumulated payload error and is used to eliminate steady state error in the system at the expense of transient performance. The proportional term will affect both the transient and steady state system performance.

Tuning the gains of a PID controller is typically a trial and error process. The literature does suggest a variety of methods for initial estimates at gain values and tuning processes, without any one method being particularly dominant

The joint's y axis is controlled in a similar manner.

4.4 The Integral Gain K_i

In general, using the integral of an error signal as part of the feedback signal is a means of eliminating steady state error in many systems. This improved steady state performance comes at the expense of the system's transient performance. As the the integral gain is increased, the system's response will become more sluggish. If the integral gain is made too big it will cause many systems to become unstable.

In the early stages of this research, before the complete spatial buoy model was developed and implemented, a planar two-body buoy system was modeled. In this formulation, the buoy's motion was constrained to the x-z plane and the joint was a single degree of freedom pivot between the two bodes. In this formulation there was no "other" axis to cause coupling into the current axis. Without this source of disturbances (even with the non-linear buoyant and drag effects) the system was well behaved enough that the PID and SMC controllers had no problems stabilizing it.

In the planar formulation, the integral term was effectively used in both PID and SMC control to bring the system's steady state error to zero. This was possible even without the feed forward term. With the feed forward term, only a very slight integral gain was required to eliminate the system's steady state error. This had minimal impact on the system's transient performance. Because of its effectiveness in the planar formulations, the integral term was included in the control laws for the spatial system.

Once the full spatial model was completed, it became clear that the dominant source of disturbances was the coupling from the other axis’s motion. In the presence of these disturbances the integral term provided no benefit. Increasing it (attempting to make it more effective) only made the spatial system’s performance worse. It is hypothesized that the increased integral gain worsened the transient performance of the system to the point that it could no longer respond fast enough to reject the disturbances induced by the other axis’s motion.

It is for this reason that in the spatial buoy model the integral gain, K_i , is set to zero for both the SMC+FF and PID+FF laws.

Additionally, the issue of “integrator windup” should always be considered whenever the integral of an error signal is used as a feedback signal. If system has a error of constant sign which the controller cannot (or is very slow at) correcting, the integral of the error signal will grow without bound. Over time, this causes the integral term to completely saturate the control signal and render the other terms ineffective at providing feedback. This issue of integrator windup is often not emphasized in elementary texts on PID control. Typical techniques for handing integrator windup include:

1. Saturating the output of the integrator. This approach is evident in the block diagram of the Maxon EPOS2 motor controller shown in [1, Figure 1] and is proposed by Fossen in [9, Sec 6.4.1].
2. A negative feedback loop can be wrapped around the integrator with a dead-zone device in the feedback path. In this configuration, when the integrator’s output exceeds the threshold of the dead-zone device, a fast feedback signal is applied to the integrator to rapidly bring the integrator’s output back into the region permitted by the dead-zone device. Such an arrangement is suggested by Stevens and Lewis in [26, p. 225].
3. A deadbeat observer can be implemented in the digital controller to provide anti-windup protection. Such an approach is presented by Stevens and Lewis in [26, p. 622-626]
4. The error signal can be defined as the difference with respect to a reference trajectory driven by a reference model. This reference model has dynamics similar to that of the plant such that large changes in the system state and the correspondingly large changes in the error signal are avoided. This is the approach presented by Fossen in [9, Sec 6.4.1].

4.5 Feed Forward Gain K_{ff}

The feed forward gain term, K_{ff} , in (4.38) is one of the most important parameters to determine the quality of the buoy’s response. It is determined by the mass distribution and joint location of the buoy and the resulting static equilibrium point.

The feed forward term places the joint near the correct angles for pointing the payload in static equilibrium. This means that 1) the SMC or PD terms are mainly driving the transient response to zero and 2) the integral term has a much smaller steady state bias to correct. This allows both groups of terms to be significantly more effective.

K_{ff} is determined by performing the following procedure on one of the payload axes. For this example the procedure will be executed about the payload’s X axis.

1. Set all control law gains to zero, except for the K_{ff} gain. Set K_{ff} to an initial guess for its value. Lacking information for a good initial guess for K_{ff} , set $K_{ff} = 1$.
2. Set the axis' payload reference angle, r_x , to 35 degrees. Set the other axis payload reference angle, r_y , to zero. By fixing these reference angles and having the other gains set to zero, this effectively locks the joint at a vertical angle equal to the joint axis angle, i.e. $\phi_v = \phi_x$.
3. Allow the buoy to come to rest in static equilibrium, and calculate the axis error from $\epsilon_x = \theta_x - r_x$, where θ_x is the actual payload roll angle (and in this case the actual payload vertical angle too) in the navigation frame.
4. Iteratively adjust K_{ff} (and therefore adjust the joint axis angle, ϕ_x , and the joint vertical angle, ϕ_v) until the axis error, ϵ_x , is very close to zero at static equilibrium.
5. The final K_{ff} value for the tested buoy configuration can be used as long as the buoy's mass parameters and joint location do not change. This K_{ff} value can be used for either the SMC+FF or PID+FF control laws. Additionally, either control law could be used in this procedure since setting all the other gains to zero makes both laws the same.

A $K_{ff} > 1$ means that the buoy's mass distribution and joint location is such that to achieve a particular payload vertical angle a *larger* joint vertical angle is required. This means that the range of payload vertical angles achievable by the system will be *less* than range of motion of the joint. Conversely, for $K_{ff} < 1$, the buoy is ballasted such that a particular payload vertical angle can be achieved with a *smaller* joint vertical angle. This allows the buoy to cover a *wider* range of payload vertical angles for a given joint design. This comes at the expense of passive stability and sensitivity to joint motion. Figure 4.4 illustrates these effects. $K_{ff} = 1$ is a conceptual idea only. A payload which has mass and a CM not at the joint location will have $K_{ff} \neq 1$.

Table 4.2: The feed forward gain values for each buoy configuration.

Configuration	K_{ff}
Prototype Buoy Configuration	1.60
BuoyGroupSonoA 5x36 J10	0.441
BuoyGroupSonoA 5x36 J15	1.255
BuoyGroupSonoA 5x36 J20	0.958
BuoyGroupSonoA 5x36 J25	0.87

4.6 Composite Pointing Error

It is useful to have a metric of how well the payload is pointing at the aim point. A good metric is the angle between the payload pointing vector and the aim point vector. These

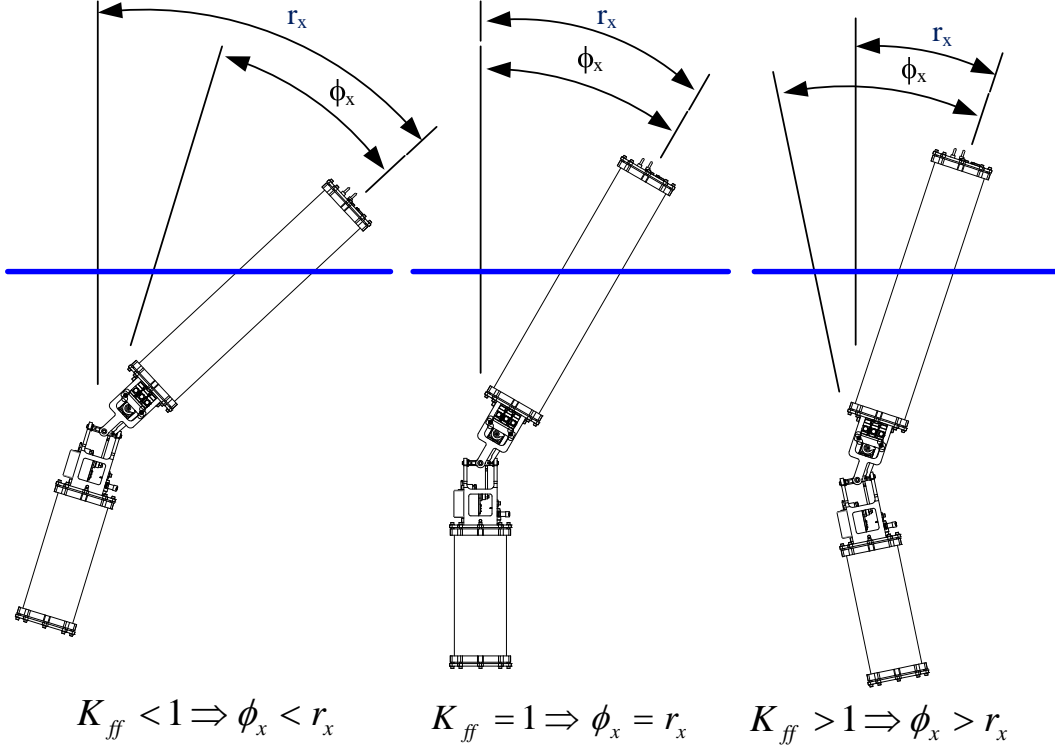


Figure 4.4: The payload reference angle, r_x , and joint axis angle, ϕ_x , for different ranges of K_{ff} values. $K_{ff} = 1$ is a conceptual idea only. A payload which has mass and a CM not at the joint location will have $K_{ff} \neq 1$. Buoys with $K_{ff} < 1$ have less passive stability than those with $K_{ff} > 1$, however, they can cover a larger arc of sky.

two vectors are calculated by:

$$\tilde{\mathbf{p}}_z = \mathbf{B}_2 \begin{bmatrix} 0 \\ 0 \\ 1 \end{bmatrix}, \quad (4.45)$$

$$\tilde{\mathbf{r}}_{aim} = \begin{bmatrix} \cos r_z \sin r_v \\ \sin r_z \sin r_v \\ \cos r_v \end{bmatrix}. \quad (4.46)$$

The payload pointing vector, $\tilde{\mathbf{p}}_z$, is equivalent to the third column of the direction cosine matrix \mathbf{B}_2 , which specifies the payload's attitude in the navigation frame.

The angular difference between the payload pointing and aim point vectors is calculated using the cross and dot products of the two vectors with the four quadrant arctangent function,

$$\epsilon_{aim} = \text{atan2}(|\tilde{\mathbf{p}}_z \times \tilde{\mathbf{r}}_{aim}|, \tilde{\mathbf{p}}_z \cdot \tilde{\mathbf{r}}_{aim}). \quad (4.47)$$

This is called the composite point error because it simultaneously accounts for both the azimuth and elevation error contributions.

4.7 Guaranteeing SMC Stability

To perform an analysis of when the sliding mode controller will guarantee stability let's return to the example two state system presented in Section 4.1. The non-linear reduced DOF model for the roll or pitch motion of the payload is given by

$$\dot{x}_1 = x_2, \quad (4.48)$$

$$\dot{x}_2 = h(\mathbf{x}) + g(\mathbf{x})u, \quad (4.49)$$

where x_1 is the roll or pitch angle, x_2 is roll or pitch angular rate, and the control u is the joint axis angle.

As in Section 4.1, we can define a sliding manifold for the system as

$$s(\mathbf{x}) = Cx_1 + x_2 = 0. \quad (4.50)$$

For the stabilizing control to be guaranteed, we need to show that

$$k(\mathbf{x}) > \left| \frac{Cx_2 + h(\mathbf{x})}{g(\mathbf{x})} \right|, \text{ for all } \mathbf{x}, \quad (4.51)$$

where C is the slope of the sliding surface and the control u is related to $k(\mathbf{x})$ by $u = -k(\mathbf{x})\text{sign}(s(\mathbf{x}))$. To calculate the right hand side of (4.51) we need to make assumptions or estimates for the following:

1. What is the maximum payload rotational rate, x_2 , we are guaranteeing stability for?
2. What is the maximum payload acceleration imparted as a function of the state vector, \mathbf{x} , alone? This is the same as asking what is the maximum magnitude of $h(\mathbf{x})$?
3. What is the minimum magnitude of the input weighting function $g(\mathbf{x})$?

To simplify this analysis, assume that the buoy can be modeled by the planar system shown in Figure 4.5 and only the buoyant righting moments are driving it.

The magnitude of the buoyant and gravity forces on each body are

$$f_{b1} = \frac{1}{4}\rho g \pi d_1^2 L_1, \quad (4.52)$$

$$f_{b2_{max}} = \frac{1}{4}\rho g \pi d_2^2 L_2, \quad (4.53)$$

$$f_{g1} = g m_1, \quad (4.54)$$

$$f_{g2} = g m_2, \quad (4.55)$$

where d_i is the diameter, L_i is the length, and m_i is the mass of each body. ρ is the density of the fluid and g is the acceleration due to gravity. $f_{b2_{max}}$ is the magnitude of the payload buoyant force which would occur if the payload were fully submerged. However, at equilibrium the payload is not fully submerged and the magnitude of the buoyant forces must be equal to the magnitude of the gravity forces. This allows the payload buoyant force at equilibrium to be estimated as

$$f_{b2} = f_{g1} + f_{g2} - f_{b1}. \quad (4.56)$$

The fraction of the payload which is submerged, f_{sub} , can be calculated from

$$f_{sub} = \frac{f_{b2}}{f_{b2_{max}}}, \quad (4.57)$$

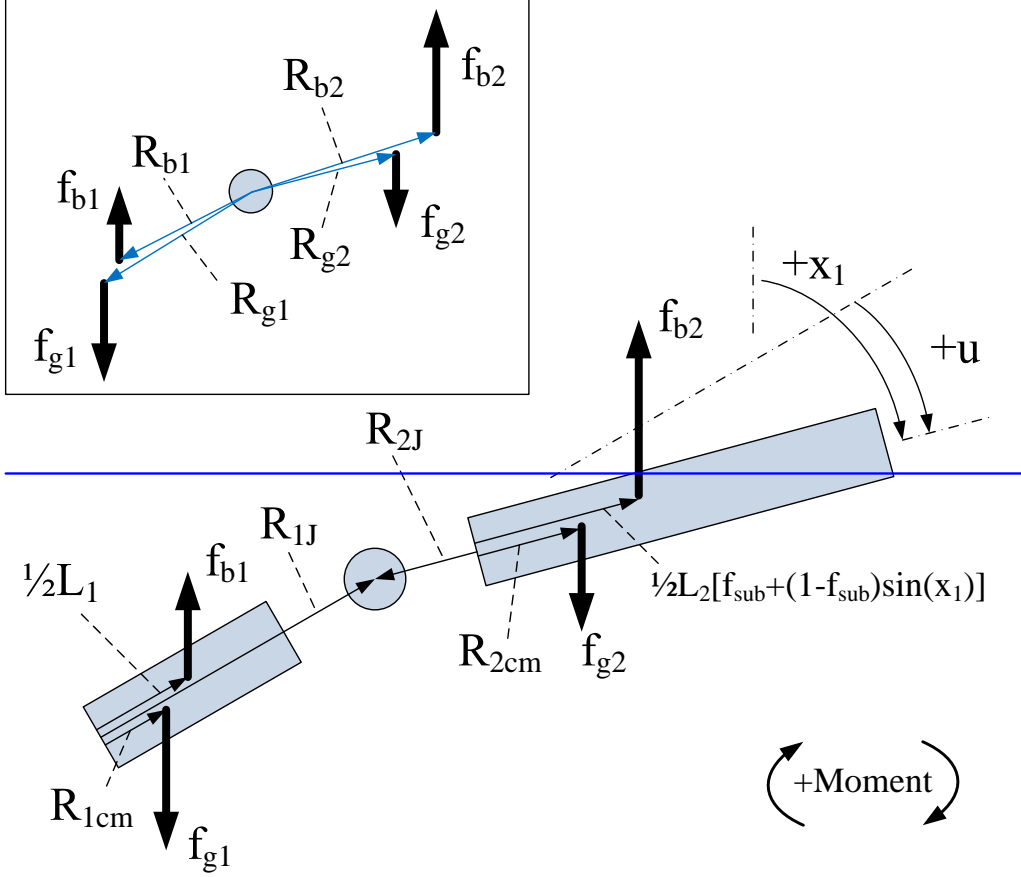


Figure 4.5: The planar system used to analyze the SMC control law for guaranteed stability.

where $0 \leq f_{sub} \leq 1$.

To calculate the buoyant and gravity moments about the buoy's joint, we need to find the distances between each force and the joint. Using Figure 4.5, these distances are found from:

$$R_{g1} = R_{1J} - R_{1cm}, \quad (4.58)$$

$$R_{g2} = R_{2J} + R_{2cm}, \quad (4.59)$$

$$R_{b1} = R_{1J} - L_1/2. \quad (4.60)$$

The location of the payload's center of buoyancy with respect to the joint, $R_{b2}(f_{sub}, x_1)$, is not constant. It is a function of both the payload's submerged fraction and angle. It is approximated in this planar model by

$$R_{b2}(f_{sub}, x_1) = R_{2J} + \frac{1}{2}L_2 [f_{sub} + (1 - f_{sub}) \sin x_1]. \quad (4.61)$$

Given these distances and forces, the total moment on this planar system is

$$M_{total} = \underbrace{[f_{g2}R_{g2} - f_{b2}R_{b2}(f_{sub}, x_1)]}_{M_p(x_1)} \sin(x_1) + \underbrace{[f_{b1}R_{b1} - f_{g1}R_{g1}]}_{M_h} \sin(x_1 - u). \quad (4.62)$$

The term M_p varies with the payload angle, x_1 , and the term M_h does not because it is assumed that the housing stays fully submerged.

This results in a payload rotational acceleration of

$$\dot{x}_2(x_1, u) = \frac{M_p(x_1)}{J} \sin(x_1) + \frac{M_h}{J} \sin(x_1 - u), \quad (4.63)$$

where J is the total rotational inertia about the buoy's CM.

Equation (4.63) it is not quite in the form of (4.49) because \dot{x}_2 is not linearly related to the control u . Recall in the SMC law specified by (4.38), the feed forward gain, K_{ff} , is responsible for positioning the payload close to its static equilibrium angle, thus leaving the SMC control terms to primarily correct for disturbances.

A Taylor series for a function $f(x)$ in vicinity of $x = a$ is

$$f(x) = f(a) + \frac{1}{1!} \frac{df(a)}{dx} (x - a) + \frac{1}{2!} \frac{d^2f(a)}{dx^2} (x - a)^2 + \frac{1}{3!} \frac{d^3f(a)}{dx^3} (x - a)^3 + \dots \quad (4.64)$$

Using the first two terms of the Taylor series for our problem, we can find the acceleration of the payload for a joint angle u' in the vicinity of u as

$$\dot{x}_2(x_1, u') \approx \frac{M_p(x_1)}{J} \sin(x_1) + \frac{M_h}{J} \sin(x_1 - u) - \frac{M_h}{J} \cos(x_1 - u)(u' - u). \quad (4.65)$$

If we assume that the joint angle is near the angle specified by the feed forward gain of

$$u = K_{ff}x_1, \quad (4.66)$$

where x_1 becomes the desired static equilibrium angle of the payload, we can substitute (4.66) into (4.65) to give

$$\dot{x}_2(x_1, \delta u) \approx \underbrace{\frac{M_p(x_1)}{J} \sin(x_1) + \frac{M_h}{J} \sin(G_{ff}x_1)}_{h(\mathbf{x})} + \underbrace{\frac{M_h}{J} \cos(G_{ff}x_1)}_{g(\mathbf{x})} \delta u. \quad (4.67)$$

Here we have made the substitutions $G_{ff} = 1 - K_{ff}$ and $\delta u = u - u'$. This gives us a system in form of (4.49) with the new control, δu , specified as the angular *difference* between the actual joint angle and the angle commanded by the feed forward term of the control law. Additionally, we have made the following assumptions:

1. The drag and inertial effects in the system are neglected. This is reasonable as drag effects should make the system easier to control because it can dissipate energy faster and therefore reach equilibrium faster. Including the inertial effect between the bodies gives the actuator more control authority due to the acceleration of the joint. By neglecting both of these effects we have made the analysis more conservative.
2. The buoy is at, or very near, vertical translational equilibrium with the housing fully submerged and the payload partially submerged. The buoy will only be out of this equilibrium condition for short periods of time. If it is significantly out of vertical equilibrium regularly, then it is likely a problem with the buoy's passive response and not the SMC control law.
3. The payload and joint angles are near the designed static equilibrium angles specified by the feed forward gain in the control law.

4. All the locations (center of mass, center of buoyancy, and joint pivot point) are located on the long axes of their respective bodies.
5. The effects of the cylinder's cross-sectional shape are neglected when calculating the center of buoyancy location for the partially submerged payload.

In the following plots the mass and location parameters for a planar representation of the prototype buoy configuration have been used.

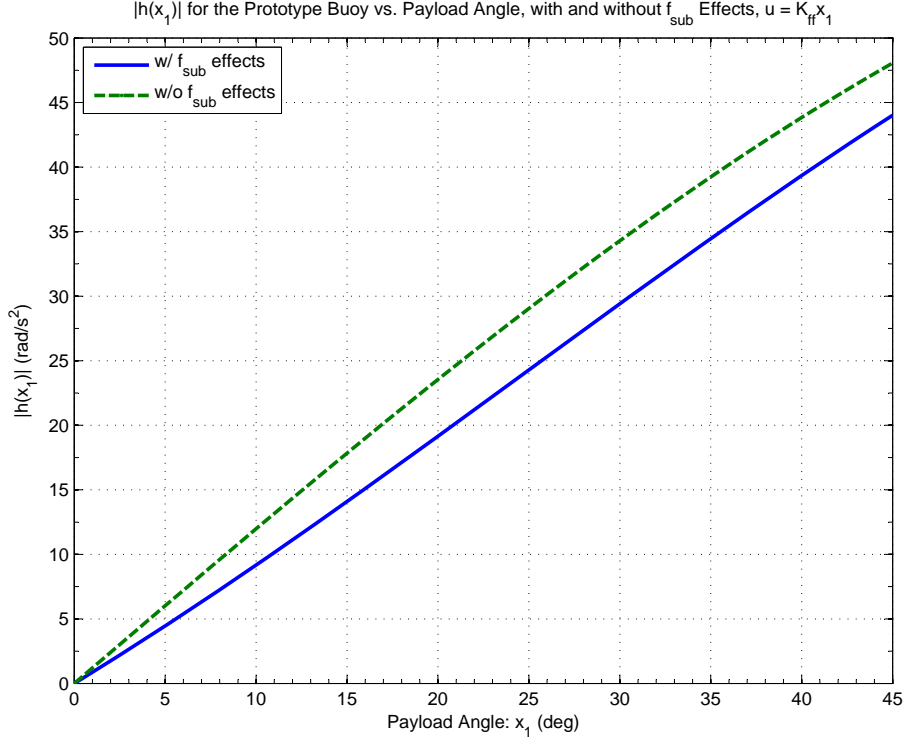


Figure 4.6: The SMC controller model $h(\mathbf{x})$ with and without f_{sub} effects. For the $h(\mathbf{x})$ curve with the f_{sub} effects (blue), the payload is assumed to be partially submerged at vertical static equilibrium. For the $h(\mathbf{x})$ curve without the f_{sub} effects (green), the payload is assumed to be completely submerged. The maximum rotational acceleration due to the states alone, $h(\mathbf{x})$, is reduced approximately 10% by including the effects of the partially submerged payload.

The magnitudes of the SMC controller model terms $h(\mathbf{x})$ and $g(\mathbf{x})$ vs. payload angle, x_1 are plotted in Figure 4.7. Here the joint control is assumed to be the angle $u = K_{ff}x_1$. As the payload angle increases, the magnitude of $h(\mathbf{x})$ also *increases* and the magnitude of $g(\mathbf{x})$ *decreases*.

Given that we now have estimates for $h(\mathbf{x})$ and $g(\mathbf{x})$ as functions of payload angle, we can substitute these values in to (4.51) to estimate the minimum gain $k(\mathbf{x})$ required to guarantee stability. We also must make an estimate for the maximum payload rotation rate which the SMC controller is required to guarantee stability for. The rotational velocity term in (4.51) is Cx_2 .

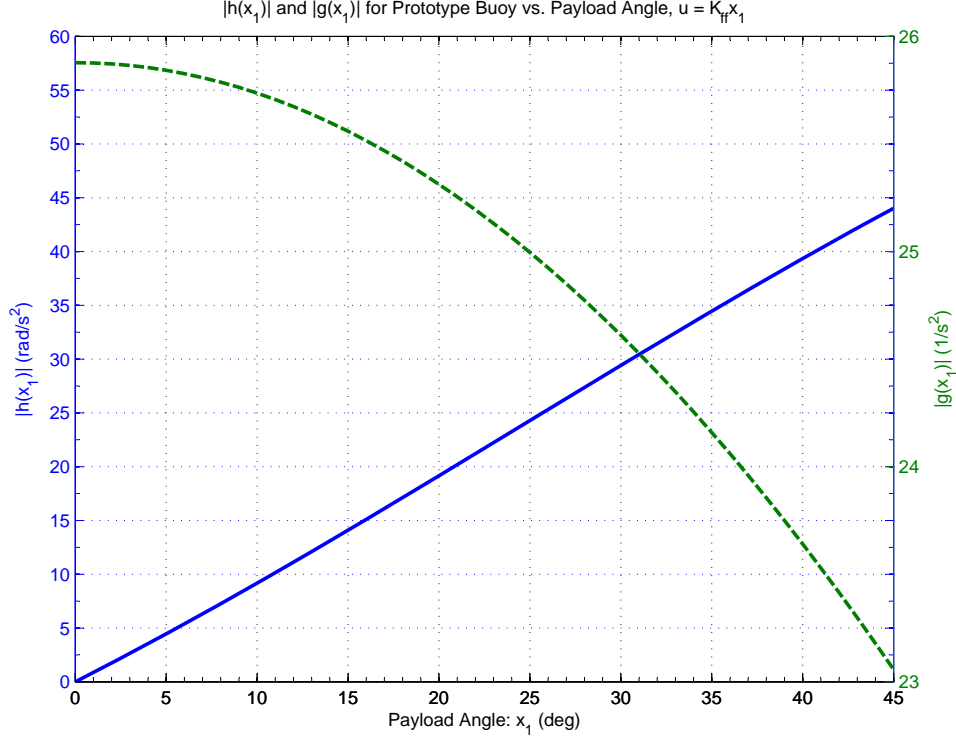


Figure 4.7: The magnitudes of the SMC controller model terms $h(\mathbf{x})$ and $g(\mathbf{x})$ vs. payload angle, x_1 . Here the joint control is assumed to be that specified by the feed forward term, $u = K_{ff}x_1$. As the desired payload equilibrium angle increases, the magnitude of $h(\mathbf{x})$ also *increases* and the magnitude of $g(\mathbf{x})$ *decreases*.

As the payload's angular equilibrium point is specified further away from the vertical, the range of motion available for the SMC controller is reduced in one direction because the joint is physically limited to a maximum joint angle of u_{max} . Therefore the maximum SMC control, δu_{max} , is given by

$$\delta u_{max} = u_{max} - |K_{ff}x_1|. \quad (4.68)$$

The minimum value of $k(\mathbf{x})$ to guarantee stability by (4.51) is plotted in Figure 4.8 for three different assumed payload rotation rates, x_2 . From this analysis stability of the SMC controller is only guaranteed up to desired payload equilibrium angles of 9 to 12 degrees from the vertical. This is a significantly more conservative estimate than the numerical trials, presented in Chapter 5 seem to indicate. It is not surprising that these results are more conservative than what we expect to actually be possible, due to the conservative assumptions of neglecting drag on the bodies and the inertia effects of the joint acceleration.

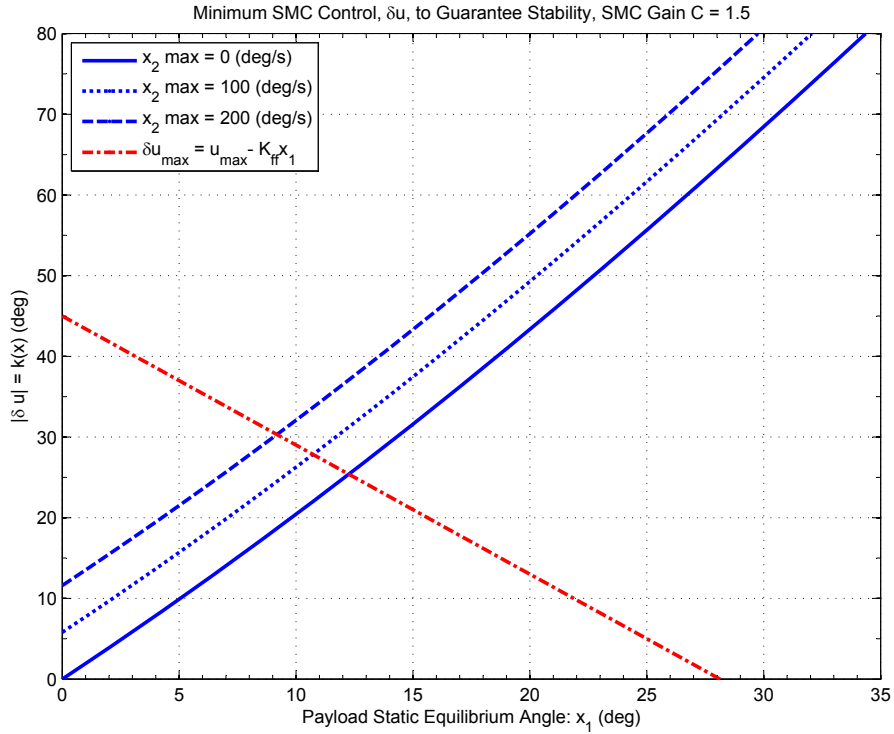


Figure 4.8: The minimum value of $k(\mathbf{x})$ to guarantee stability via (4.51). It is plotted for three different payload rotation rates (0, 100, and 200 deg/s). As the equilibrium joint angle specified by $K_{ff}x_1$ increases, the range of motion available for δu decreases because the physical joint is limited to a maximum joint angle, u_{max} (recall that $|\delta u| = k(\mathbf{x})$). From this analysis, the stability of the SMC controller is only guaranteed up to desired payload equilibrium angles of 9 to 12 degrees from the vertical. This is a significantly more conservative estimate than the numerical trials seem to indicate.

Chapter 5

Simulation Results

The development presented in Chapter 2 is the result of a desire to model the dynamics of the system at a reasonably high level of fidelity. This level of fidelity results in a system formulation that is dependent on a large amount of numerical computation to accurately capture and describe the non-linear effects in the full 8 DOF system. This dependence on numerical computation means that the system formulation is not well suited to an explicit analytic treatment to understand the effects of the major factors like control rate, latency, actuator acceleration, and the SMC gains.

We would like to understand the controller's and buoy system's performance with respect to a variety of internal parameters including: the three sliding mode gains (α , δ , and C), the controller update rate, controller/sensor latency, maximum actuator acceleration, commanded payload vertical angle, and more. This is essentially a large multidimensional search problem, where we would like to know which combinations of the above parameters produce acceptable results.

A numerical multidimensional search is very difficult to complete on this system. Section 5.2 illustrates why for the simpler case of just searching across three SMC gain values. Because of the problems associated with performing multidimensional searches on this system, these effects were evaluated by a series of single dimensional searches. The effects of each parameter to be investigated was varied while the other parameters were held constant.

To avoid complications due to the interplay of multiple suboptimal parameter values while keeping the computational burden reasonable, the best compromise seems to be that when investigating the effect on one parameter, the values for the other parameters should be selected such that they give acceptable performance. Additionally, the values selected should be reasonable for an implemented system. For example, having the control loop run at 12.5 Hz is reasonable, but having it run at 100,000 Hz is not reasonable.

The nominal scenario, presented in Section 1.1, of a buoy communicating with a satellite was used the basis for the desired performance of the prototype buoy configuration. In this scenario acceptable performance is achieved if the composite payload error is less than 10 degrees. However, it is preferred that the composite payload error be less than 5 degrees.

Numerous trials were performed by numerical simulation to evaluate the prototype buoy configuration and the SMC+FF control law under a range of gain values and conditions. Figure 5.1 shows three screen captures from a simulation trial. In the figure the prototype buoy configuration is in the process of righting it self. An example of the animated results is available at "<http://www.youtube.com/watch?v=6RwLC45CJmM>".

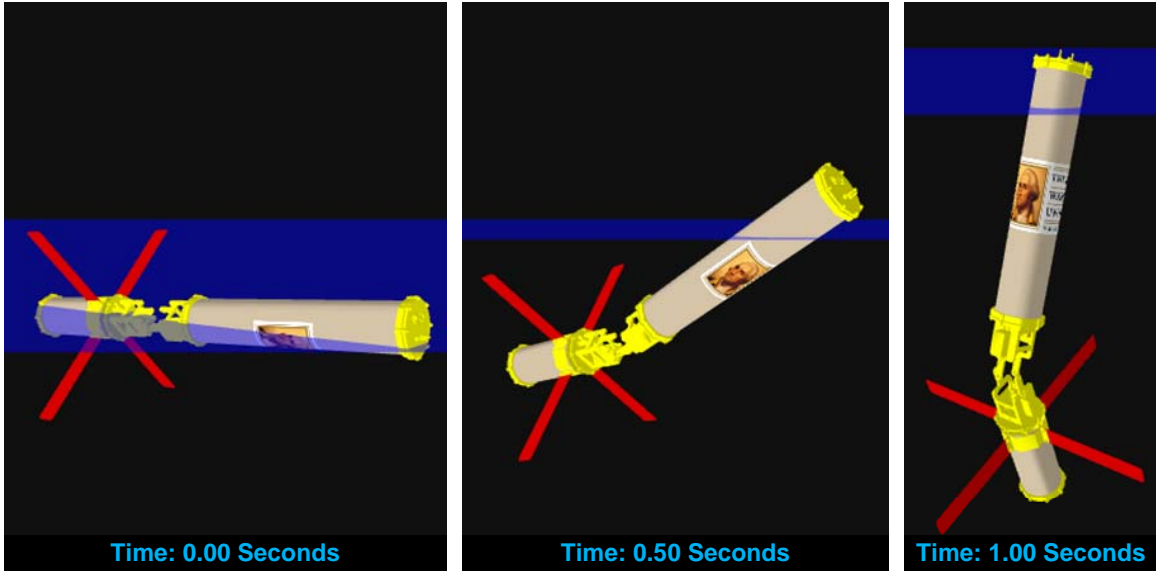


Figure 5.1: Three screen shots, half a second apart, from the animation for one of the numerical simulations. The prototype buoy is the in the process of righting itself and moving the housing to stabilize the payload.

5.1 Prototype Buoy Configuration

Initially this research was performed with crude models of four possible buoy configurations. The particulars of these “J series” models are discussed in Appendix B. For the final stages of this research a detailed mechanical model of a buoy implementation was developed.

This level of detail was to ensure that the expected performance predicted by simulation was based on a size and mass distribution of practical significance. The CAD model of the prototype buoy was used to calculate the required parameters for the numerical simulation. These parameters are listed in Table 5.1. This prototype buoy is sketched in Figures 5.2 and 5.3.

Dimensions: inches [mm]

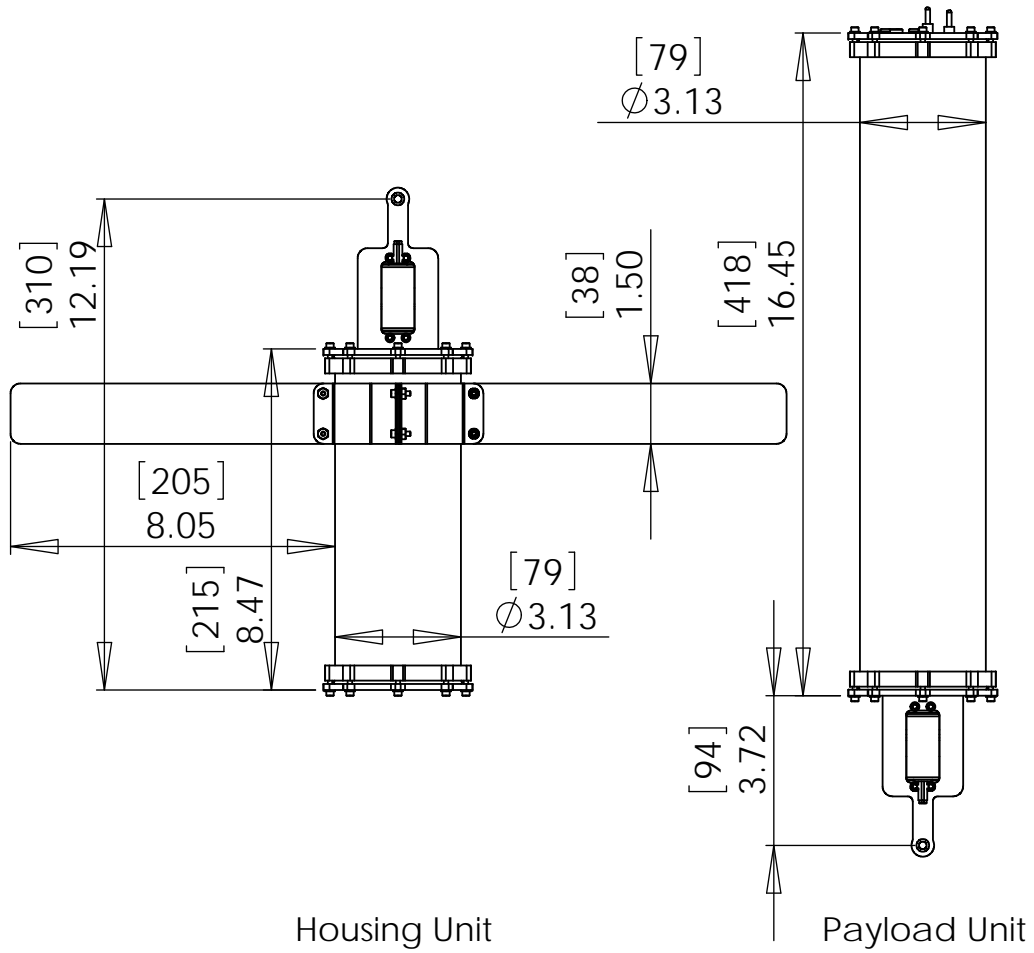


Figure 5.2: Sketches of the housing and payload units for the prototype buoy model simulated in this research.

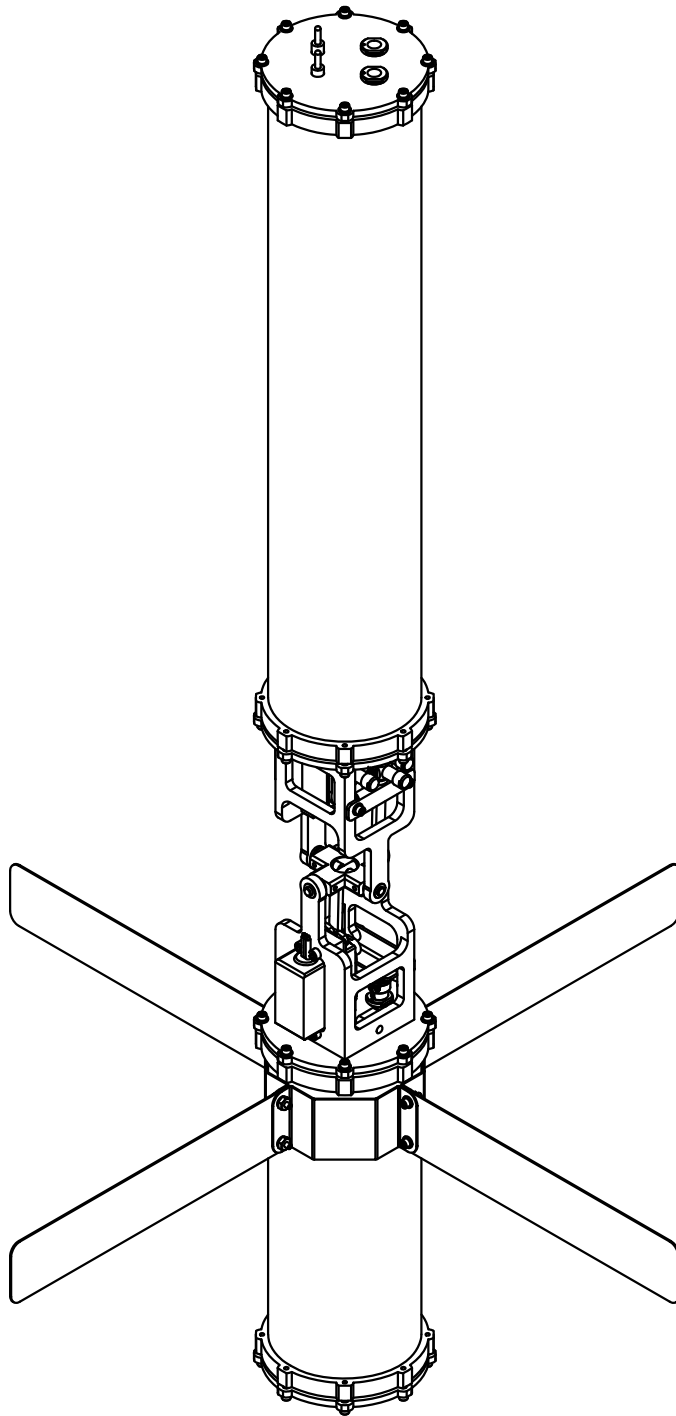


Figure 5.3: A sketch of the complete prototype buoy model.

Table 5.1: The mass and geometry parameters for the numerical simulation derived from the CAD model of the prototype buoy.

Parameter	Housing	Payload
Mass [kg] (lbs)	1.553 (3.42)	0.993 (2.19)
OD [m] (in)	0.079 (3.125)	0.079 (3.125)
Length [m] (in)	0.215 (8.47)	0.418 (16.45)
\mathbf{R}_{cm} [m]	$\begin{bmatrix} -0.0006 \\ 0 \\ 0.1002 \end{bmatrix}$	$\begin{bmatrix} 0 \\ -0.0004 \\ 0.2032 \end{bmatrix}$
\mathbf{R}_j [m]	$\begin{bmatrix} 0 \\ 0 \\ 0.309 \end{bmatrix}$	$\begin{bmatrix} 0 \\ 0 \\ -0.094 \end{bmatrix}$
\mathbf{J}_{cm} [$kg\ m^2$]	$\begin{bmatrix} 0.0109 & 0 & -0.0001 \\ 0 & 0.0109 & 0 \\ -0.0001 & 0 & 0.027 \end{bmatrix}$	$\begin{bmatrix} 0.0318 & 0 & 0 \\ 0 & 0.0317 & 0 \\ 0 & 0 & 0.010 \end{bmatrix}$
C_{Df}	1	1
C_{DmXY}	3	3
C_{DmZ}	0.1	0.1
n_{fins}	4	0
l_{fins} [m]	0.203	0
w_{fins} [m]	0.0391	0

5.2 SMC Gain Search

Early in this research, the gain values were selected by hand after many trials. The performance of the system was evaluated by comparing the composite error plot for each of the trials. Quantitative measures were calculated by evaluating the maximum and RMS error values for the payload composite pointing error from 5, 10, and 15 seconds onward. Given that the feed forward gain term is determined by the mass distribution in the buoy and the integral gain term was found to have little positive effect (and so is set to zero), this leaves three terms in the control law to tune the system performance with: C , α , and δ . The yaw damper gain, K_{yaw} , effects are discussed separately.

Some attempts were made at using a polytope simplex algorithm to perform a search across these three parameters for a set which minimizes the composite payload RMS error from 15 seconds onward. This was attempted with MATLAB's 'fminsearch' function. However, this search consistently failed to converge on values that were significantly different from initial values. The failure to converge was due to the performance metric being "noisy".

Instead of a true multidimensional search, a series of one dimensional searches were conducted. Each of the SMC parameters was varied across a range of values, while the other two were held constant. These one dimensional searches revealed good value ranges for the parameters C , α , and δ . A second round of one dimensional searches was run, where the values used for the constant terms were in the good range from the first round of searches. The results from these searches are plotted in Figure 5.4 through 5.6.

Two performance metrics were devised. 1) a "steady state" performance metric, which consists of calculating the RMS value for the composite payload pointing error from 15 seconds onward; and 2) a "transient" performance metric, which calculates the composite payload error RMS values from time 3 to 8 seconds. In all cases time zero was when the buoy was released from an extreme non-equilibrium condition. There were no other transients applied to the system, i.e. no payload re-positioning commands were applied after buoy release.

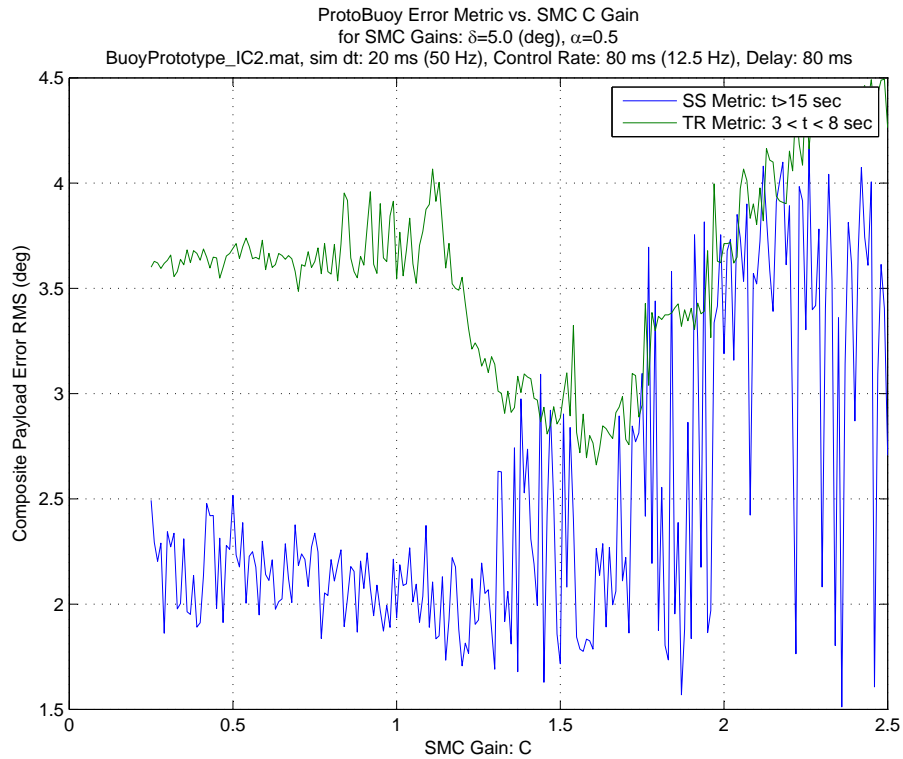


Figure 5.4: The steady state (blue) and transient (green) performance metrics as a function of the SMC Gain C . The prototype buoy model was released from flat on the water surface. $\alpha = 0.5$ and $\delta = 5 \text{ deg}$. The controller was run at 12.5 Hz and there was a system latency of 80 msec (one control period). From this data the transient metric is minimized from approximately $1.2 < C < 1.7$. The steady state metric becomes larger and noisier when $C > 1.3$.

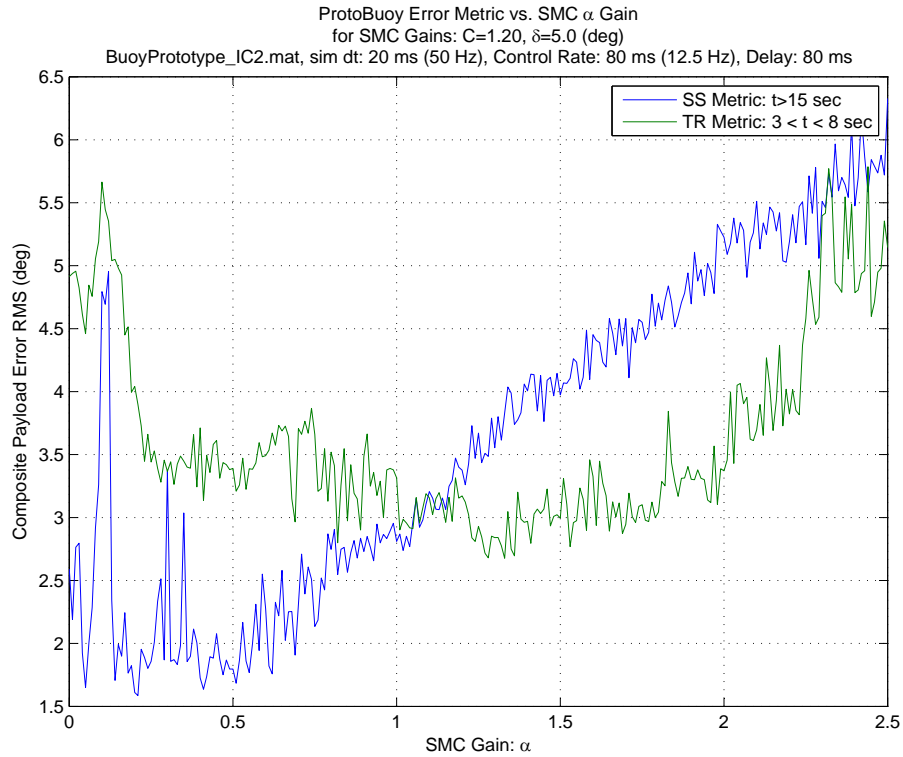


Figure 5.5: The steady state (blue) and transient (green) performance metrics as a function of the SMC Gain α . The prototype buoy model was released from flat on the water surface. $C = 1.2$ and $\delta = 5 \text{ deg}$. The controller was run at 12.5 Hz and there was a system latency of 80 msec (one control period). From this data the transient metric is minimized from approximately $0.25 < \alpha < 2.0$. The steady state metric becomes larger and noisier when $\alpha > 0.5$.

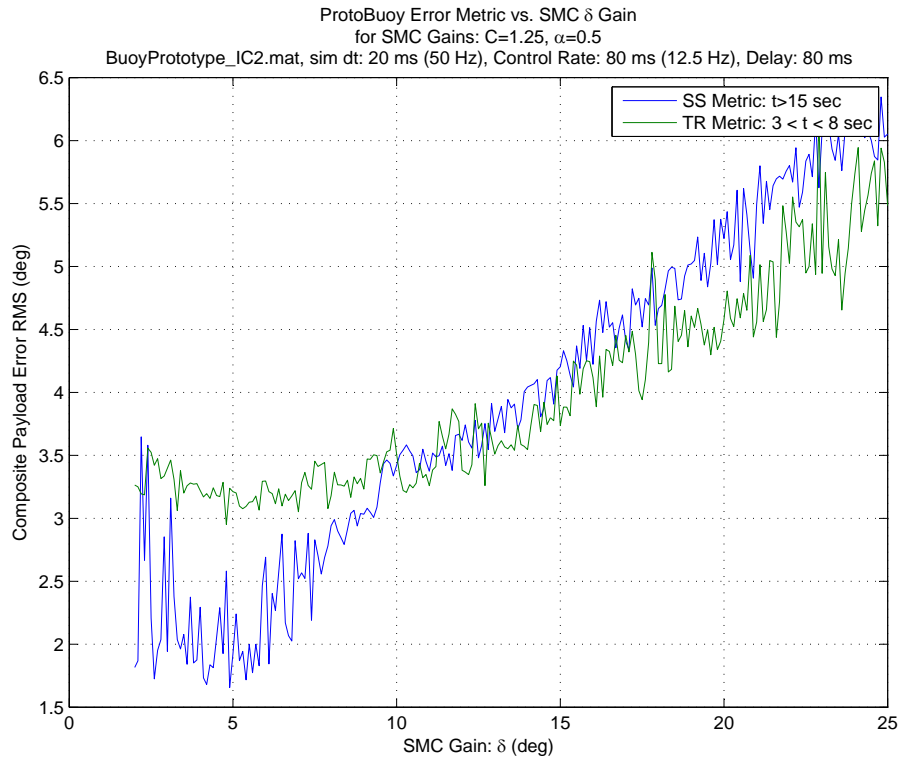


Figure 5.6: The steady state (blue) and transient (green) performance metrics as a function of the SMC Gain δ . The prototype buoy model was released from flat on the water surface. $C = 1.25$ and $\alpha = 0.5$. The controller was run at 12.5 Hz and there was a system latency of 80 msec (one control period). From this data the transient metric is minimized when $\delta < 10$ deg. The steady state metric was minimized from 4 deg $< \delta < 6$ deg.

5.3 Control Rate Effects

A series of trials was performed to understand the effects of control rate on the system performance. The simulation was performed by releasing the buoy from flat on the surface of the water and commanding it to a particular azimuth and vertical angle. At 10 seconds the payload was commanded to a new azimuth angle. For these trials the control loop was run progressively slower with *no* system latency. Figure 5.7 shows the composite payload pointing error for a number of these trials. In these trials the base simulation rate is 50 Hz (20 msec).

There was no significant change in performance when the control loop was slowed from 20 msec (50Hz) to 100 msec (10 Hz). “Acceptable” performance was still obtained when the control loop was slowed to 200 msec (5 Hz), as the composite payload error never exceed 5 degrees after the second transient. Further slowing the control loop causes the system performance to rapidly degrade.

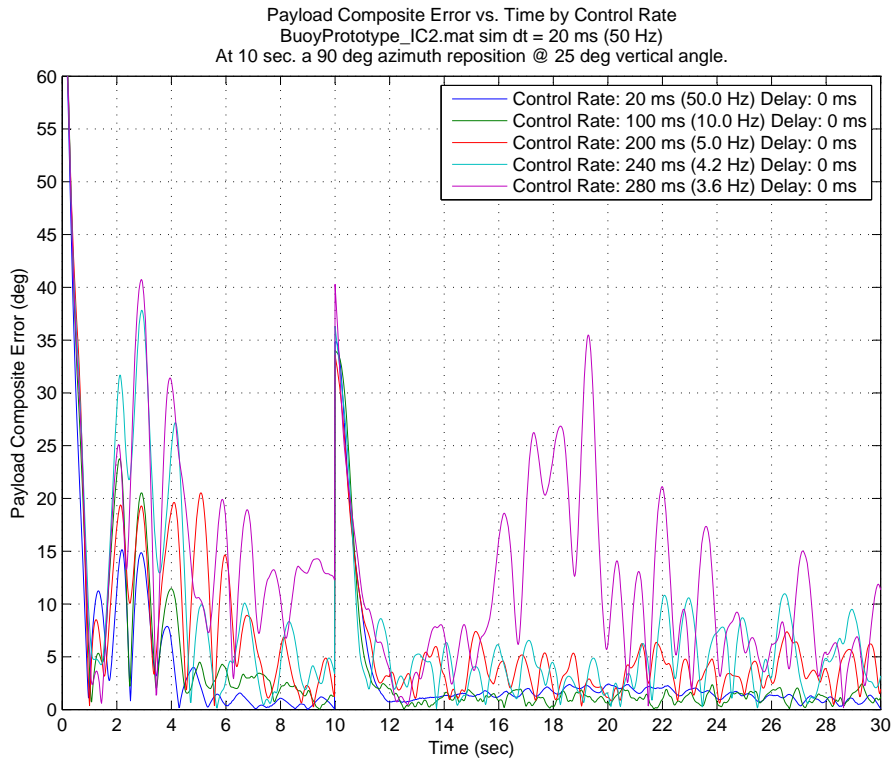


Figure 5.7: The composite payload error for the prototype buoy model responding to two transients (the release from initial conditions and an azimuth reposition at 10 seconds), with the control loop running at different rates. There is no system latency. There is not much change in performance between the 20 msec and 100 msec cases. System performance degrades rapidly when the control loop slows to less than 200 msec (5 Hz).

5.4 System Latency Effects

Here we consider the effects of delay on the system performance. These delays could come in the form of sensor delays or control actuator delays. In the simulation all these delays are lumped into a single overall system latency value. The delay is implemented by calculating the desired control signals for the joint axes, and then delaying the application of those signals to the joint by the delay value.

In all cases the control loop is running at 40 msec (25 Hz). There is no significant performance degradation through delays of approximately 120 msec. System performance starts to degrade significantly when system latency is 160 msec and longer.

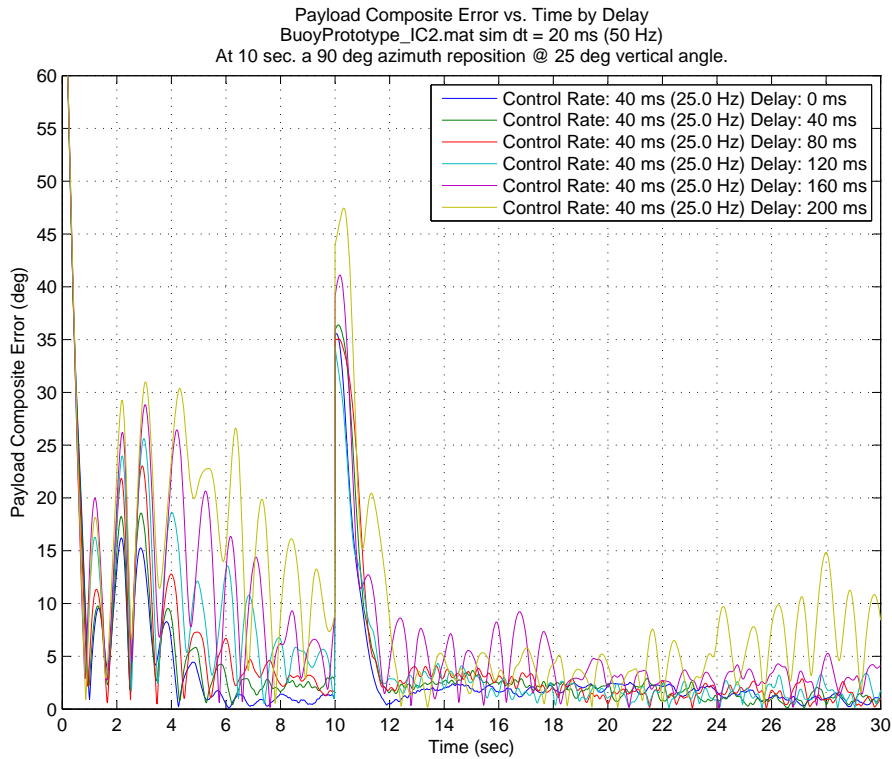


Figure 5.8: The composite payload error for the prototype buoy model responding to two transients (the release from initial conditions and an azimuth reposition at 10 seconds), with various system latency values. In all cases the control loop is running at 40 msec (25 Hz). There is no significant performance degradation through delays of approximately 120 msec. System performance starts to degrade significantly when system latency is 160 msec and longer.

5.5 Fin Effects

The prototype buoy configuration includes 4 radial fins mounted on the housing. These fins are to improve the yaw control of the buoy, by providing additional drag and inertia about the long axis of the buoy housing.

In this trial we can see that the fins provide a slight but noticeable improvement in payload composite error over the non-finned case.

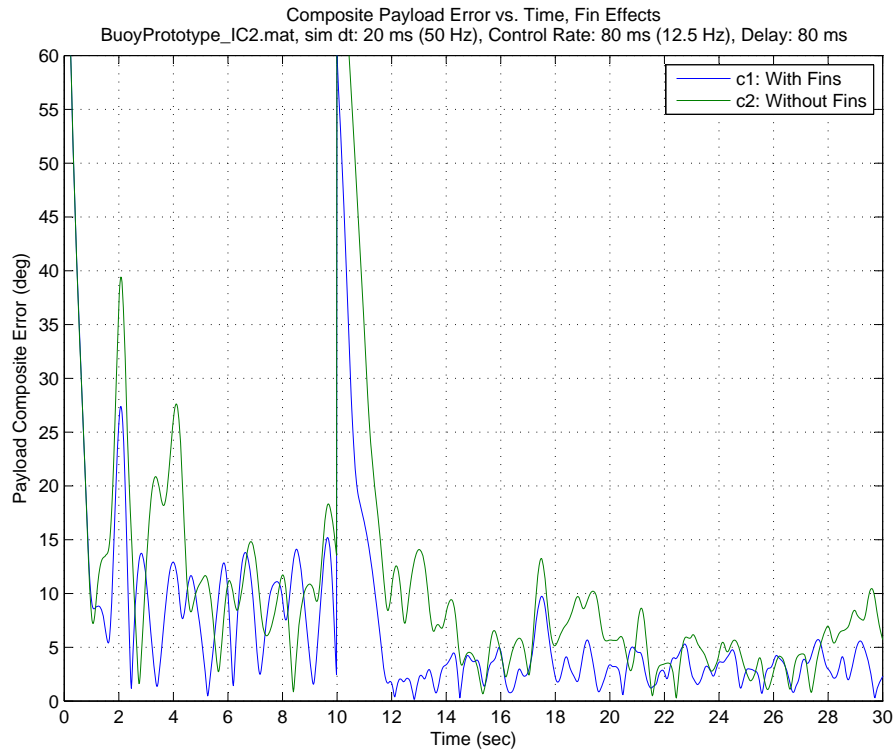


Figure 5.9: The composite payload error for the prototype buoy model responding to two transients (the release from initial conditions and an azimuth reposition at 10 seconds) with (blue) and without (green) passive yaw fins. The fins provide a slight but noticeable improvement over the non-finned case.

5.6 Yaw Damper Effects

Next the effects of the active yaw damper were evaluated. The prototype buoy configuration does not appear to benefit from the active yaw damper feature of the control law. This is shown in Figure 5.10. As K_{yaw} is increased beyond about 20, the system performance degrades.

In these cases the commanded vertical angle is 35 degrees, and at 10 seconds the payload is repositioned in azimuth by 120 degrees.

However, in earlier trials with the J series buoy configurations, there were cases where the active yaw damper clearly helped. One example is presented in Figure 5.11.

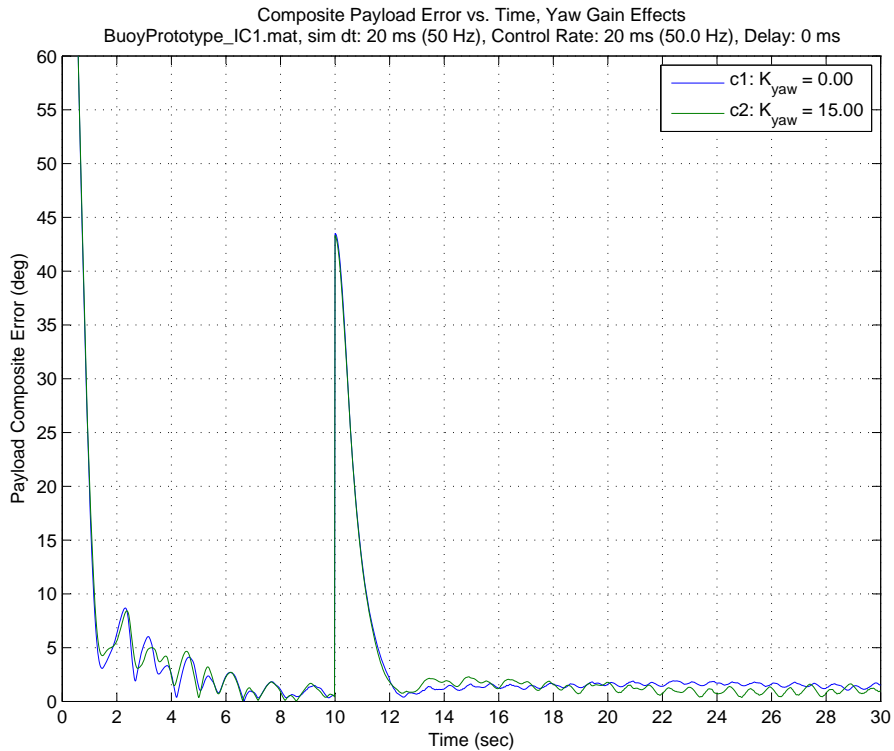


Figure 5.10: The composite payload error for the prototype buoy model responding to two transients (the release from initial conditions and an azimuth reposition at 10 seconds) with (blue) and without (green) the active yaw damper. The control loop is running at 20 msec (50 Hz) with *no* system latency. Under these conditions the active yaw damper does not significantly improve the system response.

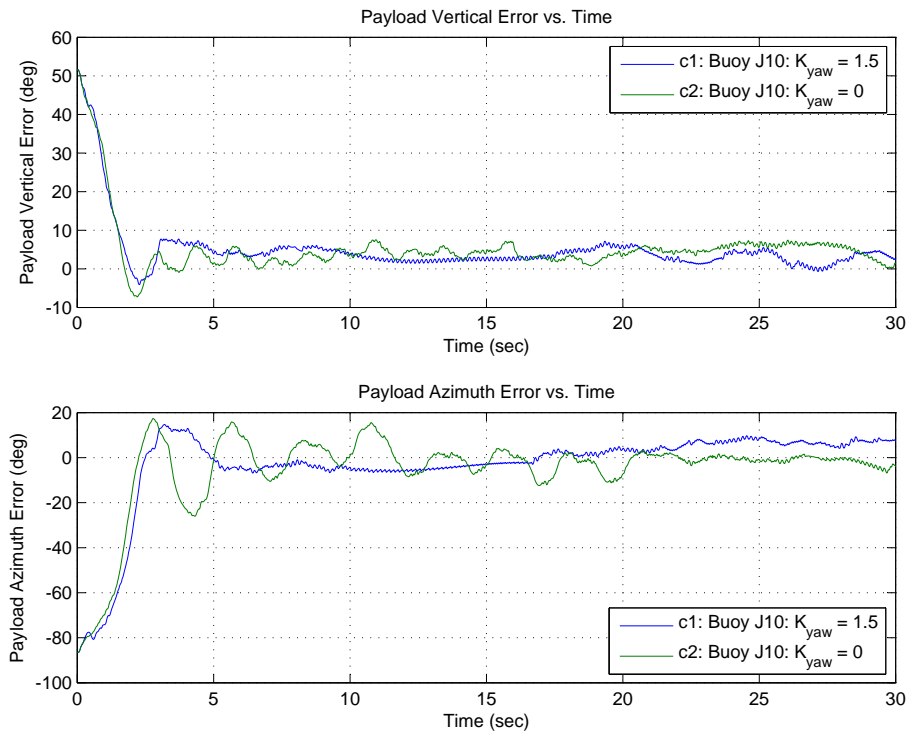


Figure 5.11: The vertical and azimuthal payload error for stabilizing the J10 buoy payload at a vertical angle of 35 degrees. The c1 system (blue) uses the active yaw damper and the c2 system (green) does not. The yaw damper's positive effects are clear in both the azimuthal and vertical responses. For this trial the other control gains are: $C = 0.25$, $K_{ff} = 0.441$, $\alpha = 0$ (deg), $\delta = 20$ (deg), $h = 0.02$, and $K_i = 0.0$.

5.7 Acceleration Limit Effects

In the simulation, the control authority of each joint axis is specified by the maximum allowed joint acceleration. Since joint acceleration is proportional to the applied joint torque, the limit on acceleration also specifies a limit on joint torque. Figure 5.12 plots the payload composite error for various joint acceleration limits. The control loop is running at 80 msec (12.5 Hz) with a system latency of 80 msec. Payload composite error does not improve significantly for system acceleration limits greater than 300 deg/sec^2 . However, system performance does degrade rapidly for acceleration limits less than 300 deg/sec^2 .

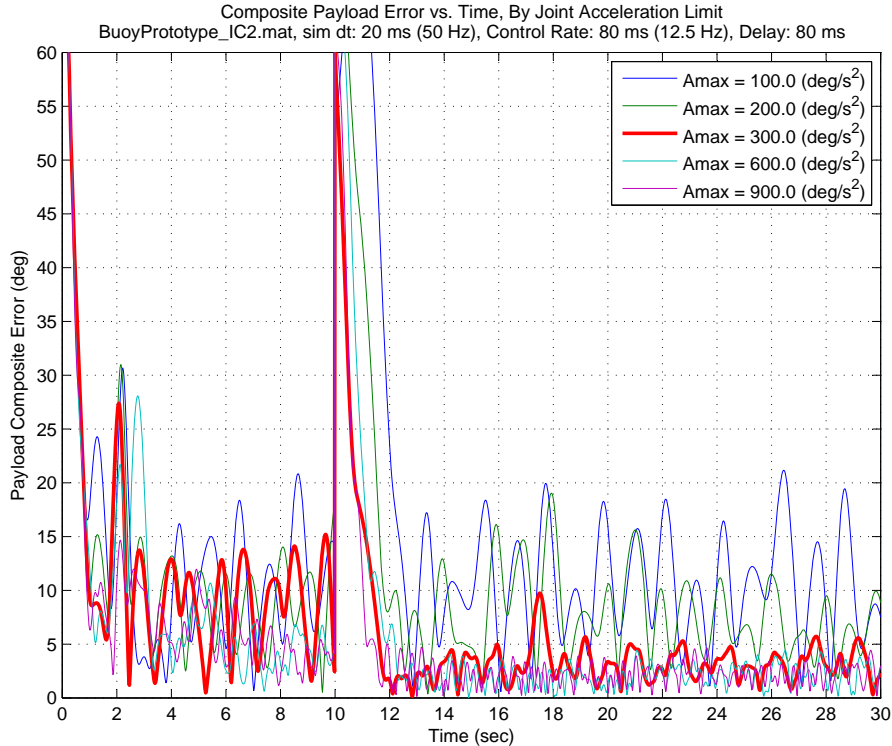


Figure 5.12: The composite payload error for the prototype buoy model responding to two transients (the release from initial conditions and an azimuth reposition at 10 seconds) for various joint acceleration limits. The control loop is running at 80 msec (12.5 Hz) with system latency of 80 msec. For this buoy configuration, a joint acceleration limit of 300 deg/sec^2 (red) is the critical value above which system performance is good and below which system performance is poor.

5.8 Initial Condition Effects

Five different sets of initial conditions were used with the prototype buoy configuration to assess how sensitive the controller's performance is to initial conditions. These sets of initial conditions place the buoy at different attitudes and are illustrated in Figure 5.13. The roll and pitch angles for each initial condition are listed in Table 5.2. The composite payload pointing error for each initial condition is plotted in Figure 5.14. The controller did a good job at stabilizing the payload from initial conditions 2, 3, and 5.

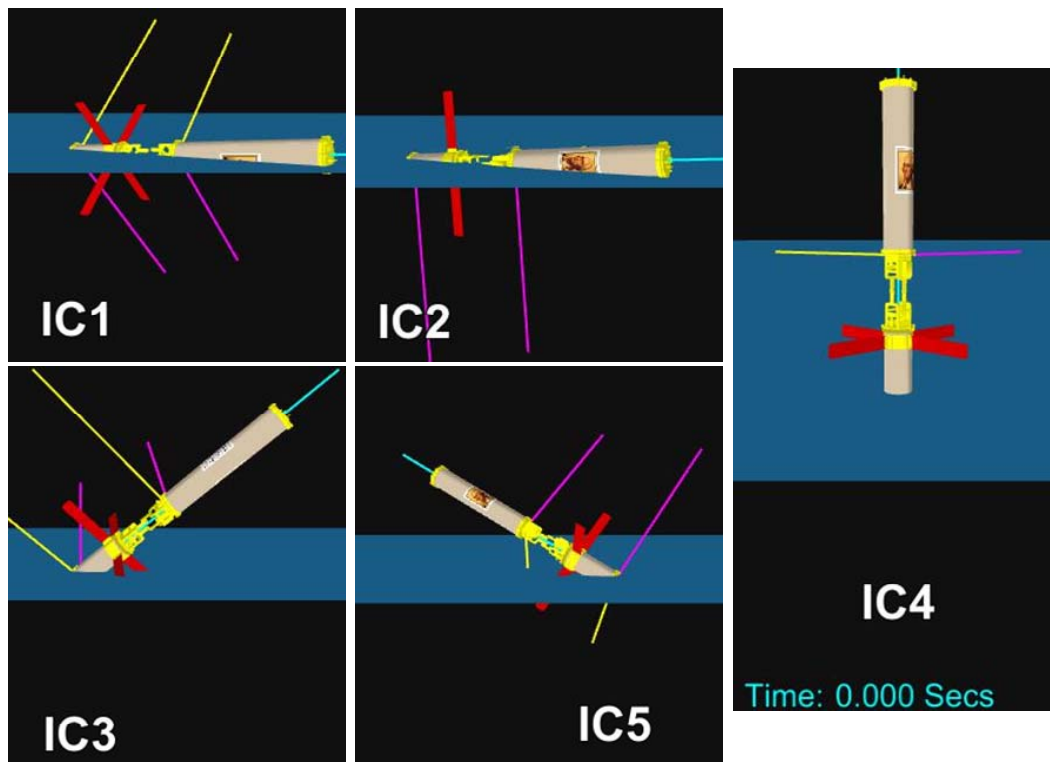


Figure 5.13: The initial positions and attitudes compared in the simulation. These conditions are numbered 1 through 5. In all cases the buoy starts at rest. The housing's and payload's x, y, and z axes are shown in purple, yellow, and cyan respectively. In all cases the housing coordinate system starts 2.5 cm (1 inch) below the water's surface. Initial conditions 1 and 2 are outwardly very similar, however, the difference is in their the orientation of their x and y axes with respect to the water's surface. This difference results in the plane of oscillation occurring in different planes of joint azimuth actuation.

For initial condition 4, the buoy starts with a vertical attitude. However, it starts with the *base* of the housing just below the water's surface. Therefore when released, it drops straight down, completely submerging, and then bobs up and down significantly.

For initial conditions 1 and 2 the overall initial attitudes of the buoy are very similar. The principal difference is in the orientation of the buoy's X and Y axes with respect to the surface of the water. It is not clear why one configuration performs well and the other does not. This could be because difference in orientation between the two trials results in a difference of the orientation of the joint axes with respect to the buoy's initial motion. However, it is difficult to draw any conclusions based on only two trials. An area for further

investigation could be performing a large number of trials in which the buoy starts flat on the water's surface, and its orientation about the long axis is selected at random. This would allow a characterization of the prevalence and cause of this phenomenon.

In all cases at time zero, the payload is commanded to a vertical angle of 35 degrees and an azimuth angle of 0 degrees. After 10 seconds, the payload azimuth angle is commanded to shift to 90 degrees.

Table 5.2: Initial roll and pitch angles for each initial condition configuration. Additionally, in all cases the buoy starts at rest with the joint straight, the housing coordinate system (located at the center of the bottom face) located 2.5 cm (1 inch) below the water's surface, and a yaw angle of zero degrees.

IC	pitch (deg)	roll (deg)
1	45	85
2	85	20
3	-30	45
4	0	0
5	-45	-45

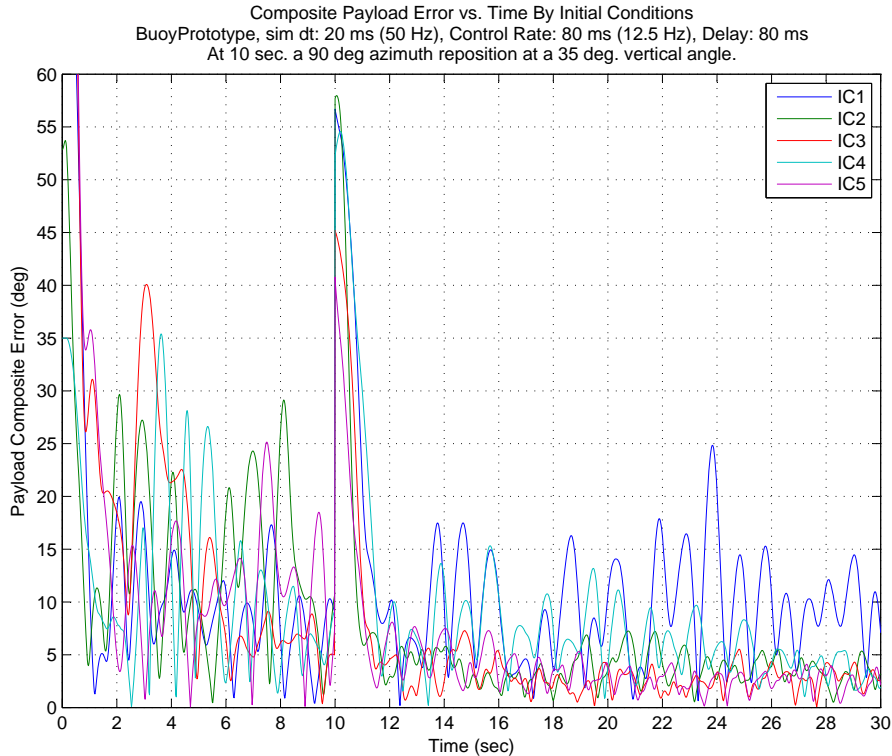


Figure 5.14: The composite payload error for the prototype buoy model responding to two transients (the release from initial conditions and an azimuth reposition at 10 seconds) for various initial conditions. The control loop is running at 80 msec (12.5 Hz) with system latency of 80 msec. Initial conditions 1 and 4 result in poor buoy performance.

The poor performance in responding to initial conditions 1 and 4 can be remedied in

several ways, including:

1. Reducing the system latency and speeding up the control loop.
2. Commanding the payload to be stabilized about the vertical right after release.

An approach to reducing the system sensitivity to the initial conditions is to command the system to its most stable configuration first. Due to symmetry, the buoy's most robust state is with the payload commanded to a vertical angle. Figure 5.15 plots the effects on initial conditions 1 and 4 by having the payload commanded to the vertical for the first 3 second after release. This is compared with immediately commanding the payload to the desired non-vertical angle. It is interesting that there is no noticeable performance improvement, until *after* the azimuthal reposition command at 10 seconds.

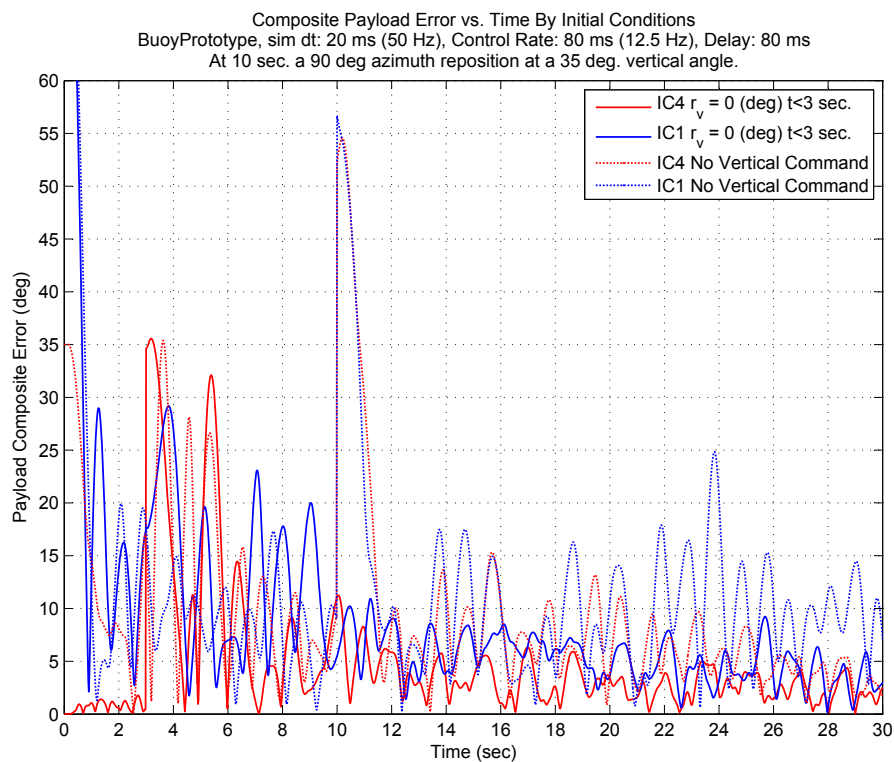


Figure 5.15: The composite payload error for initial conditions 1 (blue) and 4 (red), without an initial vertical payload command (dotted) and with the payload being commanded to vertical for the first 3 seconds (solid). By commanding the payload initially to vertical after release, we can see that system can maintain much better pointing performances from then on.

Figure 5.16 show the improved performance by getting the payload completely stable about the vertical before performing additional aiming. The payload is commanded to vertical for 15 seconds after release, then it is commanded to a vertical angle of 35 degrees and an azimuth angle of 90 degrees. All 5 initial conditions are plotted. In all cases it takes the buoy 6 seconds (or less) to stabilize the payload about the vertical.

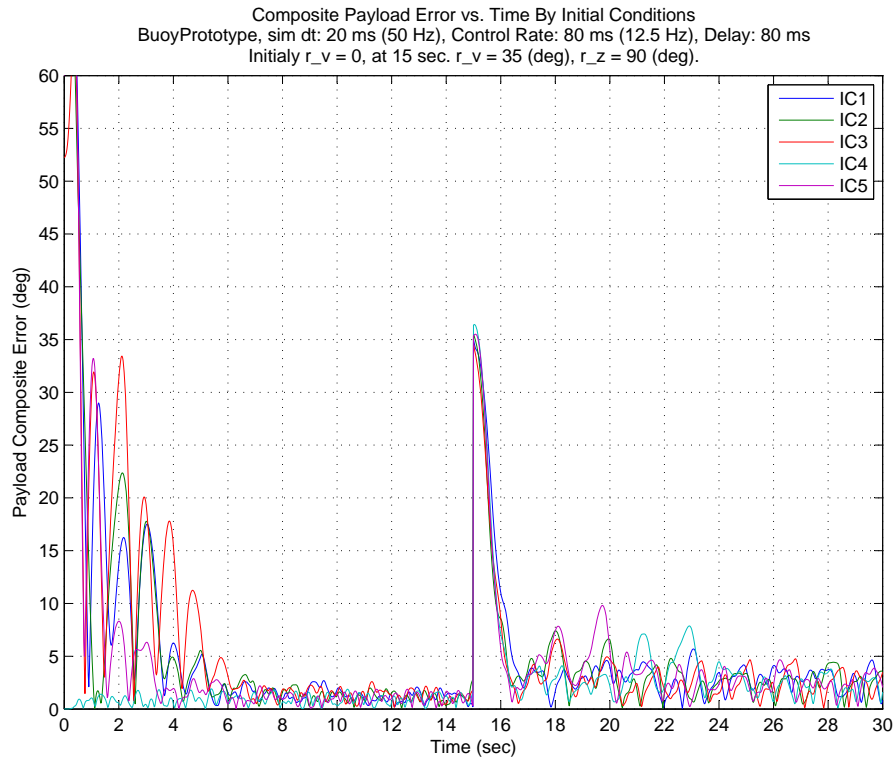


Figure 5.16: The composite payload error for all 5 initial conditions. The payload is commanded to vertical for the first 15 seconds, then it is commanded to a vertical angle of 35 degrees and an azimuth angle of 90 degrees. By completely stabilizing the payload about the vertical, we can see that after 6 seconds, the effects of all initial conditions have been eliminated.

5.9 Vertical Angle Effects

The discussion about the buoy's performance with respect to its initial conditions has illustrated a significant point. The composite payload error is much less when the payload is stabilized vertically compared with a non-vertical angle. This section presents a series of trials where the azimuth is repositioned by 90 degrees at different vertical angles. The controller/prototype buoy configuration was able to provide good results up to vertical angles of approximately 35 degrees.

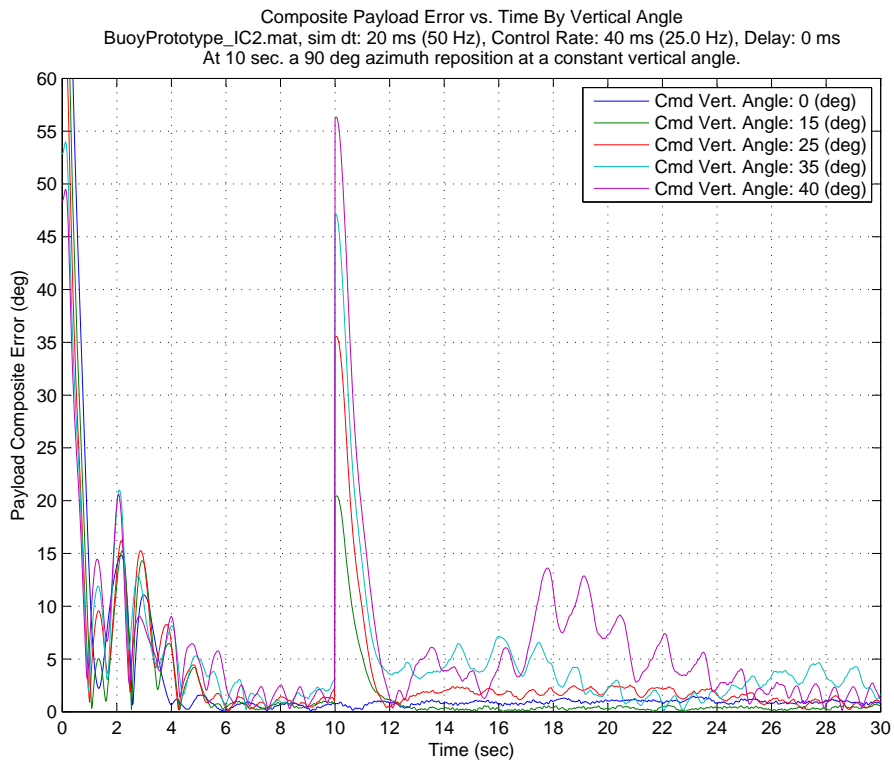


Figure 5.17: The composite payload error for various vertical angles. At 10 seconds the payload is repositioned by 90 degrees in azimuth, while maintaining a constant vertical angle. A degradation of performance begins to be evident at 35 degrees and becomes significantly worse at 40 degrees.

5.10 PID+FF Control Results

In simulation the PID+FF controller also performs well at controlling the prototype buoy configuration. Figure 5.18 compares the composite payload error for a PID+FF control (blue) and SMC+FF control (green). In terms of composite pointing error, both control laws perform equivalently.

Next a trial was run with the J15 buoy configuration, the control loop running twice as fast with half the system latency, and the correct feed forward gain, K_{ff} . The other PID and SMC gains used values tuned for the prototype buoy configuration. Figure 5.19 shows the composite payload error for this trial.

In this trial the SMC+FF control law performs noticeably better than the PID+FF control law. The PID+FF could have been retuned to give equivalent performance to the SMC+FF controller. However, by not retuning it, the trial illustrates the SMC+FF's robustness to model variation compared with the PID+FF law.

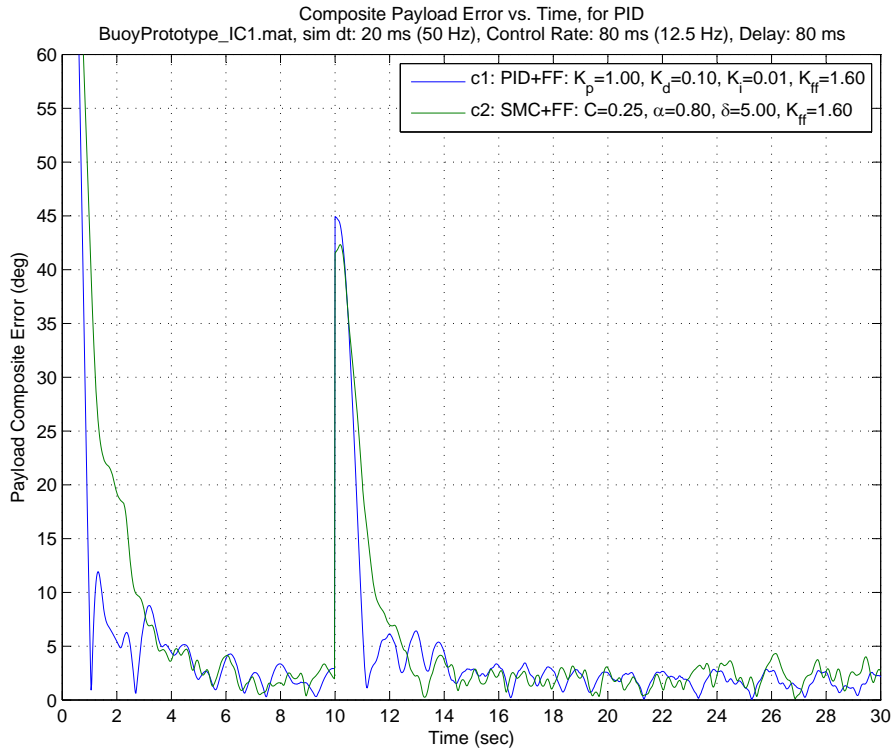


Figure 5.18: The composite payload error for the prototype buoy under PID+FF (blue) and SMC+FF (green) control. We can see that the two techniques perform approximately equally well.

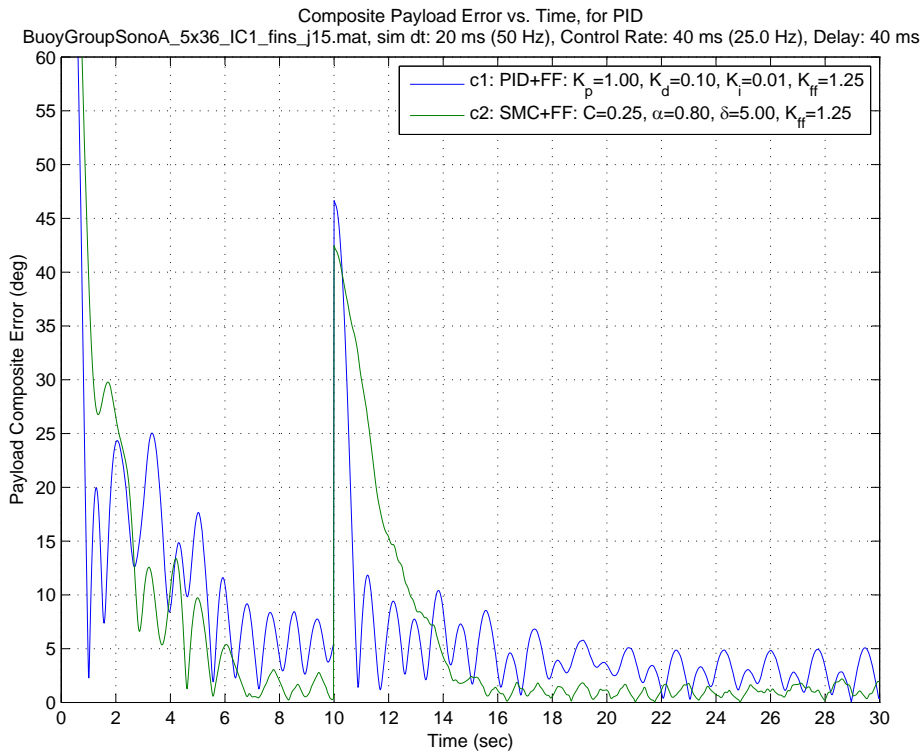


Figure 5.19: The composite payload error for the J15 buoy configuration under PID+FF (blue) and SMC+FF (green) control. We can see that the SMC+FF controller performs slightly better than the PID+FF controller. Only the feed forward gain value was changed between this trial and previous prototype buoy configuration trial shown in Figure 5.18.

5.11 Vertical Oscillation Results

It will be shown in the wave trial results, Sections 5.12 and 5.13, that the resonant frequency of vertical oscillation is the dominant factor in determining the buoy's performance.

Predicting the buoy's resonant peak from (2.110) was shown to be accurate in Section 3.3 for the large and small test cylinders. For the prototype buoy configuration, with a mass of 2.546 kg and a radius of 0.0395 meters, the resonant frequency is expected to be 4.34 rad/s (a period of 1.45 seconds). Performing a vertical drop test in simulation with the joint locked, so the buoy mimics a rigid cylinder, gives a measured frequency of vertical oscillation of 4.36 rad/s (a period of 1.44 seconds). This measure value was found by averaging the period of the first 8 oscillations. This response is shown in the upper plot of Figure 5.20.

Therefore using (2.110) to estimate the resonant frequency of vertical oscillation is validated for the prototype buoy configuration in simulation.

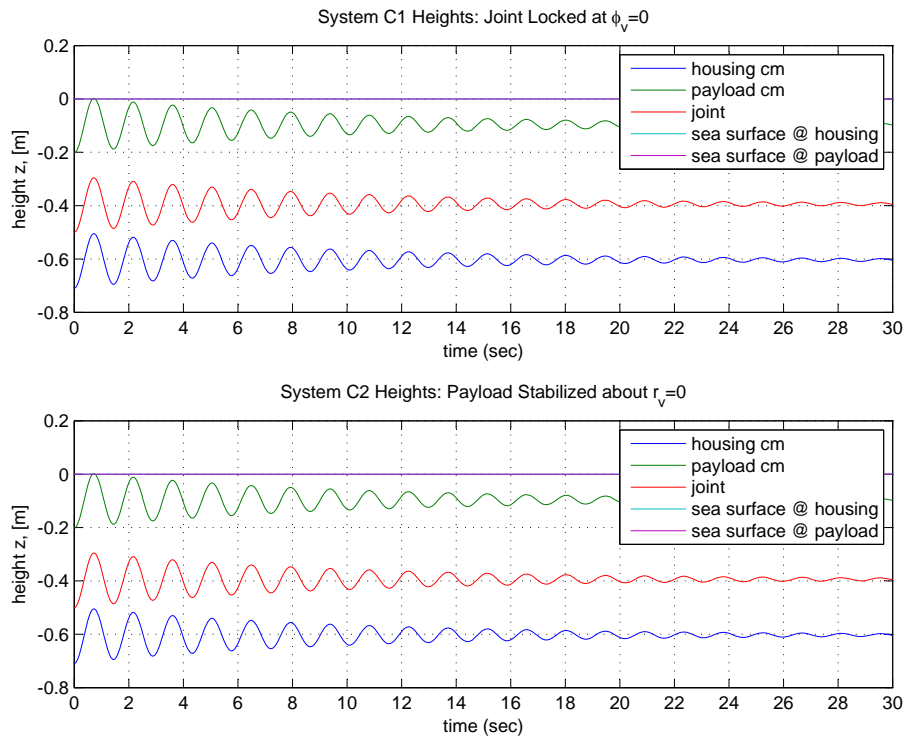


Figure 5.20: Payload CM, housing CM, and joint height vs. time for the prototype buoy configurations oscillating in the vertical direction. The c1 system (upper plot) shows the response when the joint is locked at a vertical angle of zero. This causes the buoy to behave most like a rigid cylinder. In the c2 system (lower plot), the payload is actively stabilized about the vertical using the SMC+FF control law. We can see that actively stabilizing the payload about the vertical does not change the period of vertical oscillation. Careful measurement gives the average period of oscillation for the c1 system of 1.44 seconds.

5.12 Regular Ocean Wave Effects

All the simulation trials discussed up to now have been on a calm sea, that is there were no surface waves applied to the model. A sequence of trials was performed with different surface waves to evaluate the buoy's ability to reject wave induced disturbances.

For all these regular wave trials the following conditions apply.

1. The prototype buoy configuration starts in initial condition configuration 1, See Figure 5.13.
2. The SMC control law is used with the control loop running at 80 msec and a system latency of 80 msec.
3. The payload is commanded to the vertical for the first 15 seconds of the simulation, and then it is commanded to a vertical angle of 20 degrees and an azimuth angle of 150 degrees.

5.12.1 Regular Seas Trial 1

First the prototype buoy configuration was tested with regular seas being applied to it. One regular sea has an amplitude of ± 1.0 meters (6 foot 6 inch wave height) and a period of 5 seconds. The second regular sea has an amplitude of ± 0.4 meters (2 foot 7 inch wave height), and a period of 2 seconds. The smaller shorter wave was scaled such that the slope of the water's surface was the same for both waves. The wave elevation for both seas are plotted in Figure 5.22.

Despite the smaller amplitude, the shorter period makes the buoy uncontrollable because it is similar to the natural frequency of the buoy. This results in the buoy having a vertical oscillation of almost exactly the same period as the wave train, except that the phase of the buoy oscillation is nearly 180 degrees out of phase.

This causes poor performance in the buoy system for two reasons. (1) The buoy is completely submerged for a significant amount of time. And (2) when buoy is at the top of its oscillation, the payload comes completely out of the water. This is an unstable configuration, and as a result the buoy falls over sideways.

It is very important to note that this poor performance has nothing to do with the control law selected for the joint motion. It is entirely due to the passive response of the structure to the disturbance.

This poor performance is clear from the composite payload pointing error plot shown in Figure 5.21. The relationship between the buoy's vertical position and sea surface is illustrated in Figure 5.23. The payload coming completely out of the water is evident in Figure 5.23, at the points where the joint is higher than the surface (i.e. the red curve is above the purple and cyan curves). In all cases, shortly after the joint is out of the water, Figure 5.23 shows the housing CM, payload CM, and joint all at the same height, indicating that the buoy is on its side.

The c2 system's performance is better when the payload is commanded about a vertical angle ($t < 15$ sec) than when it is commanded to a non-vertical angle.

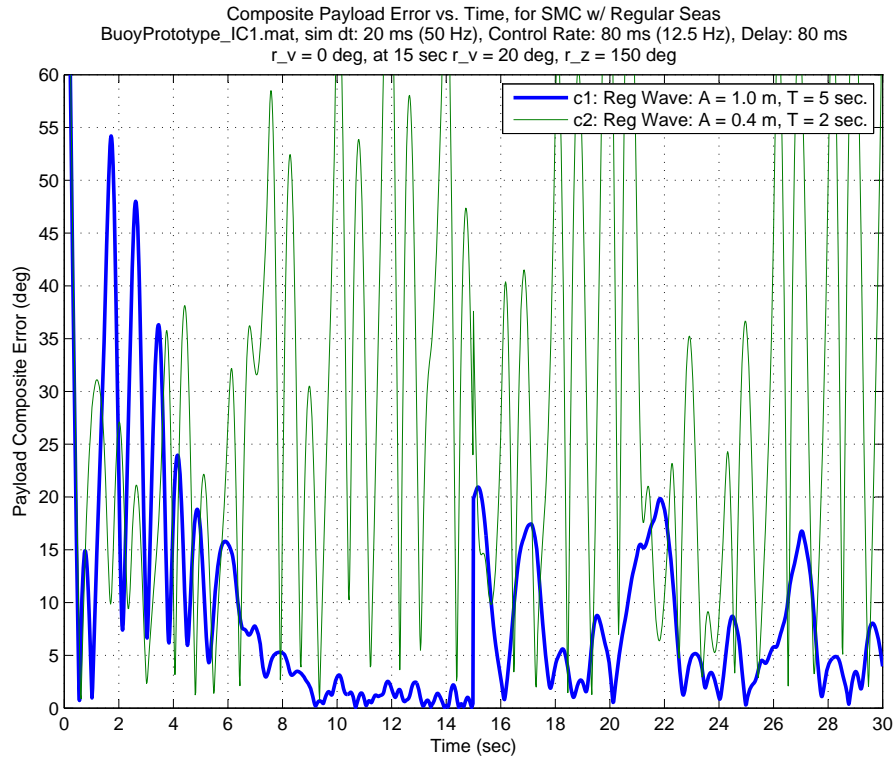


Figure 5.21: The composite payload pointing error for regular seas trial 1. Both buoys and controllers (SMC) are the same. The payload is commanded vertical for the first 15 seconds, then it is commanded to a vertical angle of 20 degrees and an azimuth angle of 150 degrees. The regular sea applied to system c1 (blue) has an amplitude of ± 1 meter and a period of 5 seconds. The regular sea applied to system c2 (green) has an amplitude of ± 0.4 meters, and a period of 2 seconds. Despite the smaller amplitude, the shorter period makes the buoy uncontrollable because it is similar to the natural frequency of the buoy. The c2 system's performance is better when the payload is commanded about a vertical angle ($t < 15$ sec) than when it is commanded to a non-vertical angle.

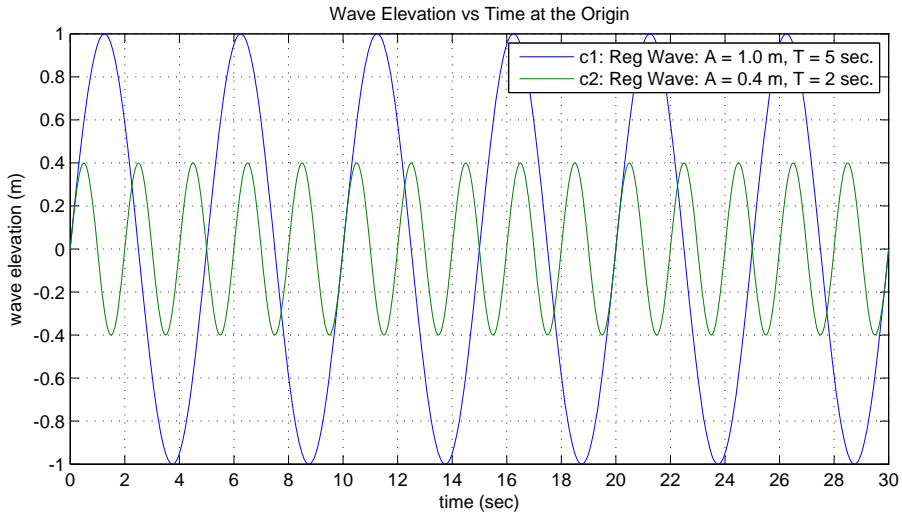


Figure 5.22: The wave elevations for regular seas trial 1 applied to each buoy. The smaller shorter sea was scaled such that the slope of the water's surface was the same for both seas.

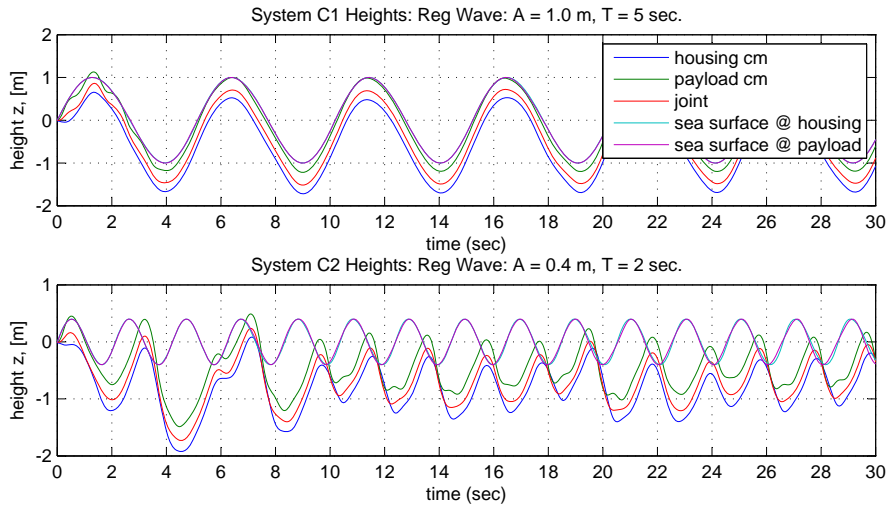


Figure 5.23: The buoy heights for the regular seas trial 1. The buoy has a vertical period of oscillation of nearly 2 seconds which is almost exactly the same as wave period which is applied to the c2 system. The plot of the c2 system clearly shows that the the phase of the buoy oscillation is nearly 180 degrees out of phase with respect to the wave. This results in the buoy being completely submerged for a significant amount of the time. Additionally, when it is not fully submerged, the buoy rises to a height out of the water sufficient to become unstable and fall over sideways.

5.12.2 Regular Seas Trial 2

Given the extremely poor performance of the buoy when excited by a wave with a two second period, this trial was to explore the maximum amplitude of a 2 second wave which the buoy system could reject. The amplitude of the waves were adjusted until a pair of waves were found such that one wave was rejected by the system and the slightly larger wave was not well rejected. After several iterations we found that a 2 second wave with an amplitude of ± 0.05 meters (4 inch wave height) could be rejected by the system, while a wave of ± 0.075 meters (6 inch wave height) caused significant performance problems.

For the smaller wave the system performed well when stabilized about the vertical (as was the case for the first 15 seconds of the simulation). The system performed marginally when the payload was commanded to vertical angle of 20 degrees. This is shown by the green curve in Figure 5.24. The commanded payload azimuth angle was 150 degrees and the seas were traveling from 180 to 000 degrees. It is clear from the blue curve in Figure 5.24 that the system would perform poorly for a wave amplitude of ± 0.075 meters regardless of the commanded payload vertical angle. The wave elevation and buoy heights are plotted in Figures 5.25 and 5.26 respectively.

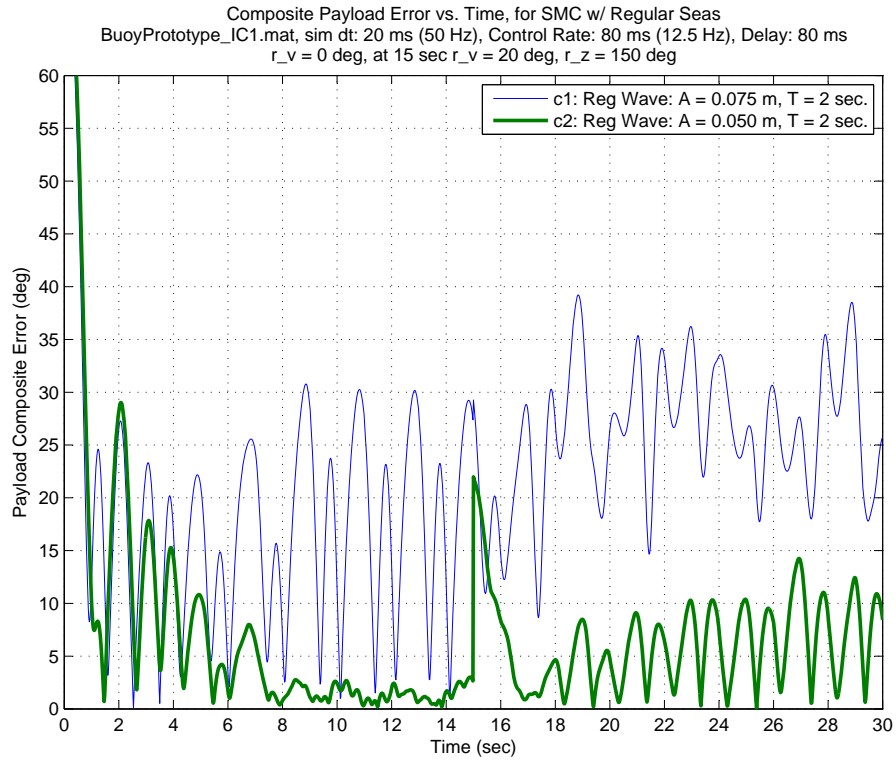


Figure 5.24: The composite payload pointing error for regular seas trial 2. Both buoys and controllers (SMC) are the same. The payload is commanded vertical for the first 15 seconds, then it is commanded to a vertical angle of 20 degrees and an azimuth angle of 150 degrees. The regular sea applied to system c1 (blue) had an amplitude of ± 0.075 meters. The regular sea applied to system c2 (green) had an amplitude of ± 0.05 meters. Both waves have periods of 2 seconds. The c2 system maintained good pointing performance in these seas when commanded to the vertical and did a marginal job when commanded to a vertical angle of 20 degrees. The c1 system did a poor job regardless of the commanded payload angle.

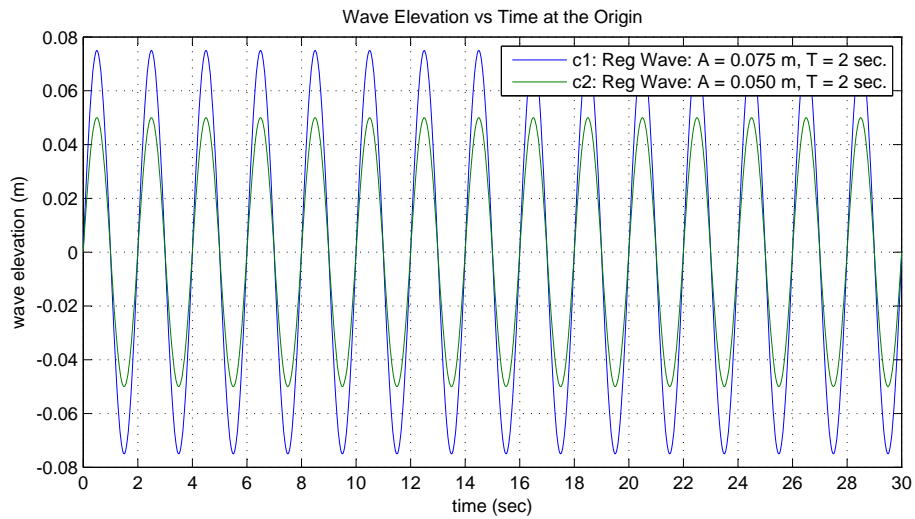


Figure 5.25: The wave elevations for regular seas trial 2 applied to each buoy. Both waves have a 2 second period.

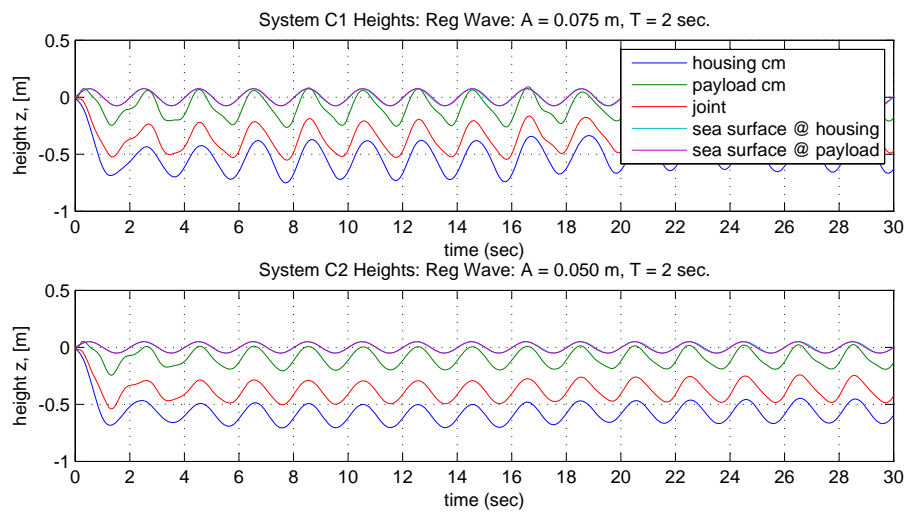


Figure 5.26: The buoy heights for the regular seas trial 2. The buoy has a vertical period of oscillation of almost 2 seconds which is nearly the same as sea's period.

5.12.3 Regular Seas Trial 3

The first two regular wave trials clearly indicate that the prototype buoy structure has a resonant peak at period of approximately 2 seconds. This prompted the third regular wave trial to evaluate the width of this resonant peak.

Regular waves of different periods were applied to the prototype buoy configuration. The amplitude of each of the waves was scaled to be proportional to the wavelength such that all the waves had an average slope of 4.5%. The average slope of a regular sinusoidal wave was approximated by

$$M = \frac{2A}{0.5\lambda} = \frac{4A}{\lambda}. \quad (5.1)$$

Where M is the slope, A is the amplitude of the wave, and λ is the wavelength. The wavelength is found using the deep water dispersion relationship (A.2), simple wave height equation (A.1), and $\omega = 2\pi/T$. This results in an equation for wavelength of

$$\lambda = \frac{gT^2}{2\pi}, \quad (5.2)$$

where g is the acceleration due to gravity and T is the wave period. This allows the wave amplitude to be expressed as a function of wave period and average slope using

$$A = \frac{MgT^2}{8\pi}. \quad (5.3)$$

The selection of 4.5% for the wave slope was somewhat arbitrary. It is a value that is reasonable for ocean waves and it causes the buoy's resonant peak to be well defined. Figure 5.27 clearly shows that the waves with the periods of 1.7 and 2.0 seconds caused the system to perform poorly, whereas the buoy performs noticeably better with the 1.0 and 2.3 second waves.

These results are very close to the predicted and measured resonant frequency of 4.3 rad/s (1.46 sec). It is a little surprising that the buoy performed as well as it did with the 1 second wave which is only 0.5 seconds off from the resonant peak, given how poorly it did with the 2 second wave which is also 0.5 seconds off. This difference is likely because the amplitude of this wave was so small (because of maintaining the 4.5% slope) that not enough energy was being coupled into the buoy.

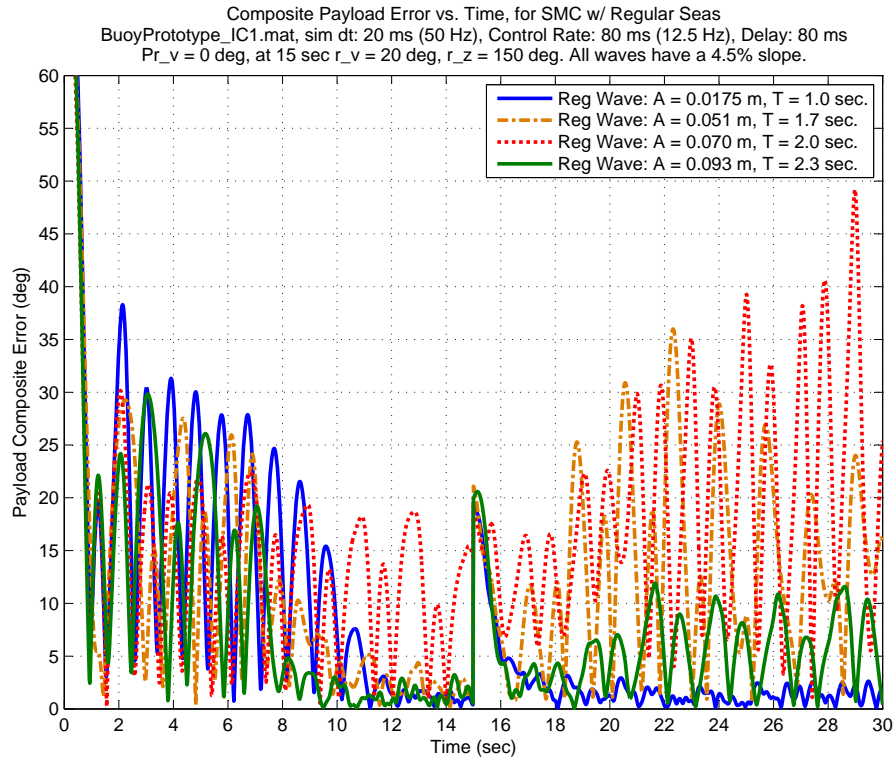


Figure 5.27: The composite payload pointing error for the system in the presences of various regular waves. The amplitude of the four regular waves were scaled such that they all had an average slope of 4.5%. The payload was initially commanded to the vertical and then at 15 seconds was commanded to a vertical angle of 20 degrees. This plot clearly shows the prototype configuration’s resonant peak from about 1.7 to 2.0 seconds. The buoy performed satisfactory for a regular wave with a period of one second when the payload was both vertical and 20 degrees away from the vertical. For the 2.3 second period wave, the buoy performed well (11-15 seconds) with the payload commanded to the vertical and it performed marginally when the payload was commanded to a vertical angle of 20 degrees.

5.13 Irregular Ocean Wave Effects

The results of the regular wave trials, presented in Section 5.12, clearly indicate the presence of a resonant peak for waves with a period of 1.7 to 2.3 seconds. This corresponds to a circular frequency of 2.7 to 3.7 radians per second. When the disturbance frequency is below this the system performs well. This leads to the following questions:

1. What are the fundamental structural characteristics which determine the magnitude and location of the resonant peak?

The examination of the small wave tank tests prompted the derivation presented in Section 2.9 to estimate the damped frequency of oscillation, ω_d , of the buoy. When comparing with the wave tank data, in Section 3.3 it was found that the damped frequency of oscillation was very close to the natural frequency, which is determined by the radius and mass of the buoy using

$$\omega_d \approx \omega_n = 175.46 \frac{R}{\sqrt{m}} = 87.73 \frac{D}{\sqrt{m}}. \quad (5.4)$$

2. Given the statistical nature of describing irregular ocean waves, is the buoy system performance qualitatively similar for different irregular wave trains generated from the same statistical parameters?

This was examined by running several trials where different irregular wave trains were generated by the same Pierson-Moskowitz spectrum and applied to the buoy system. Two of the trials are compared in Section 5.13.1 below.

3. Given, irregular seas in the open ocean, how much wave energy exists at frequencies near the buoy's resonant peak?

Assuming a Pierson-Moskowitz wave spectrum, the relative energy content can be approximated by finding the fraction of the area under the Pierson-Moskowitz density function within the frequency range of interest. Table 5.3 shows the percentage of the total energy in a Pierson-Moskowitz wave spectrum that is above 3 rad/s. The wave spectra was built up using 1000 component waves from 0.006 to 6 rad/s. A sea with a 0.5 meter significant wave height will have over 13% of its energy above 3 rad/s, while sea with a 5 meter significant wave height will only have 0.14% of its energy above 3 rad/s.

Table 5.3: The energy fraction in the Pierson-Moskowitz wave spectrum greater than 3 rad/s for various significant wave heights, $H_{1/3}$. The spectra were calculated from 0.006 to 6 rad/s.

$H_{1/3}$ (m)	Energy Fraction > 3 rad/s
0.5	13.41%
1.0	3.54%
2.0	0.90%
3.0	0.40%
5.0	0.14%
7.0	0.07%

4. Are there any effects of the irregular waves at frequencies well below that of the resonant peak which contribute to poor buoy performance which would *not* be predicted by the regular wave results?

This question was tested by comparing trials with two irregular wave trains. In one wave train all spectral content above a cutoff frequency is suppressed. By comparing these results we can see which effects are due to high the frequency content of the waves. The irregular wave trials 2 and 3 perform this comparison.

As in the regular wave trials, in the irregular wave trials the only differences between the trials were in the wave disturbances applied to the systems. For the irregular trials the following conditions applied:

1. The prototype buoy configuration starts in initial condition configuration 1, see Figure 5.13.
2. The SMC control law is used with the control loop running at 80 msec and a system latency of 80 msec.
3. The payload is commanded to the vertical for the first 45 seconds of the simulation, and then it is commanded to a vertical angle of 20 degrees and an azimuth angle of 150 degrees.

5.13.1 Irregular Seas Trial 1

The irregular seas applied to both systems were generated from the same spectral distribution for the Pierson-Moskowitz model with a significant height of 3 meters. The wave spectra were only calculated up to a maximum frequency of 2 rad/s. Because this is a stochastic description of the seas, the actual wave train applied to each system is different. We can see that there is little qualitative difference between the two buoy's response for two different seas generated from the same spectral density function when the payload is vertical.

The composite payload error for this trial is plotted in Figure 5.28. The irregular wave forms for each wave are plotted in Figure 5.29. The height of the buoy bodies CM's and joint are plotted with the wave elevation in Figure 5.30.

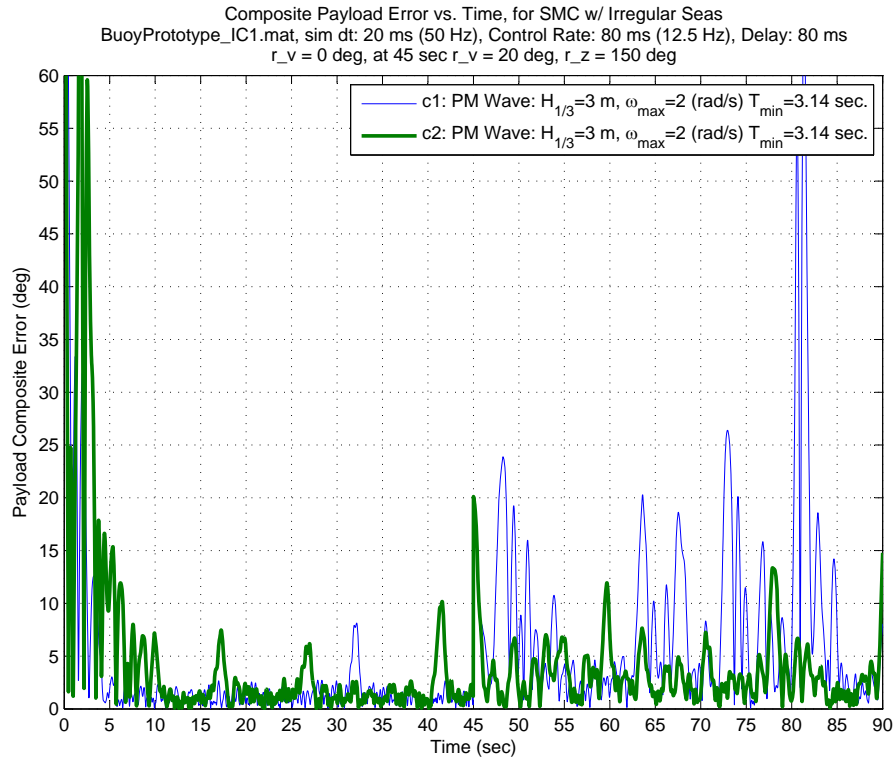


Figure 5.28: The composite payload pointing error for two trials in irregular seas. Both buoys and controllers are the same. The irregular seas applied to both systems were generated from the spectral distribution for the Pierson-Moskowitz model with a significant height of 3 meters. The wave spectra were only calculated up to a maximum frequency of 2 rad/s. Because this is a stochastic description of the seas, the actual wave train applied to each system is different. We can see that there is no qualitative difference between the c1 and c2 systems response when the payload is vertical. However, there the c2 system happens to perform noticeably better than the c1 system when the payload is commanded to a non-vertical angle.

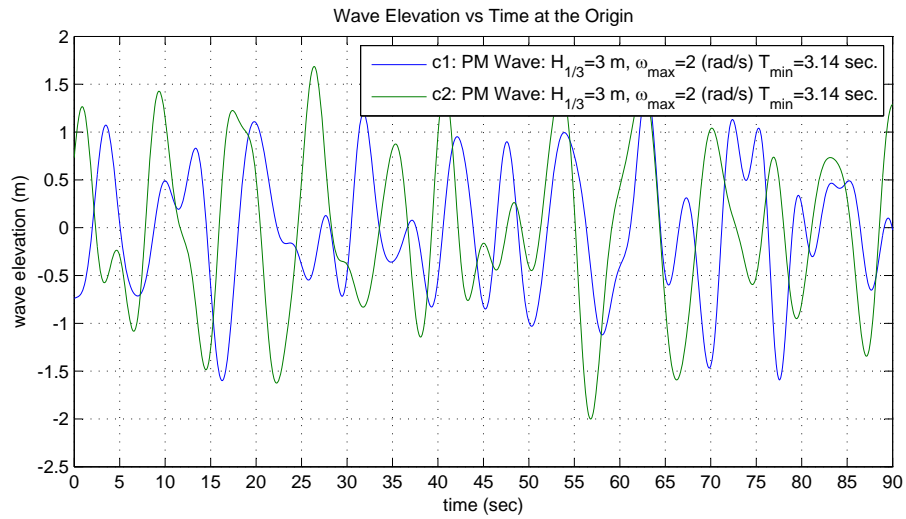


Figure 5.29: The wave elevations for the irregular seas applied to each buoy for irregular wave trial 1.

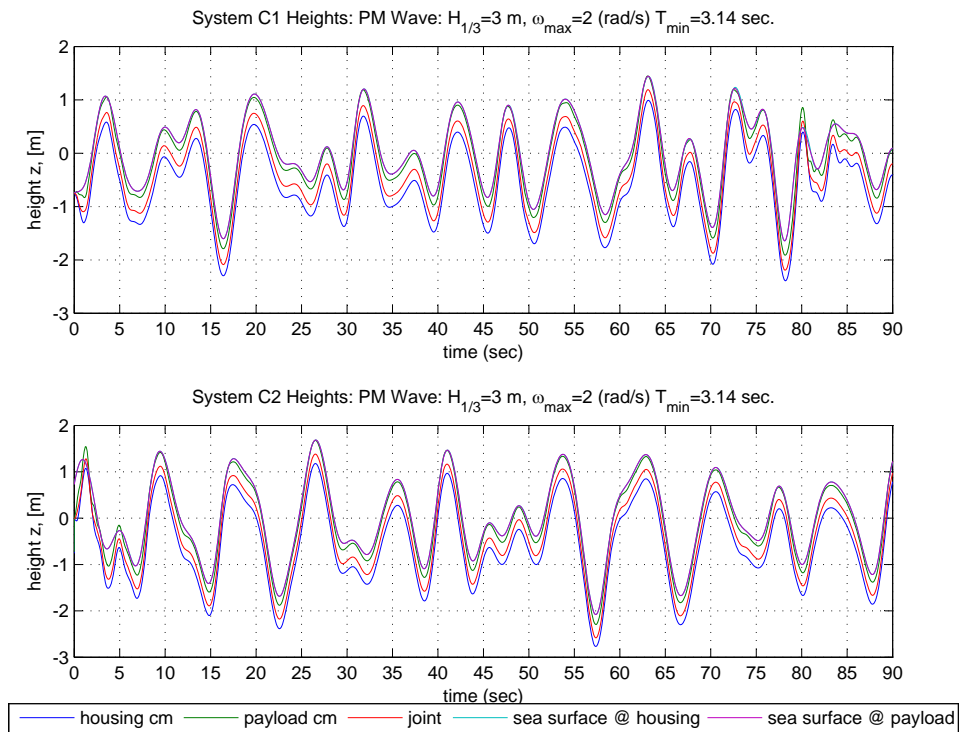


Figure 5.30: The buoy heights for the irregular seas trial 1.

5.13.2 Irregular Seas Trial 2

This trial was run to compare the effects of spectral cutoff frequency. An irregular wave was generated using the Pierson-Moskowitz spectrum with frequency component up to 6 rad/s (periods as short as 1.04 seconds). This was applied to system c1 (blue). For system c2 the same irregular wave was used except the component waves with frequencies greater than 1 rad/s (periods shorter than 6.28 seconds) were *not* included in the summation to build up the irregular wave. In this manner, two waves were generated with identical frequency content at less than 1 rad/s, while still allowing one wave to have frequency content greater than 1 rad/s.

The composite payload pointing errors of the buoy system for the two waves are plotted in Figure 5.31. Two things stand out in this plot. (1) The buoy system does an excellent job at rejecting both irregular wave trains when the payload is commanded to the vertical position. And (2) when the payload is commanded to the non-vertical angle it is the high frequency wave content that generates the abrupt failure of the pointing control.

The irregular wave forms for each wave are plotted in Figure 5.32. The height of the buoy bodies CM's and joint are plotted with the wave elevation in Figure 5.33.

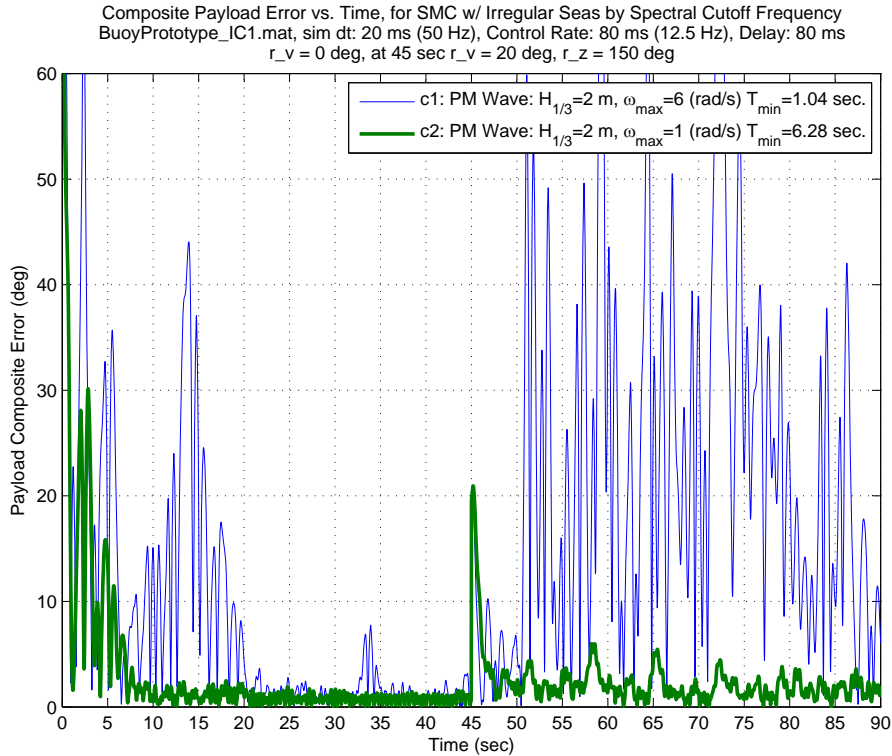


Figure 5.31: The composite payload pointing error for two trials in irregular seas. The irregular seas applied to both systems were generated from the same spectral distribution for the Pierson-Moskowitz model with a significant height of 2 meters. The spectrum used for the c1 system was calculated up to a frequency of 6 rad/s. For the c2 system the irregular wave was generated using the same component waves as the c1 system, except that component waves with a frequency greater than 1 rad/s were suppressed.

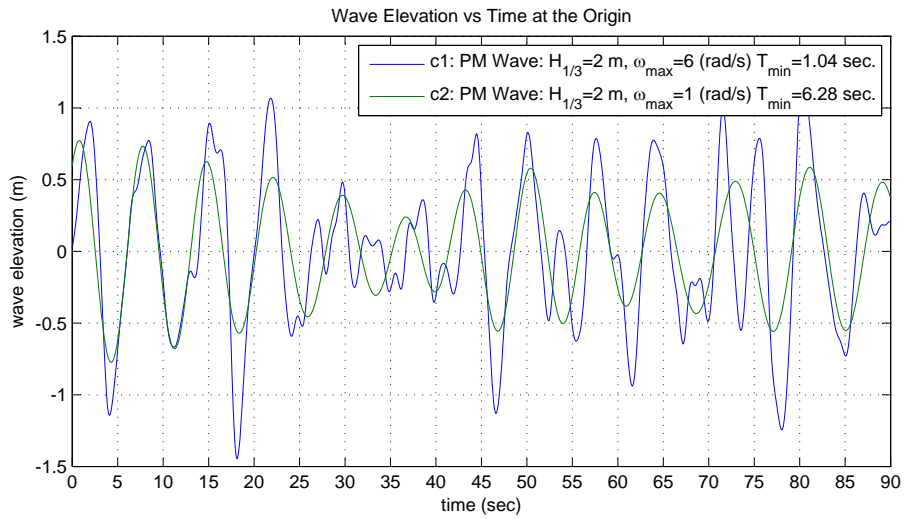


Figure 5.32: The wave elevations for the irregular seas applied to each buoy in irregular seas trial 2. The higher frequency content in the c1 wave train (blue curve) is clearly evident.

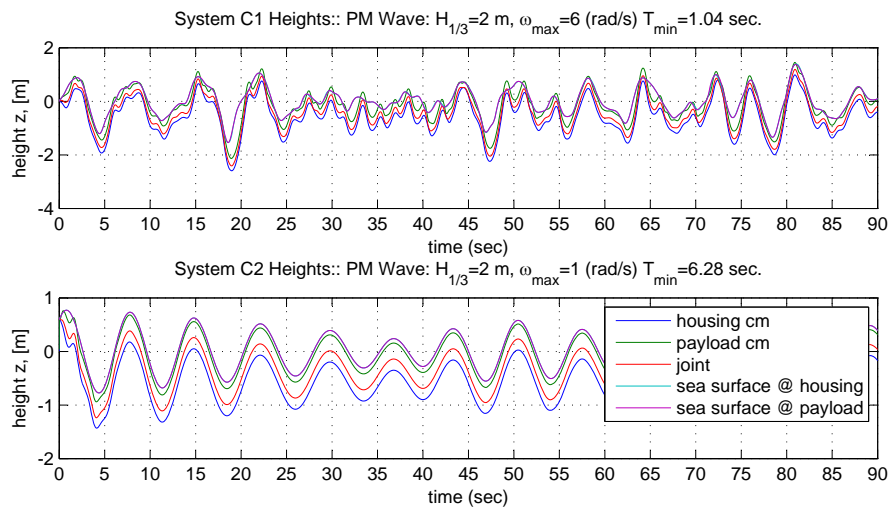


Figure 5.33: The buoy heights for the irregular seas trial 2. The higher frequency content in the c1 wave train (upper plot curve) is clearly evident.

5.13.3 Irregular Seas Trial 3

This trial is basically the same as Irregular Seas Trial 2, except that:

1. The significant wave height used to generate spectral content of the waves is 5 meters.
2. The cutoff frequencies for the waves applied to the c1 and c2 systems are 3 rad/s (periods of 2.09 seconds) and 1.5 rad/s (periods of 4.19 seconds), respectively.

As in the second irregular seas trial we see similar results. With the payload vertical the system is relatively unaffected by the high frequency wave content, but as soon as the payload is commanded to the vertical angle of 20 degrees the buoy has significant trouble maintaining the payload pointing in the proper direction. The composite payload error for this trial is plotted in Figure 5.34. The irregular wave forms for each wave are plotted in Figure 5.35. The height of the buoy body CM's and joint are plotted with the wave elevation in Figure 5.36.

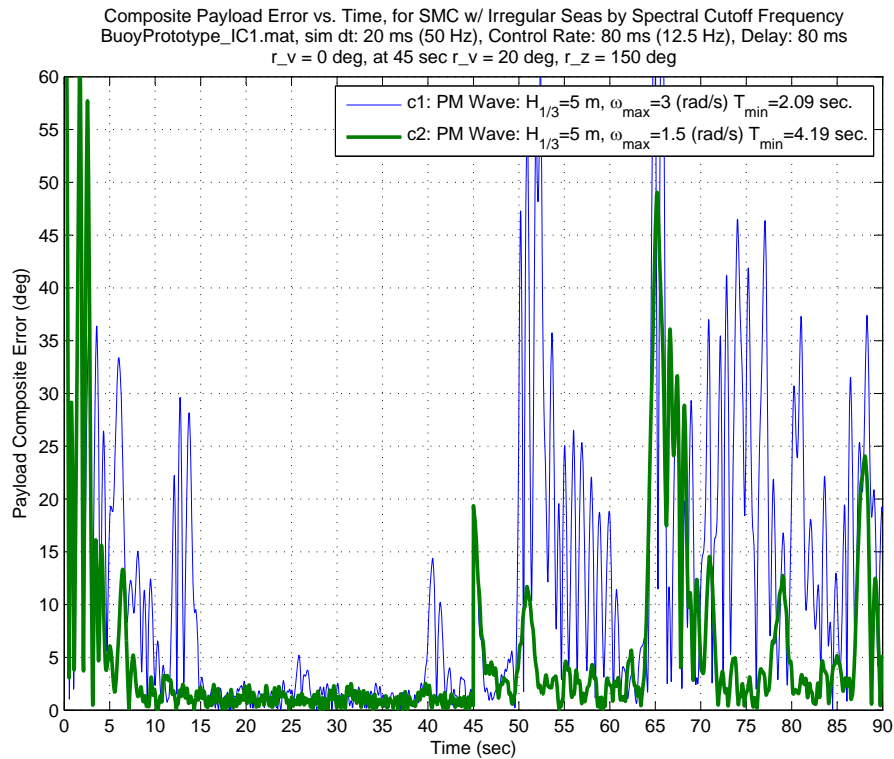


Figure 5.34: The composite payload pointing error for two trials in irregular seas.

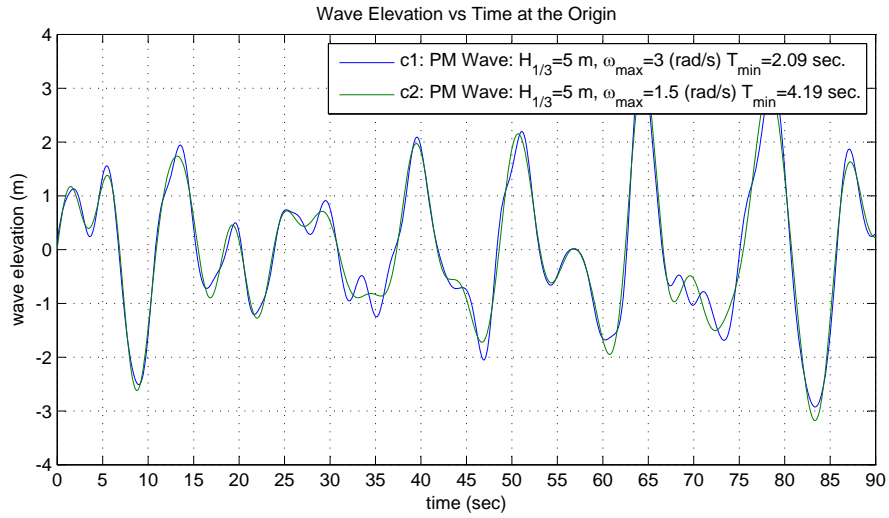


Figure 5.35: The wave elevations for the irregular seas applied to each buoy in irregular wave trial 3.

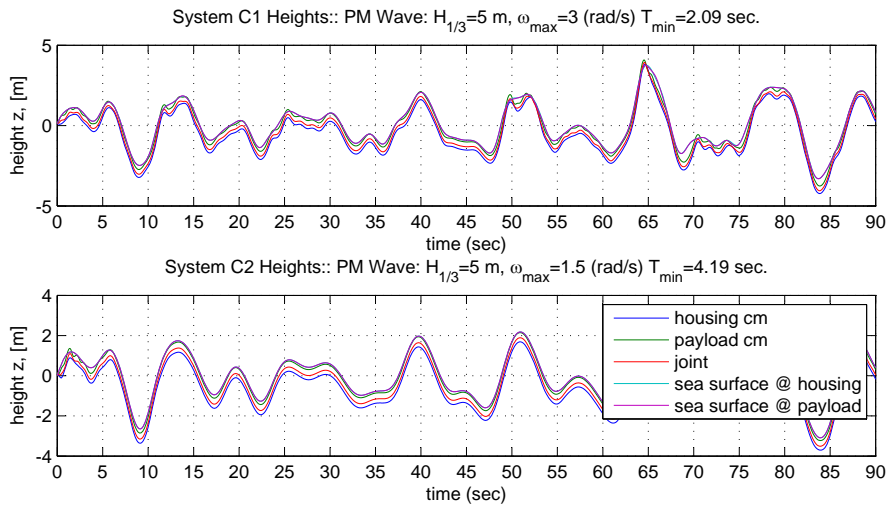


Figure 5.36: The buoy heights for the irregular seas trial 3.

5.14 Results Summary

This chapter presented a quantitative analysis of the prototype buoy configuration's performance under a variety of conditions.

For this particular configuration, on a calm surface, the following parameters all undergo an abrupt transition from acceptable performance to unacceptable performance: control rate, system latency, and maximum joint acceleration.

For the prototype configuration the passive yaw control fins only marginally improved the system's pointing performance and the active yaw damper feature did not improve the system performance. This is in contrast to the J series buoy configurations where both features noticeably improved the system performance. The use of these features needs to be determined on a case by case basis.

Both the SMC+FF and the PID+FF control laws were shown to be effective at controlling the system. When properly tuned both control laws performed equivalently well in terms of pointing performance. The PID+FF control achieved the same performance level with less joint motion than the SMC+FF control law. The SMC+FF control law was shown to be more robust to parameter uncertainty than the PID+FF law.

The resonant response of the buoy was shown to be critical parameter for the overall performance of the system in the presence of ocean waves. Due to the small size of the prototype buoy configuration, the resonant frequency is above that which is typically reported in the literature for the validity of the various standard spectral models for ocean surface waves. The results presented here for the irregular wave trials were based on the assumption that the Pierson-Moskowitz model for wave spectra is valid at frequencies greater than 1 rad/s.

The ability to accurately point and stabilize the payload deteriorated as the payload was pointed further and further away from the vertical. In a calm sea the system could not point further than about 30 degrees away from the vertical while maintaining the desired composite payload pointing error performance threshold and objective of less than 10 and 5 degrees respectively. This is likely because the joint axes are limited to a range of motion of ± 45 degrees and that the feed forward gain is for the prototype configuration is greater than one. Additionally, at these large joint angles structure is significantly asymmetric.

Chapter 6

Other Design and Modeling Issues

6.1 Perfect vs. Imperfect State Information

A standing assumption throughout all of the simulations presented is that the controller has access to perfect state information (limited only by numerical precision). Even when modeling system latency, the state information was perfect at the time of measurement. So the controller was running off of perfect but delayed state information.

This research is *not* about analyzing the performance of the navigation sensors or state estimation. By providing the results based on perfect navigation information, these results can be used as a baseline to estimate actual system performance. A designer wishing to use these result could insert a model of their particular navigation sensor into the simulation framework and then rerun the model.

Alternatively, the designer could use the simulation results to specify the maximum permitted error budget for the rest of the system. This would be accomplished by taking the difference between the required performance of the system and the performance predicted by the simulation with perfect state information. This difference gives a performance margin for the maximum allowed sensor and actuation error for static and dynamic sources in the system. Additionally, this performance margin can be compared under different simulation conditions to understand how it varies across the envelope of conditions the system could encounter.

6.2 System CM Location

One of the factors that seems to contribute to the robust performance of the prototype configuration, with either the SMC+FF or PID+FF controller, is that its system CM is located almost exactly at the joint location. The alternate buoy configuration J10 (Buoy-GroupSonoA 5x36 J10) also has a system CM very close to its joint.

We hypothesize that this improves the system response because the joint is actuating about the point that the system “wants” to rotate about. Having the CM at a significantly different location from the joint location induces more translational effects when the joint is moved. This is more disruptive to the overall system performance.

6.3 El. Over Az. Joint vs. a Universal Joint Configuration

In the early stages of this research, the joint was modeled as an “elevation over azimuth” (ELAZ) joint, as this is the type of joint configuration found on many terrestrial, airborne, and maritime antenna and camera pointing systems. As the system model and control laws were developed it soon became apparent that the ELAZ mechanism was not the best joint implementation for this application. The universal (or Hooke) joint was found to be far superior.

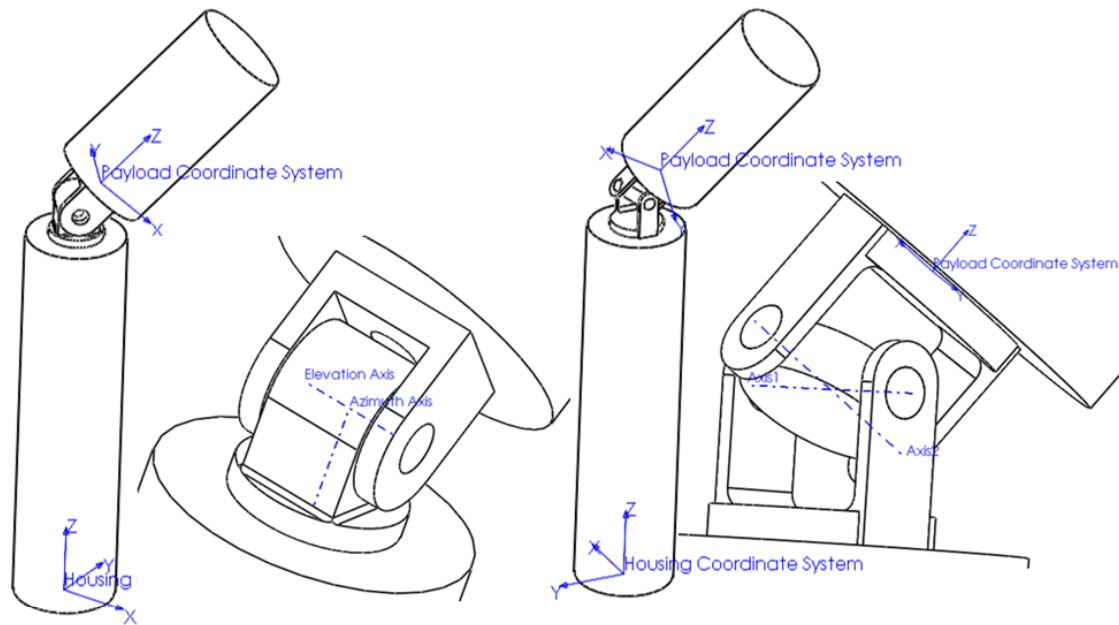


Figure 6.1: Side by side sketches of an elevation over azimuth joint implementation (left) and a universal joint implementation (right).

In this application the universal joint has a number of advantages over the ELAZ joint including:

1. In the universal joint, both joint axes can be mechanically identical and therefore cheaper to manufacture.
2. For the universal joint, continuous rotation in azimuth is possible *without* the use of electrical slip-rings. This results in a significant cost and weight savings for the design.
3. Because electrical slip-rings are not required, a much wider variety of cables can connect the housing and payload including: fully shielded electrical lines, co-axial cables, ribbon cables, fiber optic cables, and tubing (pneumatic or fluid).
4. When using a universal joint, the system dynamics are almost identical for both joint axes. This allows for the same control law to be used for both joint axes.
5. A universal joint implementation allows for disturbances in pitch and roll to be immediately and simultaneously compensated for by the joint. The ELAZ joint might be able to immediately compensate for motion in pitch and yaw, however this is inferior for two reasons:

- (a) Because of the symmetry of the buoy system it is equally susceptible to disturbances about both its roll and pitch axes. In contrast to something like a ship which is much less susceptible to pitch disturbances. If the buoy uses an ELAZ joint while it is stabilizing the payload vertically, and a disturbance is applied which is perpendicular to the joint's elevation axis, the joint will have to rotate in yaw to bring the elevation axis parallel to the axis of the disturbance (in the navigation frame) before the disturbance can begin to be rejected. Since disturbances can come from many directions simultaneously, the instantaneous axis of rotation due to the disturbances can shift very quickly from any direction to any other direction. This will likely result in system chasing the disturbance axis of rotation with the elevation axis. This is made more difficult because the system has the least control authority in yaw, which is the second problem.
 - (b) The system's control authority in yaw is potentially much less than in either roll or pitch. This is because the yaw motion of the payload is only dependent on the inertia and drag moments in the system. In contrast, shifting the payload in pitch or roll provides a restoring moment due to buoyancy that is dependent on payload *position*. Because the buoyant moments are functions of payload position, they do *not* require continuous joint acceleration or velocity to generate them.
6. With a universal joint, azimuth control is *not* simply dependent on a cylinder's acceleration (inertia) and velocity (drag) about its long axis (see item 5b above). Rather, by appropriate mixing of the roll and pitch joint axes, buoyant moments can be used to move the payload to a new yaw position.
 7. For a universal joint the azimuth control does not have to fight the "falling down hill" response to an angular disturbance perpendicular to the current pointing angle.

However, the universal joint does have two peculiarities which can limit its performance in certain applications. These are:

1. As the the universal joint moves the payload in azimuth with respect to the housing, the payload will undergo a complete revolution about its long axis for each revolution in azimuth.
2. Due to mechanical interference in the joint mechanism, universal joints are typically limited to about 45 degrees of misalignment between the sides of the joint. This is the maximum joint vertical angle in the prototype buoy configuration for *all* joint azimuth angles. There are four sectors where there the joint can achieve a greater vertical angle of $\phi_{v_{max}} = \arccos(\cos^2 \phi_{axis_{max}})$.

But both of these issues can be overcome with relatively simple means. The payload rotating about its long axis is not an issue for antenna systems that are circularly polarized, which is a common polarization for satellite and aircraft communication systems. For imaging systems an image transform can be applied to the image to correct for the roll angle.

Even if the joint is limited to a maximum angle of 45 degrees, the payload can be made to point further away from the vertical by adjusting the weight distribution in the buoy such that a given joint angle results in a larger payload moment away from vertical. This

is possible when the mass distribution is such that the feed forward gain value is less than one.

6.4 Joint Motion in SMC vs. PID Control

For the prototype buoy configuration both the SMC+FF and PID+FF controller were able to produce equivalently good payload pointing performance. However, there are differences in how they achieve this. When the payload reaches steady state with the PID+FF control, the amplitude of the joint oscillations almost immediately achieve their minimum value of about 3 degrees. In contrast to this, the SMC+FF control stabilized the payload with an initially larger amplitude of oscillations but ultimately ends up with the joint nearly at rest. Figure 6.2 compares the joint vertical angle history between the SMC+FF and PID+FF controllers for a trial. PID+FF control law results in significantly less joint oscillation when stabilizing the system. However, the SMC+FF law ultimately results in less joint motion. Also it is expected that the SMC+FF control law will have better disturbance rejection than the PID+FF control law.

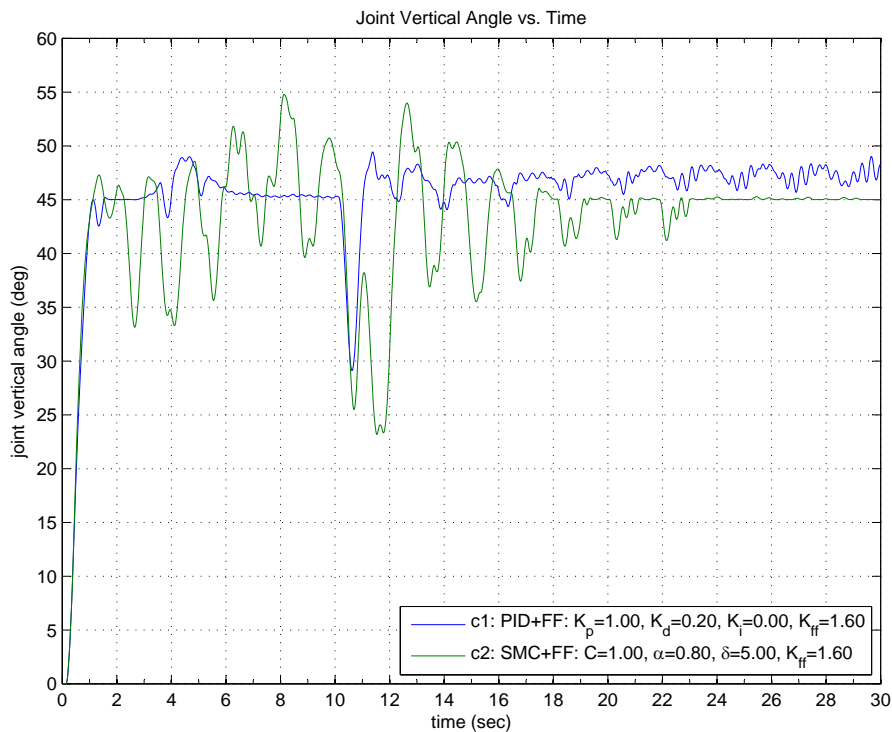


Figure 6.2: The joint vertical angle vs. time for the prototype buoy configuration released from initial condition set 1. The payload was immediately commanded to a payload vertical angle of 30 degrees. At 10 seconds the payload azimuth angle was shifted by 90 degrees. PID+FF control law results in significantly less joint oscillation when stabilizing the system. However, the SMC+FF law ultimately results in less joint motion. Also it is expected that the SMC+FF control law will have better disturbance rejection than the PID+FF control law.

6.5 Hydrodynamic (Added) Mass Effects

Hydrodynamic (added) mass effects are *not* explicitly included in the model derivation presented in Chapter 2 and added mass effects were not included any of the numerical simulations.

White in [32, p. 488] provides the following introduction to hydrodynamic mass:

When a body moves through a fluid, it must push a finite amount of fluid out of the way. If the body is accelerated, the surrounding fluid must also be accelerated. The body behaves as if it were heavier by an amount called the hydrodynamic mass (or added mass) of the fluid. . . . [The] hydrodynamic mass is a function of body shape, the direction of motion, and (to a lesser extent) flow parameters such as the Reynolds number.

Fossen in [9, Sec. 2.4.1] provides a more complete and cautionary introduction to hydrodynamic mass of:

The concept of added mass is usually misunderstood to be a finite amount of water connected to the vehicle such that the vehicle and the fluid represent a new system with mass larger than the original system. This is *not* [emphasis in the original] true since the vehicle motion will force the fluid to oscillate with different fluid particle amplitudes in phase with the forced harmonic motion of the vehicle. . . . Added (virtual) mass should be understood as pressure-induced forces and moments due to a forced harmonic motion of the body which are proportional to the acceleration of the body. Consequently, the added mass forces and acceleration will be 180 degrees out of phase to the forced harmonic motion.

To include the added mass effects, the model has to be adjusted to incorporate the added mass terms and the added mass terms themselves need to be calculated as functions of the system states.

6.5.1 Adjusting the Dynamics Model

Adjusting the dynamics model derived in Chapter 2 to include added mass effects requires making the following approximations:

1. The added mass terms for the current time step are calculated based on the state information from the previous time step.
2. The location of the bodies' and system's CM in body coordinates, as calculated by (2.27) and (2.28), do *not* include the effects of added mass.

Note that “added mass terms” can be elements with units of mass (i.e. kg) or inertia (i.e. kgm^2) depending on whether they are influencing the translational or rotational dynamics.

The above quotation by White suggests the typical method used to implement added mass effects, i.e. the mass of the object is increased.

Consider the translational dynamics first. The mass in the translational acceleration equation, (2.44), is a scalar term. So simply increasing it would apply the same added mass effect in all directions of motion. This is problematic because added mass is a function of direction of motion and body shape. This requires that the mass term can no longer be a

scalar, but must be a tensor. Defining a mass tensor which includes both the body's mass and the directionally dependent added mass terms gives

$$\mathbf{m}_i = \begin{bmatrix} m_i + m'_{i_{xx}} & 0 & 0 \\ 0 & m_i + m'_{i_{yy}} & 0 \\ 0 & 0 & m_i + m'_{i_{zz}} \end{bmatrix}. \quad (6.1)$$

Here we designate the added mass terms as $m'_{i_{jj}}$ where $i = 1$ for the housing, $i = 2$ for the payload, and $j = x, y, z$ specifies the direction which the added mass term is valid for. In general, the mass tensor's off diagonal terms may be non-zero as well [9, Remark 2, p. 35].

Once the mass tensor for each body is known, the scalar mass terms, m_1 and m_2 , in (2.44) can be replaced by their mass tensors and the calculation proceeds as before.

Similarly, for the rotational dynamics an added mass inertia tensor can be defined for each body as

$$\mathbf{J}'_i = \begin{bmatrix} J'_{i_{xx}} & 0 & 0 \\ 0 & J'_{i_{yy}} & 0 \\ 0 & 0 & J'_{i_{zz}} \end{bmatrix}, \quad (6.2)$$

where the terms $J'_{i_{jj}}$ are the inertia values about the various axes. In general, the added mass inertia tensor will not be diagonal. However, for a submerged body with 3 planes of symmetry it is [9, (2.129)].

This added mass inertia tensor is added to the inertia tensors \mathbf{J}_h and \mathbf{J}_p in (2.31) and (2.33). Also, the scalar mass values in (2.31) and (2.33) should be replaced by the mass tensor calculated in (6.1) to include the translational added mass effects in the rotational dynamics.

A simulation framework based around a solution of constraint equations would handle the added mass effects on each body in a much more elegant manner and not require the assumption about body CM locations being independent of added mass. See Appendix D a discussion about solving multi-body systems using constraint equations.

6.5.2 Calculating the Added Mass Terms

The added mass of a submerged cylinder for translation perpendicular to its axis of revolution, $m'_{i_{xx}}$ and $m'_{i_{yy}}$, is equal to its displaced mass [32, (8.104)]. For motion parallel to its axis of revolution, $m'_{i_{zz}}$, the added mass can be approximated by the mass of a sphere of water with the same diameter as the cylinder¹.

A common method of finding the added mass terms for three dimensional bodies is to use *strip theory*. The three dimensional object is divided into two dimensional slices, or *strips*, along an axis. Typically this axis is the longitudinal axis of symmetry. Tabulated added mass values are available for various 2-D shapes. The total added mass for the 3-D object is found by summing the added mass values for each 2-D slice. The tabulated values for the 2-D slides are *only for motion in the plane of the slice*. This means that finding the added mass for a 3-D object using strip theory will *only provide the added mass terms for translation perpendicular to, and rotation about, the axis normal to the slices*. An illustration of this is shown in Figure 6.3.

The added mass terms for various 2-D shapes are presented in Table 6.1 and is based on [9, Table 2.2]² and [19, Table 4.3].

¹This can be shown by treating the end of the buoy as a flat plate and using strip theory.

²Table 2.2 in [9] has an error in the J'_{zz} for the square slice. Additionally, it states that the J'_{zz} for the cylinder with fins is unknown. Newman in [19] has correct values for both.

Both Faltinsen [8] and Fossen [9] discuss the frequency dependence of the added mass terms, which is not considered here.

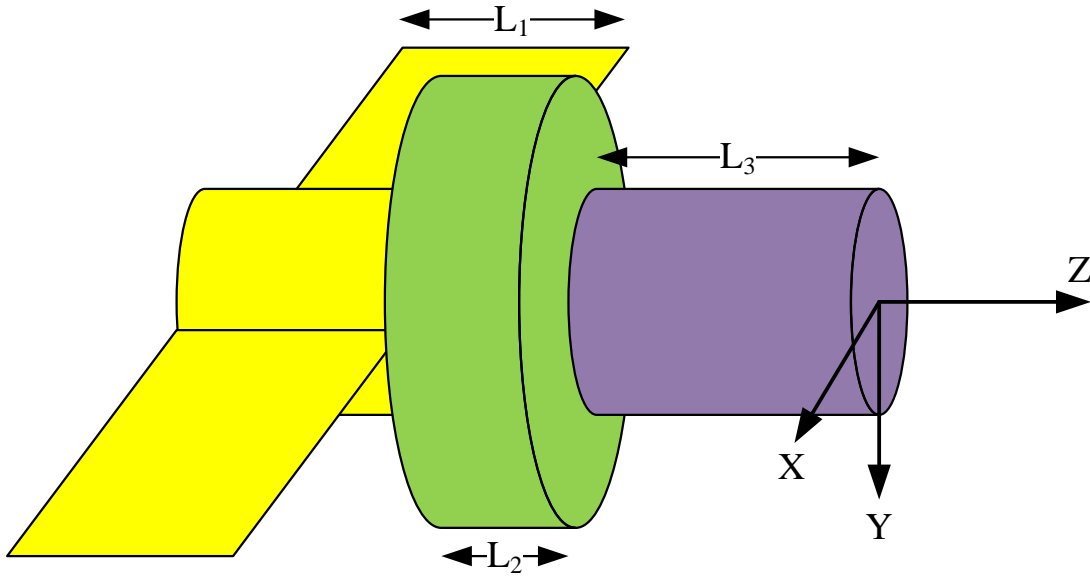


Figure 6.3: When using strip theory to calculate the added mass for a 3-D object, the 3-D object is divided into a series of 2-D slices, or strips, along an axis. The overall 3-D added mass terms are found by summing the added mass terms for each 2-D slice. This technique only provides the added mass terms for motion perpendicular to and about the axis. In this example the shape is divided into 3 slices along its Z axis. Added mass terms for each section can be found by the product of the slice’s length and the appropriate entry from Table 6.1.

6.5.3 The Effects of Added Mass On the Buoy System

Hydrodynamic mass could affect our buoy system in several ways. For each of these ways, it can be argued that including the added mass in the model will have minimal effect on the system or make the system easier to control.

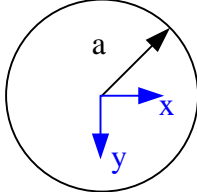
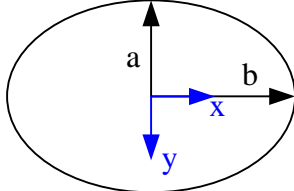
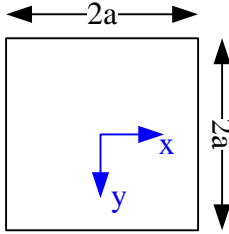
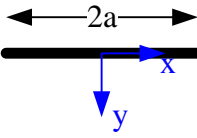
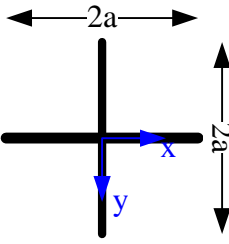
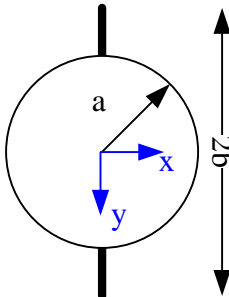
1. The added mass could lower the resonant frequency of vertical oscillation for the buoy. This may make the buoy more difficult to control because there is more wave energy at lower frequencies.

Assuming that the added mass due to the buoy’s vertical translation is the mass of water displaced by a sphere with the same radius as the buoy, the mass increase of the prototype buoy configuration is 0.258 kg (10.1%) and the mass increase of the large test cylinder is 2.22 kg (12.3%).

Without added mass effects, the predicted and measured period of oscillation for the large test cylinder agreed within 1.1% (see Section 3.3). If the added mass of 2.23 kg was included in the estimate for the period of oscillation (2.110), the estimated period of the large test cylinder would be in error by 7.0%.

Similarly, in the numerical simulations, the “measured” period of oscillation matched the predicted period of oscillation from Section 5.11 within 1%. However, including

Table 6.1: Added mass terms for various 2-D shapes from [9, Table 2.2] and [19, Table 4.3]. All values are per unit length in the z direction.

$m'_{xx} = \pi\rho a^2$ $m'_{yy} = \pi\rho a^2$ $J'_{zz} = 0$	
$m'_{xx} = \pi\rho a^2$ $m'_{yy} = \pi\rho b^2$ $J'_{zz} = \frac{1}{8}\pi\rho(b^2 - a^2)^2$	
$m'_{xx} = 4.75\rho a^2$ $m'_{yy} = 4.75\rho a^2$ $J'_{zz} = 0.725\rho a^4$	
$m'_{xx} = 0$ $m'_{yy} = \pi\rho a^2$ $J'_{zz} = \frac{1}{8}\pi\rho a^4$	
$m'_{xx} = \pi\rho a^2$ $m'_{yy} = \pi\rho a^2$ $J'_{zz} = \frac{2}{\pi}\rho a^4$	
$m'_{xx} = \pi\rho[a^2 + (b^2 - a^2)/b^2]$ $m'_{yy} = \pi\rho a^2$ $J'_{zz} = *$	
<p>* = $\rho a^4[\pi^{-1}\csc^4\alpha[2a^2 - \alpha\sin 4\alpha + \frac{1}{2}\sin^2 2\alpha] - \pi/2)$, where $\alpha = \frac{2ab}{a^2+b^2}$ and $\pi/2 < \alpha < \pi$.</p>	

the added mass in an estimate of the prototype buoy's period of oscillation would cause the estimate and simulated performance to disagree by 4.8%.

For both cases, the added mass effects do not seem to be significant with respect to the vertical oscillation of the buoy. So neglecting them with respect to this the vertical oscillation of the buoy seems reasonable.

2. The added mass could slow the horizontal translation of the buoy system. In our application we are not particularly concerned with the horizontal translation of the system, so this effect is likely to not be a concern.
3. The added mass due to the passive yaw fins could add significant inertia to the housing about its long axis due to their radial distance from the z axis. However, this increased inertia should give the system a more stable "base" and therefore more control authority in yaw. This should make the system easier to control. So neglecting added mass here may make our results more conservative.
4. The added mass about the roll and pitch axes of the payload and housing might be approximately equal if the submerged volumes of the housing and payload are similar in magnitude. The overall effect of this will likely be to just require more actuator torque to move the housing with respect to the payload.

Chapter 7

Conclusions & Future Work

7.1 Conclusion

In Chapter 2 we developed a dynamic and kinematic model for a jointed two body cylindrical buoy floating on the surface of the water. The only forces and moments applied to the buoy were those of buoyancy, gravity, and drag. Using an actuated universal joint as the actuator between the buoy bodies was found to have a number of advantages. The modeling of the drag forces and moments required making significant approximations. These approximations were informed and validated by a series of experiments which were presented in Chapter 3.

The model developed here included the effects of surface waves at a scale appropriate to the small size of the buoys envisioned. The model did not use approximations which are common (and appropriate) for modeling the interactions between waves and large ocean structures. Additionally, this model avoided the assumption that the payload's mass and inertia are negligible compared with the overall mass and inertia of the buoy.

By building up a validated non-linear model in numerical simulation, both sliding mode and PID control strategies were investigated and presented in Chapter 4. The numerical simulation also allowed an investigation of the passive characteristics of the structure in addition to the active characteristics of the controller.

The simulation results indicate that it should be possible, depending on sea state, to mechanically point a payload within about 5 degrees of an arbitrary point in the sky from a small cylindrical buoy that is articulated near the middle. The universal joint is the preferred mechanical implementation of the joint connecting the two sections of the buoy. This joint allows for immediate control authority about the buoy's pitch and roll axes. Additionally, by taking advantage of the joint's kinematic properties it is possible to exert significant yaw control when the payload and housing are not co-linear.

When the payload is stabilized about the vertical, the system is *significantly* more robust against the effects of external disturbances (including disturbances at its resonant frequency), initial conditions, system latency, control loop speed, and gain settings. Applications which only require a vertical payload can benefit significantly from this work.

For the buoy configurations tested in simulation, the payload can be stabilized up to about 35 degrees away from the vertical, with accuracy and disturbance rejection performance getting worse the farther the payload is away from the vertical.

Both a sliding mode control law with feed forward (SMC+FF) and a proportional integral and derivative control law with feed forward (PID+FF) seem to be able to control

the payload well. The feed forward term is an important part of the control law as it is responsible for the coarse positioning of the payload. This coarse positioning allows the SMC or PID elements of the control law to handle the only disturbance rejection needs of the system. The feed forward gain value is a plant specific piece of information, i.e. its value can be found by calculation rather than tuning.

This buoy system has significant coupling among the three rotational axes. Fundamentally, a control law for the buoy system can either: (a) try to model and predict the coupling between the axes and control both axes in a coordinated manner, or (b) treat each axis as independent and the coupling from the other axis as an external disturbance to be rejected. The latter approach is the one that was selected here because it results in a simpler control law and requires fewer assumptions about the plant model.

The passive yaw fins provided a slight improvement for the prototype buoy configuration considered, and the active yaw damper provided no benefit to the prototype buoy configuration. However, with different buoy configurations the active yaw damper was observed to provide a significant benefit.

The SMC+FF control law was fairly tolerant of system latency effects. There was not significance performance degradation until the total system latency was in excess of 120 milliseconds. In the simulations the system's performance was relatively insensitive to control rate down to control rates as slow as 5 Hz. If one makes the assumption that resonant frequency of the system is the time scale for the mechanical dynamics, then a 5 Hz control rate corresponds to a control rate that is 10 times faster than the mechanical dynamics. This seems like a reasonable thumb rule for the *minimum* control rate that should be considered.

Related to the control rate and system latency effects are the effects of actuator acceleration. The acceleration is proportional to the amount of torque or electrical current required of the actuator. As with the system latency and control rate effects, there was a relatively sharp transition between the system providing equally acceptable performance above a certain actuator acceleration threshold, and poor performance below it.

Actuator chatter, which is always a concern with sliding mode control, was reduced using three methods:

1. Implementing a linearized saturation function to create a small boundary layer about the sliding surface.
2. The presence of the feed forward term in the control laws.
3. The low level actuator controller (i.e. the hardware controller) acts a low pass filter to smooth the rapidly changing commanded position values resulting from the control law.

The experiments performed to validate the numerical model indicate that:

1. It is reasonable to model the translational drag forces as being linearly dependent on velocity and the rotational drag moments as being quadratically dependent on velocity.
2. Significant coupling between axes can be introduced by having the center of mass only slightly off the central longitudinal axis of the buoy.

3. A cylindrical buoy has a narrow but strong resonant peak for vertical oscillation. The frequency of this resonant peak can be accurately predicted from its radius and mass.

The buoy system's simulated performance in regular and irregular seas was mixed. If there was significant wave energy with a period of approximately 2.0 seconds, the buoy was uncontrollable. This was not a function of the control law, but rather of the passive characteristics of the buoy's structure. Here again, keeping the payload closer to the vertical significantly improved the system's performance.

7.2 Future Work

The most obvious next step is to build the prototype buoy and experimentally test the proposed SMC+FF and PID+FF control laws, first in a wave tank, and then at sea. Indeed, the prototype buoy configuration was designed for such a program, and a complete mechanical (and electrical) design exists. The major unknown is the actual effect that sea state will have on the payload pointing performance. The small and large wave tank tests conducted on the large test cylinder at the United States Naval Academy Hydrodynamics Laboratory suggested that small buoys would not be much affected by large long period swells, but they would be affected by short-period disturbances. The small structures envisioned for this work are highly susceptible to the high frequency, $\omega > 2rad/s$, spectral content of the ocean waves. This spectral content is not well characterized by common models presented in the literature. Therefore a program to characterize this high frequency content would be beneficial in tuning these structures for the best possible passive response. The results of this proposed experimental testing could then be incorporated into further design iterations, as well as improvements to the simulation model.

A different direction for future work involves the form of the buoy system itself. One of the lessons of a practical mechanical system controller design, as in our two-body buoy problem, is the essential coupling between mechanical design and controller design. Although we imposed certain constraints on the two-body buoy system in order to bound the problem, the original payload pointing problem did not require these constraints. Therefore, one could consider alternative structures and configurations to generate a stable platform for pointing a sensor from. These alternative configurations might include the use of passive structures or inflatable/unfolding structures. These structures could be deflated/folded up for their storage and launch, and then inflate/unfold to provide better passive stability while in operation. In particular the size and placement of fins on the buoy to provide good passive damping while improving the control authority due to the drag and inertial effects could benefit significantly from optimization.

In addition, alternative actuation schemes could be considered. Although we focused only on actuation of a universal joint, one could instead consider a pair of thrusters on the bottom of the buoy, some flapping fins, or a flexible structure actuated by tendon-like cables.

Naturally, any choice of morphology and actuation will have consequences for feedback control. In fact, as mechanical fabrication and actuator technology improve, for a growing class of applications (of which our buoy payload pointing application is just one example) the feedback controller is what will consume most of the design effort. Therefore, viewing the mechanical and controller design problems on an equal footing (rather than fixing a particular mechanical configuration and then designing a controller for it) is quite sensible.

One of the key features from the controller standpoint of our two-body buoy system was the decomposition of a coupled control problem (for the two universal joint axes) into a pair of decoupled problems, in which cross-coupling between axes was treated as a disturbance (and suppressed by an appropriately designed sliding mode controller on each axis). This is a natural idea which should generalize to other types of mechanical systems possessing multiple actuated degrees of freedom with some level of coupling among them. Of course, as the cautionary example in Appendix ?? illustrates, an essential part of the controller design involves performing the requisite analysis to ensure that the model error and disturbance rejection property holds.

Bibliography

- [1] Application note: Position regulation with feed forward. *Maxon EPOS Documentation*, 2008.
- [2] J. Ormondroyd and J. P. Den Hartog. The theory of the dynamic vibration absorber. *Transactions of the ASME*, 50:9–22, 1928.
- [3] W. T. Thomson and M. D. Dahleh. *Theory of Vibration with Applications*. Prentice Hall, Upper Saddle River, NJ, 1998.
- [4] R. C. Dorf and R. H. Bishop. *Modern Control Systems, 7th Edition*. Addison-Wesley Publishing Company, New York, 1995.
- [5] E. Briguglio. Antenna stabilizing buoy. *U.S. Statutory Invention Registration No. H1051*, May 1992.
- [6] K. Doherty D. Frye and A. Hinton. Design and evaluation of a directional antenna for ocean buoys. Technical Report WHOI-97-16, Woods Hole Oceanographic Institute, Woods Hole, MA.
- [7] B. Drazenovic. The invariance conditions in variable structure systems. *Automatica*, 5(3):287 – 295, 1969.
- [8] O. M. Faltinsen. *Sea Loads on Ships and Offshore Structures*. Cambridge University Press, Cambridge, UK, 1990.
- [9] T. I. Fossen. *Guidance and Control of Ocean Vehicles*. John Wiley and Sons, New York, 1994.
- [10] H. Frahm. Device for damped vibration of bodies. *U.S. Patent No. 989958*, 1909.
- [11] B. Friedland. *Control System Design*. McGraw-Hill Inc., New York, 1986.
- [12] N. Friedmann. *The Naval Institute Guide to World Naval Weapon Systems 1997-1998*. Naval Institute Press, Annapolis, MD, 1997.
- [13] K. D. Young, V. I. Utkin, and U. Ozguner. A control engineer’s guide to sliding mode control. *IEEE Transaction on Control Systems Technology*, 7:328–342, 1999.
- [14] H. K. Khalil. *Non Linear Systems, 3rd Edition*. Prentice Hall, Upper Saddle River, NJ, 2002.
- [15] S. Krenk. Frequency analysis of the tuned mass damper. *Transactions of the ASME*, 72:936–942, 2005.

- [16] N. E. Leonard. Periodic forcing, dynamics and control of underactuated spacecraft and underwater vehicles. *Proceedings of the 34 Conference on Decision and Control*, 34:3980–3985, 1995.
- [17] N.E. Leonard. Control synthesis and adaptation for an underactuated autonomous underwater vehicle. *Oceanic Engineering, IEEE Journal of*, 20(3):211–220, jul 1995.
- [18] L. Meirovitch. *Fundamentals of Vibrations*. McGraw-Hill, New York, NY, 2001.
- [19] J. N. Newman. *Marine Hydrodynamics*. MIT Press, Cambridge, MA, 1977.
- [20] P. E. Nikravesh. *Computer-Aided Analysis of Mechanical Systems*. Prentice Hall, Englewood Cliffs, NJ, 1988.
- [21] K. Ogata. *Discrete-Time Control Systems 2nd Edition*. Prentice Hall, Upper Saddle River, NJ, 1994.
- [22] R. S. Cortesi, K. S. Galloway, and E. W. Justh. A biologically inspired approach to modeling unmanned vehicle teams. *Proc. SPIE*, 6964:696405, 2008.
- [23] M. Romano and B. N. Agrawal. Attitude dynamics/control of dual-body spacecraft with variable-speed control moment gyros. *Journal of Guidance, Control, and Dynamics*, 27(4):513–525, 2004.
- [24] S. W. Smith. *The Scientist and Engineers Guide to DSP*. California Technical Publishing, CA, 1997.
- [25] K.E. Steele and M.D. Earle. Directional ocean wave spectra using buoy azimuth, pitch, and roll derived from magnetic field components. *Oceanic Engineering, IEEE Journal of*, 16(4):427–433, oct 1991.
- [26] B. L. Stevens and F. L. Lewis. *Aircraft Control and Simulation, 2nd ed.* John Wiley and Sons, Inc., Hoboken, NJ, 2003.
- [27] L. K. Timothy. Method and apparatus for an improved antenna tracking system mounted on an unstable platform. *U.S. Patent No. 6433736B1*, August 2002.
- [28] H.C. Tseng and D.W. Teo. Ship-mounted satellite tracking antenna with fuzzy logic control. *Aerospace and Electronic Systems, IEEE Transactions on*, 34(2):639–645, apr 1998.
- [29] V. I. Utkin. *Sliding Mode Control in Electromechanical Systems, 2nd Edition*. CRC Press, New York, 2009.
- [30] N. Violante-Carvalho, F.J. Ocampo-Torres, and I.S. Robinson. Buoy observations of the influence of swell on wind waves in the open ocean. *Applied Ocean Research*, 26(12):49–60, 2004.
- [31] L.-S. Wang and P.S. Krishnaprasad. A multibody analog of the dual-spin problem. In *Decision and Control, 1990., Proceedings of the 29th IEEE Conference on*, pages 1294–1299 vol.3, dec 1990.
- [32] F. M. White. *Fluid Mechanics 3rd Edition*. McGraw-Hill Inc, New York, NY, 1994.

- [33] P. C. Young and J. C. Willems. An approach to the linear multivariable servomechanism problem. *International Journal of Control*, 15:961–979, 1972.

Appendix A

Modeling Ocean Waves

This section presents a much abbreviated presentation of mechanisms for describing ocean waves. Faltinsen [8, Ch. 2] and Fossen [9, Ch. 2] are the primary references used. By assuming that sea water is incompressible and inviscid, the fluid motion is irrotational, and the ocean has a flat bottom and a free surface of infinite horizontal extent, a linear wave theory (sometimes called Airy Theory) can be developed [8, pp. 13-17]. Linear wave theory allows for straightforward description of ocean waves. Here we will only use a first order model. This is consistent with much of the work in the literature. The first order model captures the oscillatory nature of the problem. Higher order models are also presented in the literature [9, (3.14)]. However, the second order terms in these models represent the wave drift forces [9, Sec. 3.2] which are less relevant to our buoy stabilization and tracking problem.

A.1 Regular Waves

A.1.1 The Wave Elevation

One of the simplest descriptions of an ocean wave is that of the regular sinusoidal wave, propagating in a single direction, in “infinite” water depth, according to linear wave theory. The wave is fully described by its amplitude, A , its circular frequency, ω , and its wave number, k . Faltinsen in [8, Table 2.1] summarizes the various properties of regular waves for finite and infinite water depth.

Faltinsen gives the wave elevation (wave profile) as

$$\zeta(\chi, t) = A \sin(\omega t - k\chi), \quad (\text{A.1})$$

where χ is the distance in the direction of the wave’s propagation, and ζ is the height of the water’s surface with respect to its mean height.

The *dispersion relationship* relates the wave number, k , and circular frequency, ω . For “infinite” water depth this relationship is given in [9] and [8, (2.18)] as

$$k = \omega^2/g. \quad (\text{A.2})$$

If the waves are propagating across a two dimensional plane, the distance in the direction of propagation can be calculated from

$$\chi = x \cos \beta + y \sin \beta, \quad (\text{A.3})$$

where x and y are the horizontal coordinates in the plane, and β is the direction of wave propagation (direction of seas) referenced to the plane's x axis. This relationship is illustrated in Figure A.1.

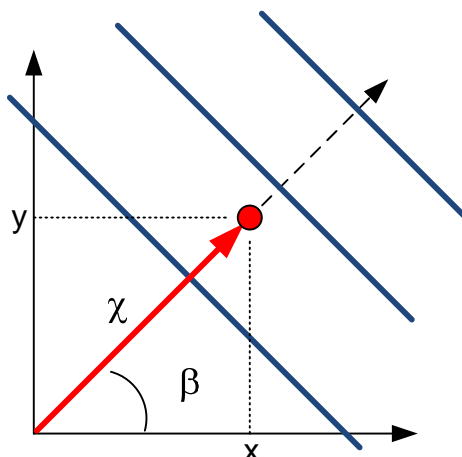


Figure A.1: The seas are propagating in the direction β . To find the distance in the direction of propagation, χ , for point in the x - y plane, one performs the coordinate transformation of rotating the coordinate system through angle β about the z -axis.

This results in an equation for the wave elevation of

$$\zeta(x, y, t) = A \sin [\omega t - k(x \cos \beta + y \sin \beta)]. \quad (\text{A.4})$$

A.1.2 Fluid Velocity Due to Wave Action

Fluid particles near the water's surface will undergo an oscillatory motion in the vertical and horizontal directions due to the wave action. Faltinsen [8, Table 2.1] states the equations for the velocity and acceleration of the fluid particles due to the wave action as:

$$v_\chi = \omega A e^{kz} \sin(\omega t - k\chi), \quad v_z = \omega A e^{kz} \cos(\omega t - k\chi), \quad (\text{A.5})$$

$$a_\chi = \omega^2 A e^{kz} \cos(\omega t - k\chi), \quad a_z = -\omega^2 A e^{kz} \sin(\omega t - k\chi), \quad (\text{A.6})$$

where v_χ and a_χ are the velocity and acceleration in the direction of propagation, and v_z and a_z are the velocity and acceleration in the vertical direction. z is the distance from the mean surface height ($z = 0$), positive upwards, in the navigation frame. A qualitative presentation of the phase relationships between (A.1), (A.5), and (A.6) is depicted in Figure A.2.

It is worth noting the depth dependence in (A.5) and (A.6). When $z = \zeta(\chi, t)$, (A.5) and (A.6) give the velocity and acceleration of the fluid particles at the surface. Additionally, because of the exponential term in (A.5) and (A.6), particles that are significantly below the mean height of the surface, $z \ll 0$, will have negligible velocity and acceleration. This is expected, because far away from the surface, wave action has no effect on the fluid.

If the waves are propagating across a 2-D plane, the fluid velocity at a point can be found by substituting (A.3) into (A.5). Additionally, since the horizontal fluid velocity in (A.5) specifies the fluid velocity in the direction of propagation, it is desirable to convert the velocity vector into the navigation frame's x and y directions. With these points in

mind, we can express the velocity of the fluid particles due to wave action in the navigation frame's coordinate system as:

$$\mathbf{v}_{fluid}(x, y, z, t) = \omega A_e^{kz} \begin{bmatrix} \sin [\omega t - k(x \cos \beta + y \sin \beta)] \cos \beta \\ \sin [\omega t - k(x \cos \beta + y \sin \beta)] \sin \beta \\ \cos [\omega t - k(x \cos \beta + y \sin \beta)] \end{bmatrix}. \quad (\text{A.7})$$

A fluid particle driven by the velocity specified by (A.7) will oscillate in both the horizontal and vertical directions. Its net motion will be in the direction of wave propagation as shown by [8, Figure 2.4]. The trajectory of a fluid particle on the water's surface in the presence of a 5 meter wave is illustrated in Figure A.3.

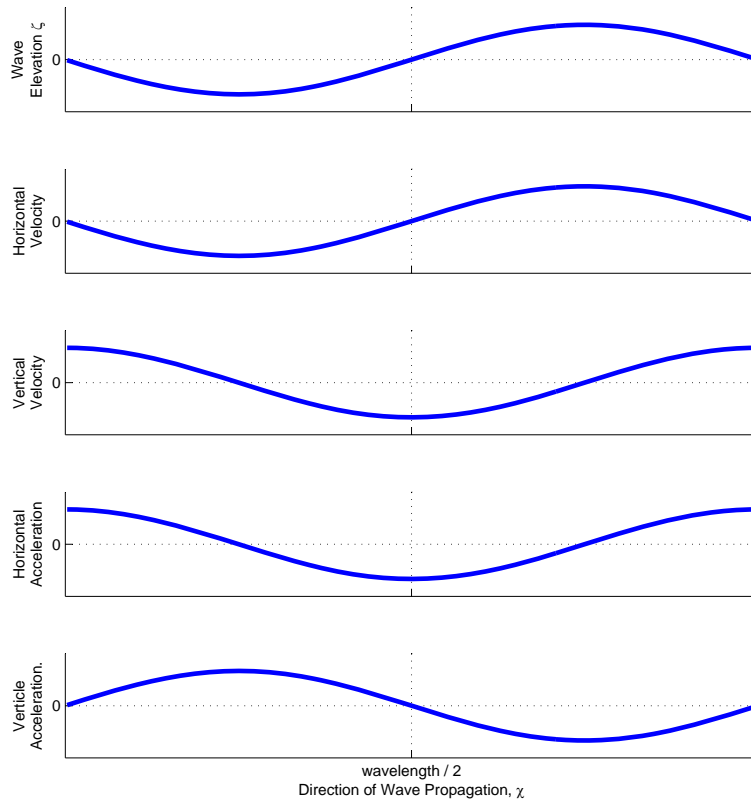


Figure A.2: A graphical depiction of the relationship between wave height, fluid particle's velocity, and the fluid particle's acceleration in the horizontal and vertical directions according to linear theory [8, Figure 2.1].

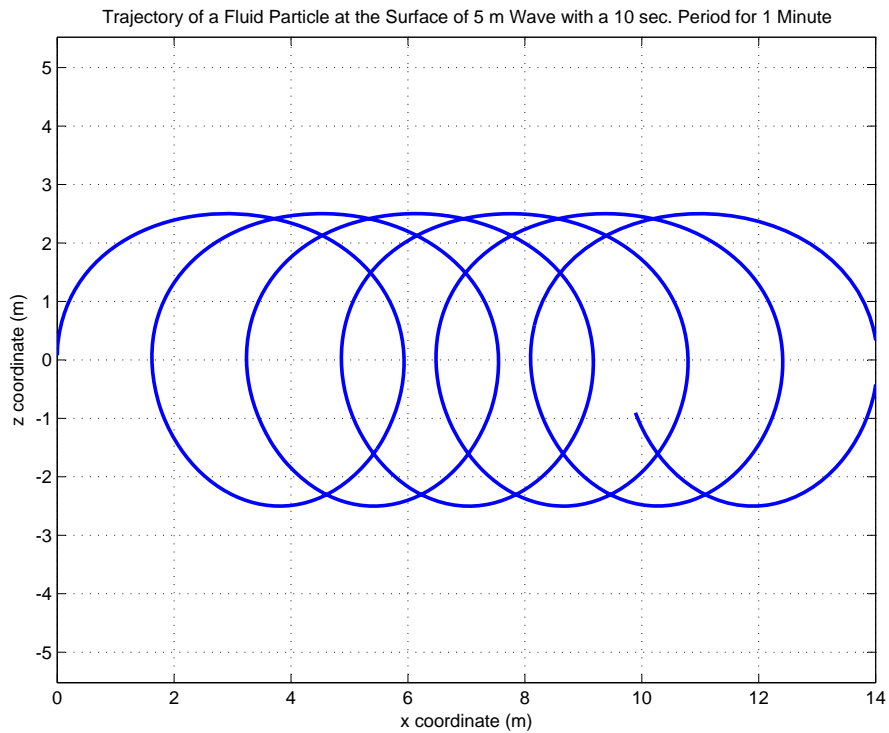


Figure A.3: The trajectory of a fluid particle on the water's surface in the presence of a 5 meter wave. The wave has a period of 10 seconds. In the figure, the particle is traveling from left to right and 60 seconds worth of the trajectory is shown. This figure is similar to [8, Figure 2.4].

A.2 Irregular Waves

Actual waves in the ocean are more accurately described by an “irregular” wave model. In this irregular wave model, the wave is represented as a sum of component waves. These component waves have different amplitudes and frequencies, which when combined give the resulting irregular wave a spectral content which is similar to the region of ocean and wind conditions desired in the model.

A.2.1 Wave Elevation in Irregular Seas

The spectral content of the surface waves will have a significant effect on the buoy’s effectiveness. It is desirable to have large, long period, non-breaking waves as these will impart the least amount of angular disturbances to the buoy system. Standard models for wind generated waves in the open ocean are presented in [9] and [8].

Using (A.4) to describe each of the component waves, we can describe an irregular wave by

$$\zeta(x, y, t) = \sum_{j=1}^N A_j \sin[\omega_j t - k_j (x \cos \beta + y \sin \beta) + \phi_j]. \quad (\text{A.8})$$

Here $\zeta(x, y, t)$ is the wave elevation as a function of position and time. N is the total number of component waves. A_j , ω_j , and k_j are the amplitude, circular frequency and wave number, respectively, for each of the component waves. ϕ_j is a random and constant phase angle uniformly distributed between 0 and 2π for each component wave. x , y , and β are the same as in (A.4).

The amplitude for each of the component waves, A_j , is a function of the particular spectral distribution function, $S(\omega_j)$, used to provide the statistical description of the sea state. A_j is calculated from

$$A_j = \sqrt{2S(\omega_j)\Delta\omega}, \quad (\text{A.9})$$

where $\Delta\omega$ is the constant difference between successive frequencies of each component wave in the summation.

Once a suitable spectral distribution function has been selected, the component waves can be calculating using the following procedure.

A.2.2 Procedure for Calculating Wave Elevation

Fossen [9, pp. 61] states a that large number of component waves may be needed, $N \approx 1000$, to accurately model the wave spectrum. Alternatively, he suggests that far fewer component waves can be used if the the frequency of each component wave is chosen at random within its frequency interval $\Delta\omega$.

The procedure for calculating the wave elevation as a function of time is [9, Algorithm 3.1]:

1. Divide the spectral distribution function, $S(\omega)$, into N intervals with width $\Delta\omega$.
2. Pick a random frequency, ω_j , in each frequency interval and compute $S(\omega_j)$.
3. Compute the wave amplitude, A_j , and the wave number, k_j , from (A.9) and (A.2) respectively.
4. Pick a random phase angle uniformly distributed on $[0, 2\pi)$ for each component wave.

5. Compute $\zeta(x, y, t)$ from (A.8).

A.2.3 Fluid Velocity in Irregular Seas

The fluid velocity in irregular seas is simply the sum of the velocities due to the component waves described by (A.4) in a form similar to (A.7). This results in a fluid velocity vector in the navigation frame of

$$\mathbf{v}_{fluid}(x, y, z, t) = \sum_{j=1}^N \omega_j A_j e^{k_j z} \begin{bmatrix} \sin[\omega_j t - k_j(x \cos \beta + y \sin \beta) + \phi_j] \cos \beta \\ \sin[\omega_j t - k_j(x \cos \beta + y \sin \beta) + \phi_j] \sin \beta \\ \cos[\omega_j t - k_j(x \cos \beta + y \sin \beta) + \phi_j] \end{bmatrix}. \quad (\text{A.10})$$

A.3 Pierson-Moskowitz Spectral Distribution

The literature suggests a variety of spectral density functions depending on location in the world and weather conditions. One such distribution is the Pierson-Moskowitz spectrum [9, (3.2)] given by

$$S(\omega) = \frac{0.0081g^2}{\omega^5} \exp\left(-\frac{3.11}{\omega^4 H_{1/3}^2}\right). \quad (\text{A.11})$$

Where $H_{1/3}$ is the *significant wave height* in meters, g is the acceleration due to gravity in m/s^2 , and ω is the wave's circular frequency in rad/s . $H_{1/3}$ is calculated as the mean of the one-third highest waves. Plots of this spectrum for several significant wave heights are shown in Figures A.4 and A.5.

Fossen [9, (3.24)] suggests a relationship between wind speed and significant wave height of

$$H_{1/3} = 0.21 \frac{V^2}{g}, \quad (\text{A.12})$$

where V is the wind speed at a height of 19.4 meters above the surface.

The Pierson-Moskowitz spectrum is one of the more generic spectral density functions as it assumes a fully developed sea, with unlimited fetch¹, and “infinite” water depth. Faltinsen and Fossen present other spectral distributions in [8] and [9] which are specific to particular regions of the world or have larger number of parameters required to specify the distribution.

¹Fetch is the distance of open water that the wind is blowing over. Unlimited fetch means the wind has enough distance to generate fully developed waves.

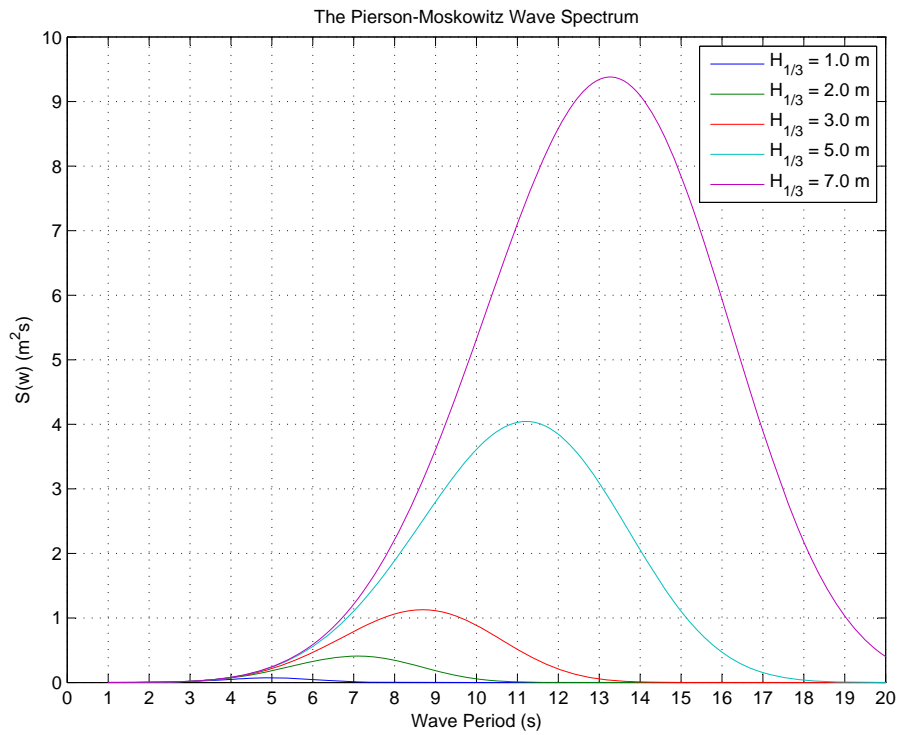


Figure A.4: The Pierson-Moskowitz spectral distribution for significant wave heights of 1, 2, 3, 5, and 7 meters. For these larger waves there is a very low percentage of energy with a period of 3 seconds or less.

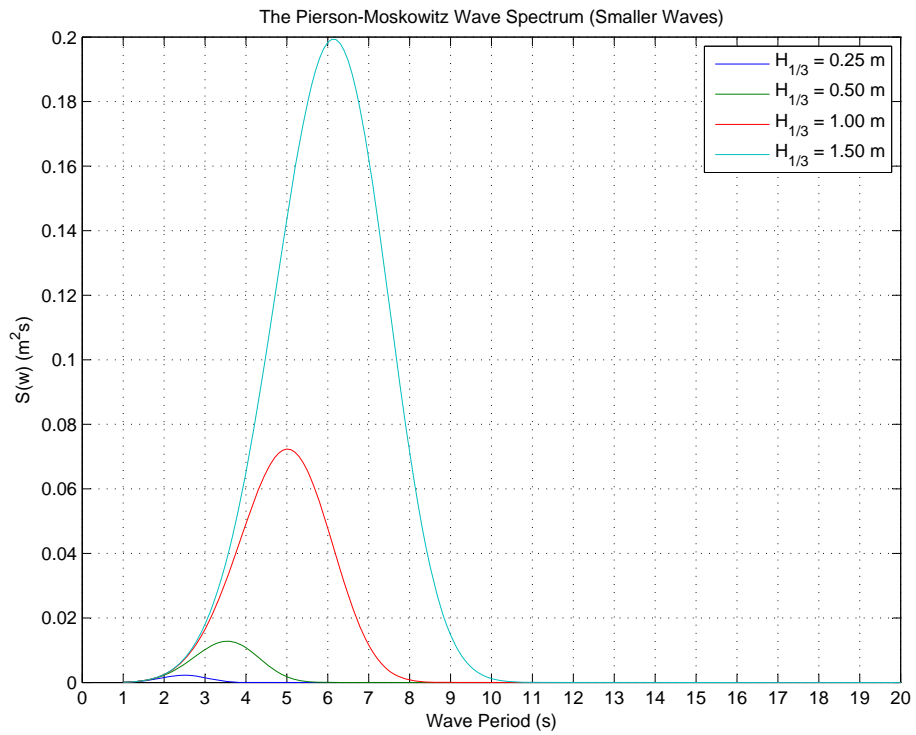


Figure A.5: The Pierson-Moskowitz spectral distribution for significant wave heights of 0.25, 0.5, 1, and 1.5 meters. Even at these much smaller wave heights, the Pierson-Moskowitz distribution predicts minimal energy with a period of 2 seconds or less.

Appendix B

Additional Buoy Models

After extensive testing it has become clear that the geometry of the buoy plays a critical roll in the success or failure of the active stabilization and pointing of the payload. There are a very large number of possible buoy configurations which meet the basic description of a cylindrical housing and payload connected by a universal joint. Parameters which can be varied within this description include:

1. Housing diameter and length
2. Housing mass and mass distribution
3. Payload diameter and length
4. Payload mass and mass distribution
5. Joint location with respect to the end of each body

Given that we already need to search across a large field of controller parameters (gain values, control rates, joint velocities, etc.), allowing all of the above listed parameters to vary makes the search several orders of magnitude longer and more difficult.

An approach to reducing the search space is to specify the buoy's size and weight based on "non-control" considerations. Practically, the size of the buoy is determined by the launch mechanism. A reasonable starting point for this work is a buoy the size of a US/NATO sonobuoy (size A): 36" long, 4.875" diameter [12, p. 644]. Once the overall buoy volume has been determined, a mass distribution must be specified. Assuming that most of the buoy contents will be specified by parties other than the controls engineer, and that denser items will be placed in the bottom to provide a passive righting moment, a notional mass distribution can be specified throughout the buoy volume.

Given this information, the controls engineer might be left to select where in the buoy the joint is located. In this work a heavy and a light region for the buoy are defined. The joint location is independent of the heavy and light regions. Several possible configurations are show in Figure B.1.

For the J series buoys¹, the configurations and parameters are listed in Tables B.1 and B.2.

¹The "J" is a reference to the fact that the only difference between the buoys is the location of the Joint.

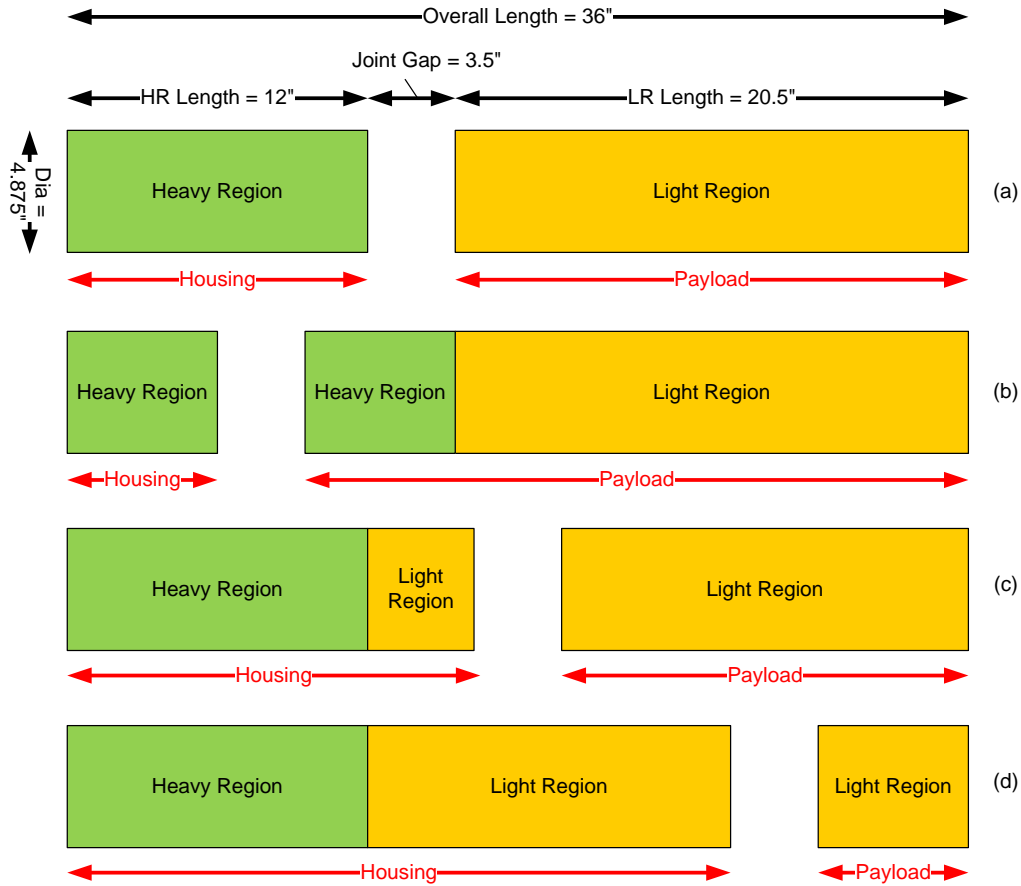


Figure B.1: Four joint locations with respect to the buoy's heavy and light regions. (a) The joint is located at the boundary between the regions. (b) The joint is located in the heavy region. (c) The joint is located in the middle of the buoy. (d) the joint is located such that the payload is small. The joint gap is sized to allow the housing and payload to rotate up to 90 degrees with respect to each other.

Table B.1: The buoy parameters used by all configurations in the J series buoys. The joint gap is the distance between the housing and payload cylinders occupied by the joint. The pivot point of the joint is in the middle of the gap. For the purpose of the model, the joint gap does not contribute to the displacement or mass of the buoy.

Equilibrium Submerged Fraction	85%	
Diameter	4.875	in
Heavy Region Mass	12.00	lbs
Heavy Region Length	12.00	in
Light Region Mass	6.59	lbs
Light Region Length	20.5	in
Joint Gap	3.5	in
Overall Length	36	in
Total Mass	18.59	lbs

Table B.2: The J series buoy configurations. The only difference between these configurations is the location of the joint.

Configuration	Housing Length	Payload Length
BuoyGroupSonoA 5x36 J10	10in	22.5 in
BuoyGroupSonoA 5x36 J15	15in	17.5 in
BuoyGroupSonoA 5x36 J20	20in	12.5 in
BuoyGroupSonoA 5x36 J25	25in	7.5 in

Table B.3: The overall center of mass locations for each of the J series buoy configurations in the housing and payload coordinate systems.

Configuration	Buoy CM Housing Coord. Sys.	Buoy CM Payload Coord. Sys
BuoyGroupSonoA 5x36 J10	13.4 in	-0.14 in
BuoyGroupSonoA 5x36 J15	12.8 in	-5.7 in
BuoyGroupSonoA 5x36 J20	12.5 in	-10.9 in
BuoyGroupSonoA 5x36 J25	12.2 in	-16.3 in

Appendix C

Detailed Joint Controller Discussion

C.1 The Primitive Motion Model

A simple low level motion controller can be modeled or implemented as an acceleration, velocity, or position controlled system. To streamline the discussion we consider a linear, rather than rotary, actuator. The fundamental equations of the system are:

$$p_b = p_a + v_a t + \frac{1}{2} a t^2, \quad (\text{C.1})$$

$$v_b = v_a + a t, \quad (\text{C.2})$$

where p_a and v_a are the initial position and velocity; and p_b and v_b are the final position and velocity which result from an acceleration, a , applied for time, t . In addition the motion model also includes limits on the magnitude of the permitted acceleration, a_{max} , and velocity, v_{max} .

C.2 Acceleration Control

This is the simplest form of control to model and implement. A commanded acceleration value is specified and applied to the system until a new value is received. If the commanded acceleration's magnitude is greater than a_{max} , then a_{max} (with the appropriate sign) is applied to the system.

In a discrete time system, at each time step the system's position and velocity are integrated forward using (C.1) and (C.2) where t is set to the step size. (C.1) should be calculated before (C.2) so that (C.1) can use the velocity value at the beginning of the step.

To implement the velocity limiting feature of the model the commanded acceleration needs to be checked to ensure that it does not result in a violation of the maximum permitted

velocity:

$$v_{desired} = v_k + a_{cmd} dt, \quad (C.3)$$

$$a_k = \begin{cases} a_{cmd} & \text{if } |v_{desired}| < v_{max}, \\ \frac{\text{sign}(v_{desired})v_{max} - v_k}{dt} & \text{if } |v_{desired}| > v_{max}, \end{cases} \quad (C.4)$$

$$p_{k+1} = p_k + v_k dt + \frac{1}{2}a_k dt^2, \quad (C.5)$$

$$v_{k+1} = v_k + a_k dt, \quad (C.6)$$

where dt denotes the discrete time step size.

Note that $v_{max} > 0$, $|v_k| \leq v_{max}$, and when the system is traveling at v_{max} the acceleration is set to zero. Additionally, these equations do not model the velocity saturating in the middle of the time step, but rather they model the controller adjusting the acceleration to bring the system to v_{max} at the end of the time step. The calculated acceleration value for any particular time step will always be smaller in magnitude than or equal to the commanded acceleration value. As long as the magnitude of the commanded acceleration does not exceed a_{max} , then this trajectory will not exceed the acceleration limit.

In continuous time systems the time and position at which the velocity will saturate is calculated by

$$t_{vsat} = \frac{\text{sign}(a)v_{max} - v}{a}, \quad (C.7)$$

$$\begin{aligned} p_{vsat} &= p + vt_{vsat} + \frac{1}{2}at_{vsat}^2 \\ &= p + \frac{v_{max}^2 - v^2}{2a}, \end{aligned} \quad (C.8)$$

where a is the applied acceleration and v is the current velocity. Note that (C.7) and (C.8) are only valid for non-zero accelerations.

C.3 Velocity Control

In this method of control a desired velocity is specified to the system and the system accelerates at maximum acceleration to the commanded velocity. When the commanded velocity can be reached in a single step, then the acceleration is set so that the commanded velocity is achieved at the end of the step.

As long as the magnitude of the commanded velocity is not permitted to exceed v_{max} , then no velocity or acceleration limits will be violated.

$$a_{desired} = \frac{v_{cmd} - v_k}{dt}, \quad (C.9)$$

$$a_k = \begin{cases} \text{sign}(v_{cmd} - v_k) a_{max} & \text{if } |a_{desired}| > a_{max}, \\ \frac{v_{cmd} - v_k}{dt} & \text{if } |a_{desired}| < a_{max}. \end{cases} \quad (C.10)$$

Next (C.1) and (C.2) are used to integrate the system forward.

In some physical systems there are differing limits on maximum acceleration depending on whether the system is speeding up or slowing down. This can be modeled by

$$a_{max} = \begin{cases} a_{maxAcc} & \text{if } v_{cmd} - v > 0, \\ a_{maxDec} & \text{if } v_{cmd} - v < 0. \end{cases} \quad (C.11)$$

C.4 Position-Velocity Control

Position-Velocity control is the most complicated form of control available to this primitive controller. The goal for this mode of control is given an initial position and velocity, the trajectory should result in a specified final position and velocity. Optionally the final time of the trajectory can be specified. Plain position control might be considered the case where the final velocity is set to zero. As always the system should not violate its velocity and acceleration limits. With position-velocity control, there are some significant differences between the continuous and discrete time implementations, so these will be treated separately. Finally, besides the algorithms listed here, there are many others which could be used, including higher order models with continuously varying accelerations and sinusoidal trajectories.

C.4.1 Equal Specified Intervals

Because there are two final states to control (position, and velocity), two accelerations will need to be specified. In general, it is not possible to achieve arbitrary final states from arbitrary initial states in a single time step because that only affords an opportunity for one acceleration value to be applied. However, it is possible to specify the required final states after two acceleration intervals. An example of the resulting trajectory is illustrated in Figure C.1.

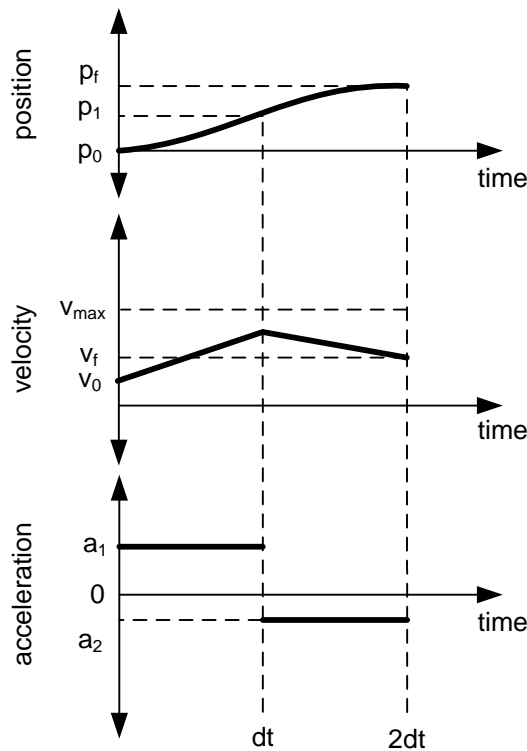


Figure C.1: The acceleration, velocity and position profiles for equal discrete sampling intervals.

Given the initial position and velocity one can calculate the required accelerations to achieve the desired final position and velocity in two steps of duration dt . Additionally,

the intermediate velocity, v_1 , after the first step needs to be calculated to ensure that the velocity limit is not exceeded.

$$a_1 = \frac{p_f - p_0}{dt^2} - \frac{3v_0 + v_f}{2dt}, \quad (\text{C.12})$$

$$a_2 = \frac{3v_f + v_0}{2dt} - \frac{p_f - p_0}{dt^2}, \quad (\text{C.13})$$

$$v_1 = v_0 + a_1 dt. \quad (\text{C.14})$$

If the magnitudes of the accelerations are less than or equal to the maximum allowed acceleration and the magnitude of the intermediate velocity is less than the allowed maximum velocity, then it is possible for the desired final states to be reached in the two steps.

In a discrete time system dt may be set to any multiple of the system sampling interval. Additionally, this formulation will work for continuous time systems.

C.4.2 Unequal Specified Intervals

This method is very similar to equal specified intervals, except that the intervals over which a_1 and a_2 are applied over are not equal. For this derivation we will specify the *total* time of the motion as t , and the transition fraction λ . The switch from a_1 to a_2 occurs at λt . An example trajectory is shown in Figure C.2. The duration over which each acceleration is applied can be written as:

$$t_1 = \lambda t, \quad (\text{C.15})$$

$$t_2 = (1 - \lambda)t. \quad (\text{C.16})$$

Given the initial and final positions and velocity, a total time interval, t , and a transition fraction, λ , the acceleration over each interval can be calculated as

$$a_1 = \frac{2(p_f - p_0)}{\lambda^2 t^2} - \frac{v_0(1 + \lambda) + v_f(1 - \lambda)}{t\lambda^2}, \quad (\text{C.17})$$

$$a_2 = \frac{v_f - v_0}{(1 - \lambda)t} - a_1 \frac{\lambda}{1 - \lambda}, \quad (\text{C.18})$$

$$v_1 = v_0 + a_1 \lambda t. \quad (\text{C.19})$$

It is important that $0 < \lambda < 1$ because $\lambda = 0$ or $\lambda = 1$ would result in one of the accelerations being applied for zero time.

Given that λ can be varied over a range of values, this leads to the possibility that λ could be selected to optimize the acceleration values. Some candidate cost functions might be

1. Minimize the magnitude of the combined accelerations, $J_1 = a_1^2 + a_2^2$. This is proportional to the applied force or moment squared.
2. Minimize the difference between the accelerations, $J_2 = (a_1 - a_2)^2$.
3. Minimize the applied energy, $J_3 = (a_1 \lambda t)^2 + (a_2 (1 - \lambda)t)^2$.
4. Minimize the applied power, $J_4 = a_1^2 \lambda t + a_2^2 (1 - \lambda)t$.

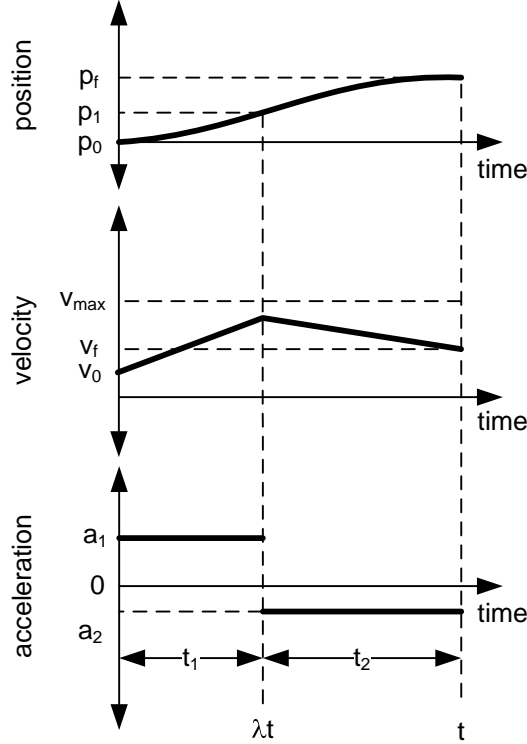


Figure C.2: The acceleration, velocity and position profiles for specified but unequal acceleration intervals.

For a position and velocity movement with $v_0 = v_f = 0$, the representative acceleration values as a function of λ are plotted in Figure C.3.

The four cost functions plotted as a function of λ in Figure C.4. The cost functions are normalized with respect to their value at $\lambda = 0.5$ to allow an easier comparison with the equal interval case. It is important to note that all of the proposed cost functions are minimized at $\lambda = 0.5$ when $v_0 = v_f$.

Next we look at the same example, except that the final velocity has a non-zero value. The four cost functions are plotted as functions of λ in Figure C.5. The cost functions are normalized with respect to their value at $\lambda = 0.5$ to allow an easier comparison with the equal interval case. In this case $v_0 \neq v_f$. This causes the force squared cost function, $J1$, and energy cost function, $J3$, to be minimized at a value of $\lambda \neq 0.5$. However, the cost function which penalizes a difference between the accelerations, $J2$, and which minimizes power, $J4$ are still minimized by setting $\lambda = 0.5$. So the decision to use the equal segment approach can be justified.

C.4.3 The Fastest Continuous Saturating Response

If the velocity is allowed to saturate at v_{max} as the system moves from p_0, v_0 to p_f, v_f in continuous time, then the movement will take the shortest amount of time possible. This trajectory has three sections:

1. Apply a_1 from t_0 to t_1 when the velocity has saturated at v_{max} heading in the direction of the final position. The position at which velocity saturation occurs is p_1 .

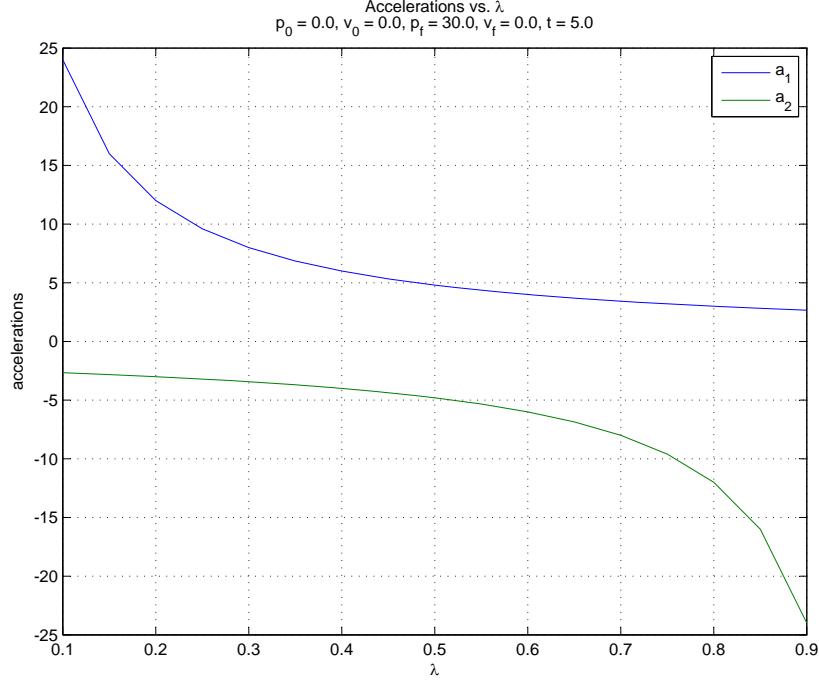


Figure C.3: The acceleration values as a function of lambda for a case where $v_0 = v_f = 0$.

2. Travel at v_{max} from time t_1 to t_2 , and positions p_1 to p_2 .
3. Beginning at time t_2 apply an acceleration, a_2 , to bring the system to its final position and velocity, p_f and v_f , at time t_f . This trajectory is illustrated in Figure C.6.

The parameters for segment 1 are calculated by

$$C_{dir} = \text{sign}(p_f - p_0), \quad (\text{C.20})$$

$$t_{01} = \frac{C_{dir}v_{max} - v_0}{a_1}, \quad (\text{C.21})$$

$$\begin{aligned} p_1 &= p_0 + v_0 t_{01} + \frac{1}{2} a_1 t_{01}^2, \\ &= p_0 + \frac{v_{max}^2 - v_0^2}{2a_1}, \end{aligned} \quad (\text{C.22})$$

where t_{01} is the time interval from points p_0 to p_1 . The two element subscript indicates that this is a time *interval* rather than an absolute time value. Additionally, to ensure that the initial acceleration, a_1 , is in the correct direction, set the sign of a_1 such that $\text{sign}(a_1) = \text{sign}(p_f - p_0)$.

The parameters for segment 3 are calculated by

$$t_{2f} = \frac{v_f - C_{dir}v_{max}}{a_2}, \quad (\text{C.23})$$

$$\begin{aligned} p_2 &= p_f - C_{dir}v_{max}t_{2f} - \frac{1}{2}a_2t_{2f}^2, \\ &= p_f + \frac{v_{max}^2 - v_f^2}{2a_2}, \end{aligned} \quad (\text{C.24})$$

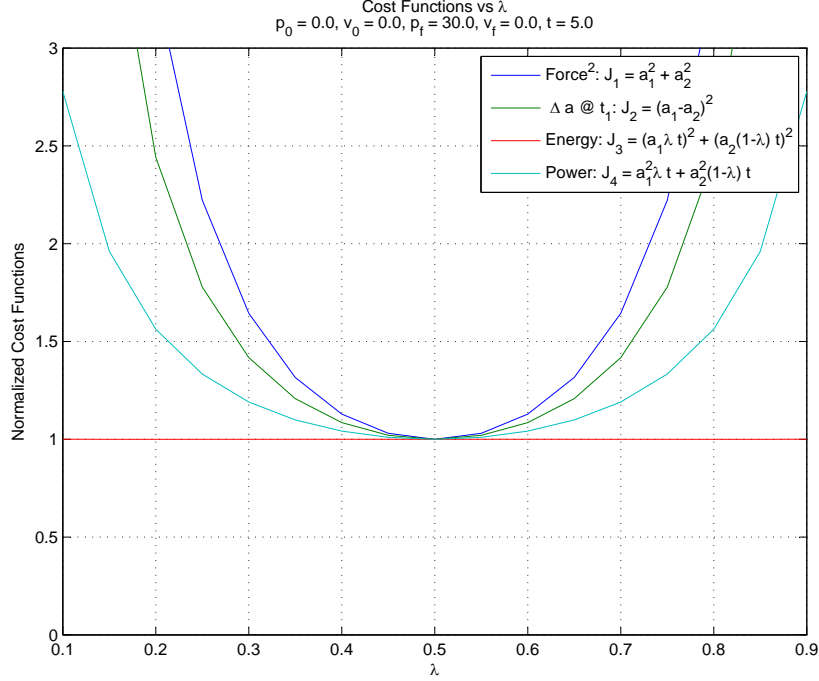


Figure C.4: The four cost functions plotted as functions of λ . The cost functions are normalized with respect to their value at $\lambda = 0.5$ to allow an easier comparison with the equal interval case.

Here again, the sign of the second acceleration segment needs to be correct. It will be opposite the first segment, i.e. $\text{sign}(a_2) = -\text{sign}(p_f - p_0)$. And t_{2f} is the time interval from the point where braking commences until the system is at its final states.

Next the time spent in segment 2 can be found as

$$t_{12} = \frac{p_2 - p_1}{C_{dir} v_{max}}. \quad (\text{C.25})$$

If t_{12} is less than zero, then the assumption that the system will be driven into velocity saturation is false, and the trajectory should be recalculated without this assumption.

The resulting total time of the movement is simply, $t = t_{01} + t_{12} + t_{2f}$. If maximum acceleration values are used, i.e. $|a_1| = |a_2| = a_{max}$, then this is also the fastest time in which final conditions can be reached.

The controller needs to be able to specify two parameters to allow it to independently adjust the two final states, p_f and v_f . Since the magnitudes of the accelerations and saturation velocity are fixed, the only parameters the controller can adjust are the time (or position) that braking commences t_2 (or p_2) and the duration of the braking, t_{2f} .

To implement this controller, a system could calculate p_2 given p_0 , v_0 , p_f , and v_f , apply the maximum acceleration towards the final position until the velocity saturates and then, when p_2 is reached, apply the maximum acceleration to slow to the final velocity.

Because the final time is *not* specified, all final positions and velocities are reachable. Some final states will require a non velocity saturated response which is discussed next. If $\text{sign}(v_f) = -\text{sign}(p_f - p_0)$, then the system will pass through p_f headed in the wrong

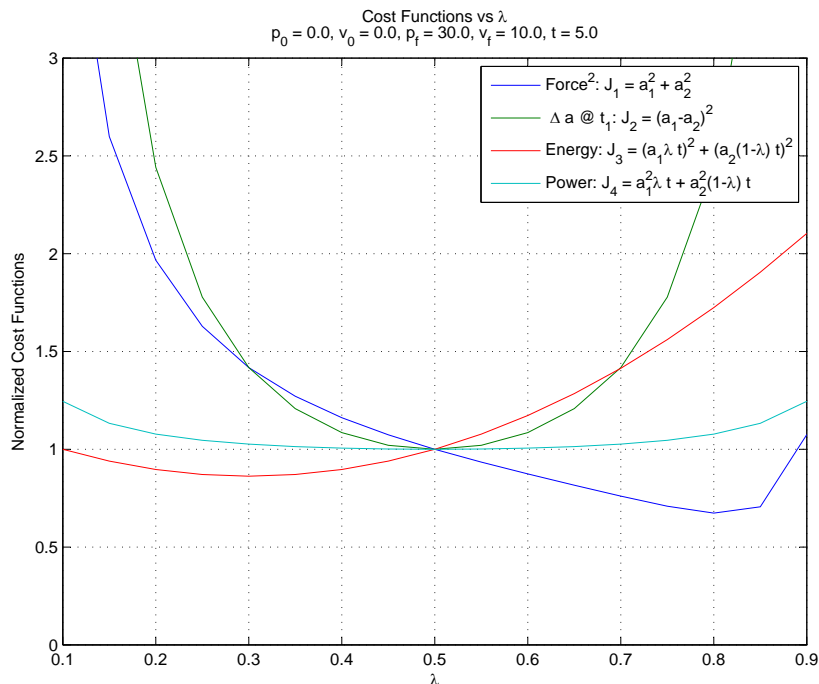


Figure C.5: The four cost functions plotted as functions of λ . The cost functions are normalized with respect to their value at $\lambda = 0.5$ to allow an easier comparison with the equal interval case. In this case $v_0 \neq v_f$. This causes the force squared cost function, J_1 , and energy cost function, J_3 , to be minimized at a value of $\lambda \neq 0.5$.

direction, before it turns around to approach p_f from the correct direction for the sign of v_f .

C.4.4 The Fastest Continuous Non-Saturating Response

As mentioned above if (C.25) gives a value for $t_{12} < 0$, then the system never saturates at v_{max} during its trajectory from the initial states to the final states. This trajectory is illustrated in Figure C.7. This trajectory consists of two segments:

1. Apply a_1 from t_0 until it is time to begin braking at t_1 . The position at which braking begins is p_1 .
2. Beginning at time t_1 apply an acceleration, a_2 , to bring the system to its final position and velocity, p_f and v_f , at time t_f .

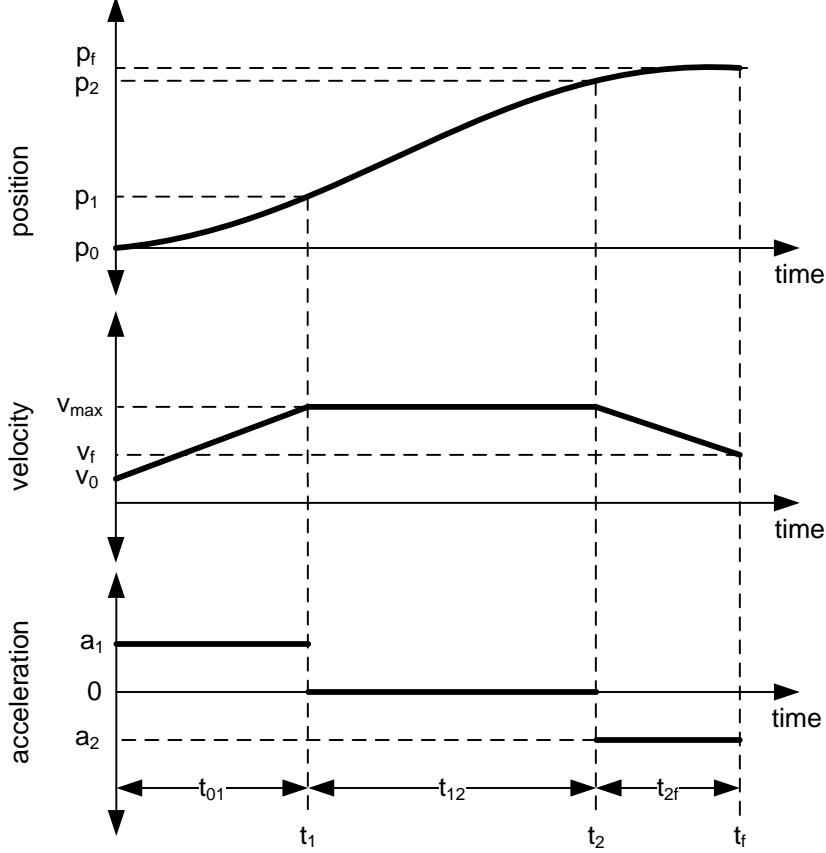


Figure C.6: The acceleration, velocity and position profiles for a continuous time, velocity saturating response.

We can derive expressions for the braking point, p_1 , and the velocity at the braking point, v_1 . Starting with these 4 relationships:

$$v_1 = v_0 + a_1 t_{01} \quad \Rightarrow t_{01} = \frac{v_1 - v_0}{a_1}, \quad (\text{C.26})$$

$$v_1 = v_f - a_2 t_{1f} \quad \Rightarrow t_{1f} = \frac{v_f - v_1}{a_2}, \quad (\text{C.27})$$

$$p_1 = p_0 + v_0 t_{01} + \frac{1}{2} a_1 t_{01}^2 \quad \Rightarrow p_1 = p_0 + \frac{1}{2a_1} (v_1^2 - v_0^2), \quad (\text{C.28})$$

$$p_1 = p_f - v_1 t_{1f} - \frac{1}{2} a_2 t_{1f}^2 \quad \Rightarrow p_1 = p_f + \frac{1}{2a_2} (v_1^2 - v_f^2), \quad (\text{C.29})$$

setting (C.28) equal to (C.29) gives

$$p_0 + \frac{1}{2a_1} (v_1^2 - v_0^2) = p_f + \frac{1}{2a_2} (v_1^2 - v_f^2). \quad (\text{C.30})$$

Now collect the terms to form a quadratic equation in terms of v_1 .

$$\underbrace{\left(\frac{1}{2a_2} - \frac{1}{2a_1} \right)}_A v_1^2 + \underbrace{0}_B v_1 + \underbrace{\left(\frac{v_0^2}{2a_1} - \frac{v_f^2}{2a_2} + p_f - p_0 \right)}_C = 0. \quad (\text{C.31})$$

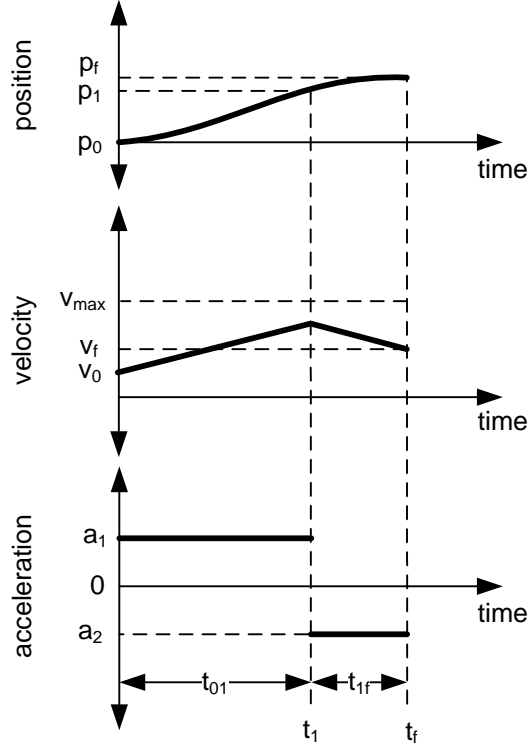


Figure C.7: The acceleration, velocity and position profiles for a continuous time, *non-velocity saturating* response.

Recalling the quadratic equation

$$x = \frac{-B \pm \sqrt{B^2 - 4AC}}{2A},$$

for $B = 0$ the two possible values of v_1 are

$$v_1 = \pm \sqrt{\frac{-C}{A}} = \pm \sqrt{\frac{-\left(\frac{v_0^2}{2a_1} - \frac{v_f^2}{2a_2} + p_f - p_0\right)}{\left(\frac{1}{2a_2} - \frac{1}{2a_1}\right)}}. \quad (\text{C.32})$$

During implementation it may be tempting to just calculate the A and C terms in (C.31) and solve the quadratic equation. Note that each term has both acceleration values in the denominator of a fraction. This implementation would give a divide by zero error if either acceleration is set to zero. However, for a significant range of initial conditions it is possible to reach the desired final position and velocity with one of the acceleration values set to zero. To admit these valid solutions simplify (C.32) to

$$v_1 = C_{dir} \sqrt{\frac{2a_1a_2(p_0 - p_f) - a_2v_0^2 + a_1v_f^2}{a_1 - a_2}}. \quad (\text{C.33})$$

Now (C.33) will only return a divide by zero error if both acceleration are set to zero. The C_{dir} term sets the sign of v_1 to match the required direction of travel, i.e. $\text{sign}(p_f - p_0)$.

The procedure for calculating the trajectory is

1. Use (C.33) to calculate v_1 from the initial and final states, and acceleration values.
2. Use either (C.26) and (C.28) or (C.27) and (C.29) to calculate the position, p_1 , at which the second acceleration commences.

As in the case where the velocity saturates, the two parameters which are adjusted are the time that a_2 commences and the duration that a_2 is applied for.

Appendix D

Solutions By Constraint Equations

This appendix presents an alternative method of calculating the kinematics and dynamics of multi-body problems using constraint equations. In this method the forces and moments are applied to each individual body. The inertia properties are specified for each body. Then the kinematic relationships between the bodies are enforced by a series of constraint equations, which describe these kinematic relationships. The complete system of equations is made up of the dynamics equations for each body and the constraint equations. The complete system is solved simultaneously at each time step of the simulation.

This approach offers the following advantages:

1. The forces and moments on each body can be calculated individually for that body and the constraint equation accounts for the coupling between the bodies.
2. Inertia tensors only need to be specified about the body's CM.
3. The motion of the joint is most easily specified by specifying the moment applied to the joint.
4. This method readily scales to systems with more than two bodies.

A constraint equation based solution does have a number of disadvantages including:

1. Specifying the joint motion by something besides moments (angle, velocity, acceleration, or jerk) requires additional constraint equations to be added to the system, thus requiring a larger set of linear equations to be solved.
2. A solution in this form may offer less physical insight into the dynamics of the system.
3. Solving this system maybe more computationally intensive than another formulation.

Two examples of the solving the two body buoy problem using constraint equation are presented next. The planar two body problem is presented first as an introduction to the technique. The second case is the full spatial version of the problem.

D.1 Planar Solution Using Constraint Equations

D.1.1 Problem Geometry

Consider a pair of planar rigid bodies, each with 3 degrees of freedom (DOF), two translational and one rotational. These two bodies are connected by a hinge joint. So the system

also has two kinematic constraint equations which require that the location of the hinge point on each body have the same coordinates in the navigation frame. This results in an system with 4 independent variables (6 eqns - 2 eqns) and requires solving 8 simultaneous equation (6 eqns + 2 eqns). This analysis draws heavily on the work in [20]. Table D.1 lists the variables used in this analysis.

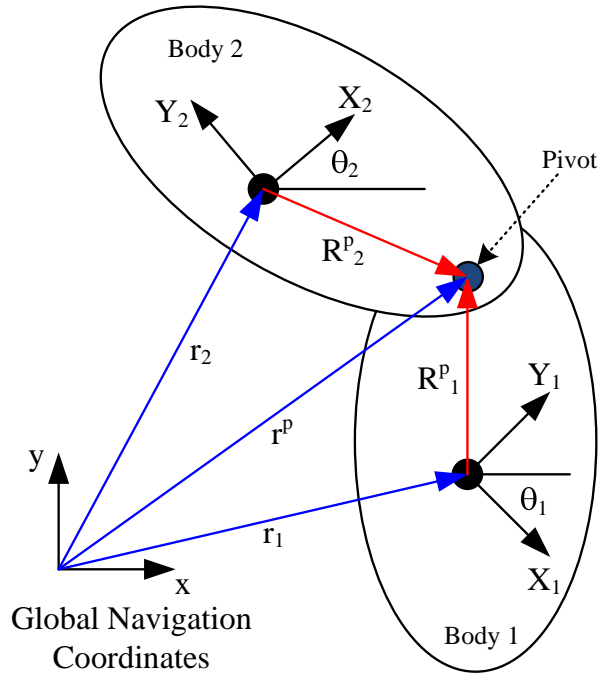


Figure D.1: The geometry of two rigid planar bodies connected by a pivot. Lower case vectors are in the navigation coordinate system. Upper case vectors are in the bodies' coordinate systems.

D.1.2 The Kinematically Constrained Dynamics

The system coordinate vector, \mathbf{q} , is a 6 element vector containing coordinates for each of the 6 DOFs in the two body planar system. It is built as

$$\mathbf{q} = \begin{bmatrix} \mathbf{r}_1 \\ \theta_1 \\ \mathbf{r}_2 \\ \theta_2 \end{bmatrix}. \quad (\text{D.1})$$

This two body system's mass matrix is a 6x6 diagonal matrix, where each body's mass or inertia is in the corresponding diagonal element to the translational or rotational DOF in the state vector \mathbf{q} . The inertia for each body is the the inertia about the *body's* center

of mass (CM). The mass matrix is

$$\mathbf{M} = \begin{bmatrix} m_1 & 0 & 0 & 0 & 0 & 0 \\ 0 & m_1 & 0 & 0 & 0 & 0 \\ 0 & 0 & J_1 & 0 & 0 & 0 \\ 0 & 0 & 0 & m_2 & 0 & 0 \\ 0 & 0 & 0 & 0 & m_2 & 0 \\ 0 & 0 & 0 & 0 & 0 & J_2 \end{bmatrix}. \quad (\text{D.2})$$

The time invariant constraint equations are a function of the state vector \mathbf{q} and have the form

$$\Phi(\mathbf{q}) = 0. \quad (\text{D.3})$$

For the planar revolute joint [20, (4.8)] gives the constraint equations as

$$\Phi(\mathbf{q}) = \begin{bmatrix} x_1^p - x_2^p \\ y_1^p - y_2^p \end{bmatrix} = \begin{bmatrix} 0 \\ 0 \end{bmatrix}, \quad (\text{D.4})$$

where x^p and y^p give the location of the hinge point in global coordinates. (D.4) is simply requiring that the global coordinates for pivot locations on each body are the same. The global coordinates for the pivot locations for each body can be found by

$$\mathbf{r}_i^p = \mathbf{r}_i + \mathbf{B}_i \mathbf{R}_i^p, \quad (\text{D.5})$$

where \mathbf{B}_i is the planar direction cosine matrix describing the body orientation and given by

$$\mathbf{B}_i = \begin{bmatrix} \cos \theta_i & -\sin \theta_i \\ \sin \theta_i & \cos \theta_i \end{bmatrix}. \quad (\text{D.6})$$

For the planar revolute joint the Jacobian matrix is given by [20, Table 4.2] as

$$\Phi_q = \begin{bmatrix} 1 & 0 & -(y_1^p - y_1) & -1 & 0 & (y_2^p - y_2) \\ 0 & 1 & (x_1^p - x_1) & 0 & -1 & -(x_2^p - x_2) \end{bmatrix}. \quad (\text{D.7})$$

The vector γ , known as the *right side of the kinematic acceleration equations*, is in general [20, eqn (3.16)]

$$\gamma = -(\Phi_q \dot{\mathbf{q}})_q \dot{\mathbf{q}}. \quad (\text{D.8})$$

For a planar revolute joint γ is [20, Table 4.3]

$$\gamma = \begin{bmatrix} (x_1^p - x_1) \dot{\theta}_1^2 - (x_2^p - x_2) \dot{\theta}_2^2 \\ (y_1^p - y_1) \dot{\theta}_1^2 - (y_2^p - y_2) \dot{\theta}_2^2 \end{bmatrix}. \quad (\text{D.9})$$

At each time step we can solve for the accelerations of the state vector and the Lagrange multipliers by solving the linear system

$$\begin{bmatrix} \mathbf{M} & \Phi_q^T \\ \Phi_q & \mathbf{0} \end{bmatrix} \begin{bmatrix} \ddot{\mathbf{q}} \\ -\lambda \end{bmatrix} = \begin{bmatrix} \mathbf{g} \\ \gamma - 2\alpha \dot{\Phi} - \beta^2 \Phi \end{bmatrix}. \quad (\text{D.10})$$

The Lagrange multipliers, λ , are associated with the constraint equations and give the forces (or moments) required to enforce the constraints. In this example, the two Lagrange

Table D.1: The variables used in the planar two body system.

Symbol	Units	Type	Description
\mathbf{r}_i	m	Vector	The location body i 's CM in global coordinates.
\mathbf{r}_i^p	m	Vector	The location body i 's pivot point in global coordinates.
θ_i	rad	Scalar	The orientation of body i in global coordinates.
\mathbf{B}_i	none	Matrix	The direction cosine matrix describing body i 's orientation.
\mathbf{R}_i^p	m	Vector	The location of body i 's pivot point in body coordinates.
m_i	kg	Scalar	The mass of body i .
J_i	$kg m^2$	Scalar	The inertia of body i about its CM.
λ	mixed	Vector	The Lagrange multipliers associated with the system constraints.
\mathbf{M}	mixed	Matrix	The system mass matrix.
\mathbf{q}	mixed	Vector	The vector of all DOFs for the system.
\mathbf{g}	mixed	Vector	The vector of all the forces and moments associated with each DOF of the system.
γ	mixed	Vector	The vector for the RHS of the kinematic acceleration equations associated with the system constraint equations.
α, β	mixed	Scalars	Numerical stabilization constants.
$\Phi(\mathbf{q})$	mixed	Matrix	The matrix of the system constraint equations.
Φ_q	mixed	Matrix	The Jacobian matrix of the system constraint equations.
$\Phi(\mathbf{q}, t)^{(d)}$	mixed	Matrix	The matrix of the optional driving constraint equations.
$\Phi_q^{(d)}$	mixed	Matrix	The Jacobian matrix of the optional driving constraint equations.
$\gamma^{(d)}$	mixed	Vector	The vector for the RHS of the kinematic acceleration equations associated with the driving constraint equations.

multipliers give the x and y components of the force acting on the hinge. These values could be useful for checking that the load capacity of the hinge is not exceeded.

The α and β terms provide negative feedback to stabilize the numerical solution about valid results. Without these stability terms, the solution becomes unstable when integrated over time due to accumulated round off errors and other noise sources. This results in the system constraints being violated. The derivation of this ‘‘Constraint Violation Stabilization Method’’ is given in [20, Section 13.3.1]. Additionally, [20] also states that for most real world problems suitable values for α and β are from 1 to 10 and that the stability will be critically damped if $\alpha = \beta$.

The time derivative of the time invariant constraint equations, $\dot{\Phi}$ is

$$\dot{\Phi} = \Phi_q \dot{\mathbf{q}}. \quad (\text{D.11})$$

D.1.3 Model Forces and Moments

For this analysis I chose to model the 2 body unit as falling through a fluid. Each of the two bodies experiences forces due to gravity and linear viscous drag. Additionally, an optional moment, τ_h , can be applied at the hinge. So the generalized force vector, \mathbf{g} , is

$$\mathbf{g} = \begin{bmatrix} -C_{D1}\dot{x}_1 \\ -9.81m_1 - C_{D1}\dot{y}_1 \\ \tau_h \\ -C_{D2}\dot{x}_2 \\ -9.81m_2 - C_{D2}\dot{y}_2 \\ -\tau_h \end{bmatrix}, \quad (\text{D.12})$$

where C_{D1} and C_{D2} are linear drag coefficients for each body.

D.1.4 Model Integration

First the state vector \mathbf{q} and state velocity vector $\dot{\mathbf{q}}$ are initialized with valid values, i.e. ones that do not violate the system’s kinematic constraints. For this analysis I assume that the bodies start at rest, $\dot{\mathbf{q}} = \mathbf{0}$. The initial position of body 1 and the orientations of both bodies are specified. The position of body 2 is calculated from

$$\mathbf{r}_2 = \mathbf{r}_1 + \mathbf{B}_1 \mathbf{R}_1^p - \mathbf{B}_2 \mathbf{R}_2^p. \quad (\text{D.13})$$

Next, the second order system is converted to a set of coupled first order ODEs by creating a new state vector \mathbf{y} such that

$$\mathbf{y} = \begin{bmatrix} \mathbf{q} \\ \dot{\mathbf{q}} \end{bmatrix}. \quad (\text{D.14})$$

Therefore,

$$\dot{\mathbf{y}} = \begin{bmatrix} \dot{\mathbf{q}} \\ \ddot{\mathbf{q}} \end{bmatrix}. \quad (\text{D.15})$$

The initial state and velocity vector can be used to create the initial \mathbf{y} value. $\Phi(\mathbf{q})$, $\dot{\Phi}_d(\mathbf{q})$, $\Phi_d(\mathbf{q})$, $\mathbf{g}(\mathbf{q}, \dot{\mathbf{q}}, t)$, and $\gamma(\mathbf{q}, \dot{\mathbf{q}})$ can be found from this initial state. This allows the system (D.10) to be solved for the initial values of $\ddot{\mathbf{q}}$ and λ using a linear system solver like MATLAB’s ‘‘linsolve’’ function. Once $\ddot{\mathbf{q}}$ is known, $\dot{\mathbf{y}}$ can be specified. At this point there is

enough information to integrate the system forward by Euler's Method or Improved Euler's Method.

$$\mathbf{y}_{k+1} = \mathbf{y}_k + \dot{\mathbf{y}}_k dt, \quad (\text{D.16})$$

or

$$\begin{aligned} \mathbf{y}_{start} &= \mathbf{y}, \\ \mathbf{y}_{temp} &= \mathbf{y}_k + \dot{\mathbf{y}}_k dt, \\ \dot{\mathbf{y}}_{temp} &= \text{recalculate } \mathbf{g} \text{ and solve (D.10) based on } \mathbf{y}_{temp}, \\ \mathbf{y}_{k+1} &= \mathbf{y}_{start} + 0.5(\dot{\mathbf{y}}_k + \dot{\mathbf{y}}_{temp}) dt. \end{aligned} \quad (\text{D.17})$$

D.1.5 Applying a Moment to the Hinge

If no moment is applied at the hinge, τ_h in the force vector \mathbf{g} , then the pivot is modeled as a frictionless joint. If a moment is applied to the hinge, equal and opposite moments are applied to each body in (D.12). This moment can be applied as a function of time, simulating a driving actuator. Alternatively, this moment could be applied as a function of the state vector \mathbf{q} . For example, a model of a rotational spring with some linear viscous friction could be written as

$$\tau_h = k(\theta_1 - \theta_2) + b(\dot{\theta}_1 - \dot{\theta}_2). \quad (\text{D.18})$$

Where k is the rotational spring constant for the joint and b is the linear viscous damping coefficient for the joint.

D.1.6 Applying a Driving Constraint to the Hinge

Driving constraints are discussed in Sections 3.2.2, 4.2.8, and 4.3 of [20]. Driving constraints are additional constraints placed on the system to enforce a particular trajectory for some or all of the DOFs. Driving constraints have the form

$$\Phi^{(d)}(\mathbf{q}, t) = 0, \quad (\text{D.19})$$

where the superscript (d) indicates terms associated with the driving constraints. These additional time dependent constraints can be included in (D.10) in a modified form as

$$\boxed{\begin{bmatrix} \mathbf{M} & \Phi_q^T & \Phi_q^{(d)T} \\ \Phi_q & \mathbf{0} & \mathbf{0} \\ \Phi_q^{(d)} & \mathbf{0} & \mathbf{0} \end{bmatrix} \begin{bmatrix} \ddot{\mathbf{q}} \\ -\lambda \\ -\lambda^{(d)} \end{bmatrix} = \begin{bmatrix} \mathbf{g} \\ \gamma - 2\alpha\dot{\Phi} - \beta^2\Phi \\ \gamma^{(d)} - 2\alpha\dot{\Phi}^{(d)} - \beta^2\Phi^{(d)} \end{bmatrix}}, \quad (\text{D.20})$$

where $\gamma^{(d)}$ is created by grouping driving constraint terms from [20, eqn (3.16)] resulting in

$$\boxed{\gamma^{(d)} = -\left(\Phi_q^{(d)}\dot{\mathbf{q}}\right)_q \dot{\mathbf{q}} - 2\Phi_{qt}^{(d)}\dot{\mathbf{q}} - \Phi_{tt}^{(d)}}. \quad (\text{D.21})$$

The Lagrange multipliers associated with the driving constraints, $\lambda^{(d)}$, give the forces (or moments) required to enforce the driving constraints and produce the required trajectory. These values can be used to calculate the power required for the actuator and to ensure that its load capacity is not exceeded.

D.1.7 Driving the Hinge's Position Directly

Applying a moment to the hinge is one method of modeling the actuator. It is a good method if the system is torque limited. However, there are many cases where the actuators are not torque limited or where the desired command to the actuator system is a position or velocity command. In these cases we can use driving constraints to command the two body system.

If the actuator has a much faster time constant than the system and is sufficiently strong, it can be assumed that it can drive the hinge to any angle. This can be modeled as a driving constraint of the form

$$\Phi^{(d)} = \theta_1 - \theta_2 - d(t) = 0. \quad (\text{D.22})$$

The Jacobian matrix of this constraint is

$$\begin{aligned} \Phi_q^{(d)} &= \begin{bmatrix} \frac{\partial \Phi^{(d)}}{\partial x_1} & \frac{\partial \Phi^{(d)}}{\partial y_1} & \frac{\partial \Phi^{(d)}}{\partial \theta_1} & \frac{\partial \Phi^{(d)}}{\partial x_2} & \frac{\partial \Phi^{(d)}}{\partial y_2} & \frac{\partial \Phi^{(d)}}{\partial \theta_2} \end{bmatrix} \\ &= \begin{bmatrix} 0 & 0 & 1 & 0 & 0 & -1 \end{bmatrix}. \end{aligned} \quad (\text{D.23})$$

The other required parameters are

$$\dot{\Phi}^{(d)} = \Phi^{(d)} \dot{\mathbf{q}} = \dot{\theta}_1 - \dot{\theta}_2, \quad (\text{D.24})$$

$$\left(\Phi^{(d)} \dot{\mathbf{q}} \right)_q = \mathbf{0}, \quad (\text{D.25})$$

$$\Phi_{qt}^{(d)} = \mathbf{0}, \quad (\text{D.26})$$

$$\Phi_{tt}^{(d)} = -\ddot{d}(t). \quad (\text{D.27})$$

So the lower block on the RHS of (D.20) is

$$\ddot{d}(t) - 2\alpha (\dot{\theta}_1 - \dot{\theta}_2) - \beta^2 (\theta_1 - \theta_2 - d(t)). \quad (\text{D.28})$$

Moments can still be applied to the hinge in the presence of the driving constraint. For example the spring and friction moments described by (D.18) can still be included in the model. While these moments will not change the position of the hinge over time, their effects will be included in the calculation of the required driving moment, $\lambda^{(d)}$.

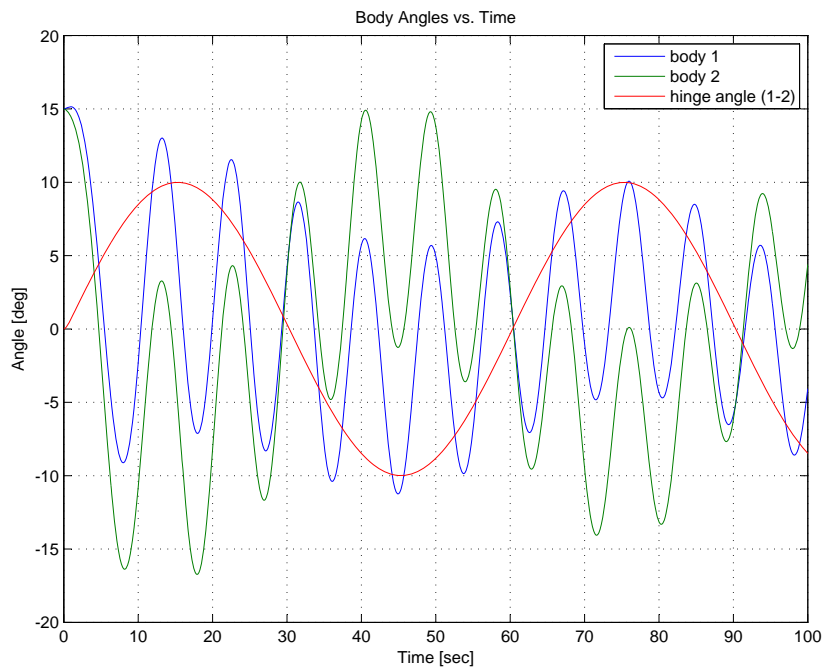


Figure D.2: Body and hinge angles vs. time for a planar example. Both bodies start out inclined at an angle of 15 degrees. The hinge is driven by sine function of amplitude 10 degrees and period 60 seconds. Body 2 has more drag and less mass and inertia. The body angles indicated that the composite body is oscillating back and forth as it falls.

D.2 Spatial Solution Using Constraint Equations

Using constraint equations, the spatial solution is very similar to the planar solution. The major differences are: the rotational acceleration equation is more complicated and allows for coupling between the axes, the system inertia is described as a tensor, and the constraint equations are more complicated.

A big difference between the spatial buoy model presented here and the model presented elsewhere in this research is that that joint here is modeled as an elevation over azimuth joint.

D.2.1 Problem Geometry

Consider a pair of rigid bodies each with 6 degrees of freedom (DOF), three translational and three rotational. These two bodies are connected by a joint that only permits rotation about two axes. Modeling this joint requires four constraint equations: three to eliminate translational motion between the bodies, and one to eliminate an axis of rotation between the bodies.

This results in an system with 8 independent variables (12 eqns - 4 eqns) and requires solving 16 simultaneous equation (12 eqns + 4 eqns). This analysis draws heavily on the work in [20].

Body 1 is the buoy housing (the lower cylinder). Body 2 is the payload (the upper cylinder). Each body has a pivot point associated with it. The pivot point is described by the vector \mathbf{R}_{p1} in the housing coordinate system. The pivot point is described by the vector \mathbf{R}_{p2} in the payload coordinate system. The orientation of these vectors in the global coordinate system are \mathbf{s}_1^p and \mathbf{s}_2^p respectively.

Two sets of constraints are used to model the joint. A spherical constraint is used to enforce the condition that the pivot points on each body are collocated with each other, and no translation is permitted between the bodies. This constraint provides three of the required four constraint equations. The fourth constraint equation determines the type of joint.

If the joint is an *elevation over azimuth* type joint, the fourth constraint equation is that, in the navigation frame, the payload's y axis is perpendicular to the housing's z axis. If the joint is a *universal* (a.k.a. Hooke) joint, the fourth constraint is that the payload's y axis is perpendicular to the housing's x axis.

The direction of the joint axes are specified by the unit vectors \mathbf{S}_1 and \mathbf{S}_2 in their respective body's coordinate systems. The unit vectors \mathbf{s}_1 and \mathbf{s}_2 describe the axes orientation in the navigation coordinate system. An example of these vectors are illustrated on an elevation over azimuth joint in Figure D.3.

D.2.2 The Joint Constraint Equations

The joint imposes four kinematic constraint equations on the system. In all the constraint equations, vectors are in the global coordinate system. These are

$$\Phi^{(s,3)} \equiv \mathbf{r}_1 + \mathbf{B}_1 \mathbf{R}_{p1} - \mathbf{B}_2 \mathbf{R}_{p2} - \mathbf{r}_2 = 0, \quad (\text{D.29})$$

$$\Phi^{(n1,1)} \equiv \mathbf{s}_1^T \mathbf{s}_2 = 0. \quad (\text{D.30})$$

The constraint described in (D.29) requires that the pivot points on each body be collocated in the global coordinate system. See [20, eqn (7.7)]. The superscript $^{(s,3)}$ is

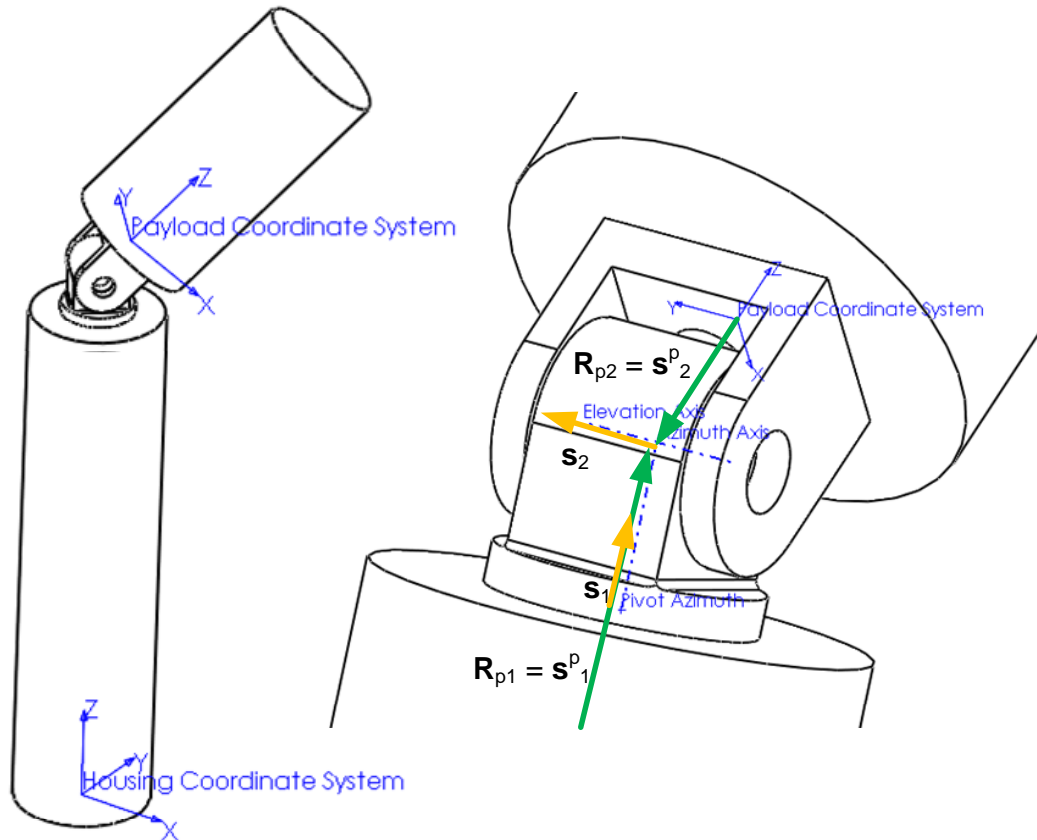


Figure D.3: Elevation over azimuth joint geometry for solving by constraint equations. The housing and payload are connected by a spherical joint with an additional constraint. The azimuth axis, s_1 , is collinear with the long axis of the housing. The elevation axis, s_2 , is perpendicular to the azimuth axis and parallel to the Y axis of the payload coordinate system.

the notation used in [20] and indicates that this is a spherical constraint with 3 constraint equations.

The constraint described in (D.30) requires that the joint axis, \mathbf{s}_1 , remains perpendicular to the other joint axis, \mathbf{s}_2 . See [20, eqn (7.3)]. The super script $^{(n1,1)}$ indicates that this is a type 1 normal constraint with 1 constraint equation. The housing axis that \mathbf{s}_1 is aligned with determines the joint type. If \mathbf{s}_1 is parallel to the housing's X axis then the joint is a universal joint. If \mathbf{s}_1 is parallel to the housing's Z axis then the joint is an elevation over azimuth joint. These values for \mathbf{s}_1 can be obtained directly from the 1st and 3rd columns of the housing's DCM, \mathbf{B}_1 .

D.2.3 The Kinematically Constrained Dynamics

The translational equations of motion (EOM) for the spatial case are the same as for the planar case, except the third dimension is added giving

$$\mathbf{N}_i \ddot{\mathbf{r}}_i = \mathbf{f}_i, \quad (\text{D.31})$$

where \mathbf{N}_i is the diagonal mass matrix of body i , $\mathbf{N}_i = \text{diag}[m, m, m]$.

Chapter 11 of [20] gives three possible formulations for the rotational spatial equations of motion. Formulation I gives the rotational EOMs in terms of the acceleration of the Euler parameters. But since the four Euler parameters are not independent, this leads to Formulation II, which adds a constraint equation to the Formulation I system to enforce the correct relationship between the Euler parameters. Formulation III, however, leaves the EOMs in terms of the rotational velocities (and accelerations) in the body's local coordinate frame. This formulation is most compatible with the rest of the buoy model and it results in fewer equations to solve, so it is used here. It is

$$\mathbf{J}_i \dot{\hat{\boldsymbol{\Omega}}}_i + \hat{\boldsymbol{\Omega}}_i \mathbf{J}_i \boldsymbol{\Omega}_i = \mathbf{T}_i, \quad (\text{D.32})$$

where \mathbf{J}_i is the inertia tensor of body i , $\boldsymbol{\Omega}_i$ is the rotational velocity vector, and \mathbf{T}_i is the applied torque vector. All terms are in body i 's coordinate system.

The system of equations for multiple constrained bodies is given by [20, eqn (11.49)], and adding the constraint stabilization terms from [20, eqn (13.18)] gives¹

$$\boxed{\begin{bmatrix} \mathbf{M} & \boldsymbol{\Phi}^{(m)T} \\ \boldsymbol{\Phi}^{(m)} & \mathbf{0} \end{bmatrix} \begin{bmatrix} \dot{\mathbf{h}} \\ -\lambda \end{bmatrix} + \begin{bmatrix} \mathbf{b} \\ \mathbf{0} \end{bmatrix} = \begin{bmatrix} \mathbf{g} \\ \gamma^\# - 2\alpha\dot{\boldsymbol{\Phi}} - \beta^2\boldsymbol{\Phi} \end{bmatrix}}, \quad (\text{D.33})$$

where \mathbf{M} is the system mass matrix consisting of the inertia tensors and masses of each body,

$$\mathbf{M} = \begin{bmatrix} \mathbf{N}_1 & & & \\ & \mathbf{J}_1 & & \\ & & \dots & \\ & & & \mathbf{N}_b \\ & & & & \mathbf{J}_b \end{bmatrix}. \quad (\text{D.34})$$

¹In [20, eqn (11.49)] the variable \mathbf{B} is used for the Jacobian matrix of the constraints. Later in table 11.1 he uses $\boldsymbol{\Phi}^{(m)}$ for the individual blocks of that matrix. So I am using $\boldsymbol{\Phi}^{(m)}$ to represent the complete formulation III modified Jacobian matrix of the constraint equations.

$\dot{\mathbf{h}}$ is the state vector of the bodies translational and rotational *accelerations* of the form

$$\dot{\mathbf{h}} = \begin{bmatrix} \ddot{\mathbf{r}}_1 \\ \dot{\hat{\boldsymbol{\Omega}}}_1 \\ \vdots \\ \ddot{\mathbf{r}}_b \\ \dot{\hat{\boldsymbol{\Omega}}}_b \end{bmatrix}. \quad (\text{D.35})$$

Note: The forces and translational accelerations are in the global navigation coordinate system and the moments and angular accelerations are in the individual body coordinate systems!

The term \mathbf{b} in (D.33) is

$$\mathbf{b} = \begin{bmatrix} \mathbf{0} \\ \hat{\boldsymbol{\Omega}}_1 \mathbf{J}_1 \boldsymbol{\Omega}_1 \\ \vdots \\ \mathbf{0} \\ \hat{\boldsymbol{\Omega}}_b \mathbf{J}_b \boldsymbol{\Omega}_b \end{bmatrix}. \quad (\text{D.36})$$

As in the planar case λ are the Lagrange multipliers associated with each of the constraints. \mathbf{g} are the forces and moments associated with each body in their coordinate systems.

The matrix $\boldsymbol{\Phi}^{(m)}$ is a modified form of the the Jacobian Matrix of the constraint equations which has the general form of

$$\boldsymbol{\Phi}^{(m)} = \left[\boldsymbol{\Phi}_{r1} \quad \frac{1}{2} \boldsymbol{\Phi}_{p1} \mathbf{L}_1^T \quad \cdots \quad \boldsymbol{\Phi}_{rb} \quad \frac{1}{2} \boldsymbol{\Phi}_{pb} \mathbf{L}_b^T \right]. \quad (\text{D.37})$$

The vector $\gamma^\#$ is a modified form of the RHS of the kinematic acceleration equations and has the general form

$$\gamma^\# = \left[\boldsymbol{\Phi}_{r1} \quad \frac{1}{2} \boldsymbol{\Phi}_{p1} \mathbf{L}_1^T \quad \cdots \quad \boldsymbol{\Phi}_{rb} \quad \frac{1}{2} \boldsymbol{\Phi}_{pb} \mathbf{L}_b^T \right] \begin{bmatrix} \ddot{\mathbf{r}}_1 \\ \dot{\hat{\boldsymbol{\Omega}}}_1 \\ \vdots \\ \ddot{\mathbf{r}}_b \\ \dot{\hat{\boldsymbol{\Omega}}}_b \end{bmatrix} = \boldsymbol{\Phi}^{(m)} \dot{\mathbf{h}}. \quad (\text{D.38})$$

Table 11.1 in [20] gives formulations of the elements of $\boldsymbol{\Phi}^{(m)}$ and $\gamma^\#$ for a number of common spatial constraints. The terms for the constraints in the buoy joint are listed in Table D.2. The rotation rates for the modified Jacobian matrix are specified in the navigation coordinate system, *not* the body coordinate system, and they found for each body by $\omega_i = \mathbf{B}_i \boldsymbol{\Omega}_i$.

Table D.2: Components of the modified Jacobian matrix, $\boldsymbol{\Phi}^{(m)}$, and modified RHS of the kinematic acceleration matrix $\gamma^\#$ for the type of constraints in the buoy's joint. The rotation rates, ω_i , are specified in the navigation coordinate system. From [20, Table 11.1]

$\boldsymbol{\Phi}$	$\boldsymbol{\Phi}_{ri}^{(m)}$	$\frac{1}{2} \boldsymbol{\Phi}_{pi}^{(m)} \mathbf{L}_i^T$	$\boldsymbol{\Phi}_{rj}^{(m)}$	$\frac{1}{2} \boldsymbol{\Phi}_{pj}^{(m)} \mathbf{L}_j^T$	$\gamma^\#$
$\boldsymbol{\Phi}^{(s,3)}$	\mathbf{I}	$-\hat{\mathbf{s}}_i^P \mathbf{B}_i$	$-\mathbf{I}$	$\hat{\mathbf{s}}_j^P \mathbf{B}_j$	$-\hat{\omega}_i \dot{\mathbf{s}}_i^P + \hat{\omega}_j \dot{\mathbf{s}}_j^P$
$\boldsymbol{\Phi}^{(n1,1)}$	$\mathbf{0}^T$	$-\mathbf{s}_i^T \hat{\mathbf{s}}_i \mathbf{B}_i$	$\mathbf{0}^T$	$-\mathbf{s}_i^T \hat{\mathbf{s}}_j \mathbf{B}_j$	$-2\dot{\mathbf{s}}_i^T \dot{\mathbf{s}}_j + \dot{\mathbf{s}}_i^T \hat{\omega}_i \mathbf{s}_j + \dot{\mathbf{s}}_j^T \hat{\omega}_j \mathbf{s}_i$

D.2.4 Calculating Buoy Specific $\Phi^{(m)}$ and $\gamma^\#$

Table D.2 presents the components of the modified Jacobian matrix and RHS of the kinematic acceleration matrix exactly as they appear in [20]. All the vectors in Table D.2 are in global coordinates. Calculating all the required terms gives:

$$\mathbf{s}_k = \mathbf{B}_k \mathbf{S}_k, \quad (\text{D.39})$$

$$\dot{\mathbf{s}}_k = \mathbf{B}_k \hat{\boldsymbol{\Omega}}_k \mathbf{S}_k, \quad (\text{D.40})$$

$$\dot{\mathbf{B}}_k = \mathbf{B}_k \hat{\boldsymbol{\Omega}}_k, \quad (\text{D.41})$$

$$\mathbf{s}_k^p = \mathbf{B}_k \mathbf{R}_{pk}, \quad (\text{D.42})$$

where $k = i$ or j .

So substituting (D.42) in the expressions for $\Phi^{(m)}$ and $\gamma^\#$ to put the locations of the joint pivot points in consistent notation gives:

$$\Phi^{(m)} = \begin{bmatrix} \mathbf{I} & -\hat{\mathbf{s}}_1^P \mathbf{B}_1 & -\mathbf{I} & \hat{\mathbf{s}}_2^P \mathbf{B}_2 \\ \mathbf{0}^T & -\mathbf{s}_2^T \hat{\mathbf{s}}_1 \mathbf{B}_1 & \mathbf{0}^T & -\mathbf{s}_1^T \hat{\mathbf{s}}_2 \mathbf{B}_2 \end{bmatrix}, \quad (\text{D.43})$$

$$\gamma^\# = \begin{bmatrix} -\hat{\omega}_1 \hat{\mathbf{s}}_1^P + \hat{\omega}_2 \hat{\mathbf{s}}_2^P \\ -2\hat{\mathbf{s}}_1^T \hat{\mathbf{s}}_2 + \hat{\mathbf{s}}_1^T \hat{\omega}_1 \mathbf{s}_2 + \hat{\mathbf{s}}_2^T \hat{\omega}_2 \mathbf{s}_1 \end{bmatrix}. \quad (\text{D.44})$$

Again, the rotation rates, ω_i , are specified in the navigation coordinate system.

D.2.5 Joint Angles and Angular Rates

In modeling the joint it is desirable to be able to calculate the relative angle between the two bodies, or the joint angles. In the physical realization of this system the joint's azimuth and elevation angles would be read by motor encoders and are the primary feedback signals for calculating the control of the payload. Given that the attitude of each body is described by the direction cosine matrices \mathbf{B}_1 and \mathbf{B}_2 which describe the orientation of the housing and payload bodies respectively in the global navigation coordinate system, the DCM describing the rotation from housing to payload can be calculated as:

$$\mathbf{B} = \mathbf{B}_1^T \mathbf{B}_2. \quad (\text{D.45})$$

Once the DCM \mathbf{B} is known, the joint angles are calculated by the usual conversion between DCM and Euler angles.

It is also desired to know the rotation rates of the joint, which can be calculated as

$$\begin{aligned} \dot{\mathbf{B}} &= \dot{\mathbf{B}}_1^T \mathbf{B}_2 + \mathbf{B}_1^T \dot{\mathbf{B}}_2 \\ &= (\mathbf{B}_1 \hat{\boldsymbol{\Omega}}_1)^T \mathbf{B}_2 + \mathbf{B}_1^T \mathbf{B}_2 \hat{\boldsymbol{\Omega}}_2 \\ &= \hat{\boldsymbol{\Omega}}_1^T \mathbf{B}_1^T \mathbf{B}_2 + \mathbf{B}_1^T \mathbf{B}_2 \hat{\boldsymbol{\Omega}}_2, \\ &= \hat{\boldsymbol{\Omega}}_1^T \mathbf{B} + \mathbf{B} \hat{\boldsymbol{\Omega}}_2. \end{aligned} \quad (\text{D.46})$$

It is important to realize that $\dot{\mathbf{B}}$ is **not** a valid DCM. For example if both bodies are stationary, then $\boldsymbol{\Omega}_1 = \boldsymbol{\Omega}_2 = \mathbf{0}$ and therefore $\dot{\mathbf{B}} = \mathbf{0}$. Once $\dot{\mathbf{B}}$ is known, the joint angular rate can be calculated by

$$\begin{aligned} \dot{\mathbf{B}} &= \mathbf{B} \hat{\boldsymbol{\Omega}} \\ \hat{\boldsymbol{\Omega}} &= \mathbf{B}^T \dot{\mathbf{B}}, \end{aligned} \quad (\text{D.47})$$

where the individual angular rate are the appropriate terms of $\hat{\boldsymbol{\Omega}}$.

D.2.6 Integrating the Model Forward

(D.33) is solved at each time step to find the translational and rotational accelerations associated with each body. These accelerations are used to integrate the system states forward to the next time step. The acceleration equations describe a system of second order ODEs. The second order system is converted to a system of first order ODEs to facilitate numerical integration. *In this section \mathbf{r} refers to the location of the center of mass, \mathbf{r}_{cm} , of the body unless otherwise noted.*

Recall the acceleration vector specified by (D.35),

$$\dot{\mathbf{h}} = \begin{bmatrix} \ddot{\mathbf{r}}_1 \\ \dot{\mathbf{\Omega}}_1 \\ \ddot{\mathbf{r}}_2 \\ \dot{\mathbf{\Omega}}_2 \end{bmatrix}.$$

So the vector of derivatives for the first order system is

$$\dot{\mathbf{y}} = \begin{bmatrix} \dot{\mathbf{r}}_1 \\ \mathbf{\Omega}_1 \\ \dot{\mathbf{r}}_2 \\ \mathbf{\Omega}_2 \\ \ddot{\mathbf{r}}_1 \\ \dot{\mathbf{\Omega}}_1 \\ \ddot{\mathbf{r}}_2 \\ \dot{\mathbf{\Omega}}_2 \end{bmatrix}, \quad (\text{D.48})$$

where $\ddot{\mathbf{r}}_1$, $\dot{\mathbf{\Omega}}_1$, $\ddot{\mathbf{r}}_2$, and $\dot{\mathbf{\Omega}}_2$, were from the solution to (D.33); and $\dot{\mathbf{r}}_1$, $\mathbf{\Omega}_1$, $\dot{\mathbf{r}}_2$, and $\mathbf{\Omega}_2$ were the velocity values used in the calculation of (D.33). These derivative vectors allow the integration of each body's position and attitude by:

$$\mathbf{r}_{k+1} = \mathbf{r}_k + \dot{\mathbf{r}}_k \Delta t, \quad (\text{D.49})$$

$$\mathbf{B}_{i\ k+1} = \mathbf{B}_{i\ k} + \mathbf{B}_{i\ k} \tilde{\mathbf{\Omega}}_k \Delta t, \quad (\text{D.50})$$

$$\dot{\mathbf{r}}_{k+1} = \dot{\mathbf{r}}_k + \ddot{\mathbf{r}}_k \Delta t, \quad (\text{D.51})$$

$$\mathbf{\Omega}_{k+1} = \mathbf{\Omega}_k + \dot{\mathbf{\Omega}}_k \Delta t. \quad (\text{D.52})$$

i is the body's subscript identifier.

D.2.7 Using Improved Euler

Section D.2.6 is an implementation of Euler's method for integration. It is useful in the initial development of the model. However, the numerical instabilities that can occur when using it are not desirable. To improve the numerical stability, the model is integrated forward using the Improved Euler's method as follows:

1. Calculate the forces and moments applied to the bodies based on their state information based at the start of the time step.
2. Calculate $\Phi_q^{(m)}$, Φ , $\dot{\Phi}$, and $\gamma^\#$ from the state information at the start of the time step.

3. Make a working copy of the state information for each body.
4. Integrate the working copy forward using Euler's method, by solving (D.33) and applying (D.49) through (D.52).
5. Using the working copy state information, calculate $\Phi_q^{(m)}$, Φ , $\dot{\Phi}$, and $\gamma^\#$.
6. Solve (D.33) using the working copy states and the updated $\Phi_q^{(m)}$, Φ , $\dot{\Phi}$, and $\gamma^\#$ values.
7. Average the velocity and acceleration values found in steps 4 and 6.
8. Integrate the original body state information forward using the *average* derivative values and (D.49) through (D.52).

It should be clear that the applied forces and moments are assumed to be piecewise constant over the time step. Calculating them is significantly more computationally intensive than other parts of model, so the piecewise constant assumption only requires computing them once per time step.

Appendix E

Use of a Tuned Mass Damper

It should be possible to dampen the buoy's resonant peak response by using a tuned mass damper (TMD). The TMD can be tuned to adjust the passive characteristics of the buoy's vertical oscillation. The use of tuned mass dampers to reduce vibration is a well established practice. The patent for a sprung mass to reduce the motion of structure was first awarded in 1909 to Frahm [10]. In 1928, Ormondroyd and Den Hartog [2] show that adding a damper increases the frequency interval over which the sprung mass is effective (in addition to dissipating energy from the structure). The basic principles of the vibration damper are presented in texts on vibrations such as [18, p. 240] and [3, p.145-149]. There are countless examples in the literature of tuned mass dampers being used to improve the response of many types of structures. Frequency analysis of tuned mass dampers is presented by Krenk in [15].

Implementing a tuned mass damper in the two body buoy simulation would make the system into a three body simulation. The direct solution simulation framework presented in Chapter 2 is not equipped to handle this. Rather this would be best implemented by using the method of constraint equations to solve for the multi-body system's dynamics. The method of constraint equations is introduced and summarized in Appendix D.

However, as a starting point to understand how a tuned mass damper might improve the buoy's vertical response, we can perform some initial analysis by modeling the buoy as a single-body cylinder. With this simplifying assumption we can proceed.

It has been shown in Section 2.9 that the damped frequency of oscillation for a cylinder floating in the water will be similar to its natural frequency which is given by

$$\omega_d \approx \omega_n = R\sqrt{\frac{\pi\rho g}{m}}. \quad (\text{E.1})$$

This result was derived using a simple second order model for the system of

$$\ddot{z} + \frac{d}{m}\dot{z} + \frac{k}{m}z = 0, \quad (\text{E.2})$$

where $k = \pi\rho gR^2$ and the usual second order system relationships of $\omega_n = \sqrt{k/m}$, $2\xi\omega_n = d/m$, and $\omega_n^2 = \omega_d^2 + (\xi\omega_n)^2$ apply. ξ is the damping ratio of the system.

Adding a TMD to the cylinder to attempt to dampen its response would result in a two mass system. Such a two mass system is similar to the one presented by Friedland in [11, Example 3H, p. 86].

This system is illustrated in Figure E.1. In this construct, m_1 is the mass of the cylinder *without* the TMD. m_2 is the mass of the TMD. k_1 is the "spring constant" associated with

the restoring action due to the buoyant force on the cylinder and $k_1 = \pi\rho gR^2$. d_1 is the viscous drag between the cylinder and water. It is typically very small. k_2 and d_2 are spring and damping effects between the TMD, m_2 , and the rest of the cylinder. It is expected that k_2 and d_2 could be tuned by the designer to provide the desired response.

The model also allows for the possibility of two active control forces being applied to the system. f_1 is a force applied to the cylinder in the vertical direction. This could be from a vertical thruster for example. f_2 is a force applied between the TMD and the cylinder. A positive value of f_2 pushes the TMD and cylinder further apart. *For all of the following analysis f_2 will be set to zero.* The external force f_1 will be used to drive the impulse response and the generate Bode plots for the system.

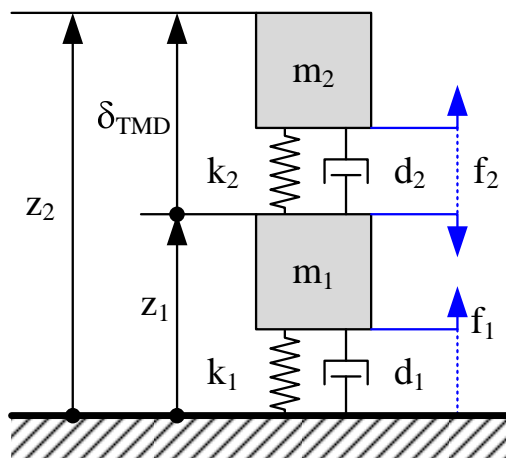


Figure E.1: The tuned mass damper model for controlling the resonant peak of vertical oscillation for a cylindrical buoy. For all the analysis presented here, the force f_2 is assumed to be zero.

The variables z_1 and z_2 specify the distances from the equilibrium heights for m_1 and m_2 respectively. Both z_1 and z_2 are referenced to ground. An alternate variable δ_{TMD} is defined as the difference in m_2 from it equilibrium point *with respect to the cylinder*. δ_{TMD} is calculated as

$$\delta_{TMD} = z_2 - z_1. \quad (\text{E.3})$$

We can write the equations of motion (EOM) for each mass using Newton's second law

$$m_1 \ddot{z}_1 = -d_1 \dot{z}_1 - k_1 z_1 + d_2 (\dot{z}_2 - \dot{z}_1) + k_2 (z_2 - z_1) + f_1 - f_2, \quad (\text{E.4})$$

$$m_2 \ddot{z}_2 = -d_2 (\dot{z}_2 - \dot{z}_1) - k_2 (z_2 - z_1) + f_2. \quad (\text{E.5})$$

To write the system in the standard form of $\dot{\mathbf{x}} = \mathbf{Ax} + \mathbf{Bu}$ we can define the state vector

\mathbf{x} , the control vector \mathbf{u} , and the system matrices \mathbf{A} and \mathbf{B} as

$$\mathbf{x} = [z_1 \quad z_2 \quad \dot{z}_1 \quad \dot{z}_2]^T, \quad (\text{E.6})$$

$$\mathbf{u} = [f_1 \quad f_2]^T, \quad (\text{E.7})$$

$$\mathbf{A} = \begin{bmatrix} 0 & 0 & 1 & 0 \\ 0 & 0 & 0 & 1 \\ -(k_1 + k_2)/m_1 & k_2/m_1 & -(d_1 + d_2)/m_1 & d_2/m_1 \\ k_1/m_2 & -k_2/m_2 & d_2/m_2 & -d_2/m_2 \end{bmatrix}, \quad (\text{E.8})$$

$$\mathbf{B} = \begin{bmatrix} 0 & 0 \\ 0 & 0 \\ 1/m_1 & -1/m_1 \\ 0 & 1/m_2 \end{bmatrix}. \quad (\text{E.9})$$

Next we can compare the performance of a cylinder with a tuned mass damper to one without. The single mass system can be described by the state and input matrices

$$\mathbf{x} = [z \quad \dot{z}]^T, \quad (\text{E.10})$$

$$\mathbf{u} = [f_1], \quad (\text{E.11})$$

$$\mathbf{A} = \begin{bmatrix} 0 & 1 \\ -k_1/m & -d_1/m \end{bmatrix}, \quad (\text{E.12})$$

$$\mathbf{B} = \begin{bmatrix} 0 \\ 1/m \end{bmatrix}, \quad (\text{E.13})$$

where k_1 and d_1 are the same as in the two mass system presented above in (E.6) through (E.9) and m is the total system mass. The parameters for both systems are presented in Table E.1. The parameters match the prototype buoy configuration. The tuned mass, m_2 , is the mass of the prototype buoy's battery. The damping term, d_1 , is selected to give a reasonable settling time for the buoy.

Table E.1: Model parameters for a cylindrical buoy with and without a tuned mass damper. The parameters match the prototype buoy configuration. The tuned mass, m_2 , is the mass of the prototype buoy's battery. The damping term, d_1 , is selected to give a reasonable settling time for the buoy.

Parameter	Variable	Cylinder w/o TMD	Cylinder w/ TMD
mass (kg)	m	2.546	2.546
radius (m)	R	0.0397	0.0397
restoring term (kg/s^2)	k_1	48.52	48.52
damping term (kg/s)	d_1	0.25	0.25
TMD mass (kg)	m_2	N/A	1.0
TMD spring (kg/s^2)	k_2	N/A	Various
TMD damper (kg/s)	d_2	N/A	Various

Using MATLAB's `impz` and `bode` commands we can compare the two systems' impulse responses and Bode plots to see the effects of using a tuned mass damper with various k_2 and d_2 values. Again, in the cylinder with the TMD, the force f_2 is set to zero and the force f_1 is used to drive the impulse response and Bode plots. In the pair of plots that

follow, the TMD spring constant, k_2 , is specified as a multiple of the cylinder's buoyant restoring constant, k_1 . Likewise, the TMD damping constant, d_2 , is specified as a multiple of the cylinder's damping constant, d_1 .

In Figure E.2 the TMD has a mass of 0.39 times of the system mass, a spring constant equal to the buoyant restoring constant, and damping constant of 30 times that of the cylinder's viscous drag in the water.

With this configuration, the TMD has improved the system performance by 1) reducing the magnitude of the resonant peak by over 14 dB, and 2) decreasing the settling time from just under 80 seconds, to 17.3 seconds. The resonant frequency is almost unchanged. It shifted from 4.37 rad/s (a 1.43 second period) to 4.09 rad/s (a 1.53 second period). The TMD has caused the resonant peak to get wider. This illustrates one way in which a tuned mass damper can be used to shape a structure's response, by reducing the magnitude of the resonant peak.

In Figure E.3 the TMD has a spring constant equal to three times buoyant restoring constant, and damping constant equal to the cylinder's viscous drag in the water.

With this configuration, the TMD has improved the system performance by 1) reducing the magnitude of the frequency response by approximately 10 dB up to a frequency of 6.55 rad/s (a 0.96 second period), 2) shifting the resonant peak to a significantly higher frequency of 8.2 rad/s (a 0.77 second period), and 3) very slightly reducing the magnitude of the resonant peak (by 2 dB). However, the TMD has caused the system's settling time to increase to 117 seconds. This illustrates another way in which a tuned mass damper can be used to shape a structure's response, by shifting the location of the resonant peak to a frequency that the structure is less likely to encounter.

Finally, when designing a tuned mass damper, it is important to check the magnitude of the relative motion between the damper's mass and the underlying structure to ensure that the damper does not exceed its available travel and render the analysis invalid. This relative translation is calculated by finding δ_{TMD} in (E.3). Plots of the δ_{TMD} vs. time for the two TMD implementations discussed above are shown in Figure E.4. The implementation with the stiffer spring and weaker drag (blue) requires approximately ± 4 cm of travel (or 3.2 inches of total travel). While the implementation with the weaker spring and more drag only requires ± 3 cm of travel (or 2.4 inches of total travel). As a first pass it seems reasonable to allow for this much travel of the prototype buoy configuration's battery within the housing.

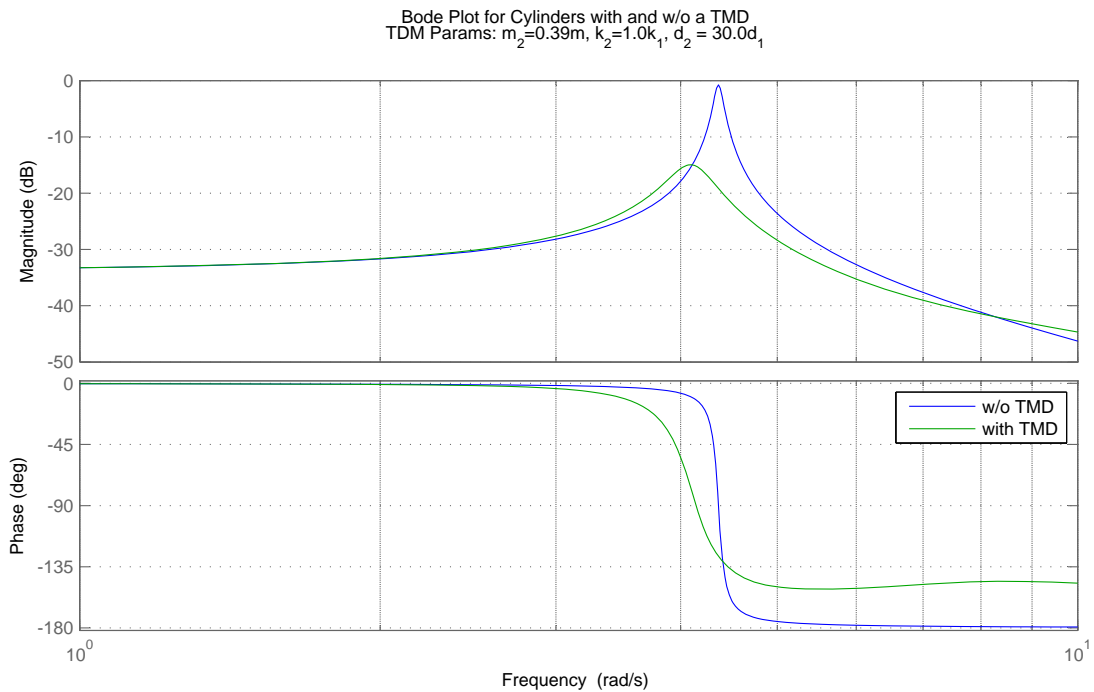
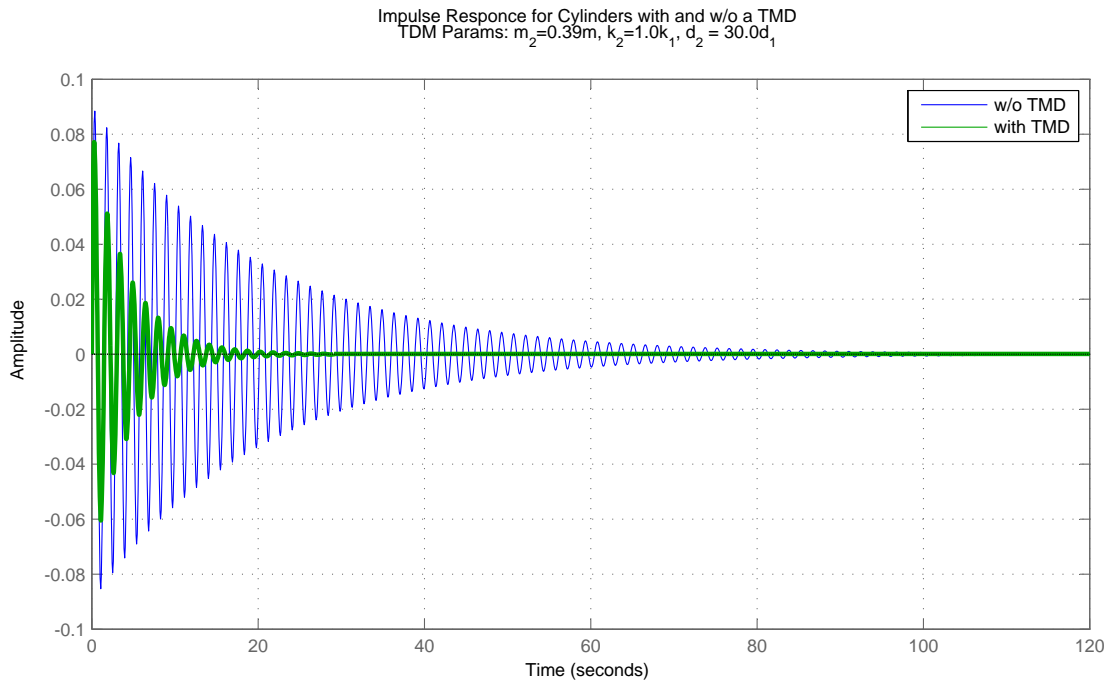


Figure E.2: The impulse response and Bode plots showing how a tuned mass damper could be used to improve a cylindrical buoy's settling time and reduce the magnitude of its resonant peak without significantly changing the frequency of the resonant peak.

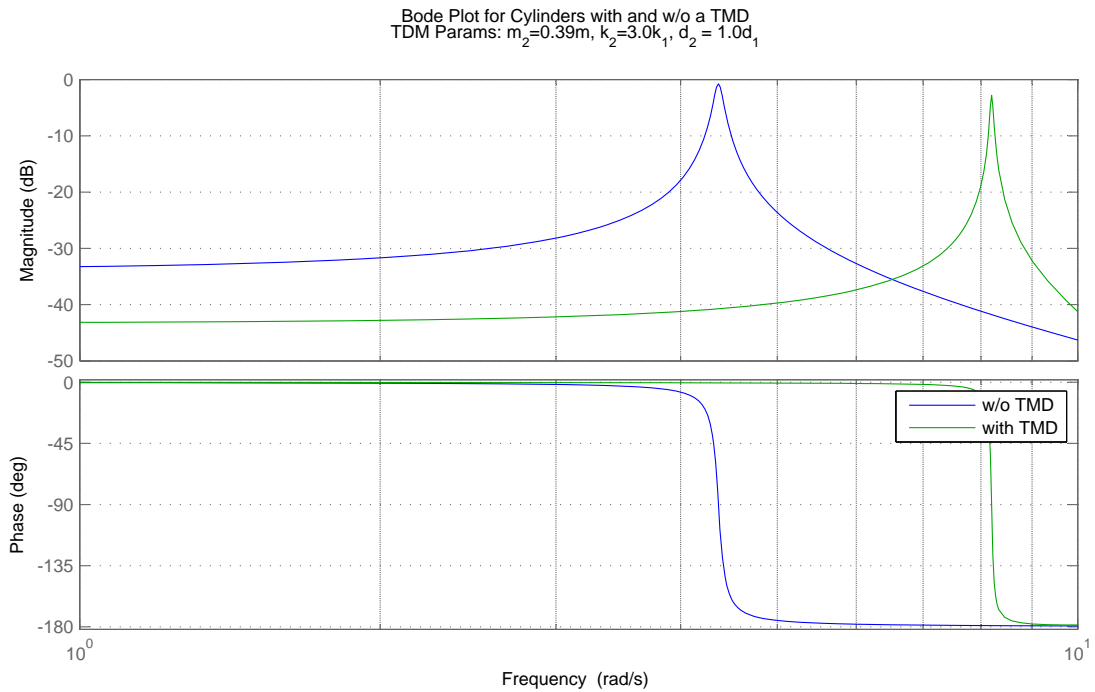
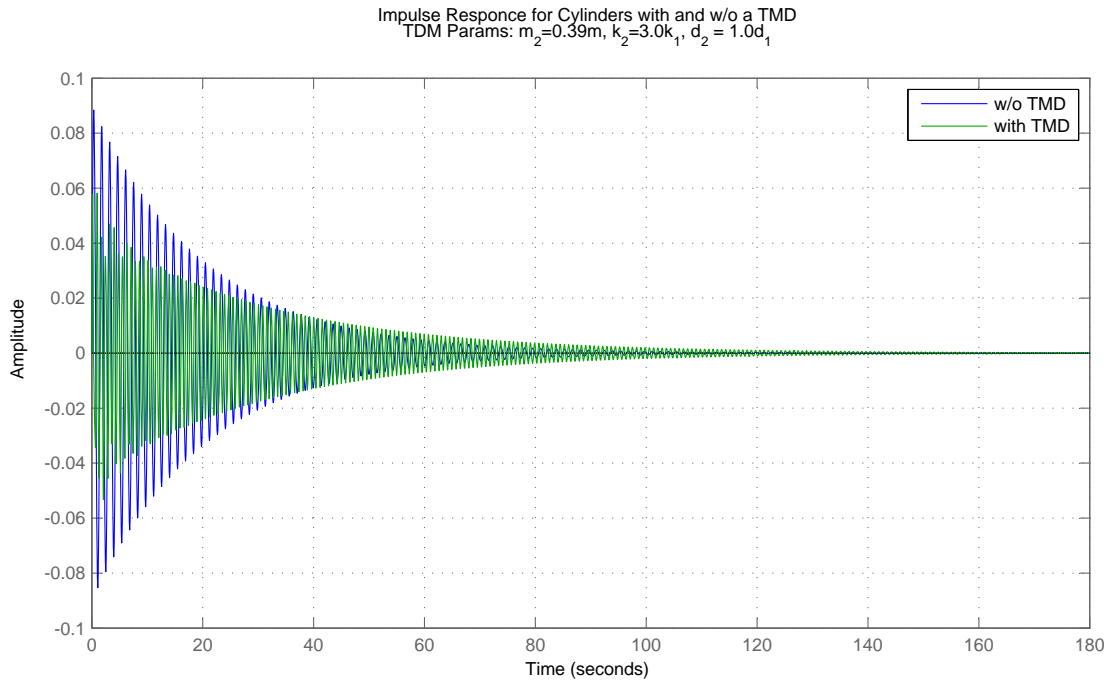


Figure E.3: The impulse response and Bode plots showing how a tuned mass damper could be used to improve a cylindrical buoy's response by shifting the resonant peak to a region that is less of a concern for the system and by reducing the magnitude of the overall response across a broad range of frequencies.

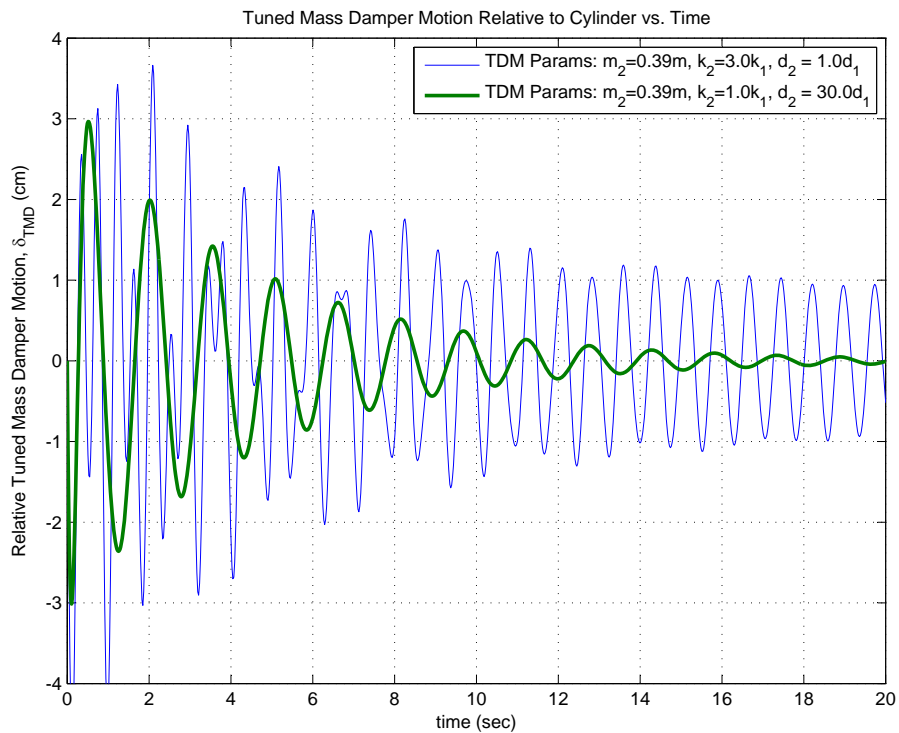


Figure E.4: The relative motion between the TMD mass and the cylinder for the two TMD implementations described in the text. The implementation with the stiffer spring and weaker drag (blue) requires approximately ± 4 cm of travel (or 3.2 inches of total travel). The implementation with weaker spring and more drag (green) requires approximately ± 3 cm of travel (2.4 inches total travel) to be effective.

Appendix F

Large Test Cylinder Data

This appendix contains the plots of the roll and pitch data for the individual inclined release trials using the large instrumented cylinder.

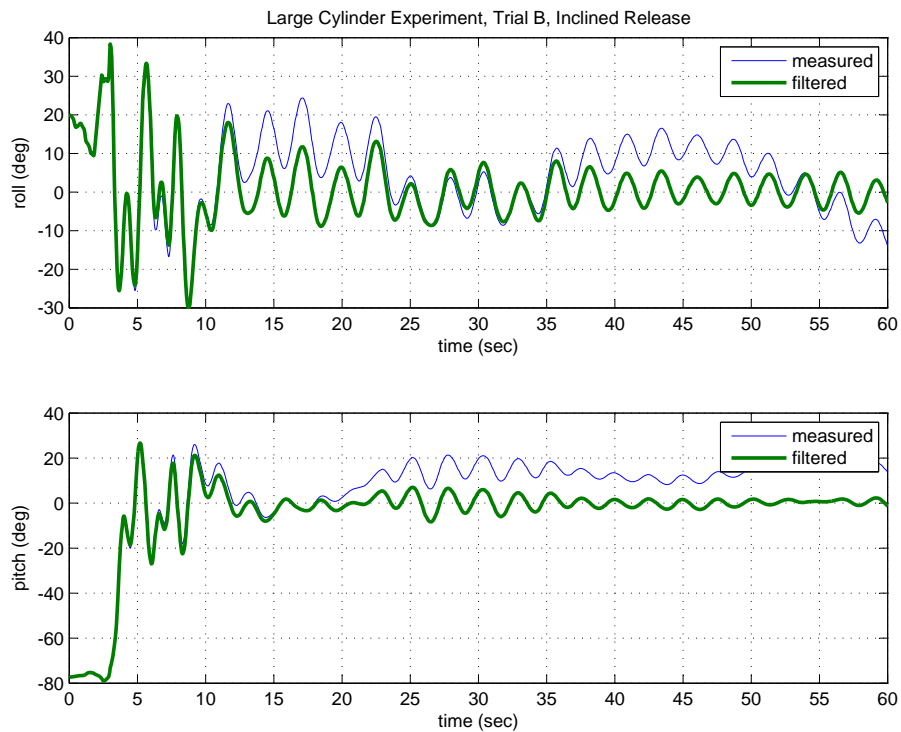


Figure F.1: Roll and Pitch Values from the Large Test Cylinder Experiment, Trial B. Trial B was an inclined release trial where the cylinder was released from 81 degrees away from the vertical (38 degrees in roll and -79 degrees in pitch). Release is at 2.5 seconds.

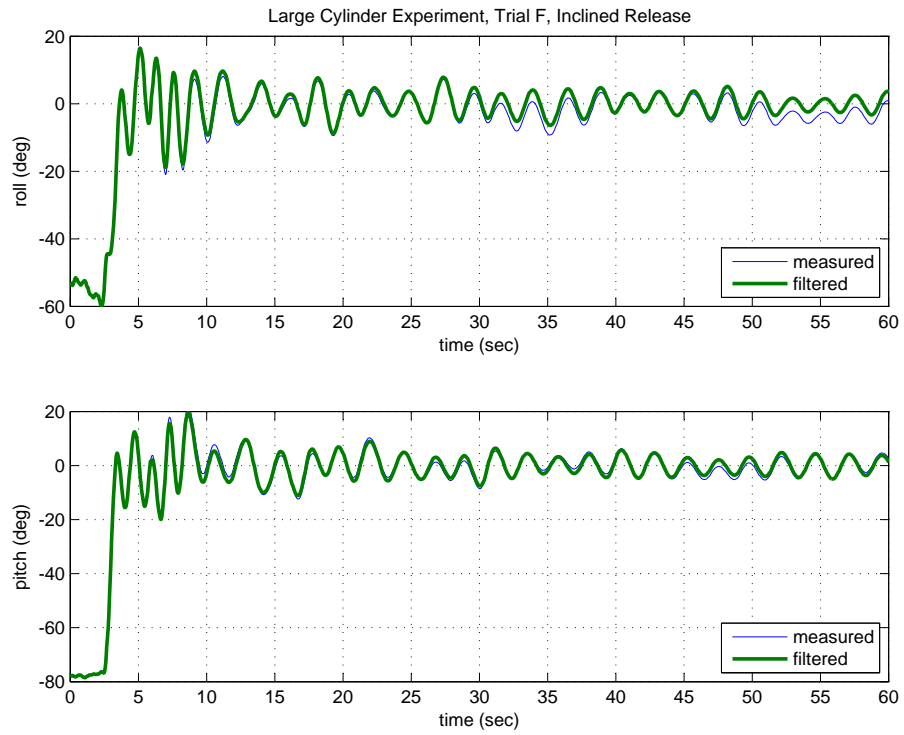


Figure F.2: Roll and Pitch Values from the Large Test Cylinder Experiment, Trial F. Trial F was an inclined release trial where the cylinder was released from 84 degrees away from the vertical (-60 degrees in roll and -78 degrees in pitch). Release is at 2.5 seconds.

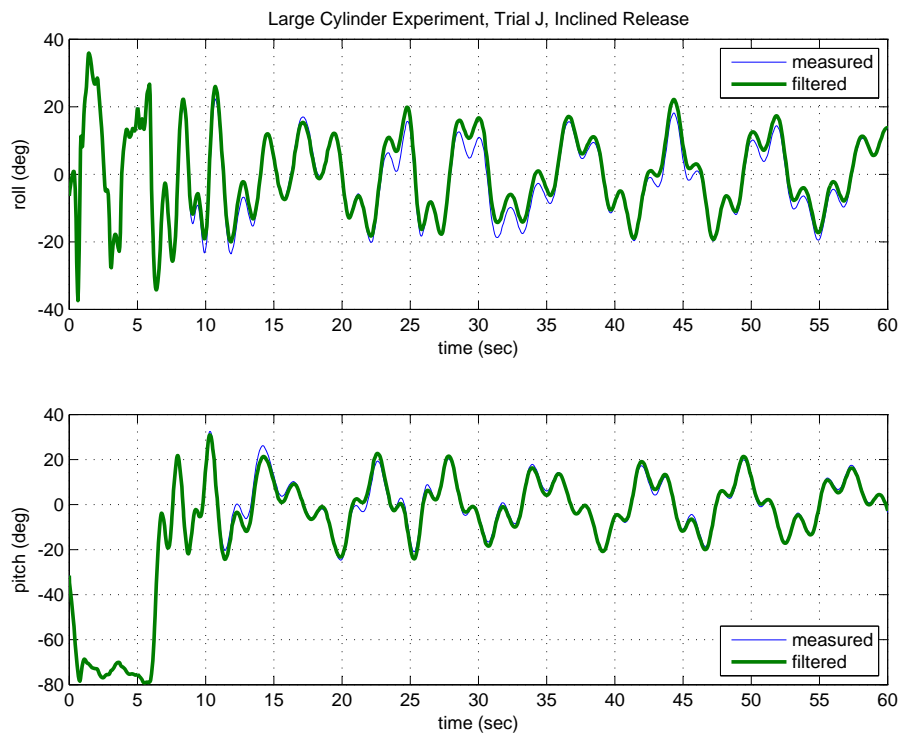


Figure F.3: Roll and Pitch Values from the Large Test Cylinder Experiment, Trial J. Trial J was an inclined release trial where the cylinder was released from 81 degrees away from the vertical (28 degrees in roll and -80 degrees in pitch). Release is at 6 seconds.

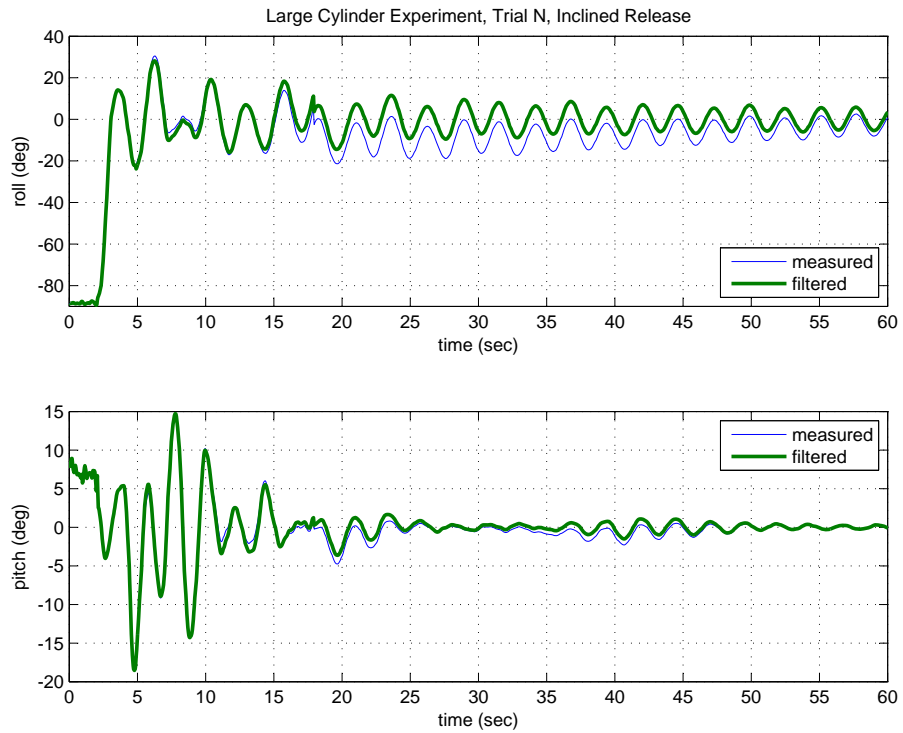


Figure F.4: Roll and Pitch Values from the Large Test Cylinder Experiment, Trial N. Trial N was an inclined release trial where the cylinder was released from 90 degrees away from the vertical (-90 degrees in roll and 7 degrees in pitch). Release is at 2 seconds.